Tuberculosis, Nanomedicine & the Zebrafish

Bridging the gap between *in vitro* and *in vivo models*

Thesis submitted for the degree of *Philosophiae Doctor*

by

Nils-Jørgen K. Dal

Section for Physiology and Cell Biology (FYS-CELL)
Department of Biosciences
The Faculty of Mathematics and Natural Sciences
University of Oslo

2022

Series of dissertations submitted to the
Faculty of Mathematics and Natural Sciences, University of Oslo
No. 2566

ISSN 1501-7710

Print production: Graphics Center, University of Oslo.

Acknowledgements

First, I would like to express my sincere gratitude to my principal and subsidiary supervisors, Professor Gareth Wyn Griffiths and Dr. Federico Fenaroli. Thank you for the opportunity and for the all the guidance and assistance that helped me complete the marathon that a PhD truly is. I would also like to express my sincere appreciation to all the former members of Griffiths group I have had the privilege to work with. Dr. Martin Speth, Dr. Noelia Alonso-Rodriguez, Dr. Julien Rességuier, M.Sc. Agnese Kocere, M.Sc. Madhavi Bhandari and M.Sc. Shanawaz Khan, thank you for your scientific contributions and for your friendship throughout these years. Furthermore, a big thanks to the EM-imaging facility here at UiO, in addition to fascinating insight into the micro-world the EM crew always had a cup of coffee ready at hand!

This thesis is based on an international collaboration and all that played a part deserves my gratitude. The collaboration have given me the opportunity to get to know people from all over the world, including Germany, Belgium, USA, India and New Zealand. Without this unique network of scientists from various fields, the work presented here would not be possible. Thank you for your scientific efforts and perspectives and of course friendship.

At the end, I would like to express my appreciation and love to my parents, Irene and Gard, my brothers John-Kristian and Jostein, my grandparents Britt and Nils and my fantastic in-law family. Thank you for your support and encouragement. You are all extremely important to me and I wish you all the best.

Finally, Christina, the love of my life, you are everything to me. Over eight years, and counting, we have built a life and a family together. On October 31 2020, our beautiful daughter Mie was born. She has truly changed my life and made me realize what is important in life. Now we are blessed with the advent of a second child this fall. I cannot wait to see what the future brings us!

I dedicate my PhD and this thesis to my two children; Mie and Henry Heiestad Dal, I love you with all my heart.

Table of contents

List of papers

Paper I: Zebrafish Embryos Allow Prediction of Nanoparticle Circulation Times in Mice and Facilitate Quantification of Nanoparticle–Cell Interactions.

Nils-Jørgen Knudsen Dal*, Agnese Kocere*, Jens Wohlmann*, Simon Van Herck, Tobias A. Bauer, Julien Rességuier, Shahla Bagherifam, Hilde Hyldmo, Matthias Barz, Bruno G. De Geest, and Federico Fenaroli, published in Small (2020).
* Equal contribution

Paper II: Biodistribution of surfactant-free poly(lactic-acid) nanoparticles and uptake by endothelial cells and phagocytes in zebrafish: Evidence for endothelium to macrophage transfer.

Julien Rességuier, Jean-Pierre Levraud*, **Nils-Jørgen Knudsen Dal***, Federico Fenaroli, Charlotte Primard, Jens Wohlmann, Gabrielle Carron, Gareth W. Griffiths, Dominique Le Guellec, Bernard Verrier, published in Journal of Controlled Release (2021).
* Equal contribution

Paper III: Rifampicin Nanoformulation Enhances Treatment of Tuberculosis in Zebrafish.

Jiří Trousil, Zdeňka Syrová, **Nils-Jørgen Knudsen Dal**, Dmytro Rak, Rafał Konefał, Ewa Pavlova, Jana Matějková, Dušan Cmarko, Pavla Kubíčková, Oto Pavliš, Tomáš Urbánek, Marián Sedlák, Federico Fenaroli, Ivan Raška, Petr Štěpánek, Martin Hrubý, published in Biomacromolecules (2019).

Paper IV: The zebrafish embryo as an *in vivo* model for screening nanoparticle-formulated lipophilic anti-tuberculosis compounds.

Nils-Jørgen Knudsen Dal*, Martin Speth*, Kerstin Johann, Matthias Barz, Claire Beauvineau, Jens Wohlmann, Federico Fenaroli, Brigitte Gicquel, Gareth Griffiths and Noelia Alonso-Rodriguez, published in Disease Models & Mechanisms (2022).
* Equal contribution

Paper V: Π-Π Interactions Stabilize PeptoMicelle-Based Formulations of Pretomanid Derivatives Leading to Promising Therapy Against Tuberculosis in Zebrafish and Mouse Models.

Nils-Jørgen Knudsen Dal*, Gabriela Schäfer*, Andrew M. Thompson*, Sascha Schmitt, Natalja Redinger, Noelia Alonso-Rodriguez, Kerstin Johann, Jessica Ojong, Jens Wohlmann, Andreas Best, Kaloian Koynov, Rudolf Zentel, Ulrich E. Schaible, Gareth Griffiths, Matthias Barz and Federico Fenaroli, manuscript submitted to Biomaterials (2022).
* Equal contribution

List of papers not included in the thesis

Real-time imaging of polymersome nanoparticles in zebrafish embryos engrafted with melanoma cancer cells: Localization, toxicity and treatment analysis.

Agnese Kocere*, Julien Rességuier*, Jens Wohlmann, Frode Miltzow Skjeldal, Shanawaz Khan, Martin Speth, **Nils-Jørgen Knudsen Dal**, Matthew Yoke Wui Ng, Noelia Alonso-Rodriguez, Edoardo Scarpa, Loris Rizzello, Giuseppe Battaglia, Gareth Griffiths and Federico Fenaroli, published in EBioMedicine (2020).

End Group Dye-labeled Polycarbonate Block Copolymers for Micellar (immuno-)Drug Delivery.

Christian Czysch, Carolina Medina-Montano, **Nils-Jørgen Knudsen Dal**, Thi Dinh, Yannick Fröder, Pia Winterwerber ,Konrad Maxeiner, Hans-Joachim Räder, Detlef Schuppan, Hansjörg Schild, Matthias Bros, Bernhard Biersack, Federico Feranoli, Stephan Grabbe, Lutz Nuhn, published in Macromolecular Rapid Communications (2022).

Antibiotic-Loaded Amphiphilic Chitosan Nanoparticles Target Macrophages and Kill an Intracellular Pathogen

Jiří Trousil, **Nils-Jørgen Knudsen Dal**, Federico Fenaroli, Inbar Schlachet, Pavla Kubíčková, Olga Janoušková, Ewa Pavlova, Miša Škorič, Kateřina Trejbalová, Oto Pavliš, Alejandro Sosnik, published in Small (2022)

Abbreviations

BBB	Blood-brain barrier
BCG	Bacille Calmette-Guèrin
BDQ	Bedaquiline
BSL	Biosafety level
BMDM	Bone marrow derived macrophages
CDC	Centers for Disease Control and Prevention
CFU	Colony forming units
Ddn	F_{420}-deazaflavin-dependent nitroreductase
DLM	Delamanid
DLS	Dynamic light scattering
DOT	Directly observed treatment
DS-TB	Drug susceptible tuberculosis
DTH	Delayed-type hypersensitivity
EM	Electron microscopy
EMA	European Medicines Agency
EMB	Ethambutol
EPR	Enhanced permeation and retention
EPTB	Extra-pulmonary tuberculosis
ESF	European Science Foundation
FCCS	Fluorescence cross-correlation spectroscopy
FCS	Fluorescence correlation spectroscopy
FDA	Food and Drug Administration
FET	Fish embryo acute toxicity test
FPC	Fluorescent pixel count
HIV	Human immunodeficiency virus
HTS	High throughput screening
HV	Hindbrain ventricle
IGRA	Interferon gamma release assay
INF-γ	Interferon gamma
INH	Isoniazid
IR-TB	Isoniazid-resistant tuberculosis
LTBI	Latent tuberculosis infection
LZD	Linezolid
MDR-TB	Multidrug resistant tuberculosis
MFX	Moxifloxacin
MIC	Minimum inhibitory concentration
Mm	*Mycobacterium marinum*
MPEO-b-PCL	methoxy poly(ethylene oxide)-*block*-poly(ε-caprolactone)
Mtb	*Mycobacterium tuberculosis*
MTB complex	*Mycobacterium tuberculosis* complex
NHP	Non-human primate
nNF	Nitronaphtofuran
NPs	Nanoparticles
NT	Neural tube
NTM	Non-tuberculous mycobacteria
Pa	Pretomanid
PAS	*Para*-aminosalicyclic acid
PCV	Posterior cardinal vein
PD	Pharmacodynamics
PEG	Polyethylene glycol
PGL	Phenolic glycolipid
PI3K	Phosphatidylinositol 3-kinase
PI3P	Phosphatidylinositol 3-phosphate
PK	Pharmacokinetics
PLA	Poly(D,L lactic acid)
PLGA	Poly(D,L-lactic acid-*co*-glycolic acid)
PMs	Polymeric micelles
PTB	Pulmonary tuberculosis
PtpA	Protein tyrosine phosphatase A
PZA	Pyrazinamide
RIF	Rifampicin
RNIs	Reactive nitrogen intermediates
ROS	Reactive oxygen species
ROIs	Reactive oxygen intermediates
RPT	Rifapentine
RR-TB	Rifampicin-resistant tuberculosis
SDGs	Sustainable Development Goals
SIV	Simian immunodeficiency virus
SM	Streptomycin
TB	Tuberculosis
TDR-TB	Totally drug-resistant tuberculosis
TNF-α	Tumor necrosis factor alpha
TST	Tuberculin skin test
UN	United Nations
V-ATPase	Vacuolar ATPase
WHO	World health organization
XDR-TB	Extensively drug-resistant tuberculosis
3R's	Reduce, replace and refine

Summary

Until the sudden arrival of the COVID-19 pandemic, tuberculosis (TB), caused by *Mycobacterium tuberculosis*, was ranked as the infectious disease that caused the highest mortality among humans. When the COVID-19 pandemic eventually fades out TB will likely regain its prominent position. For over half a century the same cocktail of four antibiotics have been used to treat drug-sensitive TB. The treatment is mostly effective but requires daily dosing of high concentrations of the antibiotics for at least six months. This is associated with severe side effects and often leads to patient non-compliance to the treatment, with the consequence of selecting for drug-resistant forms of the bacteria. The subsequent development of multi-drug resistance is a more serious and growing problem for successful TB therapy, where treatment options are limited, the available drugs much more toxic, more expensive and less effective. Around 2005 three powerful new TB drugs were synthesized that looked highly promising in clinical trials, namely bedaquiline, delamanid and pretomanid. These drugs, with novel mechanisms of action, were the first new TB drugs to be clinically approved for over 40 years. Now these drugs being used to treat patients suffering of multi drug-resistant TB. For over a decade the Griffiths group has been following the hypothesis that treatment can be improved, with increased efficacy and reduced side-effects, by formulation of drugs into nanoparticle systems that enable the possibility of targeted drug delivery, in addition to sustained and controlled drug release. A major challenge with nanoparticle research is how to study the *in vivo* behavior of the nanoparticles, since the commonly used animal models, such as the mouse, are opaque. High-resolution live-imaging is therefore very limited. An alternative animal model is the zebrafish, which is transparent in the early life stages. We introduced the see-through zebrafish embryo as a model in our lab to study the *in vivo* fate of intravenously injected nanoparticles. Furthermore the embryos are inoculated with *Mycobacterium marinum*, a natural TB pathogen in ectotherms such as fish and a close genetic relative to the human pathogen *M. tuberculosis*. The work presented in this thesis evaluates the potential of nanoparticle-mediated drug therapy against TB. Towards this goal I conducted detailed analysis of how different nanoparticle systems behave *in vivo* including the associated toxicity and therapeutic effects of NP-encapsulated drugs. This project would not have been possible without the support of an international team of expert collaborators.

Introduction

Tuberculosis disease

Origin of *Mycobacterium tuberculosis*

Tuberculosis (TB) in humans and animals are caused by the *Mycobacteria* species belonging to the *Mycobacterium tuberculosis* complex (MTB complex). The members of the MTB complex include *Mycobacterium africanum*, *M. bovis*, *M. canettii*, *M. caprae*, *M. microti*, *M. orygis*, *M. pinnipedii*, *M. suricattae M. mungi* and *M. tuberculosis* (Mtb) - the primary pathogen for TB in humans [1].

Mtb is a rod-shaped, non-motile, aerobic bacterium that is slow-growing with a generation time of about 24 hours at optimal temperature of 37 °C. In taxonomy, Mtb belongs to the phyla of Actinobacteria and to the genus *Mycobacterium* [2]. Mtb is characterized by a thick and complex cell wall, divided into three main layers [3]. Adjacent to the plasma membrane is the inner peptidoglycan layer, consisting of glycan strands of alternating N-acetylglucosamine and N-acetylmuramic acid, with adjacent strands connected via short cross-linked peptide side chains. The peptidoglycan layer is common for almost all bacterial species, providing structural integrity and osmotic stability [4]. In the middle is the arabinogalactan layer, a highly branched structure made of the sugar residues galactose and arabinose. This layer is covalently bound to and supported by the inner peptidoglycan layer and itself serves as an anchor point for mycolic acids. Mycolic acids, long fatty acid chains, form the outer layer and contribute to the fluidity and permeability of the cell wall [4]. Closely associated, but not covalently bound to the mycolic acids, are lipids and glycolipids that include important virulence factors such as trehalose dimycolate (cord factor) and phthiocerol dimycocerosates (manipulate host immune functions) [5, 6]. **Figure 1** shows a schematic illustration of the Mtb cell wall.

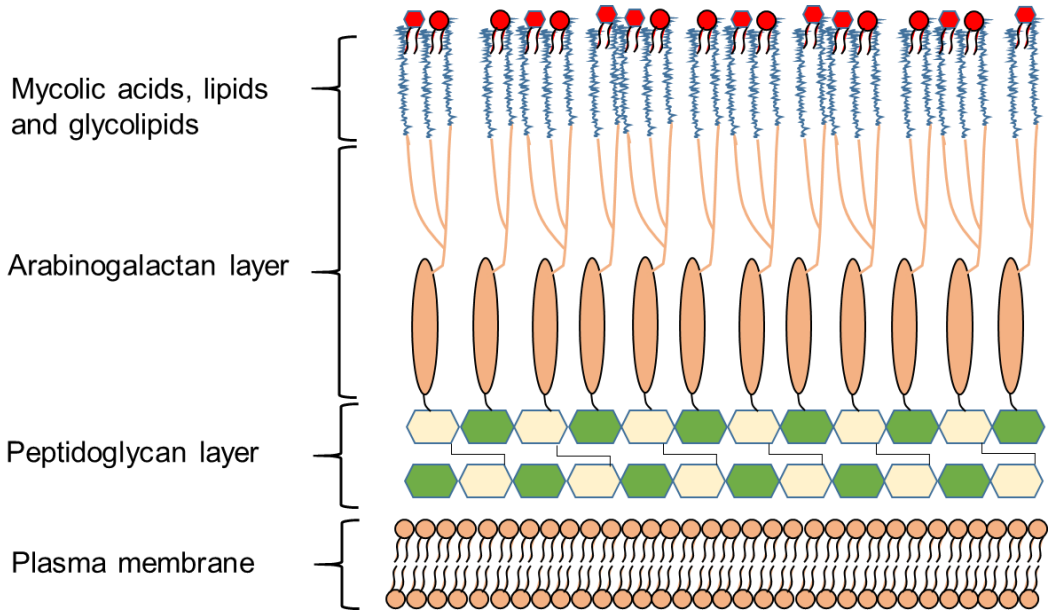

Figure 1. Schematic depiction of the Mtb cell wall, adapted from Brown *et al.* [7].

Diversification of the MTB complex into various sub-species, such as Mtb, is generally thought to have been driven purely by clonal evolution and genetic drift [8, 9]. However a more recent study suggests that this view should be moderated and that mutation, recombination and natural selection contribute significantly to the diversification [10]. The origin of Mtb and human TB is elusive and has been a matter of much debate. At the end of the last century, the consensus was that Mtb had evolved from *M. bovis*, the etiological agent of TB in cattle, due to the agricultural revolution, domestication of animals and zoonotic transmission [11]. Jared Diamond popularized this hypothesis in his Pulitzer Prize-winning book "*Guns, Germs and* Steel". However, the view changed with the advent of new technologies that made it possible to detect and analyze ancient and modern DNA of Mtb and other members of the MTB complex. Mtb and *M. bovis* were shown to have no direct evolutionary relationship, with origin from divergent lineages, with Mtb being more ancestral [12]. Based on microbial genomics and bioinformatics it has more recently been suggested that the MTB complex ascended from an ancient progenitor, *M. prototuberculosis*, dating back approximately 3 million years and potentially caused TB in early hominids [13]. This claim is however disputed [14]. The most recognized paradigm today is the "Out of and back to Africa" hypothesis [8], stating that the MTB complex emerged about 70,000 years ago as a companion of modern humans with subsequent global dissemination and diversification together with human migration and settlement [15]. Although the exact timeline and evolutionary

trajectory of the MTB complex and Mtb is not fully understood, TB as a disease has had a massive impact on humankind throughout history.

Infectious process; host-pathogen interactions

Mtb is a pathogen highly adapted to its human host, about 25 % of all humans asymptomatically carry the infection [16], but only 5-10 % will develop the active form of the disease [17]. Active TB disease is most common in adults (~ 90 %) and more prevalent in men compared to women [18]. TB infection can establish and develop in virtually any organ of the body and therefore several clinical manifestations exist (**Table 1**).

Table 1. Overview of different clinical manifestations of pulmonary- and extra-pulmonary TB, with a brief description. Adapted from Heemskerk *et al.* [19].

Clinical manifestations of TB	
Forms of pulmonary TB (PTB)	
Parenchymal disease	Typical PTB with granuloma formation followed by tissue softening, liquefaction and cavitation. Sputum production and hemoptysis being common.
Endobronchial TB	Special form of PTB affecting the trachea and major bronchi.
Intra-thoracic lymph node disease	Enlarged lymph nodes in the lungs. May obstruct airways, form abscesses with low inflammation, erode into surrounding tissue and disseminate.
Forms of extra-pulmonary TB (EPTB)	
Pleural TB	Build-up of fluid in the space between the lining of the lung and the lung tissue.
Miliary TB	Hematogenous dissemination of the bacilli and formation of small (1-3 mm) granulomas in visceral organs.
Extra-thoracic lymph node disease	Enlargement of lymph nodes outside the lungs, usually in the cervical region (known as scrofula).
Central nervous system (CNS) TB	Hematogenous spread to the brain and CNS. TB meningitis (TBM) being the most common type of CNS TB and the most lethal form of TB overall.
Pericarditis TB	Cardiac TB involving the pericardium.
Spinal TB	Commonly known as Pott's disease. Can cause deformities and in extreme cases result in paraplegia.
Other forms of EPTB	TB arthritis, gastrointestinal TB, urogenital TB, laryngeal TB. Any organ in the human body can potentially develop TB infection.

In general, the pathogenesis of TB can be divided into four stages [20]:

Stage 1: Transmission and initial infection. The respiratory route of exposure is how Mtb is transmitted among humans, and TB disease most commonly affecting the lungs, known as pulmonary TB (PTB). Thus, the different forms of TB disease usually arise from dissemination through coughing and sneezing of the bacilli from lungs in people suffering from active TB, following inhalation of bacteria laden droplets by other individuals and deposition in the alveolar space deep in the lungs. It has been shown that small droplets, between 1 and 5 μm in diameter, containing only a few Mtb bacteria are optimal for reaching the alveoli and establishing the infection [21, 22]. Droplets with a diameter larger than 5 μm are inclined to become trapped to the mucus membrane of the upper respiratory tract and later swallowed [21, 23]. In the alveoli, Mtb bacteria are engulfed by resident macrophages. The phagocytic process is initiated through activation of several surface receptors, mannose and complement receptors being the primary ones for initial detection of Mtb by the macrophage [24, 25]. A recent study in mice showed that alveolar macrophages are more disposed to Mtb infection, exhibiting lower stress and higher bacterial burden, compared to interstitial macrophages [26]. Another recent study revealed that the Mtb-infected alveolar macrophages translocated to the lung interstitium, providing an early niche for the infection to progress [27]. The encounter with alveolar macrophages is a pivotal stage in the infectious process and the outcome is largely determined by two factors; the degree of virulence of the Mtb bacilli and the bactericidal capacity of the infected macrophages. Different strains of Mtb vary in the degree of virulence and thus in their capacity to survive and replicate inside the macrophage, ranging from the extremes of avirulent to hypervirulent [28]. Furthermore, a macrophage in a highly activated state is better equipped to kill intracellular microorganisms. Classical activation of macrophages is through induction of Toll-like receptors by bacterial antigens and interferon-γ (IFN-γ) signaling [29]. Therefore, the combination of a strongly virulent bacterium ingested by a weakly activated macrophage would likely result in bacterial survival and ensuing intracellular replication.

Stage 2: Mtb exponential growth. Initial infection leads to activation of neighboring macrophages through cytokine production and ensuing auto-induction by a positive feedback loop. Successive intracellular Mtb replication results in rupturing of the host cell and further strengthening of the pro-inflammatory response that in turn will attract

blood monocytes and other inflammatory cells, such as dendritic cells, neutrophils and lymphocytes, to the site of infection [20]. Compared to the immature monocytes arriving from the periphery that are in a lower bactericidal state, the now highly activated resident macrophages are better equipped to phagocytose and kill the extracellular Mtb bacteria [30]. Before the onset of adaptive immunity, Mtb grows exponentially and there is a continuous accumulation of inflammatory cells.

Stage 3: Immunological equilibrium. In humans and mice, adaptive immunity to Mtb infection is dependent on T helper cells (Th cells), also known as $CD4^+$ lymphocytes [31, 32]. A characteristic of Mtb infection is a postponement in the onset of adaptive immunity relative to other acute infections, *e.g.* influenza [33, 34]. In humans, clinical data show that conversion to a positive tuberculin skin test (TST- an immunological diagnostic test) after primary infection takes about 5-6 weeks [35]. A study in Mtb-infected mice found that it took approximately two weeks (post aerosol infection) before antigen-specific T-cell responses were initiated [36]. The activation of adaptive immunity occurs when professional antigen presenting cells containing Mtb, typically dendritic cells, migrate from the site of infection to the mediastinal lymph node and activate $CD4^+$ T cells through antigen presentation, co-stimulation and cytokine production [37]. The recruitment and aggregation of succeeding waves of cells of the innate- and now activated adaptive immune system produces an inflammatory cascade of various chemokines and cytokines, tumor necrosis factor alpha (TNF-α) being the dominant one, at the infection site. In turn, this leads to the formation of the pathologic structure known as the granuloma or tubercle, a true hallmark of TB. Granuloma formation contains the infection and ends the exponential growth of Mtb. In humans, the granuloma is a highly organized structure, eventually causing a central necrotic zone in a semi-hypoxic state. The granulomatous core is enclosed by differentiated granuloma-specific macrophages such as foamy macrophages (rich in lipids), epithelioid macrophages (link adjacent cells), and giant cells (fused multi-nucleated macrophages), in addition to dendritic cells and neutrophils. The outer periphery of the structure is often a layer of lymphocytes together with a fibrous cuff walling off the granuloma from adjacent non-infected tissue [38-40].

Stage 4: Disease progression or arrest and potential reactivation.

Primary TB occurs if the infection is not contained by the immune responses and directly progresses into active disease. The initial granuloma (also known as the Ghon

focus), usually located amid the pleura and the body wall in proximity to the fissures separating the upper and lower lung lobes [41], will lose its solid structure, semi-hypoxic environment and the caseous (literally meaning “cheese-like”) foci will liquefy and provide excellent growth conditions for Mtb bacteria. In children, a secondary infection in the hilar lymph node is common. The secondary lesion in combination with the primary granuloma is called the Ghon complex. Healthy lung tissue is damaged by the continuous expansion of the granuloma and hematogenous dissemination and extra-pulmonary TB can occur if a blood vessel is breached.

Alternatively, the solid granuloma core with caseous necrosis and a semi-hypoxic environment can keep its structural integrity and inhibit bacterial growth; as a result, the infection may become dormant. This is usually referred to as latent TB infection (LTBI), defined as a positive response to immunological TB tests in the absence of clinical symptoms. LTBI is a somewhat vague and oversimplified concept that can be explained by both non-replicating bacteria and bacteria in a low metabolic state surviving within the body [42], or by metabolically active and replicating bacteria kept in check by the immune system. On a cellular level, LTBI more likely resembles a spectrum, where the two former explanations can occur to a varying degree depending on the immune response of the infected individual and the bacterial strain [43].

Furthermore, months or years after primary infection, LTBI can reactivate and progress into post-primary active disease, known as secondary TB. Reactivation of LTBI is generally considered a consequence of reduced immunity, often associated with old age, human immunodeficiency virus (HIV) co-infection, cancer, immunosuppressant drugs, etc. Reinfection however, distinct from reactivation, is infection with a second strain of Mtb and could result in secondary TB. The risk of developing secondary TB due to reinfection is higher among HIV-positive, compared to HIV-negative, individuals [44, 45]. In humans, two mechanisms that explain reactivation of LTBI have been identified. The first mechanism involves depletion in numbers and quality of $CD4^+$ T cells, which is the case in HIV co-infection [46]. The risk of developing TB disease dramatically increases shortly after HIV infection and continuous to rise with time [47]. The second mechanism involves blocking of the TNF-mediated immune responses, associated with the use of anti-TNF agents against inflammatory autoimmune diseases, which will interfere with both the cell-mediated- and the innate immune

responses [48]. Other risk factors for TB and reactivation of LTBI include malnutrition, diabetes, smoking and alcohol consumption.

Mycobacterium tuberculosis-macrophage interaction

Mtb replicates well extracellularly in the presence of oxygen, but the bacterium has also evolved the capacity to survive within its host cell, that is the macrophage. A major part of the life cycle is spent intracellularly where the bacterium manipulates the host cell for its own benefit. Mtb is internalized by classical phagocytosis that is dependent on a spectrum of different receptors. Under normal circumstances, the resulting intracellular vesicle called a phagosome would undergo phagosome maturation that is sequential fusion events with endocytic organelles culminating in lysosome fusion. Lysosome fusion and formation of the phagolysosome results in a hostile and bactericidal environment consisting of reactive oxygen and nitrogen intermediates (ROIs, RNIs), digestive enzymes, toxic peptides and low pH around 4.5 to 5.0 that effectively kills residing bacteria [49, 50]. However, Mtb inhibits phagosome-lysosome fusion through manipulation of host signaling pathways [51, 52]. Mtb achieves this phagosome arrest by a multitude of ways, *e.g.* retention of early endosomal markers and reduction of late endosomal markers and protein complexes involved in acidification and other bactericidal activities. Specifically, undermining and disrupting the functions of selected Rab proteins, phosphatidylinositol 3-kinase (PI3K), the vacuolar ATPase (V-ATPase) and the NADPH oxidase is known to play a role in phagosome arrest [53].

The Rab proteins regulate intracellular transport of vesicles, Rab5 and Rab7 being master regulators in the phagocytic pathway [54]. Phagosomes containing Mtb exhibit an alteration in Rab trafficking compared to phagosomes not containing Mtb [55].

On early endosomes the PI3K produces phosphatidylinositol 3-phosphate (PI3P), a phospholipid that recruits proteins involved in intracellular trafficking, protein sorting and assembly of protein complexes. Mycobacterial phagosomes contain less membrane bound PI3P than “normal” phagosomes [56].

In order to inhibit acidification, Mtb disrupts the V-ATPase proton pump both directly and indirectly. The secreted Mtb protein tyrosine phosphatase A (PtpA), interacts with V-ATPase and blocks its trafficking to the mycobacterial phagosome [57]. Furthermore,

Mtb induces a host degradative pathway that specifically targets a catalytic subunit of V-ATPase for ubiquitination and subsequently degradation [58].

The multiprotein complex NADPH oxidase catalyzes the transfer of electrons to oxygen (O_2) and generates reactive oxygen species (ROS), important for bacterial killing, but also poses a toxicity risk for the host. Thus, the protein complex is targeted to phagosomes containing pathogens and its assembly is firmly regulated. Mtb has taken advantage of the multi-regulated process, and by interfering with several steps, NADPH oxidase assembly at the mycobacterial phagosome is hindered [53].

It has also been shown that some Mtb strains are less adapted for subsistence within phagosomes. By an alternate adaptation they escape the vesicle, and reside in the cytoplasm [59].

Past to present; a story of tuberculosis

The history of tuberculosis in humans

The word *Tuberculosis* as a medical term for the disease was credited to the German professor of medicine Johann Schönlein (1793-1864) in 1829 [60], prior to this the disease went under other names, such as *Phthisis* (Greek word for wasting away), the "*White plague*" and *Consumption*. The disease now commonly referred to as TB has plagued humankind throughout recorded history and prehistory [61]. Mtb and other TB causing bacteria together with morphological signs of disease have been identified in animal and human remains dating back thousands of years. Additionally, descriptions of and references to TB can be found in the historical written record, *e.g.* the bible. **Table 2** provides examples of TB in ancient times.

Table 2. Examples of morphological and genetic identification of TB disease and recorded sources on TB from ancient times.

TB in pre- and ancient history
Morphological and DNA identification of human and animal TB • North America: Extinct bison, ~17,000 years ago (YA) [62] • Israel: Woman and child at the site of Atlit-Yam, ~9000 YA [63] • Germany: Individuals from three different sites, ~7000 YA [64] • Egypt: Skeleton of a child from the predynastic period, ~5400 YA [65] • Egypt: Male mummy from the New Kingdom, ~1500 YA [66] • Peru: Pre-Columbian human skeletons, ~1000 YA [67]
Recorded sources on TB • The Code of Hammurabi, Babylonian law, mentions a chronic lung disease likely to be TB, ~4000 YA [68] • Rig Veda, Hindu text, ~3500 YA [69] • Old Testament biblical reference to TB, ~3000 YA [70] • TB known as phthisis in classical Greece, ~2500 YA [61] • Chinese medical work, the *Huang TiNei-Ching*, ~2300 YA [69]

The collective death toll of TB through time may be the largest of all microbial diseases. It is estimated that only in the past two centuries about 1 billion people succumbed to this disease [71]. Because of the high mortality, many clinical manifestations and elusive nature of the disease, TB have been hemmed in mystery, myths and superstition. For instance, scrofula, today known to be cervical lymphatic TB, was referred to as the King's Evil in medieval times and it was believed that the crowned heads of England and France could cure the disease by royal touch. The practice lasted for more than 500 years and ended together with divine monarchy [72]. Another bizarre example of superstition is the folklore connecting TB to vampires. In 19th century New England the vampire lore was particularly strong, and it was believed that deceased TB victims would return as vampires and feed on their relatives until they also perished [73].

In the 18th and 19th centuries, TB reached pandemic proportions in Europe and North America. In the mid-18th century the mortality rate in parts of the western world reached as high as 1000 per 100,000 humans per year [61]. In England and Wales around four million succumbed to TB in the latter half of the 1800s and early 1900s, with about one million of them below the age of 35 [74]. During these centuries of death and despair,

scientific investigations increased our understanding of the disease. In 1720, a medical doctor named Benjamin Marten (1690-1752) published a book titled "*A new Theory of Consumptions: More Especially of a Phthisis or Consumption of the lungs*". In this work, Marten presents his hypothesis of TB being the manifestation of microscopic living creatures, *Animalcula*, invading and living inside the body. This was a precursor of the modern germ theory; however, the novel insight did not gain traction at the time [75]. Our modern understanding of TB can be traced back to the French physician Renè Laënnec (1781-1826). In 1804, he proposed that the diseases known as *phthisis*, *scrofula* and *consumption* had a common cause and should therefore be considered as one disease with different clinical phenotypes instead of distinct diseases. The common cause, identified by autopsy, was the tubercle more commonly today called a granuloma. This became known as the Unity Theory [60]. Laënnec also invented the stethoscope, that greatly aided in correct diagnosis of TB, and he is considered as the founder of clinical pulmonary medicine [76]. At the time, it was a matter of debate whether TB was a heritable or transmissible disease. This was resolved in 1865 when the French physician Jean-Antoine Villemin (1827-1892) showed that TB was contagious by inoculating a rabbit with liquid extract from a tuberculous human lung. The rabbit appeared healthy at first sight, nonetheless autopsy three months post infection revealed progressive TB disease. What Villemin did not know is that rabbits are relatively tolerant for Mtb infection; had he decided to work with the more susceptible guinea pig model his results would have been even more convincing [61].

On the 24th of March 1882, a major breakthrough occurred when the German microbiologist Robert Koch (1843-1910) announced the identification of the tubercle bacillus as the etiological agent for TB. He had visualized the bacteria in infected tissue of animals by alkaline methylene-blue stain for 24 hours followed by vesuvin (Bismark brown) as a contrast stain [77]. Koch originally named the bacterium *Tubercle bacillus*; it was renamed in 1883 to *Bacterium tuberculosis* and in 1884 changed to *Bacillus tuberculosis*. In 1896 it yet again changed and received its current name (Mtb) [78]. Koch was awarded the Nobel Prize in Medicine or Physiology in 1905 and the day when he announced his discovery, March 24, is now annually recognized as World TB day, which reflects the magnitude of his accomplishment. The identification of the infectious agent of TB spurred and accelerated research on the topic. Paul Ehrlich (1854-1915), the founder of chemotherapy and Nobel laureate in 1908 [79], attended

Koch's lecture on 24 March 1882. Soon after he improved the staining method of the bacillus by applying heat and acid. This method was further refined by two German doctors, Franz Ziehl (1859–1926) and Friedrich Neelsen (1854–1898), and resulted in the Ziehl-Neelsen acid-fast stain that is still in use today [77]. Koch, although involved in many types of bacteriological research, had a special interest for TB. In 1890, he presented a possible cure for TB that he called tuberculin. A substance isolated from the TB bacilli, which was claimed to inhibit infection and supposedly blocked disease progression in already infected guinea pigs. What Koch observed was the inflammatory hypersensitivity response of a tuberculous animal (or tuberculin sensitized animal) to reinfection with Mtb, in other words resistance to reinfection. The observation is today known as the "Koch phenomenon". Unfortunately, tuberculin turned out to be ineffective as a cure for TB in humans and even caused severe immune reactions in several patients [77].

However, tuberculin and the "Koch phenomenon" paved the way for screening and early diagnosis of asymptomatic TB infection, starting with the research of Clemens von Pirquet (1874-1929) published in 1909 [80], that over time turned in to the modern tuberculin skin test (TST), still being in clinical use today [81]. As a curiosity, Norway was the last country in the world to make the switch from the original Pirquet's skin test to the newer and internationally applied Mantoux test in 2004 (https://www.nrk.no/norge/slutt-pa-pirquet-proven-1.512307).

The history of tuberculosis vaccination and chemotherapy

In the early 1900s, two French scientists, Albert Calmette (1863-1933) and Camille Guèrin (1872-1961), embarked on their research aiming toward an effective vaccine against TB. By continuous sub-culturing of a virulent *M. bovis* strain in a bile, glycerin and potato medium for over 200 passages over 11 years, the strain became attenuated and non-virulent in animals. They named the new strain Bacille Calmette-Guèrin or simply BCG [82]. In Paris, France 1921, the vaccine was administered to a human subject for the first time. The subject was a baby boy, whose mother had died of TB and now was in the care of his grandmother, also suffering of TB. It was a high probability that the boy would be infected and dead within his first year of life. With this in mind, he was given the BCG vaccine and fortunately, he survived and did not display any symptoms of TB growing up. The successful vaccination initiated several BCG

vaccine trials and following mass vaccination of infants [83]. There were questions surrounding the safety of the BCG vaccine when it was introduced, especially after the tragic Lübeck disaster in 1930 where 250 infants received the vaccine and within one year 73 died and 135 developed TB but ultimately recovered. It was later shown that this tragedy was due to contamination with Mtb and not caused by the attenuated BCG strain [82, 83]. Questions regarding its efficacy was debated then and still is a matter of controversy and divergent data; regardless of that BCG is the only clinically approved vaccine against TB to date [82].

Prior to the age of antibiotics, there was no real effective cure against TB. The alternatives that existed were rest, fresh air and a nutritious diet recommended by the sanatorium movement initialized by Herman Brehmer in 1859 [84]. Alternatively, various forms of thoracic surgery were applied, such as induced pneumothorax and thoracoplasty, in order to collapse and rest the infected lung [69]. With Wilhelm Röntgen's (1845-1923) discovery of X-rays in 1895 and the possibility of chest radiography for TB diagnosis and localization of affected area of the lung, thoracic surgery further advanced. Different thoracic surgery procedures are still being applied today, especially in the context of treatment failure. The sanatorium treatment disappeared with the arrival of successful chemotherapy. The age of antibiotics and effective drugs against TB dramatically changed how we perceived the disease. Suddenly TB was curable. To illustrate how immensely this has directly affected human lives; only in the period of 2000-2020, proper diagnosis and treatment saved an estimated 66 million people from TB [85].

The age of chemotherapy started with Paul Ehrlich and Sahachiro Hata in 1910, when they discovered arsphenamine, a synthetic chemical also known as compound 606 or Salvarsan, and found it to be effective against syphilis. Although the injected drug was highly toxic and led to severe adverse effects, arsphenamine was the treatment of choice for syphilis until more effective and safer drugs such as penicillin became common after the Second World War. Penicillin, the first real antibiotic, was discovered in 1928 and published in 1929 by the Scottish physician Alexander Fleming (1881-1955), but not used for treatment purposes before the 1940s [86]. Penicillin belongs to the class of antibiotics called β-lactams. These are antibiotics with a broad spectrum of activity, both against gram-positive and gram-negative bacteria, which work by inhibiting the biosynthesis of the peptidoglycan layer of the bacterial cell wall [87].

Penicillin saved thousands of allied soldier's lives and was a contributing factor in the defeat of Nazi Germany [88]; unfortunately penicillin was not effective against TB.

In 1944 the two first moderately effective drugs against TB, but with substantial side effects, were introduced. These were *para*-aminosalicyclic acid (PAS) and streptomycin (SM) [89, 90]. **Table 5** in the chapter entitled "Prevention, diagnosis and treatment of TB" describes the molecular target and mechanism of action of these and other commonly applied anti-TB drugs. Bacterial resistance against both drugs were rapidly observed after administration as single-drug therapy. A clinical trial by the British Medical Research Council set-out to investigate the potential benefit of multidrug treatment and based on the study outcome, the practice of combinatorial drug treatment of TB became the dogma [91].

A major breakthrough in the treatment of TB occurred in 1951 when isoniazid (INH), originally synthesized in 1912 by two PhD candidates and then forgotten [86], was found to be highly effective against TB and relatively well tolerated in humans [92]. The discovery of INH led to the triple therapy drug regimen of daily oral administration of INH and PAS for 18-24 months in addition to intramuscular injections of SM for the first 6 months. This approach remained as the standard treatment of TB for many years [86]. The 1940's through 1960's were a period of drug discovery and research directed toward TB that resulted in efficient treatment against drug-susceptible strains. **Table 3** provides an overview of the drugs introduced during this productive era of anti-TB drug discovery.

Table 3. Chronological list of anti-TB drugs after the year of (re-)discovery during the mid-20th century, also called the golden era of drug discovery

Golden era of anti-TB drug discovery
• 1943, streptomycin [90]
• 1944, *para*-aminosalicyclic acid [89]
• 1951, isoniazid [92]
• 1952, pyrazinamide [93]
• 1954, cycloserine [94]
• 1956, ethionamide [95]
• 1957, kanamycin [96]
• 1957, class of rifamycins [97]
• 1960, capreomycin [98]
• 1961, ethambutol [99]
• 1963, rifampicin [100]

The therapeutic successes of this period regrettably also resulted in less attention from the public and from researchers due to declining TB cases and consequently less funding and continued research toward improved therapy options. This unfortunately led to resurgence of TB all over the world, and especially drug resistant TB, at the end of the 20th century

Tuberculosis today; a global health threat

The presumption that TB was a disease of the past in industrialized countries and close to be under control in the developing world turned out to be seriously wrong. In the 1980's TB was back with a vengeance after decades of decline due in large part to its deadly association with the then newly identified HIV virus. HIV-coinfection, with its gradual destruction of the cell-mediated immune responses made people with latent TB much more likely to develop active disease, which complicated successful treatment [46]. In the United States, TB cases increased by 20 % between 1985 and 1992 [86]. In New York the situation was especially dire and TB cases increased by approximately 150 % during the 1980s. Since TB is a disease that thrives under socioeconomic conditions such as poverty and inequity, the greatest toll of the remerging disease was, and still is, the developing world. The regions with the highest incidence rates are South-East Asia, Africa and the Western Pacific (**Figure 2**). By the early 1990s, it was estimated that 8 million people developed TB disease and 3 million

people died from TB every year. This led to the prediction that TB would cause 30 million, or more, deaths in the following decade if no action was taken. Therefore, on April 23rd 1993, the World Health Organization (WHO) declared TB a global emergency in an effort to end years of global neglect toward TB.

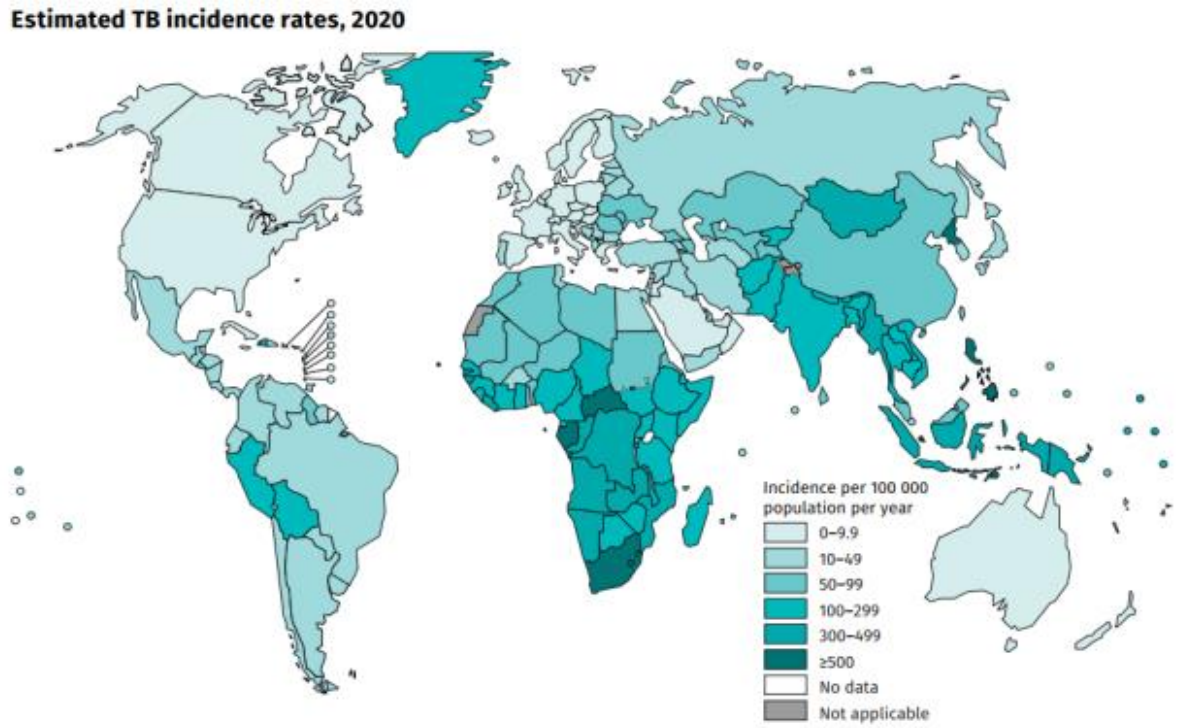

Figure 2. Estimated TB incidence rates for 2020. Taken from the WHO Global Tuberculosis Report 2021 [101].

The declaration spurred global engagement, high-level political commitment and multisectoral collaboration in the fight against TB. The two current global political strategies for ending the TB epidemic are the WHOs 'End TB' strategy and the United Nations (UN) 'Sustainable Development Goals (SDGs)', committed to by all member states in 2014 and 2015, respectively. The strategies include sub-goals and targets of reducing fatalities and incidence of TB and making treatment affordable for all in need, thereby preventing economic ruin for affected families. Both strategies were reaffirmed and new goals were added in 2018 when the UN General Assembly arranged a high-level meeting on TB. **Table 4** outlines the goals and milestones set in the strategies.

Table 4. General overview of the global political strategies and goals toward ending the TB epidemic. Adapted from the WHO Global Tuberculosis Report 2021 [101].

Joint vison	**A world free of TB**			
WHO End TB Strategy	**Milestones**		**Targets**	
(2014)	**2020**	**2025**	**2030**	**2035**
Absolute number of TB deaths (% reduction compared with 2015)	35%	75%	90%	95%
TB incidence rate (% reduction compared with 2015)	20%	50%	80%	90%
Households facing catastrophic costs due to TB	0%	0%	0%	0%
SDG Target 3.3 (2015)	By 2030, end the epidemics of AIDS, TB, malaria and neglected tropical diseases, and combat hepatitis, water-borne diseases and other communicable diseases.			
UN political declaration (2018)	**General goal**		**Included in goal**	
People treated for TB from 2018 to 2022	40 million		- 3.5 million children - 1.5 million people (115 000 children) with drug-resistant TB	
People provided with TB preventive treatment from 2018 to 2022	≥ 30 million		- 6 million with HIV - 4 million < 5 years - 20 million people in other age groups	
Funding	- ≥ US$ 13 billion per year for universal access to TB prevention, diagnosis, treatment and care by 2022 - ≥ US$ 2 billion per year for TB research from 2018 to 2022			

The joint global effort toward ending TB has resulted in a steady, but slow decline in TB cases and mortality. Since TB was declared a global emergency in 1993, the total annual mortality has been reduced by over 50 %. Before the COVID-19 pandemic, Mtb was causing more human deaths than any other single infectious agent. According to the WHO Global Tuberculosis Report 2021 [101], an estimated 1.3 million HIV-negative people and an additional 214 000 HIV-positive people died from TB in 2020. Both figures represent an increase from 2019 and the first annual increase since 2005. The COVID-19 pandemic has had a detrimental impact and reversed years of progress in the fight against TB. In addition to an increased absolute number of deaths, there

were an 18 % reduction in TB case notifications and only a minor estimated decline in TB incidence (~ 2 % for the incidence rate *per capita* and ~ 1 % for the total number of cases) compared to 2019 [101]. None of the milestones for 2020 in the WHO End TB Strategy were reached on a global level, however some targets were achieved on regional and country levels. If we are to succeed in ending the global TB pandemic by 2030, as the leaders of all UN member states agreed to in 2018, we need to increase both the effort and funding. Time is running out.

Prevention, diagnosis and current treatment of tuberculosis

As described above, many challenges remain in order to reduce and eventually end the TB epidemic. Among the hurdles that need to be tackled are inadequate prevention and diagnostic services and sub-optimal treatment options and accessibility. A major concern is the increasing prevalence of antibiotic resistance and subsequent TB treatment complication or failure, addressed further below. The following section will address the current status and problems associated with prevention, diagnosis and treatment of TB.

Prevention of TB. Most of the public attribute the decline in TB incidence and death of the early 1900's to modern medicine. However, the TB decrease in the western world started long before the discovery of any medical interventions such as the BCG vaccine or anti-TB drugs. Analysis of historical health data show that social factors, such as better housing conditions and nutritional status, in addition to improved public health interventions were the main drivers of the decline in TB at the time [102]. This also holds true today and through political action aimed at reducing TB drivers such as poverty, hunger, HIV, diabetes, smoking and alcohol consumption the global burden of TB can be reduced.

Another approach to prevent active TB disease and thereby reduce the cumulative global burden of TB is the administration of preventive treatment (usually daily doses of isoniazid for 6 months) to latently infected individuals of humans that belong to groups that have a particularly high risk of disease progression. Including people infected with HIV, for whom TB is the most common cause of fatality and preventive TB treatment is therefore of vital importance [103]. In the case of active TB, a pillar of

public health measures is the directly observed treatment (DOT) strategy, in which trained health professionals provides and observes that the anti-TB drugs are taken as prescribed by the patients. In recent time the DOT strategy has become more digitalized through the use of smartphones that facilitate direct communication via video calls and text messaging. Although the data are sparse it support treatment efforts, reduces costs and is convenient for the patient [104].

There exist only one clinically approved vaccine for the prevention of TB, namely the BCG vaccine. It has been shown that BCG vaccination of infants has a high efficacy, > 70 % for the first five years, against miliary and meningitis TB, which is more common in children than adults [105]. The vaccine efficacy in adults is disputed, but there is a consensus that it offer protective effect against TB although this vary among populations and decreases with time [106, 107]. A recent cross-sectional analysis in the United Kingdom found evidence for a protective effect against LTBI by BCG, the vaccine effectiveness being 30 % [108].

Diagnosis of TB. Diagnosis of active TB include sputum smear microscopy, chest X-ray and/or rapid molecular tests for detection of Mtb, *e.g.* the Xpert MTB/RIF assay that detects Mtb and potential resistance to the first-line anti-TB drug rifampicin (RIF) directly from sputum samples within two hours [109]. However, the gold standard for diagnosing and confirming TB disease remains culture-based methods, a tedious process that may take up to eight weeks in solid media culture, subsequently followed by drug-susceptibility testing and genotyping [101].

Reactivation of LTBI has been recognized as a major contributor of new TB cases and its diagnosis is of great importance for preventing active TB and potential transmission in the future. Current methods used to diagnose LTBI include skin tests, such as the more than 100 year old tuberculin skin test (TST) introduced above. The TST, being a cheap and simple procedure to perform, has been widely used as a diagnostic tool of LTBI. Yet, the TST is far from perfect, it does not distinguish LTBI from active disease in its early stages or from persistent TB immunoreactivity after successful clearance of initial infection. Furthermore, it requires an incubation period of 48-72 hours and a follow-up visitation from medical personnel. In addition, previous BCG vaccination can provide false positives and a weak immune system can result in false negatives, the test can also cross-react with non-tuberculous mycobacteria (NTM) species [110]. New skin tests, not yet in wide clinical use, have been developed that detect immune

responses elicited by the Mtb specific antigens ESAT-6 and CFP-10 in order to circumvent false positives due to BCG vaccination and cross-reactivity with NTM [111]. A different approach to the commonly used TST, is IFN-γ release assays (IGRAs). IGRAs measure the IFN-γ production, in response to Mtb antigens, from sensitized lymphocytes in a blood sample. Although IGRAs being more specific than the standard TST, the problem of differentiating LTBI from early stages of active disease or persistent TB immunoreactivity remains [111].

Treatment of TB. In the absence of antibiotic treatment, death is the most likely outcome if suffering from active TB and being Mtb sputum positive. A systematic review of duration and fatality of untreated, sputum-positive TB patients prior to the antibiotic era found that the mean mortality was 70 % within 10 years post diagnosis [112]. Today TB is curable, the success rate being at least 85 % for people infected with drug susceptible TB (DS-TB) and enrolled in the well-established treatment regimen involving first-line anti-TB drugs (**Table 5**). The preferred treatment of DS-TB consists of daily oral administration of the four first-line drugs, INH, RIF, pyrazinamide (PZA) and ethambutol (EMB), for a total of six months. The regimen is divided into an intensive phase that last for two months and includes daily dosing of all the four drugs, followed by a four month continuation phase of only INH and RIF [113]. Although the standard “short-course” treatment is highly effective, it involves drugs that are associated with adverse effects that are generally uncomfortable and a burden for the patient. All in all, over six months, this regimen requires 182 consecutive doses amounting to a total of 476 individual drug tablets to be taken orally. A reduction in treatment duration and/or amount of antibiotics needed for successful therapy would be a great improvement for the receiving patient. A recent clinical trial showed that a four month multidrug regimen of rifapentine (RPT), moxifloxacin (MFX), INH and PZA was equally effective to the standard six months regimen in the treatment of DS-TB [114]. Based on these results the Centers for Disease Control and Prevention (CDC, US government agency) are now recommending this new shorter regimen as a treatment option for individuals with DS-TB over the age of 12 [115].

Table 5. Overview over different anti-TB drugs, including treatment classification, abbreviation, bacterial target and effect. Divided into first-line drugs against DS-TB and drugs recommended by the WHO against MDR-TB, further separated into subgroups [116]. Bacterial target and effect from https://go.drugbank.com/.

Anti-TB drugs for the treatment of DS-TB and MDR-TB

Classification	Drug	Abbreviation	Drug target	Mechanism of action in Mtb
First-line (DS-TB)	Isoniazid	INH	Enoyl-[acyl-carrier-protein] reductase	Mycolic acid biosynthesis inhibition
	Rifampicin	RIF	RNA polymerase, B-subunit	Inhibits transcription
	Ethambutol	EMB	Arabinosyl transferases	Arabinogalactan biosynthesis inhibition
	Pyrazinamide	PZA	S1 component of 30S ribosomal subunit and aspartate decarboxylase	Inhibits translation and trans-translation and inhibits coenzyme A biosynthesis (via target degradation)
Group A (MDR-TB)	Levofloxacin or moxifloxacin	LFX MFX	Inhibits DNA gyrase and topoisomerase IV	Blocks DNA replication
	Bedaquiline	BDQ	F-ATP synthase, c and ε subunit	Inhibits ATP production
	Linezolid	LZD	23S component of 50S ribosomal subunit	Protein synthesis inhibition
Group B (MDR-TB)	Clofazimine	CFZ	Not determined	Appears to be membrane-directed
	Cycloserine or terizidone	CS TRD	L-alanine racemase and D-alanylalanine synthetase	Peptidoglycan biosynthesis inhibition
Group C (MDR-TB)	Ethambutol	EMB	Arabinosyl transferases	Arabinogalactan biosynthesis inhibition
	Delamanid	DLM	Prodrug activated by the F420 coenzyme system	Mycolic acid biosynthesis inhibition
	Pyrazinamide	PZA	S1 component of 30S ribosomal subunit and aspartate decarboxylase	Coenzyme A biosynthesis inhibition (via target degradation)
	Imipenem-cilastatin or meropenem	IPM-CLN MPM	penicillin-binding proteins	Peptidoglycan biosynthesis inhibition (in the presence of a β-lactamase inhibitor)
	Amikacin or streptomycin	AM SM	30S ribosomal subunit	Protein synthesis inhibition
	Ethionamide or prothionamide	ETO PTO	Enoyl-[acyl-carrier-protein] reductase	Mycolic acid biosynthesis inhibition
	Para-Aminosalicylic acid	PAS	pteridine synthetase	Inhibition of folic acid and mycobactin biosynthesis

Antibiotic resistance has been a problem since the first effective anti-TB drugs were introduced. In the 1940s, single-drug therapy using streptomycin (SM) temporarily treated mortally ill patients and converted their sputum from Mtb positive to negative.

However, soon thereafter the patients relapsed while still receiving SM and Mtb resistant to the drug were identified in sputum samples [117]. Today drug resistant TB is a massive global problem, despite the worldwide practice of multidrug therapy in order to prevent resistance and treatment failure. In fact, about 20 % of all TB cases is estimated to have resistance to one or more anti-TB drugs [118]. The raising prevalence of drug resistant TB mirrors the global increase in antibiotic resistance among a plethora of pathogens. Contrary to other bacteria that often acquire resistance through horizontal gene transfer of genetic material, Mtb primarily develops resistance by mutations in drug-target or drug-enabling genes [119]. Traditionally the main drivers of drug resistance in the context of TB was thought to be inadequate treatment, poor compliance to therapy and community- and facility-based transmission [120]. More recent evidence point to pharmacokinetic variability between drugs, poor drug penetration into granulomas and induction of efflux pumps as factors playing a significant role in the development of drug resistant TB [118]. The WHO has divided drug-resistant TB into five groups, defined below.

- INH-resistant TB (**IR-TB**); can be treated with first-line drugs.
- RIF-resistant TB (**RR-TB**)
- Multidrug-resistant TB (**MDR-TB**); resistance to both INH and RIF, the two most effective first-line drugs.
- Extensively drug-resistant TB (XDR-TB), reclassified into two groups in January 2021 by the WHO. The new definition include:
    - **Pre-XDR-TB** being MDR-TB in addition to resistance to any of the fluoroquinolones (levofloxacin and moxifloxacin) belonging to group A (**Table 7**) and
    - **XDR-TB** being pre-XDR-TB plus at least one additional drug from group A.

In addition to the types of drug-resistant TB defined by the WHO there have been incidences of incurable TB cases, also called totally drug-resistant TB (TDR-TB), involving Mtb strains that are resistant to all available anti-TB drugs [121-123]. However, the term TDR-TB is not endorsed by the WHO and seemingly incurable cases of TB due to drug resistance would be categorized as XDR-TB. This is in part because the correlation of *in vitro* drug-susceptibility testing and *in vivo* clinical

response is not established well enough, therefore reducing the prognostic relevance, and because new anti-TB drugs are under continuous development.

RR/MDR-TB requires a longer treatment duration than DS-TB, ranging from 9 months to almost 2 years depending on the resistance profile of the bacteria and the therapeutic response of the patient [124]. In addition the drugs are more toxic, causing significant adverse effects, as well as being much more expensive; about 40 US$ to treat a person for DS-TB compared to over 1000 US$ to treat RR/MDR-TB. The treatment success rate is also lower for RR/MDR-TB, 59 % in 2018, compared to the $\geq$ 85 % of DS-TB [101]. For XDR-TB there is no “universal regimen” and treatment has to be customized to the patient and all the factors listed above, *e.g.* duration, adverse effects and prognosis, becomes even worse.

Because of this situation new medicines and therapy options that will shorten treatment duration, induce less adverse effects and be effective against various drug resistant strains are needed.

Drug discovery; recently approved and current pipeline for new anti-TB drugs

New Year’s Eve 2012 was an important day for TB treatment and research. On this very day bedaquiline (BDQ) was approved for use against MDR-TB by the US Food and Drug Administration (FDA). This ended a 40 year drought in development and approval of a novel anti-TB drug. BDQ was developed by Janssen Therapeutics and works by inhibiting ATP production (**Table 7**), thereby killing both replicating and non-replicating Mtb. The first peer-reviewed paper on BDQ was published in 2005 [125] and eight years later it was in clinical use against TB. In the US it takes on average 7 to 12 years to progress a drug from pre-clinical testing using appropriate cell- and animal models to human clinical trials before finally receiving market approval [126]. Furthermore, according to a 2016 study the total average cost for developing a new drug is about 1.4 billion US$ (2013 dollars) [127], this immense sum illustrates why increased government and company funding is essential for research and development of new anti-TB drugs. In rapid succession after the introduction of BDQ in 2012, followed the approval of two new anti-TB agents; **(1)** Delamanid (DLM), developed by Otsuka Pharmaceutical and first approved by the European Medicines

Agency (EMA) in 2014 [128]. **(2)** Pretomanid (Pa), developed by the not-for-profit product development partnership TB Alliance, received regulatory approval by the FDA in 2019 for use in combinatorial treatment against XDR-TB or treatment intolerant/non-responsive MDR-TB together with BDQ and linezolid (LZD) [129]. This was based on the successful results from the Nix-TB clinical trial study in South Africa, where 98 out of 109 patients (90 %) diagnosed with XDR-TB or treatment intolerant/non-responsive MDR-TB (56 % with HIV co-infection) had a favorable outcome, defined as clearance of clinical TB disease and a negative culture status six months post end of treatment [130]. The study did not include a randomized control group for comparison of efficacy because no standard treatment regimen against XDR-TB existed. However, a treatment success of 90 % was impressive and resulted in the early regulatory approval of the so-called “BPaL regimen” used in the study. In the wake of this, the Nix-TB trial and specifically the approval of Pa received critical questioning relating to the sample size of the study, the isolated therapeutic effect of Pa in the “BPaL regimen” and Pa hepatotoxicity concerns [131, 132].

Both DLM and Pa are prodrugs and belong to the same class of antibiotics, namely the nitroimidazoles. To elicit anti-mycobacterial activity they require bio-reductive activation by the mycobacterial F_{420}-deazaflavin-dependent nitroreductase (Ddn) [133]. The main mechanism of action for both drugs is to inhibit mycolic acid biosynthesis, thereby killing actively replicating bacteria [134, 135]. Furthermore, DLM and Pa display bactericidal capacity against non-replicating mycobacteria through a second mechanism of action that is linked to generation of reactive nitrogen species, *e.g.* NO, and subsequent blocking of cellular respiration [134, 136]. Second-generation derivatives of Pa and their anti-TB efficacy is further addressed in **Paper V**.

The approval of three new anti-TB drugs within a time period of less than seven years was a huge improvement compared to the preceding stagnation phase of 40 years. However, this achievement alone will not, and has not solved the TB problem and cases of clinical resistance to BDQ and DLM has already been registered [137, 138]. So far, no clinical resistance to Pa has been reported [139], yet this is likely only a matter of time. The need for a bigger arsenal of effective anti-TB drugs is still very much the case. Currently there is 17 anti-TB compounds in clinical trials, the majority in phase II (**Figure 3**). There are many challenges linked to anti-TB drug discovery, the before-mentioned necessity for increased financing being one of them.

Furthermore, the robustness and versatility of the Mtb bacteria; being able to survive and replicate both intracellularly and extracellularly, in addition to manipulate and evade host immune responses, makes it a difficult target to effectively reach and kill. The bacteria can be in different metabolic states and resides in different lesions and microenvironments, all factors influencing drug efficacy [140].

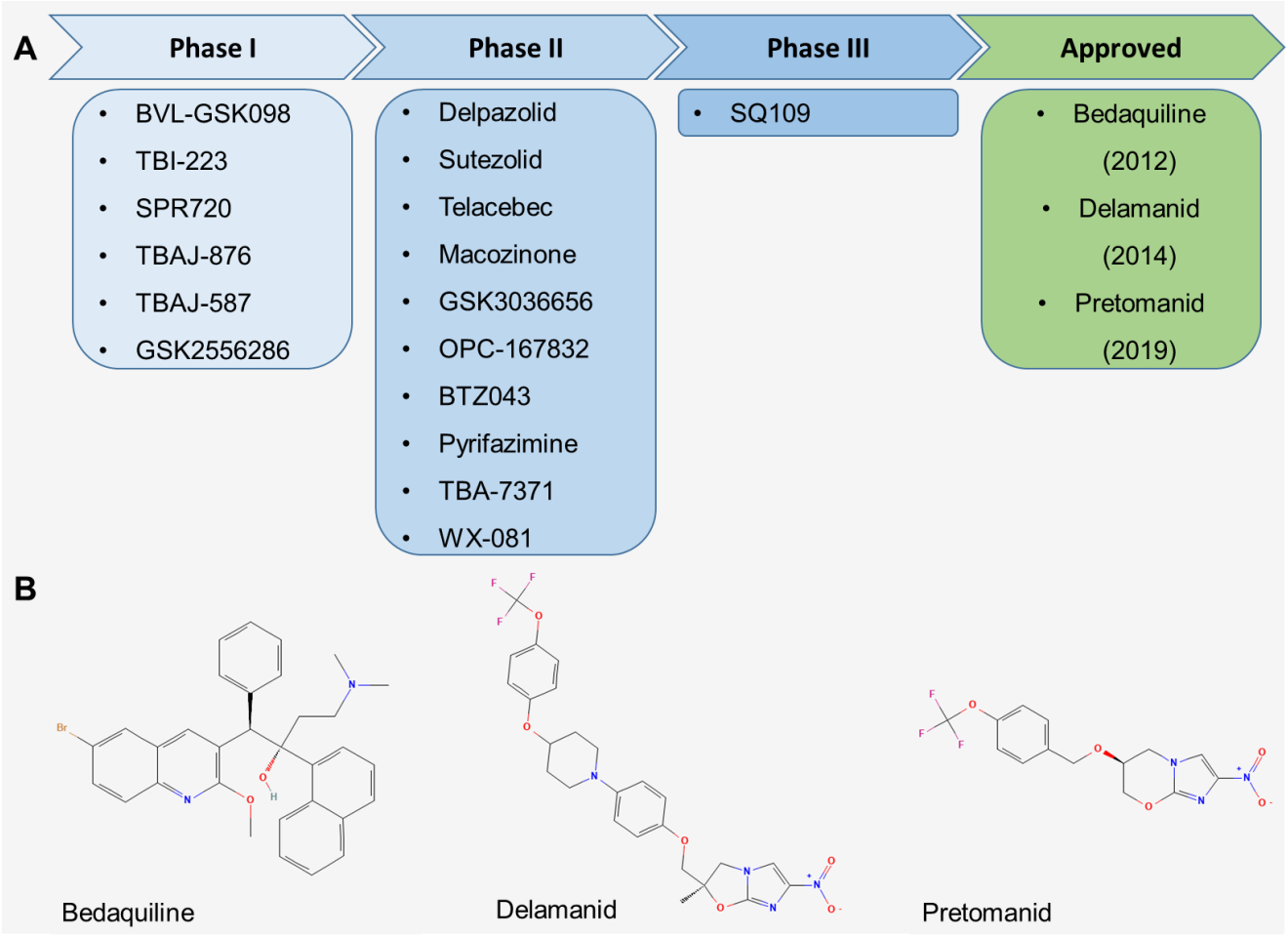

Figure 3. Overview of anti-TB drugs currently in clinical trials or recently approved. (A) Current pipeline of compounds in various stages of clinical trials. (B) Chemical structures of recently approved drugs, structures taken from https://pubchem.ncbi.nlm.nih.gov/. Figure adapted from Fernandes *et al.* [141].

Drug discovery can be divided into two main strategies; the empirical approach and the molecular approach [142]. The empirical approach is based on phenotypic screening, which is observing the effect a compound has on a cell or an organism without knowing the molecular target. The molecular approach is target-based and the process begins with a defined molecular target hypothesized to be important for the disease in question, *e.g.* being vital for bacterial survival or cancer cell proliferation. Due to advances in genomics and molecular biology, the latter approach has been the dominating strategy in drug discovery for the last three decades. However, phenotype-

based strategies have gained traction in recent time. This in part because of improved technologies making the hit-to-lead process more efficient and a good track record in discovery of first-in-class drugs, better than the target-based approach. In addition, the phenotype-based strategy can identify effective compounds even though the complexity of pathogenesis and host-pathogen interactions being incompletely understood [142, 143], which is the case for TB. Notably, all of the three recently approved anti-TB drugs, BDQ, DLM and Pa, were discovered through phenotypic high throughput screening (HTS) [144]. Despite the successes, a caveat of the empirical approach of anti-TB drug discovery and phenotypic HTS is the high proportion of hydrophobic hits [145] that might pose as a problem in the following hit-to-lead process with respect to solubility, ADME parameters (absorption, distribution, metabolism and excretion) and toxicity *in vivo* [146]. Encapsulation of hydrophobic compounds having anti-mycobacterial activity into biocompatible nanoparticles (NPs) displaying desirable biopharmaceutical properties has the potential to circumvent the above-mentioned problems associated with drug hydrophobicity. This topic will be addressed in the following chapter.

Nanomedicine, a novel approach for treatment

Nanomedicine, a brief introduction

The European Science Foundation (ESF) described nanomedicine in 2005 as follows: *"Nanomedicine uses nano-sized tools for the diagnosis, prevention and treatment of disease and to gain increased understanding of the complex underlying pathophysiology of disease. The ultimate goal is improved quality of life."* [147]. There is no strict consensus on what, with respect to size, defines the term nano. However, in various publications, commonly used definitions are $\leq$ 100 nm or $\leq$ 1000 nm. The latter is often used in the context of pharmaceutical sciences with respect to NPs [148]. Since NPs constitute a major part of this thesis, I will use the broader nano-size definition of $\leq$ 1000 nm.

The scientific field of nanomedicine and NPs is relatively new but in rapid development, with the bulk of the accumulated research having taken place in the last two decades [149]. However, the vision of targeted therapy by drugs and small molecules, a so-

called “magic bullet”, was conceptualized by no other than Paul Ehrlich [150], the founder of chemotherapy and close friend of Robert Koch, who discovered Mtb. I find this historical convergence of the TB and NP fields quite interesting and worth pointing out! The modern field of nanotechnology, and thereby nanomedicine and NPs, is by many credited to the American theoretical physicist and Nobel Prize Laureate Richard Feynman (1918-1988), because of a lecture he gave in 1959 titled “There’s Plenty of Room at the Bottom”. There, he talked about the concept and enormous potential of manipulating matter at the atomic level [151].

The development of NPs as a delivery strategy of drugs and vaccines for medical purposes dates back approximately 50 years. An early pioneer in the field was Professor Peter Paul Speiser (1921-) and his research group that in the late 1960s initiated innovative work on drug delivery systems [152]. Around the same time extensive research and progress in understanding drug transport in the vascular system and subsequent accumulation into cells and tissues led to the establishment of PK and pharmacodynamics (PD) [152-154]. In simple terms PK can be described as “what the body does to the drug” and PD as “what the drug does to the body” [155]. The increased understanding and appreciation of the effect PK/PD properties take on the therapeutic effectivity of a drug *in vivo*, influenced Speiser and his group to work on delivery systems that would enable delayed and controlled drug release with minimal off-target effects. Gerd Birrenbach, a graduate student of Speiser, started working on this project in 1969 and developed the first polymer based NP-drug formulation for treatment purposes [156].

In general, NPs can be divided into three main classes based on the material they consist of; lipid-based NPs (*e.g.* liposomes), polymeric NPs (natural or synthetic polymers) and inorganic NPs (*e.g.* gold, iron and silica). Each class has its unique strengths and weaknesses. NPs, of all classes can be utilized in numerous stages of clinical practices and are used for both diagnosis and treatment purposes within biomedicine [157]. The work described in this thesis mainly concerns the use of polymeric NPs as a drug delivery system. The fundamental goal of NP-mediated drug delivery is to circumvent and overcome problems associated with free drugs, such as poor aqueous solubility and bioavailability, short half-life, toxicity and adverse side-effects. The basic idea is that a NP delivery system will serve as an interface, with

more desirable PK/PD properties, shielding the drug from the surrounding microenvironment and thereby making treatment more effective.

A key concept in NP mediated drug delivery is **targeted therapy**. Contrary to conventional free therapeutics, where the drug is systemically distributed throughout the body, NPs possesses the potential of reaching the diseased tissue site or specific cell type of interest more selectively and therefore efficiently. Targeted delivery can be either passive or active. **Active targeting** can be achieved through attachments of targeting moieties, *e.g.* carbohydrates, antibodies or receptors, to the particle surface. These targeting moieties will interact and bind with high affinity, via specific receptor-ligand interactions, to specific molecules present on the surface of the cell type of interest [157-159]. The alternative to active targeting is **passive targeting**, which is accumulation of NPs at the tissue site or in the cell type of interest without any specific targeting molecules on the particle-surface [157-159]. Passive targeting and NP accumulation is influenced by the particles circulation time in the vasculature, extravasation into adjacent tissue or uptake by the mononuclear phagocyte system or endothelial cells lining the blood vessels. NP properties, such as surface and material composition, size, shape and charge, are important for the *in vivo* dynamics and cell interactions, passive targeting can therefore be optimized through NP design [157]. For example, by incorporating polyethylene glycol (PEG) chains on the particle surface, so-called PEGylation, the NP surface becomes hydrated and less prone to protein adsorption. This reduces cellular uptake by the mononuclear phagocyte system and consequently increases the blood circulation time [160].

A well-established phenomenon that occur in tissues affected by inflammation and hypoxia (*e.g.* a cancer tumor or a TB granuloma) is that the intertwined and adjacent blood vessels lose their integrity and becomes more permeable for macromolecules [161, 162]. Additionally, hypoxia triggers angiogenesis, the formation of new blood vessels from pre-existing vessels, which also display a relatively high permeability [163]. Furthermore, inflammation results in abnormal and poor lymphatic drainage and therefore increased retention of accumulated macromolecules. This phenomenon was first described by Matsumura and Maeda in the 1980s and is now referred to as the **enhanced permeation and retention (EPR) effect** [164]. The EPR effect is widely exploited as a strategy for passive targeting of long-circulating NPs to the diseased site, our research group has studied this targeting strategy using zebrafish and mouse

models of TB and found NPs to accumulate passively into granulomas in zebrafish and mice [161].

Current status of nanomedicine

The first NP-drug formulation to be clinically approved by the FDA was Doxil® (also known as Caelyx®) in 1995 for use against the cancer type Kaposi's sarcoma [165]. Doxil® consists of PEGylated liposomes encapsulating the highly active, but toxic, chemotherapeutic drug doxorubicin. Doxil® passively targets the tumor by having a long circulation time and taking advantage of the EPR effect. Furthermore, the NP-drug formulation significantly reduces toxicity, allowing for higher doses and consequently more effective therapy [166]. Even with extensive research and development within the NP field since the approval of Doxil®, especially in the context of cancer treatment, the number of clinically approved NP-drug/vaccine formulations remains disappointingly low. Only between 20 to 30 formulations in clinical practice today [157, 167]. There are several reasons for this shortcoming in transition from basic research and the pre-clinical stage into NP therapies approved for market use; these include increased cost and time associated by getting approved an extra component (NP) to the treatment (drug) and a gap between academia (basic research) and the pharmaceutical industry (clinical research and development) [168]. Furthermore, there exists a translational gap between animal models and humans, to put it simply, what works in a mouse might not work in a human or be of clinical relevance.

Recently, nanomedicine has been used in the fight to end the ongoing COVID-19 pandemic; both the Moderna vaccine (mRNA-1273) and BioNTech/Pfizer vaccine (BNT162) aimed for protection against COVID-19 are formulated using a lipid NP system [169, 170]. The global need, combined with the tremendous success of these vaccines, will hopefully aspire an even greater interest in the potential of nanomedicines and NP mediated drug and vaccine delivery to accelerate the process from bench-to-bedside of new NP based therapies.

Nanomedicine and tuberculosis

NP mediated drug delivery is a very interesting and promising approach for the treatment of TB. NPs can increase therapeutic efficacy and reduce toxicity by targeted delivery, lowering the amount of drug needed and also reduce dosing frequency

through controlled drug release over time. This can make the treatment regimen more tolerable for the patient and thereby increase compliance to therapy, this is extremely relevant for the treatment of MDR/XDR-TB which requires less effective and highly toxic drugs. Thus, the problems that come with conventional free therapy can be lessened and treatment can be improved by a shift to NP carrier-based drug delivery systems.

Superior efficacy and reduced toxicity of NP mediated drug delivery over free drug delivery has been demonstrated *in vitro* and *in vivo* using different cell and animal models of TB [159, 171, 172]. Some of the most impressive data concerning NP mediated treatment of TB and a great inspiration for our research comes from India and the group of Gopal K. Khuller. Through encapsulation of the highly active first-line anti-TB drugs RIF, INH and PZA into NPs made by the biodegradable polymer poly(D,L-lactic acid-*co*-glycolic acid) (PLGA), they showed significantly prolonged presence of drugs in blood plasma, relative to free drugs, and therapeutic drug concentrations in tissues for more than a week in uninfected mice. Furthermore, in mice intravenously infected with Mtb, five doses of drug-loaded PLGA NPs, given orally over 46 days with a ten day interval, resulted in no detectable bacilli in lung and spleen homogenates by plating and counting colony forming units (CFU). The same result was achieved with daily administration of the same drugs in their free form [173]. Similar results were obtained using the guinea pig model of TB, here only three doses given fortnightly over 45 days cleared the infection [174].

Targeting of NPs with respect to TB disease has two major advantages. Firstly, macrophages serve as host-cells for Mtb infection. Additionally, uninfected blood- and tissue resident macrophages will migrate to the infected area due to chemotaxis. This can be exploited by using short-circulating NPs (*e.g.* non-PEGylated liposomes) that are rapidly cleared from the circulatory system by the mononuclear phagocyte system and subsequently transferred to the diseased area. This NP targeting approach was first visualized in an animal model of TB by our group in 2014 [175]. In that study Fenaroli *et al.* used the transparent zebrafish embryo model of TB in combination with fluorescently labelled PLGA NPs, in order to visualize the fate of intravenously injected NPs. Secondly, TB granulomas share some features with cancer tumors that are needed for the EPR effect to take place, such as permeable blood vessels, hypoxia and angiogenesis [176]. Our group recently showed that long-circulating NPs escaped

the vasculature and significantly accumulated in a time-dependent manner, relative to healthy tissue, in granuloma-like structures using the zebrafish embryo TB model and in lung granulomas using a mouse TB model [161]. The enrichment of NPs in zebrafish granulomas was suggested to occur by an EPR-like process, and this was supported by observations obtained by live-imaging and electron microscopy (EM).

Animal models of tuberculosis

Mtb infection, TB disease progression and host immune responses is a series of heterogeneous, often poorly understood events that could result in vastly different clinical outcomes depending on the individual in question. The use of different animal models is therefore important in order to increase our understanding of TB and the underlying mechanisms. Unfortunately there is no such thing as a perfect model. In nature Mtb infects only humans, so an ideal animal model is particularly difficult to find. Not a single animal perfectly reproduces the infectious process, immune responses and TB disease observed in humans. Despite this, animal models have significantly aided in our understanding of TB and they play an important role in the development and testing of new drugs and vaccines against TB, as well as other diseases. The following section will briefly describe the most common animal models for TB and the pros and cons associated with them.

The mouse model of TB

Mice, *Mus musculus*, are utilized as a model system for virtually all human diseases. A major reason for the wide use of the model is that about 99 % of all mouse genes have a human homolog [177]. Furthermore, mice are relatively cheap, compared to other animal models, similar to humans in their response to anti-TB drugs and several transgenic and knockout strains exists and are readily available [178]. Mice are susceptible to TB infection and the most commonly used strains (C57BL/6 and BALB/c) are not able to control the infection in a structured granuloma, which often being the case in humans. Instead, these mouse strains form unstructured granulomas, without caseous necrosis and local regions of hypoxic conditions [179, 180]. Because of this, its relevance as a model for studying the pathogenesis of and host-responses against TB has been questioned [181]. However, mouse strains that are able to recapitulate human-like granuloma conditions such as high structural integrity, hypoxic conditions

and caseous necrosis do exist, *e.g.* the C3HeB/FeJ strain also known as the “Kramnik” mouse [182, 183].

The rabbit model of TB

The rabbit, *Oryctolagus cuniculus*, is much more susceptible to infection with *M. bovis* compared to Mtb infection [184, 185] and the rabbit-*M. bovis* model system more closely mimics human Mtb infection and pathogenesis than what typically observed in mice [23]. Unlike the standard mouse model, rabbits exhibit caseous necrosis and is considered a better model when it comes to the pathology of TB. The rabbit has been an important model for understanding TB and influential findings were discovered using this model. For example, it was in rabbits that alveolar macrophages were found to be the initial target cell for Mtb infection [186] and where the delayed-type hypersensitivity (DTH) was illuminated [187]. More recently the rabbit model has been used to study both pathogenesis and treatment of TB, reactivation of LTBI by immunosuppression and following analysis of bacillary gene expression [188] and pharmacokinetics (PK) and drug penetration into tubercular lesions [189] serving as examples. Compared to mice and guinea pigs, discussed next, rabbits are expensive and require a larger space for optimal living and experimental conditions.

The guinea pig model of TB

To be a guinea pig, *Cavia porcellus*, means to be the subject of experimentation, and there is a reason for this double meaning of the word. Guinea pigs have been used for scientific purposes for hundreds of years, dating back at least to the 17th century [190]. The guinea pig has been used as a model for several human diseases, TB being a prominent one [191]. Guinea pigs are highly susceptible to Mtb infection, especially by the aerosol route of exposure [192]. The guinea pig is not able to arrest the disease progression, corresponding to LTBI and infection invariably leads to death. However, the model reproduces many of the core features of human TB, such as heterogeneous granulomas with a human-like structure and caseous necrosis, haematogenous dissemination and a strong DTH response [193]. Liquefaction of caseous necrosis in granulomas and following cavity formation is rare in guinea pigs, but does occur with certain highly pathogenic strains [194]. Guinea pigs are important for clinical research, especially concerning vaccine safety and efficacy testing. Here the guinea pig is

favored over mice, which lack certain immunological features important for humans [195]. Guinea pigs are also used for drug efficacy testing, an advantage over mice is the wider diversity in granulomatous lesions, closer resembling the human pathology [196]. A downside with guinea pigs as a model system is the limited availability of species-specific immunological reagents [195].

Non-human primate (NHP) models of TB

NHPs are the most accurate animal model systems in replicating the human TB pathology. Old world NHPs, originating from Africa and Asia such as the macaques, are the most commonly used NHPs for TB research. New world NHPs, originating from America such as marmosets, are also used for TB research purposes, but less common. Both the rhesus (*Macaca mulatta*) and cynomolgus (*Macaca fascicularis*) macaques replicate the full spectrum of human TB infection and disease, including primary and secondary TB as well as LTBI [197]. Because of this, these NHPs have been extensively used for research on the pathogenesis of and host-responses to TB, in addition to drug and vaccine development. An important feature made possible using NHPs is the coinfection with Mtb and the simian immunodeficiency virus (SIV). This can be used to study the interaction between SIV and TB as a model for human HIV/TB coinfection, for example in the context of HIV induced TB reactivation [198]. The use of NHPs for scientific purposes in general and especially for TB research is connected with several drawbacks such as high cost, large space and biosafety level (BSL) 3 facility requirements and a significant risk for potential transmission of the disease to laboratory workers. In addition, work with NHPs raises ethical questions that should be taken into account. Because of these reasons, the use of NHPs as an animal model is highly limited and restricted.

The experimental animal models introduced so far have a common problem, they are all opaque and poorly suited for *in vivo* live imaging. Making it difficult to observe and study infectious events and to follow up NP behavior and dynamics in real-time. The small and transparent zebrafish embryo is however ideally suited for this purpose and will be addressed in the following chapter.

The zebrafish model of tuberculosis and nanomedicine

The preclinical stage require appropriate animal models in order to test and verify safety and activity of new drugs and treatment approaches, such as NP drug delivery systems, before human testing. Over the last decades, the zebrafish (*Danio rerio*) has gained momentum and is now considered as a relevant animal model to study human biology and disease [199]. Teleost fish, such as the zebrafish, have a similar immune system to mammals and is therefore useful as preclinical immunology model [200]. Furthermore, the transparency of the fish during the early life stages allows for high-resolution live-imaging at the cellular level [201, 202], which is a major advantage that enable for studies not possible in mammalian models.

Although the zebrafish is a major model organism within life sciences, fairly little is known about its natural history, behavior, biotic and abiotic environment. It is a small freshwater fish native to South Asia, first described by the Scottish physician Francis Hamilton in 1822 while living and working in India [203]. Wild zebrafish thrive in shallow water habitats such as slow-running rivers and streams, still bodies of water and rice paddies with a temperature and pH ranging from about 25 °C to 34 °C and 5 to 8 respectively [204, 205]. A field study found a large population of zebrafish, in good physical condition and without signs of stress, in a body of water with a temperature of about 39 °C, suggestive of the adaptability and robustness of the fish species [204]. In a laboratory setting the optimal water temperature is considered to be 28.5 °C and with physiological pH [206].

The zebrafish as a model organism for biomedical research was initiated by George Streisinger (1927-1984) at the University of Oregon and introduced to the scientific community in 1981 when Streisinger *et al.* in *Nature* published the landmark paper announcing the creation of zebrafish clonal lines free of lethal mutations by gynogenetic (development of embryos without genetic contribution from the male) methods [207]. After his early death in 1984 the work was continued and brought forward by others, such as Charles Kimmel and Christiane Nüsslein-Volhard. The story of the establishment and early years of this model system is excellently communicated in the review article *Headwaters of the zebrafish - emergence of a new model vertebrate* [208].

The zebrafish is a well-suited model to study infectious diseases, especially host-pathogen interactions due to its transparency, and for performing antimicrobial drug screens [200]. The zebrafish embryo model for TB was established in 2002 by the group of Lalita Ramakrishnan at the University of Washington [202]. The model applies the bacterium that causes TB-like disease in fish and frogs, *Mycobacterium marinum* (Mm) as a surrogate for the human Mtb bacterium [209, 210]. Mm is closely related to Mtb [211], but whereas Mtb grows above 35 -37°C, Mm grows optimally around 28-30 °C, as does the zebrafish. For this reason Mm is not able to systemically infect humans, which display core temperatures incompatible with Mm survival and replication, and therefore only considered as a BSL-2 organism (Mtb being BSL-3). Mm can however establish infection in the extremities of humans, such as hands and feet, so called fish tank or swimming pool granulomas. The zebrafish is susceptible to systemic Mm infection at both the embryo/larvae stage and as an adult (considered an embryo until feeding occurs approximately five days post fertilization, then a larvae). The zebrafish do not develop a fully functional adaptive immune system before about four weeks post fertilization [212], therefore the larvae offers a unique opportunity to study the early stages of infection solely in the context of innate immunity. Establishment of Mm infection is usually performed through micro-injection of bacterial suspension at various sites. In the embryo, the common routes of infection by micro-injections being the posterior cardinal vein (PCV) [175, 202], trunk/neural tube (NT) [161, 213] and the hindbrain ventricle (HV) [175, 214]. Natural Mm infection by the immersion method is also possible [215, 216], but not as effective as the direct injection method.

The zebrafish model for TB has significantly aided our understanding of mycobacterial pathogenicity and visualized early events of infection. For instance, Levitte *et al.* found that Mm were able to survive and even replicate, at a declined rate, inside the phagolysosome in zebrafish larvae [217]. The virulence factor MarP, a membrane serine protease, was identified as crucial for Mm survival inside the acidic compartment. Another recent example of this using zebrafish larvae are Cambier *et al.* [218]. They showed that resident macrophages, capable of bacterial killing, were the first responders to infection in the HV. To circumvent this and promote bacterial survival, Mm prompted recruitment of susceptible blood monocytes through activation of the STING pathway in resident macrophages by the virulence factor phenolic

glycolipid (PGL). In turn, the STING pathway produces chemokines attracting monocytes to the site of infection creating a niche for Mm survival. Perhaps the most important and well-known discoveries using the zebrafish larvae TB model relates to the granuloma, its initiation and role in disease progression. The first paper using the zebrafish larva TB model showed that granuloma formation was possible without involvement of the adaptive immune system, in contrast to previous consensus [202]. The model has also greatly contributed in changing the dogma of how we view the granulomatous response. Previously the granuloma was considered as an exclusively host-protective response, now we view it as a more nuanced mechanism that offer both containment of the infection but also serve as a bacterial niche for evading the immune system and dissemination of infection [209].

The zebrafish larvae is also an ideal organism for nanomedicine research. It is used to study NP circulation and accumulation dynamics, cell interactions and therapeutic effects against cancer diseases and different infectious diseases. It is increasingly being used for evaluating NP toxicity and biocompatibility [219], which is not only relevant for the biomedical field but also for other industrial applications [220]. Our group has over the years undertaken research comprising all the aspects listed above in the larger context of improved TB and cancer treatment [175, 221].

Aims of the thesis

The main goal of the thesis was to assess the potential of various NP-mediated drug therapies against TB, and optimize them with respect to toxicity and therapeutic efficacy. This was predominately done using the zebrafish embryo model for TB. A special focus was put on investigating the suitability of the embryonic zebrafish model as an intermediate screening stage for NP post *in vitro* cell studies and prior to pre-clinical studies in mammalian models, *e.g.* the mouse.

By establishing and implementing the zebrafish as a commonly used model system for drug and nanomedicine screening, the long-term aim is to shorten the road from bench to bedside of new therapies, in addition to cutting research expenses and improving the 3R's principle (reduce, replace and refine) by decreasing the number of mammalian animals needed in order to achieve reproducible data and results [222]. Especially the imaging possibilities offered by the transparent zebrafish embryo were taken advantage of. This led to data difficult to obtain in mouse models but that could be validated in mammalian models afterwards as shown in **Papers I and V**.

Summary of papers

Paper I

Zebrafish Embryos Allow Prediction of Nanoparticle Circulation Times in Mice and Facilitate Quantification of Nanoparticle–Cell Interactions.

With the overarching aim of establishing the zebrafish embryo as an intermediate model system for nanomedicine characterization and screening, we sought to develop a simple, standardized and user-friendly method for quantitative determination of key *in vivo* NP parameters. We believe that this zebrafish screen can facilitate the identification and selection of the most promising NP therapeutics that in the next level can be tested in higher animal models. We took advantage of the optical transparency of the zebrafish embryo and readily available fluorescent transgenic lines to develop a simple method to quantify circulation times of intravenously injected fluorescently labelled NPs in the vascular system and subsequent uptake by macrophages and endothelial cells. Prolonged time in the circulatory system is positively correlated with selective NP accumulation, mediated by the EPR effect, at diseased sites, *e.g.* cancer tumors and TB granulomas. Circulation time is reduced upon uptake by cells, especially macrophages but also by the endothelial cells lining the blood vessels.

In this study, we applied a stereomicroscope for non-invasive live-imaging of NP injected zebrafish. The acquired images were subsequently uploaded in the image processing program ImageJ using a dedicated macro programmed to analyze NP circulation time, macrophage and endothelial cell uptake. The macro, developed specifically for this study, and following quantification of the three above-mentioned parameters, circulation time, macrophage and endothelial cell uptake, were based on thresholding of fluorescent signals (NPs and/or specific cells), outlining of a region of interest (ROI) and measurement of signal within the ROI. For example; NP uptake by macrophages is the result of the signal from the ROI corresponding to macrophages that co-localize with the NP ROI signal. Using this set-up we analyzed and compared seven different NP formulations. To further validate the use of the zebrafish embryo as an intermediate model, we explored whether the data obtained in the zebrafish could be predictive for the mouse model. For this, the circulation time of four of the NP

formulations were investigated in a mouse model. Similar NP circulation pattern were observed in mice and fish, showing that the zebrafish embryo model is indeed able to predict, with reasonable precision, NP behavior in mice.

Paper II

Biodistribution of surfactant-free poly(lactic-acid) nanoparticles and uptake by endothelial cells and phagocytes in zebrafish: Evidence for endothelium to macrophage transfer.

As mentioned above the leap from cell systems to higher vertebrates is big and the opacity and complexity of working with mammalian models, such as the mouse, obstructs a thorough understanding of the *in vivo* dynamics and cell interactions of NP drug delivery systems.

In this study we investigated the biological behavior; circulation, biodistribution, accumulation and cell interactions, of a safe-by-design and surfactant-free NP system made up of the biocompatible and FDA approved polymer Poly(D,L lactic acid) (PLA) in the zebrafish embryo model. The fluorescently labelled PLA-NPs were highly homogenous with a strong negative surface charge (about -55 mV) and a size of approximately 175 nm. Through combination of live-imaging and imaging of prepared samples using stereomicroscopy, confocal microscopy and EM, in addition to flow cytometry we were able to study the behavior and cell interactions in great detail and gain new insight of how NPs interact with the endothelial cells outlining the vasculature. The PLA-NPs were found to be short-circulating, and were completely cleared from the bloodstream after about 30 minutes. They were found to be internalized largely by endothelial cells and macrophages, with relatively little accumulation in internal organs and no observable uptake by neutrophils. Surprisingly, the anionic particles were taken up by endothelial cells throughout the vasculature and not restricted to certain venous vessels as reported by others. The PLA-NPs were found to lose structural integrity, starting from 72 h post internalization into cells and after one week the particles had degraded completely. This was shown by EM and through NP encapsulation of colloidal gold particles. A novel and potentially therapeutically important finding was the observation of a previously undescribed cell-to-cell transfer mechanism of NPs

from endothelial cells to macrophages. The exact nature of this mechanism and its relevance from a nanotherapeutic treatment perspective remains to be elucidated.

Paper III

Rifampicin Nanoformulation Enhances Treatment of Tuberculosis in Zebrafish.

Nanomedicine has the potential to overcome many limitations associated with conventional TB therapy. Encapsulation of established anti-TB drugs into NPs can increase the efficacy of treatment and reduce off-target effects. In this collaborative and interdisciplinary work with scientists from the Czech Republic we described and characterized a polymeric nanocarrier system encapsulating the key anti-TB drug RIF and carried out *in vitro* and *in vivo* experiments to determine biocompatibility, safety and efficacy against TB infection. We identified a promising nanoformulation that is both biocompatible and biodegradable and significantly improved RIF monotherapy compared to free drug administration. In line with the aim of our group of using the zebrafish as an intermediate screening stage, this work can serve as a source for a more comprehensive following study using mammalian models.

The nanoformulations used in this study were a type of polymeric NPs made up of the copolymer methoxy poly(ethylene oxide)-*block*-poly(ε-caprolactone) (MPEO-b-PCL) with a water insoluble core and a hydrophilic surface. The copolymers were synthesized by metal-free ring-opening polymerization and five different MPEO-b-PCL NPs (designated P1 to P5) were prepared, varying in the ratio of hydrophobic and hydrophilic monomer units in the copolymer. The physiochemical properties of the NP samples were characterized by dynamic light scattering (DLS), asymmetrical flow field-flow fractionation (AFFFF) and cryo-transmission EM (cryo-TEM). The resulting NPs were spherical in shape and ranged in size from about 20-110 nm. The lipase-catalyzed biodegradability of the NPs were investigated by DLS and ^{1}H NMR spectroscopy, both methods yielded similar results. Drug loading and encapsulation efficiency were determined by UV/vis spectroscopy and ranged from about 11 to 23 % and 15 to 30 % respectively. Drug release profile in the presence and absence of lipase were also investigated by a dialysis-based study; surprisingly we did not detect any increased drug release when enzyme were present, which would be expected since lipase were shown to degrade the particles. *In vitro* cytotoxicity was evaluated using

Raw 264.7 macrophages and zebrafish embryonic fibroblast ZF4 cells, non-drug-loaded NPs did not cause any significant toxicity. RIF-loaded NPs however caused toxicity at higher concentrations and were more toxic than RIF alone, most likely indicating better targeting of drug to cells. NP internalization into cells and following degradation were studied using confocal microscopy and flow cytometry. Different uptake rates and intracellular localization and degradation were observed among the five different NP samples. Based upon the before-mentioned studies a lead formulation was selected, identified as sample P4, and its anti-TB efficacy was investigated *in vitro* and found superior to free RIF at equivalent concentrations. Finally, the lead formulation was examined *in vivo* using the zebrafish embryo model. Fluorescently labeled P4 NPs were injected into healthy embryos and live-imaging revealed that most particles were taken up by the endothelial cells lining the vascular system 2 h post injection. Lastly, the therapeutic efficacy of free RIF, NP-RIF and empty NPs were compared in Mm infected zebrafish embryos. Although free RIF had a protective effect against the infection, as expected, and slowed the mortality compared to the control group, NP-RIF treatment was superior, with 50 % of the fish remaining alive at the final day of the experiment. NP alone had no therapeutic or detrimental effect on the survival analysis.

Paper IV

The zebrafish embryo as an *in vivo* model for screening nanoparticle-formulated lipophilic anti-tuberculosis compounds.

Here we present how the zebrafish embryo model can be systematically utilized as an intermediate screening stage in the preclinical evaluation of nanotherapeutics and anti-TB drugs following and complementary to *in vitro* studies. We show that the zebrafish can aid in identifying and excluding compounds that are found to be poorly tolerated *in vivo*, but deemed non-toxic in cell culture, as well as identifying promising formulations that can be progressed to further investigation in higher animal models. This work can be used as a blueprint for how the zebrafish can be implemented to bridge the gap between *in vitro* bacterial and other cell culture studies and more laborious, costly and time consuming studies in preclinical mammalian models.

In this study we thoroughly tested five poorly water-soluble nitronaphtofuran (nNF) derivatives, which were recently identified to possess anti-Mtb activity and low cytotoxicity in a phenotypic HTS. In a hierarchical and systematic fashion we first established their antimicrobial activity against extracellular Mm using a standard minimum inhibitory concentration (MIC) assay, and against intracellular Mm using mouse bone marrow-derived macrophages (BMDM). Next we sought to determine the *in vivo* toxicity and therapeutic efficacy using the zebrafish embryo model for TB. However, due to the low solubility of the compounds they were impossible to administer in their free form, via micro-injection, at therapeutically relevant doses. The five nNF drug derivatives, in addition to RIF, were therefore formulated into a biocompatible and biodegradable NP system. The NPs were polymeric micelles (PMs) made with the polypept(o)ide copolymer; poly(γ-benzyl-L-glutamic acid)-*block*-polysarcosine [Glu(OBn)-b-pSar]. The PMs had an average size of about 85 to 150 nm and a slight negative surface charge. The outer polysarcosine layer provided stealth-like properties, similar to PEGylation, making the PMs long-circulating (further investigated in **Paper V**). First we tested the toxicity of the nanoformulations at four different doses in healthy embryos in a survival study. Two of the compounds (C4 and C20) that were found to be non-toxic in cell culture in addition to the toxicity control compound C16 were poorly tolerated in zebrafish and excluded from the following infection-treatment studies. Compounds C7, C11 and C12 did not induce any toxicity in the survival analysis and were further examined in a more comprehensive toxicity score assay at the highest dose (50 ng). All three compounds were deemed non-toxic and well-tolerated at the highest dose and therefore progressed to the treatment studies. In the infection-treatment studies, zebrafish embryos were first infected with fluorescently labelled Mm and the following day were challenged with a single therapeutic dose of one of the remaining nNF or RIF nanoformulations. Initially, we directly compared three different approaches for determining the bacterial burden five days post infection. We imaged live embryos using a stereomicroscope and quantified the total Mm-associated fluorescent signal of each fish (Method 1: fluorescent pixel count – FPC) using ImageJ and a customized macro. This is a non-invasive approach that is compatible with the survival analysis, which was ended at day eight post infection. Next we pooled and homogenized fish in the different treatment groups and recorded the total fluorescence by a plate reader (Method 2). In the third approach we developed a protocol for plating on solid media and estimated the bacterial burden by a classical CFU assay (Method

3). The three methods provided comparable results and validated the next step which involved the use of FPC in combination with survival analysis. The three PM encapsulated non-toxic nNF derivatives reduced the bacterial burden and improved survival in a dose-dependent manner, however the RIF nanoformulation was superior in efficacy.

Paper V

Π-Π Interactions Stabilize PeptoMicelle-Based Formulations of Pretomanid Derivatives Leading to Promising Therapy Against Tuberculosis in Zebrafish and Mouse Models.

Here we made a systematic test of novel anti-TB drugs NPs at different levels, starting with NP synthesis and characterization and *in vitro* studies of free drugs in bacterial- and mammalian cell cultures, followed by the intermediate zebrafish model. Based on these results, this led to the identification and testing of a lead formulation in a preclinical mouse model of TB. This work is a result of a broad and interdisciplinary collaboration between various fields, including drug- and polymer chemistry, tuberculosis research, cell biology- and microbiology.

In this study we selected four novel second-generation derivatives, identified as compounds A, B, C and D, of the recently approved anti-TB drug pretomanid for toxicity and efficacy screening. All compounds, including the parental pretomanid, were initially screened *in vitro* for antimicrobial activity against Mm and Mtb and for cytotoxicity in mammalian cells. In an effort to improve bioavailability, therapy and reduce potential off-target effects we formulated the hydrophobic compounds into polypept(o)ides based PMs (same as in **Paper IV**). We started with synthesizing and thoroughly characterizing the physiochemical properties of the drug delivery system, with and without encapsulated compounds. In addition, we used DLS, fluorescence correlation spectroscopy (FCS) and EM to determine morphology (rods and spheres), average size (around 100 nm), surface charge (slightly negative, close to neutral) and drug encapsulation efficiency (> 95 %), we showed that these PMs were stabilized in the core by π-π interactions. The stabilizing effect was through aromatic benzyl groups in the side chains of the hydrophobic block polypeptide, facilitating the efficient encapsulation of the aromatic pretomanid derivatives. The stability of the PMs were

demonstrated by fluorescence cross-correlation spectroscopy (FCCS) in aqueous solution, blood plasma and lung surfactant. Next, the nanoformulations were examined in detail in the zebrafish embryo. First, the high stability of the PMs were indirectly confirmed through an extensive circulation time in the vascular system for more than three days. We then extended previous studies confirming that the zebrafish embryo model is an ideal platform for toxicity and efficacy screening against Mm infection of drugs and nanotherapeutics *in vivo*. In particular we identified one highly potent PM formulated pretomanid derivative (drug D) against Mm infection that was superior to the free form of the drug. This lead formulation was then tested against Mtb in the susceptible C3HeB/FeJ mouse model, which develops human-like necrotic granulomas, known to be difficult to treat. Following a minimal dosing schedule of just 7 doses over 14 days, a substantial one to two log reduction in bacterial burden was observed in both lungs and spleens of infected mice. Notably, inflammatory areas of granulomas and serum cytokine markers such as TNF-α were also reduced for the NP formulation relative to the free drug, which had to be administered in a mixture of PEG400 and DMSO. The study underlines the enormous potential of nanomedicines in TB therapy. The combination of π-π-stabilized PeptoMicelles (as an efficient drug delivery vehicle) with the zebrafish embryo model of TB provides a rapid and powerful early drug screening system to assess *in vivo* efficacy and toxicity, which could have broad applicability in drug discovery settings.

Discussion

In 2009 Professor Gareth Griffiths, my principal supervisor, moved from the EMBL Heidelberg to the University of Oslo and established the research group I have been so privileged to do my PhD in. The original aim of the group was to establish the use of the zebrafish embryo model and apply it for nanomedicine research directed toward TB treatment. The use of NPs for therapy applications, especially against TB, was largely inspired by the Indian biochemist Gopal Khuller and his group. Their cumulative work clearly illustrated the advantages of NPs as drug delivery vehicles by showing the superiority of different nanoformulations over conventional free drug administration for TB treatment, using mouse and guinea pig models of TB. However, despite the fact that advantages offered by NP mediated drug delivery had been shown and reported on by them in multiple publications, the *in vivo* dynamics and underlying mechanisms for improved therapy and reduced toxicity of NPs were unknown. There were no publications using any microscopy focused on following the *in vivo* behavior and distribution of NPs. My principal supervisor, Gareth Griffiths, had previously researched phagocytosis of latex beads by macrophages for many years. He hypothesized that NPs would efficiently end up in macrophages and that this could explain the impressive therapy reported by Khuller. Contrary to the application of NP therapy for cancer treatment, where macrophage uptake of NPs is problematic and considered as an undesirable off-target effect, macrophage uptake is actually beneficial for TB treatment as pointed out by Griffiths *et al.* [159]. The rationale for this being that the macrophage is the preferred host-cell for the pathogen, be it Mtb in humans or *M. marinum* (Mm) in zebrafish. This led to the hypothesis that uninfected macrophages that phagocytose NPs are redirected toward the infection site due to chemotaxis, and thereby these cells function as a taxi, transporting the encapsulated drug to the infection.

To verify this hypothesis and study the *in vivo* fate of NPs in detail, as well as cell interactions and early events of TB infection, our group started using the zebrafish embryo model of TB that is infected with Mm, as pioneered by the Ramakrishnan group [202]. This allowed for high-resolution visualization of the pathogen, host-cells and NPs within a live biological system.

My work, presented in this thesis, is an extension of previous work in this group, and especially the research done by my co-supervisor Dr. Federico Fenaroli has been both important and inspirational. Two of his papers in particular have been fundamental and served as a direct groundwork for moving forward with this project, namely *"Nanoparticles as drug delivery system against tuberculosis in zebrafish embryos: direct visualization and treatment" from 2014 [175]* and *"Enhanced permeability and retention-like extravasation of nanoparticles from the vasculature into tuberculosis granulomas in zebrafish and mouse models"* from 2018 [161]. The former, for the first time, introduced the zebrafish embryo as a model system for NP mediated therapy against Mm infection and simultaneous live-imaging of fluorescently labelled NPs, host-cells and bacteria. The latter publication takes advantage of a new infection model, first described by Oehlers *et al.* and referred to as the "trunk" [223]. Federico Fenaroli showed that this injection site, the "trunk", was in fact the neural tube of the embryo and further developed the infection model. Injection of Mm into this site resulted in a massive localized granuloma, more closely resembling the human TB pathology compared to the standard blood infection model introduced by Ramakrishnan.

With this background my objectives were to expand the use of the zebrafish NP-TB model and develop it as an intermediate screening stage between cell culture and experiments in mice through systematic testing of various new anti-TB drugs and nanoformulations found active *in vitro*.

Goals and challenges for TB therapy

TB treatment requires many drugs for long periods of time, which often leads to toxicity and patient non-compliance. This in turn contributes to the increasing prevalence of drug-resistant strains, which severely complicates successful treatment, and is considered the biggest challenge facing us in ending TB as a world problem. There is therefore a critical need for more effective and less toxic drugs, in addition to simpler and shorter combinatorial treatment regimens directed toward TB and especially against MDR/XDR-TB.

There are many challenges related to TB drug development [224, 225]. One major challenge is to shorten the long and complicated process of progressing with anti-TB

drugs from the initial testing up to the clinical testing. Several years passes from when a new drug candidate is discovered until it reaches the market and only a small fraction of drugs that enter human clinical studies are eventually successful. This process is even more time-consuming for nanotherapeutics. Due to the additional complexity introduced by the NP and the diversity of NP types, no standard rule exist for market approval and regulatory agencies such as the FDA and EMA consider new nanotherapeutics on a product-by-product basis [226].

We are indeed in great need of new and effective TB drugs. Therefore, it is important that promising treatments of free compounds and/or nanoformulations are quickly identified and thoroughly investigated in preclinical studies and progressed forward to human clinical trials. Today, despite impressive preclinical data in different animal models of TB showing the advantages offered by NP-mediated drug delivery, no NP-based treatments against TB are in clinical use or even in any stage of clinical trials. I believe the work presented in this thesis can improve preclinical research and aid in the development of new drugs and nanoformulations by facilitating their passage to clinical testing.

The problem of following an infection *in vivo*

A major bottleneck of the drug-development process, prior to human clinical trials, is the transition from *in vitro* cell culture experiments to pre-clinical studies using different animal models [227]. A general problem with all mammalian models, including human patients, is the difficulty of visualizing the TB infection, for example to see the bacteria in the body in a non-invasive way [228]. The main experimental animal used for pre-clinical studies, the mouse, like all mammals, is opaque and poorly suited to visualize the main infectious events, pathogen-cell interactions, granuloma formation, dissemination and establishment of new foci, using optical imaging [228]. In order to observe and study such events the animal must be sacrificed and an autopsy needs to be performed, which is time-consuming and inferior to observing the infection in a live organism. Live-imaging in mammals is possible in a limited way, but the resolution and the level of detail is limited [229, 230]. Furthermore, toxicity and therapy studies in mice and other mammals are complex, expensive and time consuming. In general, the step from cell systems to testing in mice and other mammals is big and an intermediate

model that could bridge the gap by improving the imaging possibilities and make toxicity and therapy testing easier would be beneficial for the drug-development process.

The small and see-through zebrafish, an attractive intermediate model

The zebrafish encompasses several factors that make it a desirable model system for biologists. These factors include small mass, large clutch size (number of eggs produced), short generation time, rapid development and relatively low cost and maintenance needs. The zebrafish also has a fully sequenced genome with a high level of genetic homology to humans and is comparatively easy to manipulate genetically, which has resulted in the availability of multiple transgenic strains [199, 231]. Furthermore, the optical transparency and genetic versatility facilitates non-invasive, high-resolution live-imaging of the entire organism. All these features enable observations that would be impossible to execute in a mouse, such as observing the early-events of TB infection at the cellular level in detail or following the fate of intravenously injected NPs.

General advantages of zebrafish for biological research

In the next sections I will summarize and discuss the advantages of the zebrafish embryo model for biological research in general. An overall advantage with the zebrafish embryo and a recurring theme in the following sections is the see-through nature of this embryo that allows high-resolution microscopy at the cellular level, including visualization of internal structures and the localization of fluorescent structures; be it cells, pathogens or nanoparticles.

Ethics in animal research

Philosophical beliefs in society are changing in favor of reducing our extensive use of animals for human benefit. In science this can be seen by the increasingly implemented and widely accepted concept of the 3R’s (replacement, reduction and refinement)

concerning animal research. **Replacement** includes absolute replacement and relative replacement. In absolute replacement, alternative systems such as cell cultures or computer models are being used instead of animals. Relative replacement means to use “lower” animals believed to have a lower threshold for pain perception relative to more complex organisms [222]. Our use of zebrafish in the early developmental stages instead of mice falls under the term relative replacement. **Reduction** includes any approach that will result in less animals used for research purposes or maximizing the data obtained per animal so the need for subsequent animal studies are reduced [222]. The use of zebrafish embryos to screen free drugs and/or nanoformulations, in order to narrow down test groups in subsequent mouse studies can be viewed as a reduction measure, at least in terms of mass of animal. An additional benefit of zebrafish is that until day five post fertilization the embryo is not protected by the regulatory frameworks dealing with animal research in the EU because at this point the embryo is not considered sufficiently developed [232]. **Refinement** refers to any modification that would increase animal welfare and reduce pain and distress. This includes both general husbandry as well as experimental procedures. Identifying humane endpoints is an example of refinement [222].

These principles, developed by William Russell and Rex Burch in the 1950s, aim toward improving the treatment of research animals, as well as the quality of science in animal studies [222]. A consensus is now emerging that the zebrafish offers significant ethical advantages over mammals [232].

Toxicology

Toxicology deals with testing new chemicals for their safety and at some point this must be done in an animal. While toxicology screens in mammals are time-consuming, inefficient and costly, the zebrafish embryo and adult fish represents alternative models that are both faster and cheaper to work with and that raise fewer ethical concerns. It can be argued that both are also more sensitive than mammals; for sure since they are smaller, they require much less toxins. For example; a zebrafish embryo weighs approximately 1 mg [175, 233, 234], which is minute compared to a mouse of about 25 g. In order to inject an equivalent dose in mg/kg, with the same solution, in the two species, the mouse requires a volume that is 25,000 times higher.

The zebrafish embryo is increasingly being used to identify the effects of environmental pollutants, for example; zebrafish have been used to study the effects of organic pollutants in two Norwegian fresh-water lakes [235]. In the pharmaceutical industry, this fish is used to assess the safety of various drugs, and there appears to be a growing pharmaceutical industry acceptance of zebrafish-embryo-based toxicity screens to identify and prioritize less harmful compounds for further drug development [236, 237].

The small size, transparent nature and being a sensitive indicator of toxicity, makes the zebrafish embryo ideal for noninvasive examination of morphological and behavioral signs of toxicity [236]. Our group have developed two main toxicology assays to determine the toxicity and tolerability of various drugs and nanoformulations. **1. Survival assay**, where we simply keep track of cumulative mortality post drug administration over several days and consider safety based on average survival. **2. Toxicity multi-score assay**, originally described by Palha *et al.* [238] and introduced to our group in the publication by Vibe *et al.* [233]. The toxicity score assay evaluates toxicity based on embryo behavior, such as escape response to light touch, and physical indicators of toxicity, such as development of edemas and spinal cord deformities.

In **Paper IV**, we developed a simplified toxicity score assay (**Table 6**) that removed much of the potential for subjective interpretation and bias during analysis. For instance, in the original assay the body shape could be categorized as straight, slightly curved or strongly curved, giving a toxicity score of 0, 1 or 2 respectively. Where to draw the line between a slight or a strong curve is vague, therefore we chose to categorize it simply as normal or malformed.

Table 6. Toxicity indicators and criteria for scoring. Table taken from **Paper IV**.

Toxicity indicators	**Criteria for scoring drug toxicity**	
	0	**1**
Equilibrium	Upright	Sideways
Escape response to light touch	Quick	Slow or none
Body shape	Normal (straight)	Malformed; curved
Blood flow	Normal	Slow or not in all body parts
Heartbeat	Normal	Irregular; very slow or fast
Edema	Absent	Present
Swim bladder inflation	Normal	Small or absent

Our rationale in **Paper IV** was to use the survival assay as an initial toxicity screen to rule out any compounds that induced a high degree of early mortality, and subsequently apply the toxicity multi-score assay to more closely examine the remaining compounds and check if they induced any non-lethal toxic effects.

The zebrafish embryo can be adapted for large-scale toxicity screens. At the early stages of development, the zebrafish can be placed into separate wells of multiwell plates, enabling toxicity screens of multiple individual organisms simultaneously. A widely accepted and much used zebrafish toxicity screen is the standardized fish embryo acute toxicity test (FET), included as test guideline number 236 in the Organization for Economic Co-operation and Development (OECD). FET evaluates the toxicity of chemicals based on the development and survival of fertilized eggs in response to compound exposure [239]. The small size of the fish and the low volume of water require only minute amounts of compound to be tested [236], which is a great advantage, if the compound is expensive and/or is complicated to synthesize and only accessible in small amounts. The most common dosing method in large-scale drug screens is the addition of the compounds directly to the water, referred to as in-water or bath dosing. This is of course a very efficient way of administering the compounds to be tested to a large number of individuals; however, this approach is associated with several limitations [236]. The in-water exposure gives you no control over the actual dose received by each individual fish. This affects the translatability of the data when progressing to higher animal models. For example, in-water dosing concentrations cannot be used to predict safe and non-toxic drug doses administered by conventional routes in mammals, such as the oral and intravenous route [236]. Furthermore, for compounds with inherently low water solubility, in-water dosing might be impossible to test at therapeutically active concentrations. An alternative to in-water dosing are micro-injections, which will be discussed in the zebrafish-TB model section further below.

Development, disease models and therapy studies

In biomedical research, both *in vitro* and *in vivo* model systems are needed to study human biology and diseases at the preclinical stages. However, *in vitro* cell culture models do not include the complex physiology and complete framework offered by *in*

vivo models [199]. Data obtained *in vitro*, for instance the antimicrobial activity of a drug in bacterial culture needs to be validated in a whole-organism context, for example in zebrafish or mice. There is a wide selection of animal models to study human diseases and their respective underlying mechanisms, pathogenesis and treatment options. Many basic cellular processes linked to development, genetic diseases and innate immunity are functionally conserved between invertebrates, such as the fruit fly *Drosophila melanogaster*, and vertebrates, including mammals [240-242]. Furthermore, invertebrate models facilitate large-scale screens in a short period. However, invertebrates are morphologically distinct from humans, lacking structures and organs associated with different human diseases, and therefore their capacity and relevance as disease models are limited. Mammalian models, such as the mouse, are closer to humans and therefore better suited to study many diseases. Then again, the caveat with mammals are increased costs, time and ethical concerns, in addition to poor imaging possibilities.

In contrast, the zebrafish embryo combines many of the advantages offered either by invertebrate or mammalian models. The zebrafish is a vertebrate and therefore phylogenetically closer to humans than any invertebrate model. Like invertebrates, zebrafish facilitates the use of large-scale screens; this includes genetic and therapeutic screens [243]. The small size, optical transparency and several transgenic strains with fluorescently labeled cells makes it possible to follow and study a disease process in real-time and also directly visualize the effect of a given treatment [175, 244]. Such observations can shed light onto processes that are inaccessible or highly limited to observe in mammalian models. The zebrafish embryo as a model for human diseases and its use in therapy studies has resulted in a new paradigm in pharmaceutical drug discovery, which is whole-organism, large-scale drug screening [243]. This is an improvement from traditional *in vitro* whole-cell screens.

Historically the zebrafish embryo has been mostly applied to study development, including human congenital and hereditary disorders [245-247]. Apart from this, the zebrafish is increasingly used to model acquired human diseases and for drug discovery purposes. Different cancer types and infectious diseases, including gram-positive (e.g. *Listeria monocytogenes*), gram-negative (e.g. *Salmonella Typhimurium*) and mycobacterial diseases, are being studied using the zebrafish [248, 249]. The

latter includes the Mm bacterium and the zebrafish-TB model and will be discussed in the next section.

M. marinum and the zebrafish-TB model

***M. marinum*.** Bacterial surrogates for various pathogens, e.g. Mtb, are needed in order to minimize biosafety risks and regulations and thereby make the drug discovery and development process more efficient. Bacteria used as surrogates for Mtb include *M. smegmatis*, the attenuated bovine-strain BCG and Mm [250-252]. All three are categorized as BSL-2 organisms, meaning that the researcher only needs to wear a lab coat, protective glasses and gloves when handling and working with the bacteria. This is a huge advantage compared to Mtb, which is a BSL-3 bacterium, and requires full protective gear and a specialized facility for culturing and experimentation that is restricted to highly trained researchers.

Mm has a close genetic relationship with Mtb; sharing more than 85 % nucleotide identity and 3000 gene orthologs. The genome of Mm is approximately 1.5 times larger than the Mtb genome, 6.6 Mb versus 4.4 Mb, reflecting the broader environmental and biological range of Mm over the specialized human pathogen Mtb [252]. Compared to the 24 hours generation time of Mtb, Mm is a relatively fast grower, with a generation time of 4-6 hours [252]. Greatly reducing the time needed to obtain *in vitro* data; in our lab, a typical minimum inhibitory concentration (MIC) experiment using Mm takes less than a week, a similar experiment using Mtb would take several weeks. Another important difference between Mm and Mtb is the growth temperature. Mtb grows optimally at 37 °C, while Mm has its temperature optimum at around 30 °C. This is vital to consider when designing experiments involving the use of Mm and mammalian cells, which similar to Mtb grow best at 37 °C. In **Paper IV**, we tested the antimicrobial effect of the nitronaphthofurans (nNF) compounds against intracellular Mm, internalized by bone marrow-derived macrophages (BMDM) from mice. The experiment was done at 32.5 °C, a compromise that facilitated normal Mm growth and at the same time was well tolerated by mouse macrophages [253-255]. Overall, the high degree of genetic identity and gene function, in addition to being safer and significantly faster to work with, justifies the use of Mm as a surrogate model for at least the early stages of Mtb research.

However, as always when using a model system, one should be careful when interpreting and translating data obtained using a bacterial substitute to the original pathogen. Susceptibility to different TB drugs can vary widely between Mtb and bacterial models for Mtb. A relatively recent study by Namouchi and colleagues reported on the phenotypic and genomic similarity of *M. aurum*, *M. smegmatis* and Mm to Mtb [256]. All three surrogates displayed a high degree of phenotypic and genomic similarity to Mtb, but a MIC screen of 12 TB drugs revealed significant differences in drug susceptibility. For example, Mm is highly sensitive to RIF but not to INH, both being cornerstone drugs in TB therapy. Susceptibility differences are crucial to be aware of when assessing drugs using Mtb surrogate bacteria, such as Mm.

The recently approved TB drug pretomanid is highly active against Mtb *in vitro*, however when we tested pretomanid in a MIC assay using Mm it was virtually ineffective and all the derivatives tested displayed higher MIC against Mm than they did against Mtb. Nevertheless, unpublished data from our group revealed that the mechanism of action of pretomanid and its derivatives is the same between Mm and Mtb. This is based on the work initiated by our colleague Dr. Noelia Alonso-Rodriguez, who generated spontaneous Mm resistant mutants to the pretomanid derivatives A, B, C and D. The Mm mutants were submitted to whole genome sequencing and mutations were detected in fbiC and fbiA genes, which are known to cause pretomanid resistance in Mtb [257, 258]. Furthermore, in order to verify that F_{420}-deazaflavin-dependent nitroreductase (Ddn) was the enzyme responsible of the bio-reductive activation of pretomanid and its derivatives, as is the case in Mtb [133], a screening of an Mm transposon mutant library was performed to select resistant clones to compound D and then search for possible interruptions of the Ddn gene by polymerase chain reaction (PCR). In both of the two mutants selected, Ddn interruptions were detected, thereby confirming that Ddn is the enzyme responsible for activation of the prodrug in Mm as well.

The activity trends we observed in Mm, which diverged from activity against Mtb, suggested that small sequence variations of the derivatives affect drug binding to the target between the two bacterial species. We are working on elucidating this structural activity pattern. In the forefront of the investigation is the organic chemist Dr. Andrew Thompson from The University of Auckland, New Zealand. He has been systematically designing new derivatives of pretomanid that were tested against Mm and Mtb in our

lab at the University of Oslo. **Table 7** presents the *in vitro* data on free drug activity and toxicity obtained so far in the continued and ongoing project related to next-generation pretomanid derivatives.

Table 7. Compound name/ID, CLogP value, *in vitro* antibacterial activities against Mm and Mtb and cytotoxicity in VERO cells of pretomanid and derivatives investigated. Compounds displayed in bald text are also tested in the zebrafish-TB model. CLogP values calculated using the ACD LogP prediction software (version 12.02, Advanced Chemistry Development Inc., Toronto, Canada). * Pretomanid derivatives that are included in **Paper V**.

		MIC (µM)	MIC_{90} (µM)	IC_{50} (µM)
Compound name/ID	CLogP	*M. tb*	*M. marinum*	VERO
Pretomanid	**2.70**	**0.51 ± 0.31**	**209 ± 70**	**>200**
Delamanid	4.75		<0.03	
A*	**4.36**	**0.029 ± 0.019**	**1.3 ± 0.6**	**>200**
B*	**2.99**	**0.028 ± 0.018**	**6.4 ± 2.0**	**>200**
C (TBA-354)*	**3.01**	**0.025 ± 0.017**	**7.6 ± 4.8**	**>200**
D*	**3.77**	**0.015 ± 0.009**	**0.75 ± 0.40**	**>200**
E	**3.77**	**0.025 ± 0.007**	**2.4 ± 0.8**	**>200**
F	**5.26**	**0.016 ± 0.008**	**0.33 ± 0.12**	**>200**
G	**3.33**	**0.008 ± 0.004**	**0.50 ± 0**	**>200**
H	**3.33**		**3.4 ± 0.9**	**>200**
I	**2.77**	**0.015 ± 0**	**1.7 ± 0.5**	**>200**
J	3.47	0.023 ± 0.008	>200	>200
K	**4.70**		**0.22 ± 0.04**	**>100**
L	4.67		>80	>100
M	6.02	>8	>80	>100
N	**4.85**		**0.75 ± 0.35**	**>100**
O	4.85		>80	>100
P	**3.33**		**0.83 ± 0.24**	**>200**
Q	**3.53**		**0.42 ± 0.12**	**>200**
R	**3.53**		**0.67 ± 0.24**	**>200**
S	3.50		6.0 ± 2.0	>200
T	3.50		>64	>200
U	2.28		2.0 ± 0	>200
V	3.49		>64	>200
W	3.46		>64	>200
X	3.11		>64 (87%)	>200
Y	2.01		>64	>100
Z	**2.67**		**1.3 ± 0.5**	**>100**
AA	3.38		>64	>100
BB	**2.85**		**1.1 ± 0.4**	**>100**
CC	3.11		0.71 ± 0.30	
DD	3.42		>64	
EE	3.04		2.0 ± 0	>100
FF	2.19		7.3 ± 1.5	>100
GG	1.52		4.7 ± 1.5	
HH	2.63		4.0 ± 0	
II	3.05		43 ± 15	
Des-nitro D	4.04		53 ± 39	85

In order to avoid excluding potent drugs against Mtb or include inactive drugs against Mtb due to susceptibility differences between Mtb and surrogate species, we suggest that *in vitro* activity testing should be done using Mm and later confirmed in Mtb. Ideally, the *in vitro* testing should be done against bacteria intracellularly in macrophages instead of bacterial culture. This is in order to assess the drug activity in the context of the host cell, as extensively pointed out by Liu and colleagues [259].

The zebrafish TB model. Several years of working with the zebrafish embryo and using it as a model system for TB and nanomedicine research has made me aware of the strengths and opportunities of the model. One major advantage offered by the zebrafish-TB model is the time needed to obtain results. As discussed previously, TB drug development is a complicated and lengthy process. The cell to mouse transition is challenging and TB therapy studies in mouse models can take several months. In mice, time is needed for acclimatization, infection to progress, followed by consecutive dosing over several weeks for therapeutic effect to occur. The zebrafish embryo, in stark contrast to mouse studies, require less than two weeks to get results, typically only 10 days from fertilization until end of experiment as seen in **Figure 4** below.

Our group has primarily used the zebrafish TB model as a screening stage for nanotherapeutics. This means characterizing *in vivo* behavior of fluorescently labeled NPs and/or assessing the toxicity and therapy response of drug loaded NPs. A standard experiment involves the following steps:

1. Micro-injecting the bacteria into the embryo, by the intravenous route or in the neural tube. Exclusive for therapy studies.
2. Micro-injecting the treatments, by the intravenous route; free drugs, drug loaded NPs or fluorescently labeled NPs. For toxicity, therapy or other types of studies, e.g. circulation time.
3. Documenting cumulative survival over several days. For toxicity and therapy studies.
4. Live-imaging; stereomicroscopy or confocal microscopy. Stereomicroscopy being used for various purposes, quantifying the bacterial burden in therapy studies, examining signs of toxicity, NP co-localization with specific cells and determining circulation time. Confocal microscopy being used for more in-depth investigations of infectious events and/or NP behavior and cell interactions.

Although tedious and technically challenging, the consensus within our research group, is that micro-injection of both Mm and treatments is necessary when working with the zebrafish embryo in order to obtain reproducible and reliable data. We consider the alternative strategy, infection and delivery of drugs by adding bacteria and drugs directly to the water, as a non-viable option for our purposes (see the toxicology section above). In contrast to our view; a paper published in 2016 by Dalton *et al.* reported on the screening of TB drugs in zebrafish embryos, infected through water immersion, using bioluminescent labelled Mm [215]. Here, the infection were located to the lower jaw and developing gills and did not result in early mortality. In addition, the compounds were added directly to the water and the activity was determined by measuring the increase or decrease in bacteria associated fluorescence between days 0 to 3 post treatment. Our group has previously investigated the strategy of adding Mm directly to the water, so called natural infection (unpublished data). Our studies resulted in transient infections in the gastrointestinal tract and we were unable to establish a proper infection located within the body, even when fish were exposed to high levels of bacteria in the water for several hours. However, in the paper by Dalton and colleagues, the embryos were incubated together with Mm bacteria for four days. Had we extended the incubation time to days instead of hours we would most likely have obtained a similar infection. Regardless, we consider intravenous administration of bacteria and treatments, allowing us to control the infectious burden and drug dose administered to each fish, as a more consistent strategy compared to natural infection and in-water dosing.

In the work presented in this thesis, two micro-injection-based infection models have been used (**Figure 4**). That is **the intravenous infection model** and **the neural tube infection model**.

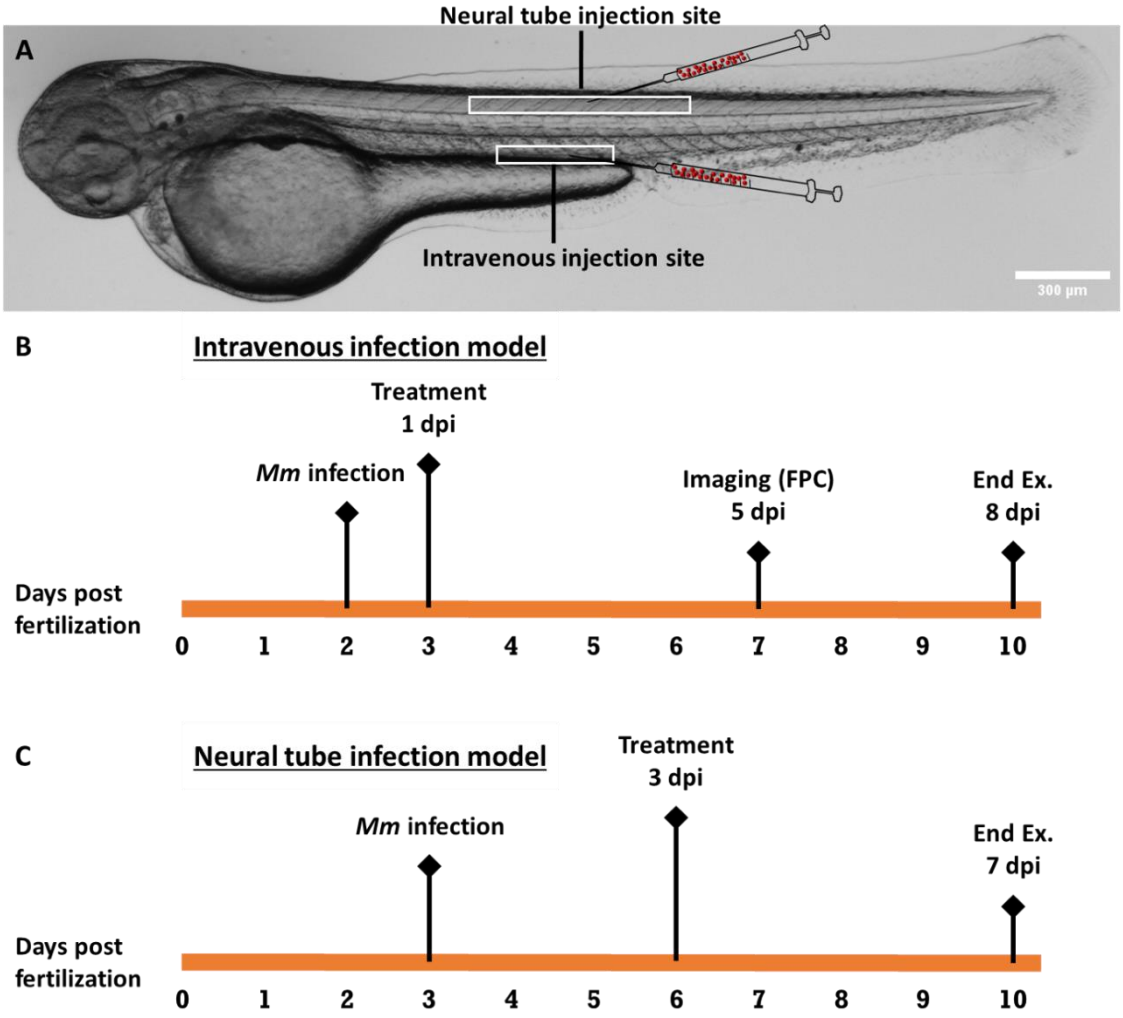

Figure 4. Illustration of general injection areas and schematic timelines of the two zebrafish embryo infection models applied in Griffiths group at the University of Oslo. Dpi = days post infection, FPC = fluorescent pixel count, End Ex. = end of the experiment. (A) Wild-type zebrafish embryo three days post fertilization. The white boxes outline the two injection sites used for Mm infection. (B) Schematic timeline of the intravenous infection model. (C) Schematic timeline of the neural tube infection model. Figure modified from **Paper V**.

The intravenous infection model results in a systemic infection driven by fast bacterial uptake by macrophages residing in the blood and the formation of relatively small and dynamic granuloma structures associated with the vasculature [175]. If not provided any treatment, infected fish will start to die in about five days. Infection on day two post fertilization (dpf), followed by treatment administration the next day, allows time for the treatment to have an effect on the bacterial burden before mortality occurs in the control groups. This facilitates both imaging and quantification of the bacteria-associated fluorescence signal to complement the survival analysis. Because of this, the intravenous infection method is well-suited for therapy screens and has been the infection model mostly applied in the work presented here.

Contrary to the intravenous route, the neural tube infection model results in a localized infection with larger and more stable granuloma structures with a higher bacterial load. A direct comparison of the Mm associated fluorescence, corresponding to the bacterial burden, between intravenous and neural tube infection, resulted in approximately 7 times stronger Mm-fluorescent signal in neural tube infected embryos compared to intravenously infected embryos (data not published). The neural tube granuloma closer resemble human pathology. Among these features are infiltration into the granuloma of newly sprouted blood vessels (angiogenesis) in response to local hypoxia, and ultimate cavity formation leading to release of bacteria to the outer medium [161]. The latter is reminiscent of the mechanism which Mtb is released from necrotic cavities in humans via the airways. In the neural tube model, treatment administration is delayed until day 3 post infection to allow time for proper granuloma-formation. Imaging to determine therapeutic efficacy is therefore difficult since the untreated control fish often begin to die in the days between treatment administration and imaging. However, the model is compatible with survival analyses and is used to study NP accumulation into granulomas.

Micro-injection mediated administration of poorly water-soluble drugs can be challenging due to clogging of the fine needle. Hydrophobic drugs in their free form must often be solubilized in organic solvents, such as DMSO, to facilitate micro-injections. The solvents used are poorly tolerated at larger volumes and can induce toxic responses and premature death. This problem is avoided if the drugs are encapsulated into NP systems. The advantages provided by NP-mediated therapy will be discussed in the next chapter.

Advantages of nanoparticle-mediated therapy

Lipophilicity and anti-mycobacterial activity

Lipophilicity or low water solubility of compounds is considered an undesirable property in medicinal chemistry and in conflict with Lipinski's "rule of five", which are guidelines to assess whether a compound would be within acceptable ranges of solubility and permeability *in vivo* [260]. Here, the logP cut-off value is set to below 5. LogP is a measurement of the hydrophilicity of a compound; low value means high water

solubility and vice versa [261]. However, strict compliance to these principles or similar rules of thumb within medicinal chemistry is a poor strategy for discovery and development of new anti-TB drugs. A bioinformatic analysis of a large library of over 300,000 compounds screened against Mtb revealed that the compounds classified as active against Mtb had a statistically higher logP value compared to the inactive compounds, on average about 0.7 higher logP values [262]. Furthermore, the trend of positive correlation between lipophilicity and anti-mycobacterial activity is evident within drug classes as well. Hydrophobic derivatives are usually found to be more active against Mtb than the more hydrophilic parental compound or analogues. For instance, the majority of the second-generation pretomanid derivatives synthesized in the last decade had a lower MIC against Mtb and a higher logP compared to pretomanid itself [263-265]. All the four derivatives (arbitrarily designated A, B, C and D) investigated in **Paper V** were less water-soluble and had higher activity against Mtb than pretomanid. The augmented activity of lipophilic compounds is related to the thick and waxy cell wall of mycobacterial species and hence improved penetrability of hydrophobic drugs over hydrophilic ones [266]. Additionally, the interaction of hydrophobic compounds with the bacterial membrane can potentially alter its stability and integrity and thereby have a bactericidal effect [267]. Taken together this results in a paradox where TB drugs represent an “activity-through-lipophilicity” principle that is in direct opposition to standard guidelines and principles in medicinal chemistry that favors water solubility.

Our group realized that NP-mediated drug delivery could fulfil both these opposing needs simultaneously. Particles with a hydrophilic surface and a hydrophobic core containing lipophilic drugs would have a good biodistribution, circulate within the body and in theory be taken up by macrophages or accumulate directly into granulomas. In both locations, the breakdown of the particles would free the entrapped drugs in direct proximity to the pathogen. With this rationale since the early beginnings in 2009 our group has built a strong international and interdisciplinary collaboration consisting of NP experts, drug chemists and TB researchers using different animal models. A key figure in this collaboration is Dr. Thompson (The University of Auckland, New Zealand), who was working on nitroheterocyclic compounds for the treatment of neglected diseases, including the development of pretomanid derivatives against Mtb. His goal was to develop highly active and relatively

water-soluble compounds for oral administration. We introduced our concept of NP mediated drug delivery and were interested in the more hydrophobic derivatives with high activity against Mtb. Dr. Thompson was intrigued and sent us a selection of derivatives that were investigated and resulted in **Paper V**. The collaboration has been very fruitful and based on the initial findings Dr. Thompson has continued designing and synthesizing antitubercular pretomanid derivatives for NP delivery. As shown in **Table 7** above, about 30 pretomanid derivatives have been screened in their free form for *in vitro* activity against Mm and for their toxicity to mammalian cells, and around 15 compounds, formulated in NPs, have been analyzed by myself in detail in the zebrafish-TB model.

Nanoparticle targeting strategies for TB treatment

NP targeting can be divided into passive and active approaches. We have primarily focused on passive targeting of NPs to TB granulomas, which can be divided into two different strategies and briefly summarized as: **1. Short-circulating NPs**, are rapidly phagocytosed by blood macrophages that in turn respond to chemical signals, induced by the Mtb infection, which redirects the macrophages to the infected area, thereby transporting the drug carrying NP in close proximity to the bacteria [159, 214]. **2. Long-circulating NPs** avoiding protein opsonization and macrophage uptake, through NP surface modifications and thereby staying in circulation longer. As described in the introduction, attachment of PEG to the NP surface and the formation of a hydrating layer provides the stealth-properties needed for prolonged blood circulation [160]. An outer NP layer of polysarcosine, based on the amino acid sarcosine, also enables stealth-properties, and this design was used in **Papers IV** and **V** to achieve sustained circulation [268]. Over time, long-circulating NPs passively concentrate in inflamed areas, such as granulomas, due to reduced structural integrity of the vasculature surrounding the diseased site and increased retention time due to poor lymphatic drainage. This phenomenon is referred to as the EPR effect and was originally discovered in cancer tumors [164]. Yet, the EPR effect is a complicated and controversial topic, and in recent time several authors have questioned the therapeutic relevance and extent of the EPR effect in human patients [269, 270].

Contrary to passive targeting, **active targeting** includes attachment of specific ligands to the NP surface and recognition by the corresponding surface-receptor on the target

cell and subsequent NP internalization by receptor mediated endocytosis. In the context of TB treatment, a promising target for NP delivery is the macrophage C-type lectin receptor specific for mannose that recognizes the mannan-coated cell wall of Mtb and other microorganisms and mediates phagocytosis. The attachment of mannose moieties to the NP surface is therefore being explored as a mean of targeted delivery toward macrophages and ultimately improved efficacy [271, 272].

The transparent zebrafish uncovering *in vivo* nanoparticle behavior

The transition from physicochemical characterization and cell culture assays to *in vivo* applications for new NP systems is challenging. The fate of intravenously administered NPs; blood circulation, cell and tissue distribution, and as a consequence, the safety and efficacy of the encapsulated drug, is heavily dependent on the chemical properties of the NP formulations. It is however difficult to predict NP behavior in a multicellular complex organism, such as a human, based on chemical properties and cell culture studies alone. There is a lack of *in vitro – in vivo* translatability and this shortcoming represents a bottleneck in the nanomedicine drug development process. The process can be made more efficient by replacing the mouse with the zebrafish embryo as the first animal model for *in vivo* characterization.

In **Paper I** we used the zebrafish embryo model to develop a quantitative method to characterize vascular flow kinetics of NPs and their interaction with key cell types, namely macrophages and endothelial cells, involved in clearing NPs from circulation. The circulation time of NP formulations is an important factor to characterize, for instance longer circulation times results in increased passive accumulation at inflamed sites and therefore relevant for both cancer and TB treatment. Semi-quantitative methods for NP circulation kinetics in zebrafish embryos were previously reported on in two individual publications [273, 274]. Both studies relied on confocal microscopy and the imaged area, used for circulation analysis, was limited to the caudal region and did not include the whole organism. The circulation kinetics were either given as the ratio between mean fluorescence intensity from free unbound NPs within the vasculature normalized by the vascular area, referred to as a “circulation factor” [274] or as the average intravascular fluorescence within the dorsal aorta [273]. In contrast

our method applied the stereomicroscope to evaluate circulation times of various NPs, which is a more user-friendly and less laborious imaging technique than confocal microscopy, but with lower resolution. We also measured the mean intravascular fluorescence, but importantly, divided this value by the mean NP fluorescence from the whole fish, obtained at a lower magnification. The last step was conversion into percentage, so different NPs could be directly compared to each other without any need for interpretation. **Paper I** describes a robust and relatively simple approach to quickly characterize and quantify the *in vivo* behavior and distribution pattern of fluorescently labeled NPs. All analyses were automated through a customized macro in ImageJ, minimizing the risk of introducing bias. The method outlined in **Paper I** can be used as a first *in vivo* screen of new nanomedicines directly following cell culture studies. In contrast, **Paper II** describes a more in-depth methodology for *in vivo* NP characterization, aiming toward understanding the biological interactions of NPs at the cellular level, using sophisticated microscopy techniques such as high resolution 3D live-imaging and EM.

In mammals, 30-99 % of systemically administered NPs will end up in the liver and normally less than 5 % will reach the diseased area [275]. Macrophages have been viewed as the main cell type responsible for NP clearance from the circulatory system, because of the positive correlation between organs with high macrophage density and where NPs accumulate in the body, e.g. the liver [276]. However, new evidence points toward another cell type of the reticuloendothelial system, the scavenger endothelial cells (SECs), in regards to clearance of NPs from the blood. A recent study found SECs in zebrafish embryos, restricted to certain venous sites, to be functionally homologous to the SECs counterpart in humans called liver sinusoidal cells [273]. The same study showed that uptake of anionic (negatively charged) NPs in SECs were through a charge dependent surface receptor named stabilin-2. A pre-injection of dextran sulfate ($DexSO_4$), a competitive inhibitor of stabilin-2, resulted in reduced uptake of anionic NPs by SECs and consequently prolonged circulation time and relative higher uptake by macrophages. Another recent study using the zebrafish embryo model found that the relative contribution in sequestration of anionic NPs from the blood were 77 % for SECs and only 2 % for macrophages [277]. When the embryos received a pre-injection with dextran sulfate, the relative uptake changed dramatically to 22 % and 65 % for SEC and macrophages, respectively. In **Paper II** we obtained similar results with

anionic PLA NPs after pre-injection with $DexSO_4$ at various concentrations, thereby strengthening the hypothesis introduced by Campbell *et al.* that charge-dependent recognition by the stabilin-2 surface receptor and subsequent uptake by SECs is the main driving force behind removing anionic NPs from circulation [273]. The potential to reduce NP uptake by SECs and consequently increase macrophage uptake, through pre- or co-administration of a competitive inhibitor of stabilin-2, represents a possible strategy to reduce off-target effects, such as NP uptake by the liver. This is relevant for TB therapy, where the macrophage is the main host cell and the disease usually manifests in the lungs.

An intriguing observation made in **Paper II** was that macrophages seemed to keep internalizing NPs after being cleared from the circulation. To verify and quantify the observation we applied the method developed in **Paper I** for determining macrophage uptake based on fluorescence co-localization. This analysis showed that macrophages indeed kept internalizing NPs, despite them being cleared from the blood. Flow cytometry analysis revealed that the fraction of macrophages containing NPs increased with time and plateaued at 4 h post injection. We hypothesized that this observation could be explained by NP transfer to macrophages from live cells and/or apoptotic events of cells containing NPs and subsequent macrophage uptake. To investigate this in more detail, we performed high-resolution live-imaging on double transgenic zebrafish, having red macrophages and green endothelial cells, and injected with far-red labeled NPs. This led to the identification of two separate mechanisms involving the transfer of cytoplasmic material from endothelial cells to macrophages.

One mechanism exhibited formation of protruding structures, resembling microvesicles, from the plasma membrane of endothelial cells that eventually were dislodged and subsequently taken up by macrophages in close proximity. We did not observe any NPs being transferred by this process, yet we cannot dismiss the possibility of it occurring. The other mechanism involved direct contact and transfer of cellular structures containing NPs together with cytoplasmic material from endothelial cells to macrophages. This process resembled a previously described phagocytosis-like mechanism, called trogocytosis. Trogocytosis, first observed in amoeba attacking mammalian cells [278], is the partial phagocytosis, or cell nibbling, of a donor cell. In recent years, trogocytosis has been identified in several cell types and play a role in

immune- and developmental processes [279, 280]. Macrophages can perform trogocytosis [281], however, macrophage trogocytosis of endothelial cells has not been observed until now.

In the context of TB treatment, NP transfer from endothelial cells to macrophages is highly relevant. As discussed previously, macrophages are the first line of defense against TB infection and the main host cell harboring the bacteria. Therefore, this cell type is a desired target for NP delivery and the transfer of NPs from endothelial cells, which are responsible for much of the NP uptake in the first place, to macrophages would reduce off-target accumulation and potentially improve therapy. However, more knowledge is needed on the extent of the transfer mechanism before conclusions are made.

Screening of new nanotherapeutics against TB using the zebrafish

The NP system investigated in **Paper III** (MPEO-b-PCL), significantly increased the therapeutic effect of RIF within an NP compared to RIF in its free form when tested in the zebrafish-TB model. Since its discovery in the 1960s, RIF remains the backbone of today's TB therapy. The daily RIF dosing of 10 mg/kg has been standard practice in TB treatment regimens for about 50 years [282]. However, studies have shown that the standard RIF dose results in suboptimal drug concentrations in different tissues and organs [283-285]. As reviewed by Véronique Dartois [286], a problem with current TB therapy is the inadequate penetration of many TB drugs into the human granulomas where the bacteria reside. This leads to suboptimal concentrations of drugs at certain granuloma areas that are difficult to reach which facilitates bacterial survival and drug resistance. Drug distribution studies using HPLC coupled to tandem mass spectrometry (LC-MS/MS) and MALDI mass spectrometry imaging (MALDI-MSI) have been used to quantify concentrations of different TB drugs in rabbit granulomas [287, 288]. How effective a drug penetrates into the granuloma and the local distribution within the lesion vary between drugs. For instance, RIF displayed low concentration in granulomas relative to plasma concentration [287]. In contrast, moxifloxacin resulted in higher concentrations in granulomas relative to plasma [287], however MALDI-MSI

revealed that despite high granuloma concentrations, moxifloxacin did not reach the necrotic center where extracellular bacilli reside in a low-metabolic state [288].

To date, several clinical trials have examined the treatment benefits linked with higher RIF doses to combat sub-therapeutic local drug concentrations, and the data are promising. Recently, the first report of the use of high-dose RIF in a clinical setting shows that daily doses as high as 2400 mg were safe and well tolerated by patients [289]. As high-dose RIF therapy illustrates, refinement of today's current TB treatment regimens can be done through re-evaluating existing dosage levels [282]. The use of NPs as drug delivery systems can further assist in this refinement process, as illustrated in **Paper III**. NP-mediated therapy is shown to reduce drug toxicity [233, 244], and can therefore minimize any augmented adverse- or off-target effects linked with higher doses, which is the main fear associated with an increased dosing schedule. In addition to reduced toxicity, NP therapy can enhance treatment outcome by improving the PK/PD properties of the drug and facilitate targeted delivery and sustained release [159]. For instance, our data show that intravenously injected NPs accumulate significantly more in zebrafish granulomas (about 5 %) relative to uninfected tissue. Even if the NPs are not able to penetrate deep into the pathological structures and rather concentrate outside the surrounding blood vessels and in the periphery of the granuloma, they may deliver the encapsulated drugs in relative close vicinity to the bacteria, which is still a big advantage over free drug delivery that is systemically distributed.

Based on the promising data presented in **Paper III**, our collaborators from the Czech Republic tested the NP system encapsulating RIF as monotherapy in a mouse model [290]. Here the NP-RIF formulation displayed both improved pharmacokinetics as well as improved treatment outcome (determined by CFU) over free RIF. This is yet another example showing the advantages offered by NP mediated therapy in the context of TB treatment, and demonstrates that the NP approach can be used to refine current treatment regimens by improving the efficacy of drugs already in clinical use. Furthermore, the progression to mouse studies based partly on zebrafish data, validates the use of the zebrafish embryo as a model with predictive capabilities.

Although the refinement of current treatment regimens, such as escalated dosing and/or encapsulation of approved drugs into NPs is a promising strategy for better TB treatment, the main effort in this work has been directed toward screening of new drugs

with a novel mechanism of action. The nNF compounds explored in **Paper IV** were previously found to be active against Mtb in a high-throughput phenotypic drug screen (Paris, France, data not published). Our investigation revealed that the selected nNF compounds were also active against Mm. Whether the mechanism of action against Mm is the same as against Mtb remains to be validated. Our group is currently investigating the mechanism of action of nNF compounds against Mm and Mtb to determine if there exists any differences or alternative mechanisms between the bacterial species and how the drugs exert their activity. Despite the mechanism of action not being completely clear, our study presented a framework for hierarchical testing; Mm as a surrogate for *in vitro* Mtb studies, followed by *in vivo* zebrafish studies. Our investigations identified three promising compounds that can be progressed to therapy studies in a higher animal model.

Our main effort recently has been directed toward pretomanid derivatives. In **Paper V** we tested four second-generation pretomanid compounds, designated drugs A, B, C and D. Previous *in vitro* activity testing against Mtb [263-265], replicated and verified by our group, showed that all of the compounds were superior to pretomanid. The compounds were also found to be nontoxic in mammalian cells [263-265], results that we could verify. However, drug A was poorly tolerated and deemed toxic in the zebrafish embryo model, both when administered in the NP formulation and when given in its free form. This was similar to what we observed when studying the nNF compounds, here none of the compounds displayed cytotoxicity *in vitro* (except C16, included as a toxicity control), but in the zebrafish embryo two of the compounds, C4 and C20, induced toxic responses. False negatives in toxicity screening is a problem within drug development [236], the sooner false negatives are ruled out the better. We show that the zebrafish embryo can identify poorly tolerated and/or toxic drugs missed by cell culture assays, and exclude them before being tested in higher animal models.

Due to the toxicity observed in zebrafish, drug A was excluded from further investigations. The remaining drugs, B, C and D formulated in NPs, were compared for their therapeutic effect against Mm in the zebrafish using the intravenous infection model. Here drug D was identified as the most promising compound of the three. Subsequent therapy studies revealed that the drug D nanoformulation resulted in better therapy than solubilized (using organic solvents; PEG400 and DMSO mixture) free drug D. This was the case when both the intravenous and neural tube infection

model were used. In addition, the nanoformulation allowed for higher doses to be administered than what was possible with free drug. The free drug was limited by the solubility of the drug in the organic solvent mixture and that the injection volume could not exceed 2 nL due to solvent related toxicities. The safe and potent nanoformulation containing drug D identified in the zebrafish embryo were tested in a mouse model of TB and compared to the free drug, also here by intravenous drug administration.

Based on the work presented in **Paper V**, the identification of a lead compound and an effective NP system for TB therapy, we continued and expanded our new generation pretomanid derivatives project. The aim remained the same, to develop a new, safe and effective adjunct therapy for MDR-TB, mediated by NP drug delivery. Drug D, which was non-toxic and provided good therapy in zebrafish and mice, was used as a prototype for the chemical structure and as a benchmark for anti-bacterial activity and treatment responses. Pretomanid and the second-generation derivatives were originally developed as free treatments to be administered orally by the TB Alliance. Initially they selected, drug C, better known as TBA-354, as the preferred preclinical candidate and entered it to phase I clinical trials, dealing with safety and dosage testing, in early 2015 [291]. Nevertheless, these trials were discontinued in 2016 due to safety issues; namely, TBA-354 crossed the blood-brain barrier (BBB) and caused mild signs of reversible neurotoxicity at higher doses [292]. Although we are using a NP system for drug targeting and delivery, thereby reducing the risk of significant accumulation in the nervous system, we have implemented permeability profiling of new derivatives as an experimental step to avoid neurotoxicity issues. **Figure 5** outlines the work flow and the hierarchical testing approach used in this large and multidisciplinary collaboration.

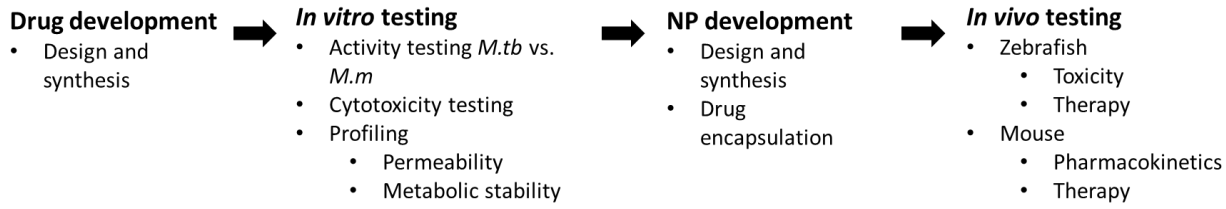

Figure 5. Flowchart of hierarchical testing for the new generation pretomanid derivatives project.

The new hypothesis was that we can modify and optimize the chemical structure to decrease BBB permeability, thus avoiding neurotoxicity (as was the problem with drug C/TBA-354 [292]), without losing anti-bacterial activity. The superior safety and efficacy

NP formulation offered over free drugs solubilized in organic solvents was shown in **Paper V**. Therefore, moving forward, we did not focus on testing free drugs versus NP drugs and screened the new derivatives, encapsulated in NPs only, in the zebrafish-TB model. We are now in the last stages of experimental work of the extended new generation pretomanid derivatives project and a manuscript is under preparation. Our hope is that the work will contribute to identify one or more new and improved pretomanid derivatives that eventually will enter clinical trials. Furthermore, in a broader view, promote the use of nanotherapeutics in TB treatment and build up the use of the zebrafish-TB model in drug development as a powerful intermediate screening stage.

Concluding remarks

The work presented in this thesis shows in a systematic way, how the zebrafish embryo can be used as an intermediate model in TB and nanomedicine research. The included publications demonstrate that the zebrafish embryo can facilitate the transition of research from in vitro cell culture systems to *in vivo* mammalian models. This is because of the unique imaging potential, the possibility of following events in real-time, the speedy acquisition of data and the ease obtaining results from a large number of individuals, which facilitates statistical analysis. All these criteria enabled us to characterize several new drugs and NP systems in detail. This included 16 different pretomanid derivatives (four of them presented in **Paper V**) and 6 different nitronaphtofuran (nNF) derivatives. The *in vivo* activity of most of these chemical compounds was for the first time assessed in this thesis.

When possible, the NP encapsulated drugs were compared against the free drugs, for example RIF and drug D were found to be superior when formulated into NPs. However, a comparison between the free and NP formulated drugs was often impossible due to the low water solubility of the free drugs. For example, the nNF could not be micro-injected at therapeutically relevant doses in their free form since they formed large aggregates and clogged the glass needle. For each NP-drug formulation, we could provide reproducible data on toxicity and therapeutic capacity, in addition to biodistribution kinetics and localization of the NP.

These zebrafish data provided a foundation for predicting how drugs and NP systems would respond in a mouse infection of TB. A previous publication by our group revealed that NPs accumulated in a similar fashion in the fish Mm and mouse Mtb granulomas [161]. We also established that the circulation profiles of different NPs were similar in zebrafish and mice. Furthermore, our data indicate that the zebrafish-TB model can be used to predict therapeutically active doses in mice infected with Mtb. For instance, comparable doses of NP encapsulated drug D provided therapeutic effect in both zebrafish and mouse models of TB.

In summary, the thesis provides the framework for how to apply the zebrafish-TB model in a hierarchical fashion and introduces robust methodologies for determining safety, effect and behavior of nanomedicines against TB disease. The system we have established can in less than two weeks, screen free and nanoformulated drugs in a

vertebrate model of TB and pinpoint promising leads to be progressed to mammalian testing.

References

1. Bespiatykh, D., et al., *A Comprehensive Map of Mycobacterium tuberculosis Complex Regions of Difference.* mSphere, 2021. **6**(4): p. e0053521.
2. Gordon, S.V. and T. Parish, *Microbe Profile: Mycobacterium tuberculosis: Humanity's deadly microbial foe.* Microbiology, 2018. **164**(4): p. 437-439.
3. Chiaradia, L., et al., *Dissecting the mycobacterial cell envelope and defining the composition of the native mycomembrane.* Sci. Rep., 2017. **7**(12807).
4. Jankute, M., et al., *Assembly of the Mycobacterial Cell Wall.* Annu. Rev. Microbiol., 2015. **69**: p. 405-423.
5. Augenstreich, J., et al., *Phthiocerol Dimycocerosates From Mycobacterium tuberculosis Increase the Membrane Activity of Bacterial Effectors and Host Receptors.* Front. Cell. Infect. Microbiol., 2020. **10**(420).
6. Indrigo, J., R.L. Hunter, and J.K. Actor, *Cord factor trehalose 6,6'-dimycolate (TDM) mediates trafficking events during mycobacterial infection of murine macrophages.* Microbiology, 2003. **149**(8): p. 2049-2059.
7. Brown, L., et al., *Through the wall: extracellular vesicles in Gram-positive bacteria, mycobacteria and fungi.* Nat. Rev. Microbiol., 2015. **13**(10): p. 620-630.
8. Hershberg, R., et al., *High functional diversity in Mycobacterium tuberculosis driven by genetic drift and human demography.* PLoS Biol., 2008. **6**(12): p. e311.
9. Smith, N.H., et al., *Bottlenecks and broomsticks: the molecular evolution of Mycobacterium bovis.* Nat. Rev. Microbiol., 2006. **4**(9): p. 670-681.
10. Namouchi, A., et al., *After the bottleneck: Genome-wide diversification of the Mycobacterium tuberculosis complex by mutation, recombination, and natural selection.* Genome Res., 2012. **22**(4): p. 721-734.
11. Manchester, K., *Tuberculosis and leprosy in antiquity: an interpretation.* Med. Hist., 1984. **28**(2): p. 162-173.
12. Brosch, R., et al., *A new evolutionary scenario for the Mycobacterium tuberculosis complex.* Proc. Natl. Acad. Sci. U.S.A., 2002. **99**(6): p. 3684-3689.
13. Gutierrez, M.C., et al., *Ancient origin and gene mosaicism of the progenitor of Mycobacterium tuberculosis.* PLoS Pathog., 2005. **1**(1): p. e5.
14. Smith, N.H., *A re-evaluation of M. prototuberculosis.* PLoS Pathog., 2006. **2**(9): p. e98.
15. Comas, I., et al., *Out-of-Africa migration and Neolithic coexpansion of Mycobacterium tuberculosis with modern humans.* Nat. Genet., 2013. **45**(10): p. 1176-1182.
16. Houben, R.M. and P.J. Dodd, *The Global Burden of Latent Tuberculosis Infection: A Re-estimation Using Mathematical Modelling.* PLoS Med., 2016. **13**(10): p. e1002152.
17. Bibbins-Domingo, K., et al., *Screening for Latent Tuberculosis Infection in Adults US Preventive Services Task Force Recommendation Statement.* JAMA, 2016. **316**(9): p. 962-969.
18. Horton, K.C., et al., *Sex Differences in Tuberculosis Burden and Notifications in Low- and Middle-Income Countries: A Systematic Review and Meta-analysis.* PLoS Med., 2016. **13**(9).
19. Heemskerk, D., et al., *Clinical Manifestations*, in *Tuberculosis in Adults and Children*. 2015, Springer: London.
20. van Crevel, R., T.H. Ottenhoff, and J.W. van der Meer, *Innate immunity to Mycobacterium tuberculosis.* Clin. Microbiol. Rev., 2002. **15**(2): p. 294-309.
21. Fennelly, K.P. and E.C. Jones-Lopez, *Quantity and Quality of Inhaled Dose Predicts Immunopathology in Tuberculosis.* Front. Immunol., 2015. **6**(313).
22. Wells, W.F., H.L. Ratcliffe, and C. Grumb, *On the mechanics of droplet nuclei infection; quantitative experimental air-borne tuberculosis in rabbits.* Am. J. Hyg., 1948. **47**(1): p. 11-28.
23. Dannenberg, A.M., *Pathogenesis of Human Pulmonary Tuberculosis: Insights from the Rabbit Model*. 2006: ASM Press.
24. Kang, P.B., et al., *The human macrophage mannose receptor directs Mycobacterium tuberculosis lipoarabinomannan-mediated phagosome biogenesis.* J. Exp. Med., 2005. **202**(7): p. 987-999.

25. Schlesinger, L.S., *Macrophage phagocytosis of virulent but not attenuated strains of Mycobacterium tuberculosis is mediated by mannose receptors in addition to complement receptors.* J. Immunol., 1993. **150**(7): p. 2920-2930.
26. Huang, L., et al., *Growth of Mycobacterium tuberculosis in vivo segregates with host macrophage metabolism and ontogeny.* J. Exp. Med., 2018. **215**(4): p. 1135-1152.
27. Cohen, S.B., et al., *Alveolar Macrophages Provide an Early Mycobacterium tuberculosis Niche and Initiate Dissemination.* Cell Host Microbe, 2018. **24**(3): p. 439-446 e4.
28. Wong, K.C., et al., *Molecular characterization of clinical isolates of Mycobacterium tuberculosis and their association with phenotypic virulence in human macrophages.* Clin. Vaccine Immunol., 2007. **14**(10): p. 1279-1284.
29. Mosser, D.M. and J.P. Edwards, *Exploring the full spectrum of macrophage activation.* Nat. Rev. Immunol., 2008. **8**(12): p. 958-969.
30. Fenton, M.J. and M.W. Vermeulen, *Immunopathology of tuberculosis: roles of macrophages and monocytes.* Infect. Immun., 1996. **64**(3): p. 683-690.
31. Mogues, T., et al., *The relative importance of T cell subsets in immunity and immunopathology of Airborne Mycobacterium tuberculosis infection in mice.* J. Exp. Med., 2001. **193**(3): p. 271-280.
32. Perlman, D.C., et al., *Variation of chest radiographic patterns in pulmonary tuberculosis by degree of human immunodeficiency virus-related immunosuppression.* Clin. Infect. Dis., 1997. **25**(2): p. 242-246.
33. Miao, H.Y., et al., *Quantifying the Early Immune Response and Adaptive Immune Response Kinetics in Mice Infected with Influenza A Virus.* J. Virol., 2010. **84**(13): p. 6687-6698.
34. Ennis, F.A., et al., *HLA restricted virus-specific cytotoxic T-lymphocyte responses to live and inactivated influenza vaccines.* Lancet, 1981. **2**(8252): p. 887-891.
35. Behr, M.A., P.H. Edelstein, and L. Ramakrishnan, *Revisiting the timetable of tuberculosis.* BMJ, 2018. **362**(k2738).
36. Chackerian, A.A., et al., *Dissemination of Mycobacterium tuberculosis is influenced by host factors and precedes the initiation of T-cell immunity.* Infect. Immun., 2002. **70**(8): p. 4501-4509.
37. Wolf, A.J., et al., *Initiation of the adaptive immune response to Mycobacterium tuberculosis depends on antigen production in the local lymph node, not the lungs.* J. Exp. Med., 2008. **205**(1): p. 105-115.
38. Ramakrishnan, L., *Revisiting the role of the granuloma in tuberculosis.* Nat. Rev. Immunol., 2012. **12**(5): p. 352-366.
39. Russell, D.G., et al., *Foamy macrophages and the progression of the human tuberculosis granuloma.* Nat. Immunol., 2009. **10**(9): p. 943-948.
40. Russell, D.G., *Who puts the tubercle in tuberculosis?* Nat. Rev. Microbiol., 2007. **5**(1): p. 39-47.
41. Blacklock, J.W., *The Primary Lung Focus of Tuberculosis in Children.* Proc. R. Soc. Med., 1932. **25**(5): p. 725-733.
42. Lillebaek, T., et al., *Stability of DNA patterns and evidence of Mycobacterium tuberculosis reactivation occurring decades after the initial infection.* J. Infect. Dis., 2003. **188**(7): p. 1032-1039.
43. Lin, P.L. and J.L. Flynn, *Understanding latent tuberculosis: a moving target.* J. Immunol., 2010. **185**(1): p. 15-22.
44. Glynn, J.R., et al., *High rates of recurrence in HIV-infected and HIV-uninfected patients with tuberculosis.* J. Infect. Dis., 2010. **201**(5): p. 704-711.
45. Sonnenberg, P., et al., *HIV-1 and recurrence, relapse, and reinfection of tuberculosis after cure: a cohort study in South African mineworkers.* Lancet, 2001. **358**(9294): p. 1687-1693.
46. Kwan, C.K. and J.D. Ernst, *HIV and tuberculosis: a deadly human syndemic.* Clin. Microbiol. Rev., 2011. **24**(2): p. 351-376.
47. Sonnenberg, P., et al., *How soon after infection with HIV does the risk of tuberculosis start to increase? A retrospective cohort study in South African gold miners.* J. Infect. Dis., 2005. **191**(2): p. 150-158.
48. Harris, J. and J. Keane, *How tumour necrosis factor blockers interfere with tuberculosis immunity.* Clin. Exp. Immunol, 2010. **161**(1): p. 1-9.
49. Levin, R., S. Grinstein, and J. Canton, *The life cycle of phagosomes: formation, maturation, and resolution.* Immunol. Rev., 2016. **273**(1): p. 156-179.
50. Flannagan, R.S., G. Cosio, and S. Grinstein, *Antimicrobial mechanisms of phagocytes and bacterial evasion strategies.* Nat. Rev. Microbiol., 2009. **7**(5): p. 355-366.

51. Podinovskaia, M., et al., *Infection of macrophages with Mycobacterium tuberculosis induces global modifications to phagosomal function.* Cell Microbiol., 2013. **15**(6): p. 843-859.
52. Armstrong, J.A. and P.D. Hart, *Response of cultured macrophages to Mycobacterium tuberculosis, with observations on fusion of lysosomes with phagosomes.* J. Exp. Med., 1971. **134**(3): p. 713-740.
53. Upadhyay, S., E. Mittal, and J.A. Philips, *Tuberculosis and the art of macrophage manipulation.* Pathog. Dis., 2018. **76**(4).
54. Prashar, A., et al., *Rab GTPases in Immunity and Inflammation.* Front. Cell. Infect. Microbiol., 2017. **7**(435).
55. Seto, S., K. Tsujimura, and Y. Koide, *Rab GTPases regulating phagosome maturation are differentially recruited to mycobacterial phagosomes.* Traffic, 2011. **12**(4): p. 407-420.
56. Purdy, G.E., et al., *Kinetics of phosphatidylinositol-3-phosphate acquisition differ between IgG bead-containing phagosomes and Mycobacterium tuberculosis-containing phagosomes.* Cell. Microbiol., 2005. **7**(11): p. 1627-1634.
57. Wong, D., et al., *Protein tyrosine kinase, PtkA, is required for Mycobacterium tuberculosis growth in macrophages.* Sci. Rep., 2018. **8**(155).
58. Queval, C.J., et al., *Mycobacterium tuberculosis Controls Phagosomal Acidification by Targeting CISH-Mediated Signaling.* Cell. Rep., 2017. **20**(13): p. 3188-3198.
59. Jamwal, S.V., et al., *Mycobacterial escape from macrophage phagosomes to the cytoplasm represents an alternate adaptation mechanism.* Sci. Rep., 2016. **6**(23089).
60. Jay, S.J., et al., *Modern theory of tuberculosis: culturomic analysis of its historical origin in Europe and North America.* Int. J. Tuberc. Lung Dis., 2018. **22**(11): p. 1249-1257.
61. Daniel, T.M., *The history of tuberculosis.* Respir. Med., 2006. **100**(11): p. 1862-1870.
62. Rothschild, B.M., et al., *Mycobacterium tuberculosis complex DNA from an extinct bison dated 17,000 years before the present.* Clin. Infect. Dis., 2001. **33**(3): p. 305-311.
63. Hershkovitz, I., et al., *Tuberculosis origin: The Neolithic scenario.* Tuberculosis, 2015. **95**: p. S122-126.
64. Nicklisch, N., et al., *Rib lesions in skeletons from early neolithic sites in Central Germany: on the trail of tuberculosis at the onset of agriculture.* Am. J. Phys. Anthropol., 2012. **149**(3): p. 391-404.
65. Crubezy, E., et al., *Identification of Mycobacterium DNA in an Egyptian Pott's disease of 5,400 years old.* C. R. Acad. Sci. III, 1998. **321**(11): p. 941-951.
66. Nerlich, A.G., et al., *Molecular evidence for tuberculosis in an ancient Egyptian mummy.* Lancet, 1997. **350**(9088): p. 1404.
67. Bos, K.I., et al., *Pre-Columbian mycobacterial genomes reveal seals as a source of New World human tuberculosis.* Nature, 2014. **514**(7523): p. 494-497.
68. Herzog, H., *History of tuberculosis.* Respiration, 1998. **65**(1): p. 5-15.
69. Pezzella, A.T., *History of Pulmonary Tuberculosis.* Thorac. Surg. Clin., 2019. **29**(1): p. 1-17.
70. Daniel, V.S. and T.M. Daniel, *Old Testament biblical references to tuberculosis.* Clin. Infect. Dis., 1999. **29**(6): p. 1557-1558.
71. Paulson, T., *Epidemiology: A mortal foe.* Nature, 2013. **502**(7470): p. S2-3.
72. Murray, J.F., H.L. Rieder, and A. Finley-Croswhite, *The King's Evil and the Royal Touch: the medical history of scrofula.* Int. J. Tuberc. Lung Dis., 2016. **20**(6): p. 713-716.
73. Sledzik, P.S. and N. Bellantoni, *Brief communication: bioarcheological and biocultural evidence for the New England vampire folk belief.* Am. J. Phys. Anthropol., 1994. **94**(2): p. 269-274.
74. Frith, J., *History of Tuberculosis. Part 1 - Phthisis, consumption and the White Plague.* J. Mil. Veterans' Health., 2014. **22**(2): p. 29-35.
75. Doetsch, R.N., *Benjamin Marten and his "New Theory of Consumptions".* Microbiol. Rev., 1978. **42**(3): p. 521-528.
76. Daniel, T.M., *Rene Theophile Hyacinthe Laennec and the founding of pulmonary medicine.* Int. J. Tuberc. Lung Dis., 2004. **8**(5): p. 517-518.
77. Sakula, A., *Robert Koch: centenary of the discovery of the tubercle bacillus, 1882.* Thorax, 1982. **37**(4): p. 246-251.
78. Frith, J., *History of Tuberculosis. Part 2 - the Sanatoria and the Discoveries of the Tubercle Bacillus.* J. Mil. Veterans' Health., 2014. **22**(2): p. 36-41.
79. Kaufmann, S.H.E., *Paul Ehrlich: founder of chemotherapy.* Nat. Rev. Drug Discov., 2008. **7**(5): p. 373-373.
80. Clemens, V.P., *Frequency of tuberculosis in childhood.* JAMA, 1909. **52**(9).

81. Gualano, G., et al., *Tuberculin skin test - Outdated or still useful for Latent TB infection screening?* Int. J. Infect. Dis., 2019. **80S**: p. S20-S22.
82. Luca, S. and T. Mihaescu, *History of BCG Vaccine.* Maedica, 2013. **8**(1): p. 53-58.
83. Calmette, A., *Preventive Vaccination Against Tuberculosis with BCG.* Proc. R. Soc. Med., 1931. **24**(11): p. 1481-1490.
84. Daniel, T.M., *Hermann Brehmer and the origins of tuberculosis sanatoria.* Int. J. Tuberc. Lung Dis., 2011. **15**(2): p. 161-162.
85. WHO. *Tuberculosis Key facts*. 2021; Available from: https://www.who.int/news-room/fact-sheets/detail/tuberculosis.
86. Murray, J.F., D.E. Schraufnagel, and P.C. Hopewell, *Treatment of Tuberculosis. A Historical Perspective.* Ann. Am. Thorac. Soc., 2015. **12**(12): p. 1749-1759.
87. Spratt, B.G., *The mechanism of action of penicillin.* Sci. Prog., 1978. **65**(257): p. 101-128.
88. Wainwright, M., *Hitler's penicillin.* Perspect. Biol. Med., 2004. **47**(2): p. 189-198.
89. Lehmann, J., *Para-aminosalicylic acid in the treatment of tuberculosis.* Lancet, 1946. **1**(6384): p. 15.
90. Schatz, A., E. Bugie, and S.A. Waksman, *Streptomycin, a substance exhibiting antibiotic activity against gram positive and gram-negative bacteria.* Proc. Soc. Exp. Biol. Med., 1944. **55**(1): p. 66-69.
91. *Treatment of pulmonary tuberculosis with streptomycin and para-aminosalicylic acid; a Medical Research Council investigation.* Br. Med. J., 1950. **2**(4688): p. 1073-1085.
92. Robitzek, E.H., I.J. Selikoff, and G.G. Ornstein, *Chemotherapy of human tuberculosis with hydrazine derivatives of isonicotinic acid; preliminary report of representative cases.* Q. Bull., Sea View Hosp., 1952. **13**(1): p. 27-51.
93. Kushner, S., et al., *Experimental Chemotherapy of Tuberculosis .2. The Synthesis of Pyrazinamides and Related Compounds.* J. Am. Chem. Soc., 1952. **74**(14): p. 3617-3621.
94. Cummings, M.M., R.A. Patnode, and P.C. Hudgins, *Effects of cycloserine on Mycobacterium tuberculosis in vitro.* Antibiot. Chemother., 1955. **5**(4): p. 198-203.
95. Riddell, R.W., S.M. Stewart, and A.R. Somner, *Ethionamide.* Br. Med. J., 1960. **2**(5207): p. 1207-1208.
96. Umezawa, H., *Kanamycin: its discovery.* Ann. N. Y. Acad. Sci., 1958. **76**(2): p. 20-26.
97. Sensi, P., P. Margalith, and M.T. Timbal, *Rifomycin, a new antibiotic; preliminary report.* Farmaco. Sci., 1959. **14**(2): p. 146-147.
98. Popplewell, A.G., et al., *Capreomycin in original treatment cases of pulmonary tuberculosis.* Ann. N. Y. Acad. Sci., 1966. **135**(2): p. 989-1005.
99. Thomas, J.P., et al., *A new synthetic compound with antituberculous activity in mice: ethambutol (dextro-2,2'-(ethylenediimino)-di-l-butanol).* Am. Rev. Respir. Dis., 1961. **83**: p. 891-893.
100. Maggi, N., et al., *Rifampicin: a new orally active rifamycin.* Chemotherapy, 1966. **11**(5): p. 285-292.
101. WHO, *Global Tuberculosis Report 2021*. 2021: Geneva.
102. Merrill, R.M., et al., *Explanations for 20th Century Tuberculosis Decline: How the Public Gets It Wrong.* J. Tuberc. Res., 2016. **4**(3): p. 111-121.
103. Melgar, M., et al., *Tuberculosis Preventive Treatment Scale-Up Among Antiretroviral Therapy Patients-16 Countries Supported by the US President's Emergency Plan for AIDS Relief, 2017-2019.* Morb. Mortal. Wkly. Rep., 2020. **69**(12): p. 329-334.
104. Ngwatu, B.K., et al., *The impact of digital health technologies on tuberculosis treatment: a systematic review.* Eur. Respir. J., 2018. **51**(1).
105. Trunz, B.B., P. Fine, and C. Dye, *Effect of BCG vaccination on childhood tuberculous meningitis and miliary tuberculosis worldwide: a meta-analysis and assessment of cost-effectiveness.* Lancet, 2006. **367**(9517): p. 1173-1180.
106. Abubakar, I., et al., *Systematic review and meta-analysis of the current evidence on the duration of protection by bacillus Calmette-Guerin vaccination against tuberculosis.* Health Technol. Assess., 2013. **17**(37).
107. von Reyn, C.F., *Correcting the record on BCG before we license new vaccines against tuberculosis.* J. R. Soc. Med., 2017. **110**(11): p. 428-433.
108. Katelaris, A.L., et al., *Effectiveness of BCG Vaccination Against Mycobacterium tuberculosis Infection in Adults: A Cross-sectional Analysis of a UK-Based Cohort.* J. Infect. Dis., 2020. **221**(1): p. 146-155.
109. Eddabra, R. and H.A. Benhassou, *Rapid molecular assays for detection of tuberculosis.* Pneumonia, 2018. **10**(4).

110. Farhat, M., et al., *False-positive tuberculin skin tests: what is the absolute effect of BCG and non-tuberculous mycobacteria?* Int. J. Tuberc. Lung Dis., 2006. **10**(11): p. 1192-1204.
111. Gong, W.P. and X.Q. Wu, *Differential Diagnosis of Latent Tuberculosis Infection and Active Tuberculosis: A Key to a Successful Tuberculosis Control Strategy.* Front. Microbiol., 2021. **12**(745592).
112. Tiemersma, E.W., et al., *Natural History of Tuberculosis: Duration and Fatality of Untreated Pulmonary Tuberculosis in HIV Negative Patients: A Systematic Review.* Plos One, 2011. **6**(4).
113. Nahid, P., et al., *Executive Summary: Official American Thoracic Society/Centers for Disease Control and Prevention/Infectious Diseases Society of America Clinical Practice Guidelines: Treatment of Drug-Susceptible Tuberculosis.* Clin. Infect. Dis., 2016. **63**(7): p. 853-867.
114. Dorman, S.E., et al., *Four-Month Rifapentine Regimens with or without Moxifloxacin for Tuberculosis.* N. Engl. J. Med., 2021. **384**(18): p. 1705-1718.
115. Carr, W., et al., *Interim Guidance: 4-Month Rifapentine-Moxifloxacin Regimen for the Treatment of Drug-Susceptible Pulmonary Tuberculosis - United States, 2022.* Morb. Mortal. Wkly. Rep., 2022. **71**(8): p. 285-289.
116. WHO, *WHO Consolidated Guidelines on Drug-Resistant Tuberculosis*. 2019: Geneva.
117. Pyle, M.M., *Relative Numbers of Resistant Tubercle-Bacilli in Sputa of Patients before and during Treatment with Streptomycin.* Proceedings of the Staff Meetings of the Mayo Clinic, 1947. **22**(21): p. 465-473.
118. Dheda, K., et al., *The epidemiology, pathogenesis, transmission, diagnosis, and management of multidrug-resistant, extensively drug-resistant, and incurable tuberculosis.* Lancet Respir. Med. , 2017. **5**(4): p. 291-360.
119. Gillespie, S.H., *Evolution of drug resistance in Mycobacterium tuberculosis: Clinical and molecular perspective.* Antimicrob. Agents Chemother., 2002. **46**(2): p. 267-274.
120. Seung, K.J., S. Keshavjee, and M.L. Rich, *Multidrug-Resistant Tuberculosis and Extensively Drug-Resistant Tuberculosis.* Cold Spring Harb. Perspect. Med., 2015. **5**(9).
121. Dheda, K., et al., *Outcomes, infectiousness, and transmission dynamics of patients with extensively drug-resistant tuberculosis and home-discharged patients with programmatically incurable tuberculosis: a prospective cohort study.* Lancet Respir. Med. , 2017. **5**(4): p. 269-281.
122. Klopper, M., et al., *Emergence and Spread of Extensively and Totally Drug-Resistant Tuberculosis, South Africa.* Emerg. Infect. Dis., 2013. **19**(3): p. 449-455.
123. Parida, S.K., et al., *Totally drug-resistant tuberculosis and adjunct therapies.* J. Intern. Med., 2015. **277**(4): p. 388-405.
124. Lee, A., et al., *Current and future treatments for tuberculosis.* BRIT. MED. J., 2020. **368**.
125. Andries, K., et al., *A diarylquinoline drug active on the ATP synthase of Mycobacterium tuberculosis.* Science, 2005. **307**(5707): p. 223-227.
126. Van Norman, G.A., *Drugs, Devices, and the FDA: Part 1: An Overview of Approval Processes for Drugs.* JACC Basic Transl. Sci., 2016. **1**(3): p. 170-179.
127. DiMasi, J.A., H.G. Grabowski, and R.W. Hansen, *Innovation in the pharmaceutical industry: New estimates of R&D costs.* J. Health Econ., 2016. **47**: p. 20-33.
128. Ryan, N.J. and J.H. Lo, *Delamanid: First Global Approval.* Drugs, 2014. **74**(9): p. 1041-1045.
129. Keam, S.J., *Pretomanid: First Approval.* Drugs, 2019. **79**(16): p. 1797-1803.
130. Conradie, F., et al., *Treatment of Highly Drug-Resistant Pulmonary Tuberculosis.* N. Engl. J. Med., 2020. **382**(10): p. 893-902.
131. Krishnan, V., *Tuberculosis: experts question evidence and safety data used to approve latest drug.* BRIT. MED. J., 2019. **367**.
132. McKenna, L. and J. Furin, *Are pretomanid-containing regimens for tuberculosis a victory or a victory narrative?* Lancet Respir. Med. , 2019. **7**(12): p. 999-1000.
133. Cellitti, S.E., et al., *Structure of Ddn, the deazaflavin-dependent nitroreductase from Mycobacterium tuberculosis involved in bioreductive activation of PA-824.* Structure, 2012. **20**(1): p. 101-112.
134. Manjunatha, U., H.I. Boshoff, and C.E. Barry, *The mechanism of action of PA-824: Novel insights from transcriptional profiling.* Commun. Integr. Biol., 2009. **2**(3): p. 215-218.
135. Matsumoto, M., et al., *OPC-67683, a nitro-dihydro-imidazooxazole derivative with promising action against tuberculosis in vitro and in mice.* PLoS Med., 2006. **3**(11): p. 2131-2144.
136. Van den Bossche, A., et al., *Transcriptional profiling of a laboratory and clinical Mycobacterium tuberculosis strain suggests respiratory poisoning upon exposure to delamanid.* Tuberculosis, 2019. **117**: p. 18-23.

137. Hoffmann, H., et al., *Delamanid and Bedaquiline Resistance in Mycobacterium tuberculosis Ancestral Beijing Genotype Causing Extensively Drug-Resistant Tuberculosis in a Tibetan Refugee.* Am. J. Respir. Crit. Care Med., 2016. **193**(3): p. 337-340.
138. Yoshiyama, T., et al., *Multidrug Resistant Tuberculosis With Simultaneously Acquired Drug Resistance to Bedaquiline and Delamanid.* Clin. Infect. Dis., 2021. **73**(12): p. 2329-2331.
139. Gils, T., et al., *Pretomanid for tuberculosis: a systematic review.* Clin. Microbiol. Infect., 2022. **28**(1): p. 31-42.
140. Yuan, T.A. and N.S. Sampson, *Hit Generation in TB Drug Discovery: From Genome to Granuloma.* Chem. Rev., 2018. **118**(4): p. 1887-1916.
141. Fernandes, G.F.S., et al., *Tuberculosis Drug Discovery: Challenges and New Horizons.* J. Med. Chem., 2022. **65**(11): p. 7489-7531.
142. Swinney, D.C. and J. Anthony, *How were new medicines discovered?* Nat. Rev. Drug Discov., 2011. **10**(7): p. 507-519.
143. Moffat, J.G., et al., *Opportunities and challenges in phenotypic drug discovery: an industry perspective.* Nat. Rev. Drug Discov., 2017. **16**(8): p. 531-543.
144. Grzelak, E.M., et al., *Strategies in anti-Mycobacterium tuberculosis drug discovery based on phenotypic screening.* J. Antibiot., 2019. **72**(10): p. 719-728.
145. Goldman, R.C., *Why are membrane targets discovered by phenotypic screens and genome sequencing in Mycobacterium tuberculosis?* Tuberculosis, 2013. **93**(6): p. 569-588.
146. Tarcsay, A. and G.M. Keseru, *Contributions of Molecular Properties to Drug Promiscuity Miniperspective.* J. Med. Chem., 2013. **56**(5): p. 1789-1795.
147. ESF. *ESF Scientific Forward Look on Nanomedicine*. 2005; Available from: http://archives.esf.org/fileadmin/Public_documents/Publications/Nanomedicine_01.pdf.
148. Duncan, R. and R. Gaspar, *Nanomedicine(s) under the Microscope.* Mol. Pharm., 2011. **8**(6): p. 2101-2141.
149. Astruc, D., *Introduction to Nanomedicine.* Molecules, 2016. **21**(1).
150. Witkop, B., *Paul Ehrlich and his magic bullets - Revisited.* Proc Am Philos Soc, 1999. **143**(4): p. 540-557.
151. Junk, A. and F. Riess, *From an idea to a vision: There's plenty of room at the bottom.* Am. J. Phys., 2006. **74**(9): p. 825-830.
152. Kreuter, J., *Nanoparticles - a historical perspective.* Int. J. Pharm., 2007. **331**(1): p. 1-10.
153. Vargason, A.M., A.C. Anselmo, and S. Mitragotri, *The evolution of commercial drug delivery technologies.* Nat. Biomed. Eng., 2021. **5**(9): p. 951-967.
154. Nelson, E., *Kinetics of Drug Absorption, Distribution, Metabolism, and Excretion.* J. Pharm. Sci., 1961. **50**(3): p. 181-192.
155. Holford, N.H.G. and L.B. Sheiner, *Kinetics of Pharmacologic Response.* Pharmacol. Ther., 1982. **16**(2): p. 143-166.
156. Birrenbach, G. and P.P. Speiser, *Polymerized Micelles and Their Use as Adjuvants in Immunology.* J. Pharm. Sci., 1976. **65**(12): p. 1763-1766.
157. Mitchell, M.J., et al., *Engineering precision nanoparticles for drug delivery.* Nat. Rev. Drug Discov., 2021. **20**(2): p. 101-124.
158. Attia, M.F., et al., *An overview of active and passive targeting strategies to improve the nanocarriers efficiency to tumour sites.* J. Pharm. Pharmacol., 2019. **71**(8): p. 1185-1198.
159. Griffiths, G., et al., *Nanobead-based interventions for the treatment and prevention of tuberculosis.* Nat. Rev. Microbiol., 2010. **8**(11): p. 827-834.
160. Harris, J.M. and R.B. Chess, *Effect of pegylation on pharmaceuticals.* Nat. Rev. Drug Discov., 2003. **2**(3): p. 214-221.
161. Fenaroli, F., et al., *Enhanced Permeability and Retention-like Extravasation of Nanoparticles from the Vasculature into Tuberculosis Granulomas in Zebrafish and Mouse Models.* Acs Nano, 2018. **12**(8): p. 8646-8661.
162. Torchilin, V., *Tumor delivery of macromolecular drugs based on the EPR effect.* Adv. Drug Deliv. Rev., 2011. **63**(3): p. 131-135.
163. Carmeliet, P. and R.K. Jain, *Angiogenesis in cancer and other diseases.* Nature, 2000. **407**(6801): p. 249-257.
164. Matsumura, Y. and H. Maeda, *A New Concept for Macromolecular Therapeutics in Cancer-Chemotherapy - Mechanism of Tumoritropic Accumulation of Proteins and the Antitumor Agent Smancs.* Cancer Res., 1986. **46**(12): p. 6387-6392.
165. Barenholz, Y., *Doxil (R) - The first FDA-approved nano-drug: Lessons learned.* J. Control. Release, 2012. **160**(2): p. 117-134.

166. Solomon, R. and A.A. Gabizon, *Clinical pharmacology of liposomal anthracyclines: Focus on pegylated liposomal doxorubicin.* Clin. Lymphoma Myeloma, 2008. **8**(1): p. 21-32.
167. Anselmo, A.C. and S. Mitragotri, *Nanoparticles in the clinic: An update post COVID-19 vaccines.* Bioeng. Transl. Med., 2021. **6**(3).
168. Hua, S., et al., *Current Trends and Challenges in the Clinical Translation of Nanoparticulate Nanomedicines: Pathways for Translational Development and Commercialization.* Front. Pharmacol., 2018. **9**(790).
169. Sahin, U., et al., *COVID-19 vaccine BNT162b1 elicits human antibody and TH1 T cell responses.* Nature, 2020. **586**(7830): p. 594-599.
170. Jackson, L.A., et al., *An mRNA Vaccine against SARS-CoV-2-Preliminary Report.* N. Engl. J. Med., 2020. **383**(20): p. 1920-1931.
171. Patil, K., et al., *Recent therapeutic approaches for the management of tuberculosis: Challenges and opportunities.* Biomed. Pharmacother., 2018. **99**: p. 735-745.
172. Sosnik, A., et al., *New old challenges in tuberculosis: Potentially effective nanotechnologies in drug delivery.* Adv. Drug Deliv. Rev., 2010. **62**(4-5): p. 547-559.
173. Pandey, R., et al., *Nanoparticle encapsulated antitubercular drugs as a potential oral drug delivery system against murine tuberculosis.* Tuberculosis, 2003. **83**(6): p. 373-378.
174. Sharma, A., S. Sharma, and G.K. Khuller, *Lectin-functionalized poly (lactide-co-glycolide) nanoparticles as oral/aerosolized antitubercular drug carriers for treatment of tuberculosis.* J. Antimicrob. Chemother., 2004. **54**(4): p. 761-766.
175. Fenaroli, F., et al., *Nanoparticles as Drug Delivery System against Tuberculosis in Zebrafish Embryos: Direct Visualization and Treatment.* Acs Nano, 2014. **8**(7): p. 7014-7026.
176. Datta, M., et al., *Anti-vascular endothelial growth factor treatment normalizes tuberculosis granuloma vasculature and improves small molecule delivery.* Proc. Natl. Acad. Sci. U.S.A., 2015. **112**(6): p. 1827-1832.
177. Waterston, R.H., et al., *Initial sequencing and comparative analysis of the mouse genome.* Nature, 2002. **420**(6915): p. 520-562.
178. Bucsan, A.N., et al., *The current state of animal models and genomic approaches towards identifying and validating molecular determinants of Mycobacterium tuberculosis infection and tuberculosis disease.* Pathog. Dis., 2019. **77**(4).
179. Kramnik, I. and G. Beamer, *Mouse models of human TB pathology: roles in the analysis of necrosis and the development of host-directed therapies.* Semin. Immunopathol., 2016. **38**(2): p. 221-237.
180. Flynn, J.L., *Lessons from experimental Mycobacterium tuberculosis infections.* Microbes Infect., 2006. **8**(4): p. 1179-1188.
181. Kaufmann, S.H.E., et al., *Mycobacterium tuberculosis and the host response.* J. Exp. Med. , 2005. **201**(11): p. 1693-1697.
182. Harper, J., et al., *Mouse Model of Necrotic Tuberculosis Granulomas Develops Hypoxic Lesions.* J. Infect. Dis., 2012. **205**(4): p. 595-602.
183. Driver, E.R., et al., *Evaluation of a Mouse Model of Necrotic Granuloma Formation Using C3HeB/FeJ Mice for Testing of Drugs against Mycobacterium tuberculosis.* Antimicrob. Agents Chemother., 2012. **56**(6): p. 3181-3195.
184. Lurie, M.B., *The fate of human and bovine tubercle bacilli in various organs of the rabbit.* J. Exp. Med. , 1928. **48**(2): p. 155-182.
185. Smith, T., *A Comparative Study of Bovine Tubercle Bacilli and of Human Bacilli from Sputum.* J. Exp. Med., 1898. **3**(4-5): p. 451-511.
186. Henderson, H.J., M.B. Lurie, and A.M. Dannenberg, *Phagocytosis of Tubercle Bacilli by Rabbit Pulmonary Alveolar Macrophages and Its Relation to Native Resistance to Tuberculosis.* J. Immunol., 1963. **91**(4): p. 553-&.
187. Dannenberg, A.M., *Delayed-Type Hypersensitivity and Cell-Mediated-Immunity in the Pathogenesis of Tuberculosis.* Immunol. Today, 1991. **12**(7): p. 228-233.
188. Kesavan, A.K., et al., *Tuberculosis genes expressed during persistence and reactivation in the resistant rabbit model.* Tuberculosis, 2009. **89**(1): p. 17-21.
189. Rifat, D., et al., *Pharmacokinetics of rifapentine and rifampin in a rabbit model of tuberculosis and correlation with clinical trial data.* Sci. Transl. Med., 2018. **10**(435).
190. *The all-purpose guinea pig.* Lab. Anim., 2014. **43**(3): p. 79-79.
191. Padilla-Carlin, D.J., D.N. McMurray, and A.J. Hickey, *The guinea pig as a model of infectious diseases.* Comp. Med., 2008. **58**(4): p. 324-340.

192. Smith, D.W. and G.E. Harding, *Animal-Model of Human Disease - Pulmonary Tuberculosis - Animal Mode - Experimental Airborne Tuberculosis in Guinea-Pig.* Am. J. Pathol., 1977. **89**(1): p. 273-276.
193. Dharmadhikari, A.S. and E.A. Nardell, *What Animal Models Teach Humans about Tuberculosis.* Am. J. Respir. Cell Mol. Biol., 2008. **39**(5): p. 503-508.
194. Kato-Maeda, M., et al., *Beijing Sublineages of Mycobacterium tuberculosis Differ in Pathogenicity in the Guinea Pig.* Clin. Vaccine Immunol., 2012. **19**(8): p. 1227-1237.
195. Clark, S., Y. Hall, and A. Williams, *Animal Models of Tuberculosis: Guinea Pigs.* Cold Spring Harb. Perspect. Med., 2015. **5**(5).
196. Basaraba, R.J., *Experimental tuberculosis: the role of comparative pathology in the discovery of improved tuberculosis treatment strategies.* Tuberculosis, 2008. **88**: p. S35-S47.
197. Kaushal, D., et al., *The non-human primate model of tuberculosis.* J. Med. Primatol., 2012. **41**(3): p. 191-201.
198. Diedrich, C.R., et al., *SIV and Mycobacterium tuberculosis synergy within the granuloma accelerates the reactivation pattern of latent tuberculosis.* PLoS Pathog., 2020. **16**(7): p. e1008413.
199. Lieschke, G.J. and P.D. Currie, *Animal models of human disease: zebrafish swim into view.* Nat. Rev. Genet., 2007. **8**(5): p. 353-367.
200. Meijer, A.H. and H.P. Spaink, *Host-Pathogen Interactions Made Transparent with the Zebrafish Model.* Curr. Drug Targets, 2011. **12**(7): p. 1000-1017.
201. White, R., K. Rose, and L. Zon, *Zebrafish cancer: the state of the art and the path forward.* Nat. Rev. Cancer, 2013. **13**(9): p. 624-636.
202. Davis, J.M., et al., *Real-time visualization of Mycobacterium-macrophage interactions leading to initiation of granuloma formation in zebrafish embryos.* Immunity, 2002. **17**(6): p. 693-702.
203. Parichy, D.M., *Advancing biology through a deeper understanding of zebrafish ecology and evolution.* Elife, 2015. **4**.
204. Engeszer, R.E., et al., *Zebrafish in the Wild: A Review of Natural History and New Notes from the Field.* Zebrafish, 2007. **4**(1): p. 21-40.
205. McClure, M.M., P.B. McIntyre, and A.R. McCune, *Notes on the natural diet and habitat of eight danionin fishes, including the zebrafish Danio rerio.* J. Fish Biol., 2006. **69**(2): p. 553-570.
206. Avdesh, A., et al., *Regular Care and Maintenance of a Zebrafish (Danio rerio) Laboratory: An Introduction.* J. Vis. Exp., 2012(69).
207. Streisinger, G., et al., *Production of Clones of Homozygous Diploid Zebra Fish (Brachydanio-Rerio).* Nature, 1981. **291**(5813): p. 293-296.
208. Grunwald, D.J. and J.S. Eisen, *Timeline - Headwaters of the zebrafish emergence of a new model vertebrate.* Nat. Rev. Genet., 2002. **3**(9): p. 717-724.
209. Ramakrishnan, L., *Looking Within the Zebrafish to Understand the Tuberculous Granuloma*, in *New Paradigm of Immunity to Tuberculosis*. 2013, Springer. p. 251-266.
210. Bouley, D.M., et al., *Dynamic nature of host-pathogen interactions in Mycobacterium marinum granulomas.* Infect. Immun., 2001. **69**(12): p. 7820-7831.
211. Tonjum, T., et al., *Differentiation of Mycobacterium ulcerans, M-marinum, and M-haemophilum: Mapping of their relationships to M-tuberculosis by fatty acid profile analysis, DNA-DNA hybridization, and 16S rRNA gene sequence analysis.* J. Clin. Microbiol., 1998. **36**(4): p. 918-925.
212. Lam, S.H., et al., *Development and maturation of the immune system in zebrafish, Danio rerio: a gene expression profiling, in situ hybridization and immunological study.* Dev. Comp. Immunol., 2004. **28**(1): p. 9-28.
213. Oehlers, S.H., et al., *Infection-Induced Vascular Permeability Aids Mycobacterial Growth.* J. Infect. Dis., 2017. **215**(5): p. 813-817.
214. Davis, J.M. and L. Ramakrishnan, *The Role of the Granuloma in Expansion and Dissemination of Early Tuberculous Infection.* Cell, 2009. **136**(1): p. 37-49.
215. Dalton, J.P., et al., *Screening of anti-mycobacterial compounds in a naturally infected zebrafish larvae model.* J. Antimicrob. Chemother., 2017. **72**(2): p. 421-427.
216. Prouty, M.G., et al., *Zebrafish-Mycobacterium marinum model for mycobacterial pathogenesis.* FEMS Microbiol. Lett., 2003. **225**(2): p. 177-182.
217. Levitte, S., et al., *Mycobacterial Acid Tolerance Enables Phagolysosomal Survival and Establishment of Tuberculous Infection In Vivo.* Cell Host Microbe 2016. **20**(2): p. 250-258.
218. Cambier, C.J., et al., *Phenolic Glycolipid Facilitates Mycobacterial Escape from Microbicidal Tissue-Resident Macrophages.* Immunity, 2017. **47**(3): p. 552–565.

219. Haque, E. and A.C. Ward, *Zebrafish as a Model to Evaluate Nanoparticle Toxicity.* Nanomaterials, 2018. **8**(7).
220. Stark, W.J., et al., *Industrial applications of nanoparticles.* Chem. Soc. Rev., 2015. **44**(16): p. 5793-5805.
221. Evensen, L., et al., *Zebrafish as a model system for characterization of nanoparticles against cancer.* Nanoscale, 2016. **8**(2): p. 862-877.
222. Tannenbaum, J. and B.T. Bennett, *Russell and Burch's 3Rs Then and Now: The Need for Clarity in Definition and Purpose.* J. Am. Assoc. Lab. Anim. Sci., 2015. **54**(2): p. 120-132.
223. Oehlers, S.H., et al., *Interception of host angiogenic signalling limits mycobacterial growth.* Nature, 2015. **517**(7536): p. 612–615.
224. Dartois, V.A. and E.J. Rubin, *Anti-tuberculosis treatment strategies and drug development: challenges and priorities.* Nat. Rev. Microbiol., 2022.
225. Ginsberg, A.M. and M. Spigelman, *Challenges in tuberculosis drug research and development.* Nat. Med., 2007. **13**(3): p. 290-294.
226. Desai, N., *Challenges in development of nanoparticle-based therapeutics.* AAPS J., 2012. **14**(2): p. 282-295.
227. Seyhan, A.A., *Lost in translation: the valley of death across preclinical and clinical divide – identification of problems and overcoming obstacles.* Transl. Med. Commun., 2019. **18**(4).
228. Ordonez, A.A., et al., *Visualizing the dynamics of tuberculosis pathology using molecular imaging.* J. Clin. Investig., 2021. **131**(5).
229. Sharan, R., et al., *Imaging Mycobacterium tuberculosis in Mice with Reporter Enzyme Fluorescence.* J. Vis. Exp., 2018(132).
230. Yang, H.J., et al., *Real-time Imaging of Mycobacterium tuberculosis, Using a Novel Near-Infrared Fluorescent Substrate.* J. Infect. Dis., 2017. **215**(3): p. 405-414.
231. Howe, K., et al., *The zebrafish reference genome sequence and its relationship to the human genome.* Nature, 2013. **496**(7446): p. 498-503.
232. Strahle, U., et al., *Zebrafish embryos as an alternative to animal experiments-A commentary on the definition of the onset of protected life stages in animal welfare regulations.* Reprod. Toxicol., 2012. **33**(2): p. 128-132.
233. Vibe, C.B., et al., *Thioridazine in PLGA nanoparticles reduces toxicity and improves rifampicin therapy against mycobacterial infection in zebrafish.* Nanotoxicology, 2016. **10**(6): p. 680-688.
234. Hu, N., et al., *Structure and function of the developing zebrafish heart.* Anat. Rec., 2000. **260**(2): p. 148-157.
235. Berg, V., et al., *Accumulation and Effects of Natural Mixtures of Persistent Organic Pollutants (POP) in Zebrafish after Two Generations of Exposure.* J. Toxicol. Environ. Health Part A, 2011. **74**(7-9): p. 407-423.
236. Cassar, S., et al., *Use of Zebrafish in Drug Discovery Toxicology.* Chem. Res. Toxicol., 2020. **33**(1): p. 95-118.
237. Ordas, A., et al., *Testing tuberculosis drug efficacy in a zebrafish high-throughput translational medicine screen.* Antimicrob. Agents Chemother., 2015. **59**(2): p. 753-762.
238. Palha, N., et al., *Real-Time Whole-Body Visualization of Chikungunya Virus Infection and Host Interferon Response in Zebrafish.* PLoS Pathog., 2013. **9**(9).
239. Braunbeck, T., et al., *The fish embryo test (FET): origin, applications, and future.* Environ. Sci. Pollut. Res. Int., 2015. **22**(21): p. 16247-16261.
240. Yamamoto, S., et al., *A drosophila genetic resource of mutants to study mechanisms underlying human genetic diseases.* Cell, 2014. **159**(1): p. 200-214.
241. Buchmann, K., *Evolution of Innate Immunity: Clues from Invertebrates via Fish to Mammals.* Front. Immunol., 2014. **5**(459).
242. Nusslein-Volhard, C. and E. Wieschaus, *Mutations affecting segment number and polarity in Drosophila.* Nature, 1980. **287**(5785): p. 795-801.
243. Zon, L.I. and R.T. Peterson, *In vivo drug discovery in the zebrafish.* Nat. Rev. Drug Discov., 2005. **4**(1): p. 35-44.
244. Kocere, A., et al., *Real-time imaging of polymersome nanoparticles in zebrafish embryos engrafted with melanoma cancer cells: Localization, toxicity and treatment analysis.* Ebiomedicine, 2020. **58**.
245. Amsterdam, A., et al., *Identification of 315 genes essential for early zebrafish development.* Proc. Natl. Acad. Sci. U.S.A., 2004. **101**(35): p. 12792-12797.
246. Haffter, P., et al., *The identification of genes with unique and essential functions in the development of the zebrafish, Danio rerio.* Development, 1996. **123**: p. 1-36.

247. Driever, W., et al., *A genetic screen for mutations affecting embryogenesis in zebrafish.* Development, 1996. **123**: p. 37-46.
248. Torraca, V. and S. Mostowy, *Zebrafish Infection: From Pathogenesis to Cell Biology.* Trends Cell Biol., 2018. **28**(2): p. 143-156.
249. van der Sar, A.M., et al., *A star with stripes: zebrafish as an infection model.* Trends Microbiol., 2004. **12**(10): p. 451-457.
250. Mohan, A., et al., *Complete Genome Sequences of a Mycobacterium smegmatis Laboratory Strain (MC2 155) and Isoniazid-Resistant (4XR1/R2) Mutant Strains.* Genome Announc., 2015. **3**(1).
251. Altaf, M., et al., *Evaluation of the Mycobacterium smegmatis and BCG models for the discovery of Mycobacterium tuberculosis inhibitors.* Tuberculosis, 2010. **90**(6): p. 333-337.
252. Stinear, T.P., et al., *Insights from the complete genome sequence of Mycobacterium marinum on the evolution of Mycobacterium tuberculosis.* Genome Res., 2008. **18**(5): p. 729-741.
253. Carlsson, F., et al., *Host-detrimental role of Esx-1-mediated inflammasome activation in mycobacterial infection.* PLoS Pathog., 2010. **6**(5): p. e1000895.
254. Stamm, L.M., et al., *Mycobacterium marinum escapes from phagosomes and is propelled by actin-based motility.* J. Exp. Med., 2003. **198**(9): p. 1361-1368.
255. Ramakrishnan, L. and S. Falkow, *Mycobacterium marinum persists in cultured mammalian cells in a temperature-restricted fashion.* Infect. Immun., 1994. **62**(8): p. 3222-3229.
256. Namouchi, A., et al., *Phenotypic and genomic comparison of Mycobacterium aurum and surrogate model species to Mycobacterium tuberculosis: implications for drug discovery.* BMC Genom., 2017. **18**(530).
257. Rifat, D., et al., *Mutations in fbiD (Rv2983) as a Novel Determinant of Resistance to Pretomanid and Delamanid in Mycobacterium tuberculosis.* Antimicrob. Agents Chemother., 2021. **65**(1).
258. Haver, H.L., et al., *Mutations in genes for the F420 biosynthetic pathway and a nitroreductase enzyme are the primary resistance determinants in spontaneous in vitro-selected PA-824-resistant mutants of Mycobacterium tuberculosis.* Antimicrob. Agents Chemother., 2015. **59**(9): p. 5316-5323.
259. Liu, Y.C., et al., *Immune activation of the host cell induces drug tolerance in Mycobacterium tuberculosis both in vitro and in vivo.* J. Exp. Med., 2016. **213**(5): p. 809-825.
260. Lipinski, C.A., et al., *Experimental and computational approaches to estimate solubility and permeability in drug discovery and development settings.* Adv. Drug Deliv. Rev., 1997. **23**(1-3): p. 3-25.
261. Ghose, A.K., V.N. Viswanadhan, and J.J. Wendoloski, *Prediction of hydrophobic (lipophilic) properties of small organic molecules using fragmental methods: An analysis of ALOGP and CLOGP methods.* J. Phys. Chem. A, 1998. **102**(21): p. 3762-3772.
262. Ekins, S., et al., *Analysis and hit filtering of a very large library of compounds screened against Mycobacterium tuberculosis.* Mol. Biosyst., 2010. **6**(11): p. 2316-2324.
263. Palmer, B.D., et al., *Synthesis and structure-activity relationships for extended side chain analogues of the antitubercular drug (6S)-2-nitro-6-{[4-(trifluoromethoxy)benzyl]oxy}-6,7-dihydro-5H-imidazo[2,1-b][1, 3]oxazine (PA-824).* J. Med. Chem., 2015. **58**(7): p. 3036-3059.
264. Palmer, B.D., et al., *Synthesis and structure-activity studies of biphenyl analogues of the tuberculosis drug (6S)-2-nitro-6-{[4-(trifluoromethoxy)benzyl]oxy}-6,7-dihydro-5H-imidazo[2,1-b][1, 3]oxazine (PA-824).* J. Med. Chem., 2010. **53**(1): p. 282-294.
265. Kmentova, I., et al., *Synthesis and Structure-Activity Relationships of Aza- and Diazabiphenyl Analogues of the Antitubercular Drug (6S)-2-Nitro-6-{[4-(trifluoromethoxy)benzyl]oxy}-6,7-dihydro-5H-imidazo[2,1-b][1,3]oxazine (PA-824).* J. Med. Chem., 2010. **53**(23): p. 8421-8439.
266. Jarlier, V. and H. Nikaido, *Mycobacterial Cell-Wall - Structure and Role in Natural-Resistance to Antibiotics.* FEMS Microbiol. Lett., 1994. **123**(1-2): p. 11-18.
267. Hurdle, J.G., et al., *Targeting bacterial membrane function: an underexploited mechanism for treating persistent infections.* Nat. Rev. Microbiol., 2011. **9**(1): p. 62-75.
268. Hu, Y.L., et al., *Polysarcosine as an Alternative to PEG for Therapeutic Protein Conjugation.* Bioconjug. Chem., 2018. **29**(7): p. 2232-2238.
269. Wilhelm, S., et al., *Analysis of nanoparticle delivery to tumours.* Nat. Rev. Mater., 2016. **1**(5).
270. Danhier, F., *To exploit the tumor microenvironment: Since the EPR effect fails in the clinic, what is the future of nanomedicine?* J Control Release, 2016. **244**(Pt A): p. 108-121.
271. Mosaiab, T., et al., *Carbohydrate-based nanocarriers and their application to target macrophages and deliver antimicrobial agents.* Adv. Drug Deliv. Rev., 2019. **151-152**: p. 94-129.

272. Azad, A.K., M.V. Rajaram, and L.S. Schlesinger, *Exploitation of the Macrophage Mannose Receptor (CD206) in Infectious Disease Diagnostics and Therapeutics.* J. Cytol. Mol. Biol., 2014. **1**(1).
273. Campbell, F., et al., *Directing Nanoparticle Biodistribution through Evasion and Exploitation of Stab2-Dependent Nanoparticle Uptake.* Acs Nano, 2018. **12**(3): p. 2138-2150.
274. Sieber, S., et al., *Zebrafish as an early stage screening tool to study the systemic circulation of nanoparticulate drug delivery systems in vivo.* J Control Release, 2017. **264**: p. 180-191.
275. Zhang, Y.N., et al., *Nanoparticle-liver interactions: Cellular uptake and hepatobiliary elimination.* J Control Release, 2016. **240**: p. 332-348.
276. Weissleder, R., M. Nahrendorf, and M.J. Pittet, *Imaging macrophages with nanoparticles.* Nat. Mater., 2014. **13**(2): p. 125-138.
277. Hayashi, Y., et al., *Differential Nanoparticle Sequestration by Macrophages and Scavenger Endothelial Cells Visualized in Vivo in Real-Time and at Ultrastructural Resolution.* ACS Nano, 2020. **14**(2): p. 1665-1681.
278. Brown, T., *Observations by immunofluorescence microscopy and electron microscopy on the cytopathogenicity of Naegleria fowleri in mouse embryo-cell cultures.* J. Med. Microbiol., 1979. **12**(3): p. 363-371.
279. Zeng, F. and A.E. Morelli, *Extracellular vesicle-mediated MHC cross-dressing in immune homeostasis, transplantation, infectious diseases, and cancer.* Semin. Immunopathol., 2018. **40**(5): p. 477-490.
280. Weinhard, L., et al., *Microglia remodel synapses by presynaptic trogocytosis and spine head filopodia induction.* Nat. Commun., 2018. **9**(1228).
281. Sarvari, A.K., et al., *Interaction of differentiated human adipocytes with macrophages leads to trogocytosis and selective IL-6 secretion.* Cell Death Dis., 2015. **6**: p. e1613.
282. Grobbelaar, M., et al., *Evolution of rifampicin treatment for tuberculosis.* Infect. Genet. Evol., 2019. **74**(103937).
283. Donald, P.R., *Cerebrospinal fluid concentrations of antituberculosis agents in adults and children.* Tuberculosis, 2010. **90**(5): p. 279-292.
284. Goutelle, S., et al., *Population modeling and Monte Carlo simulation study of the pharmacokinetics and antituberculosis pharmacodynamics of rifampin in lungs.* Antimicrob. Agents Chemother., 2009. **53**(7): p. 2974-2981.
285. Elliott, A.M., et al., *Failure of drug penetration and acquisition of drug resistance in chronic tuberculous empyema.* Tuber. Lung Dis., 1995. **76**(5): p. 463-467.
286. Dartois, V., *The path of anti-tuberculosis drugs: from blood to lesions to mycobacterial cells.* Nat. Rev. Microbiol., 2014. **12**(3): p. 159-167.
287. Kjellsson, M.C., et al., *Pharmacokinetic evaluation of the penetration of antituberculosis agents in rabbit pulmonary lesions.* Antimicrob. Agents Chemother., 2012. **56**(1): p. 446-457.
288. Prideaux, B., et al., *High-sensitivity MALDI-MRM-MS imaging of moxifloxacin distribution in tuberculosis-infected rabbit lungs and granulomatous lesions.* Anal. Chem., 2011. **83**(6): p. 2112-2118.
289. Seijger, C., et al., *High-dose rifampicin in tuberculosis: Experiences from a Dutch tuberculosis centre.* PLoS One, 2019. **14**(3): p. e0213718.
290. Trousil, J., et al., *Antitubercular nanocarrier monotherapy: Study of In Vivo efficacy and pharmacokinetics for rifampicin.* J Control Release, 2020. **321**: p. 312-323.
291. Upton, A.M., et al., *In vitro and in vivo activities of the nitroimidazole TBA-354 against Mycobacterium tuberculosis.* Antimicrob. Agents Chemother., 2015. **59**(1): p. 136-144.
292. Ntshangase, S., et al., *The downfall of TBA-354 - a possible explanation for its neurotoxicity via mass spectrometric imaging.* Xenobiotica, 2018. **48**(9): p. 938-944.

Scientific papers (I-V)

PAPER I

NANO · MICRO small
www.small-journal.com

Zebrafish Embryos Allow Prediction of Nanoparticle Circulation Times in Mice and Facilitate Quantification of Nanoparticle–Cell Interactions

*Nils-Jørgen Knudsen Dal, Agnese Kocere, Jens Wohlmann, Simon Van Herck, Tobias A. Bauer, Julien Resseguier, Shahla Bagherifam, Hilde Hyldmo, Matthias Barz, Bruno G. De Geest, and Federico Fenaroli**

The zebrafish embryo is a vertebrate well suited for visualizing nanoparticles at high resolution in live animals. Its optical transparency and genetic versatility allow noninvasive, real-time observations of vascular flow of nanoparticles and their interactions with cells throughout the body. As a consequence, this system enables the acquisition of quantitative data that are difficult to obtain in rodents. Until now, a few studies using the zebrafish model have only described semiquantitative results on key nanoparticle parameters. Here, a MACRO dedicated to automated quantitative methods is described for analyzing important parameters of nanoparticle behavior, such as circulation time and interactions with key target cells, macrophages, and endothelial cells. Direct comparison of four nanoparticle (NP) formulations in zebrafish embryos and mice reveals that data obtained in zebrafish can be used to predict NPs' behavior in the mouse model. NPs having long or short blood circulation in rodents behave similarly in the zebrafish embryo, with low circulation times being a consequence of NP uptake into macrophages or endothelial cells. It is proposed that the zebrafish embryo has the potential to become an important intermediate screening system for nanoparticle research to bridge the gap between cell culture studies and preclinical rodent models such as the mouse.

1. Introduction

The zebrafish embryo is rapidly becoming an attractive tool for screening nanoparticles.[1] This transparent vertebrate system develops rapidly, and already after 48 h a beating heart and robust blood circulation are readily observable under a stereomicroscope.[2] Intravenously injected fluorescent nanoparticles (NPs) can therefore be directly observed at the whole animal level.[3] In addition, the availability of several fluorescent transgenic zebrafish lines with selectively labeled cells allows the assessment of NP interactions with important cells such as macrophages and endothelial cells.[3–5] These characteristics, together with the much lower costs of maintenance in comparison to murine models, place the zebrafish in an ideal position to become an important intermediate system for screening NPs between cell cultures and mice. However, only semiquantitative methods for NP analysis have been applied until now, using confocal microscopy, which is more time consuming than the use of a stereomicroscope and therefore allows fewer animals to be analyzed.[6,7] Among the parameters that are crucial for understanding NP behavior is the circulation time. This factor, which can also be studied in adult zebrafish, is essential for designing new nanomaterials since a long circulation time is associated with increased accumulation at diseased sites in

N.-J. K. Dal, A. Kocere, J. Wohlmann, Dr. J. Resseguier, H. Hyldmo, Dr. F. Fenaroli
Department of Biosciences
University of Oslo
Blindernveien 31, 0371 Oslo, Norway
E-mail: federico.fenaroli@ibv.uio.no
Dr. S. Van Herck, Prof. B. G. De Geest
Department of Pharmaceutics
Ghent University
Ottergemsesteenweg 460, 9000 Ghent, Belgium
The ORCID identification number(s) for the author(s) of this article can be found under https://doi.org/10.1002/smll.201906719.

DOI: 10.1002/smll.201906719

T. A. Bauer, Dr. M. Barz
Institute for Organic Chemistry
Johannes Gutenberg-University Mainz
Duesbergweg 10–14, 55099 Mainz, Germany
Dr. S. Bagherifam
Department of Radiation Biology
Institute for Cancer Research
Norwegian Radium Hospital
Montebello, N-0310 Oslo, Norway

cancer and tuberculosis.[8–10] NP flow is greatly influenced by their uptake into blood macrophages (or monocytes). Moreover, for nanocarriers destined for the cancer therapy, uptake by macrophages is generally considered to decrease the chances of accumulation in tumor sites and is therefore considered a detrimental factor for therapeutic efficiency. However, some recent reviews and publications[11,12] suggest that direct targeting of some macrophages may be desirable since a subset of these cells can be selectively recruited to diseased sites, such as tumor-associated macrophages (TAMs) in solid tumors.[13–15] Moreover, a number of intracellular pathogens reside and replicate within macrophages, and several publications now recognize the importance of targeting this cell type using NPs for fighting intracellular infections.[16,17] This approach has been reported for *Mycobacterium marinum*,[4] *Francisella novicida*,[18] *Staphylococcus aureus*,[19] and *Salmonella enterica*.[20]

Another important cell type that affects NP distribution is endothelial cells, which line the blood vessels through which NP flow along the body; by binding and taking up NPs, they are also capable of influencing their circulation times. This phenomenon is not easily noticed in mouse models. Even in the zebrafish, only a few studies have described the uptake of NPs into endothelial cells in vivo.[3,21] Although uptake into endothelial cells may be undesirable since they reduce circulation time, some researchers have added specific ligands to NPs in order to enhance this process, targeting specific diseases such as thrombosis and ischemia.[22,23]

Here, we describe methods to reliably quantify NP (see **Table 1**) circulation time and estimate the relative accumulation of NPs in macrophages or endothelial cells in the zebrafish embryo using a stereomicroscope and a user-friendly imageJ MACRO for automated image analysis. From the seven NP formulations, four were selected to compare NP circulation time in zebrafish with mice.

2. Experimental Section

2.1. Zebrafish Embryo Handling

In this study, different strains of zebrafish embryos were used. For the manual analysis of the circulation (MACRO manual circulation), wild-type (WT) zebrafish embryos were used. For the automatic analysis of the circulation (MACRO automatic analysis) zebrafish expressing enhanced green fluorescence protein (EGFP) in the vasculature, Tg(fli1a:EGFP), were used; for the macrophage uptake analysis (MACRO macrophage uptake): Tg(mpeg1:cherry); and for the endothelial uptake analysis (MACRO endothelial uptake): double transgenic Tg(mpeg1:cherry) and Tg(fli1a:EGFP). After fertilization, the harvested embryos were kept at 28.5 °C in zebrafish egg water containing phenylthiourea (0.003%). All experiments were approved by the Norwegian authorities regulating animal research.

2.2. Nanoparticle Preparations

2.2.1. Liposomes

Phosphatidyl choline (PC) was bought from Lipoid (product E PC-3), cholesterol (Chol) from Sigma, while phosphoethanolamine polyethylene glycol (PEG) 2000 (PE-PEG) and ATTO633-1,2-dioleoyl-sn-glycero-3-phosphoethanolamine (DOPE) from ATTO-TEC, and biotinyl phosphoethanolamine (B-PE) from Avanti Lipids (products 880120P and 870282).

Procedure: 3 mL of chloroform and 5 µL of a solution 1 mg mL^{-1} in ethanol of ATTO-633-labeled DOPE were added to a flask containing 2.4 mg of PC, 0.64 mg of Chol, and 0.69 mg of PE-PEG for PEGylated liposomes without biotin; 2.3 mg of PC, 0.1 mg of B-PE, 0.64 mg of Chol, and 0.69 mg of PE-PEG for PEGylated liposomes with biotin; or 3.09 mg of PC and 0.64 mg of Chol for non-PEGylated liposomes.

These mixtures were dried using a rotatory evaporator in three consecutive steps: 150 mbar for 30 min, 80 mbar for 30 min, and 16 mbar for 10 min. The dried phospholipids were then hydrated with 1 mL of phosphate-buffered saline (PBS) at 70 °C and vortexed thoroughly. The resuspended mixture was then introduced in a gas-tight syringe which allowed the passage of the solution through filters of different sizes mounted on a mini extruder (Avanti lipids) at 70 °C. For liposomes 100 nm PEG and 99 nm PEG biotin, a 0.05 µm pore size was used, while for liposomes 580 nm PEG and 623 nm NO PEG, a 0.8 µm filter was used. Liposomes were analyzed by dynamic light scattering (DLS) and a Zetasizer.

2.2.2. Poly(Sar-b-pCys(SO_2Et)) NP

The preparation of core cross-linked polymeric micelles was adapted from the literature and modified.[24] Poly(sarcosine)-*b*-poly((*S*-ethylsulfonyl)cysteine) ($pSar_{225}$-*b*-$pCys(SO_2Et)_{31}$) was

Table 1. NPs used in the study. Hydrodynamic diameter measures the peak intensity obtained by DLS.

NP type	Hydrodynamic diameter (D_h) [nm]	Polydispersity index (PDI)	Zeta potential [mV]
1) PEGylated liposomes	100 ± 0.55	0.04 ± 0.01	−3.54 ± 1.19
2) PEGylated liposomes with biotin	99 ± 0.58	0.07 ± 0.02	−1.49 ± 0.59
3) PEGylated liposomes	580.9 ± 12	0.4 ± 0.07	−1.53 ± 0.96
4) Non-PEGylated liposomes	623.7 ± 12	0.37 ± 0.06	−5.12 ± 0.81
5) Poly(DMA-*b*-BzKetAc) NP	65.8 ± 0.6	0.174 ± 0.0006	−28.9 ± 16
6) Poly(Sar-*b*-pCys(SO_2Et)) NP	86.1 ± 0.93	0.131 ± 0.007	−1.94 ± 3.84
7) Poly(Sar-*b*-pCys(SO_2Et)) NP	47.4 ± 0.45	0.094 ± 0.001	−3.36 ± 5.86

dissolved in dimethyl sulfoxide (DMSO) at a concentration of 7.5 g L^{-1} for 1 h. Next, 20 vol% of 1×10^{-3} M acetate buffer (pH 4.75) was added to adjust the concentration to 6.6 g L^{-1}. The solution was left to equilibrate at room temperature for 5 h, followed by dialysis against 1×10^{-3} M acetate buffer (pH 4.75). The solution was filtered (GHP 450) and concentrated to 6.6 g L^{-1} by spin filtration (Amicon Ultra, molecular weight cut-off (MWCO) = 3 kDa), yielding the micelle solution. For the preparation of nanoparticle type 7 (Table 1), DMSO and acetate buffer were equipped with 1 and 10×10^{-3} M thiourea, respectively. For cross-linking, in a separate flask, the liponamide cross-linker was dissolved in ethanol at a concentration of $\beta = 10$ g L^{-1} and one equivalent of an aqueous solution of tris(2-carboxyethyl)phosphine hydrochloride (TCEP·HCl) (50 g L^{-1}) was added per disulfide. After 18 h, the cross-linker solution was added to the micelle solution at equimolar amounts of thiols per cysteines. The reaction mixture was allowed to stand at room temperature for 48 h. To remove residual cross-linker and free polymer, the solution was dialyzed against DMSO and MilliQ water (MWCO = 6–8 kDa), followed by repetitive spin filtration (Amicon Ultra, MWCO = 100 kDa). For labeling, 1.0 equivalent of cyanine 5 NHS–ester stock solution (0.3 eq of Atto647N NHS-ester for NP7) in DMSO (5 g L^{-1}) was added per polymer end group at pH 7.4 (adjusted with 1 M $NaHCO_3$ solution). After 72 h, excess dye was removed by repetitive spin filtration (Amicon Ultra, 100 kDa) using ethanol/water mixtures, and the final particle solution (in MilliQ water) was stored at 4 °C. The absence of free polymer and free dye was verified by gel permeation chromatography in hexafluoro isopropanol.

The preparation of poly(*N*,*N*-dimethylacrylamide)-*b*-poly(2-((2-(benzyloxy)propan-2-yl)oxy)ethyl acrylate) (poly(DMA-*b*-BzKetAc))) NP was performed according the method described in ref. [10].

2.3. Nanoparticle Injections

In order to intravenously inject the zebrafish embryos, NP solutions (4 mg mL^{-1}) were loaded into borosilicate needles (GC100T-10, Harvard instruments) previously prepared using a micropipette puller (P-97, Sutter instruments). The needles were then attached to an Eppendorf Femtojet Express microinjector and controlled by a Narishige MN-153 micromanipulator. The injection of a precise quantity of NPs was done by careful manipulation of the pressure and time of injection. Once the desired volume was achieved, zebrafish embryos were anesthetized using zebrafish egg water supplemented with tricaine (0.02%). The injection of these embryo occurred on a Petri dish that had previously been filled with a solution of 2% agarose, which solidifies upon cooling. All the injections were made in the posterior cardinal vein at 2 days post fertilization.

2.4. Imaging of Zebrafish Embryos

Each zebrafish embryo injected with NPs was subsequently imaged at different times and in different channels depending on the type of analysis, using a Leica stereomicroscope DFC365FX (1.0× planapo lens) obtaining images of both the caudal region (120× magnification) and the whole fish (30× magnification). Prior to the imaging session, zebrafish were kept in Petri dishes wrapped in aluminum foil to avoid any possible photobleaching.

- *For Circulation Time, Manual*: Images were taken at 5 min and at 1, 4, 8, 24, 48, and 72 h, in transmission and the far red (Cy5, NP) fluorescence channel.
- *For Circulation Time, Automatic*: Images were taken at 5 min and at 1, 4, 8, 24, 48, and 72 h, in transmission, far red (Cy5, NP), and green (green fluorescence protein (GFP), endothelium) fluorescence channels.
- *For Macrophage Uptake Evaluation, Automatic*: Images were taken at 6 h in transmission, far red (Cy5, NP), and red (DsRed, macrophage) fluorescence channels.
- *For Endothelial Uptake Evaluation, Automatic*: Images were taken at 6 h in transmission, far red (Cy5, NP), red (DsRed, macrophage), and green (GFP, endothelium) fluorescence channels.

2.5. Functioning of the ImageJ MACRO

The ImageJ MACRO is available at https://github.com/wohlmann/IJ_ZF_NP_Quantification.

Once started, the MACRO will ask, via a file handling dialogue, the folder where the images to be analyzed are stored and another folder, where the output results will become available. The Leica *.lif format or *.tif images will be accepted by the MACRO file handling.

As the MACRO includes various types of analyses, a second dialogue will enable the selection of the desired analysis as well as the definition of an individual channel order and assignment. Analysis options are 1) circulation times, manual; 2) circulation times, automatic; 3) macrophage uptake, automatic; or 4) endothelial uptake, automatic. Fluorescent channels will be assigned to 1) transmission image, 2) NP, 3) macrophage, or 4) endothelium fluorescence.

Additionally, the user has the option to verify the measurements by analyzing quality control output images for the detected regions of interest (ROIs). If the images are not satisfactory, the levels of thresholding of each analysis can also be customized.

2.5.1. Circulation Time Analysis: Manual

After automatic sorting of the images depending on the magnification, the MACRO will open and show the higher magnification images (120× magnification images) as well as predefined rectangles of adaptable number and size to be positioned on the caudal vein by the user as indicated in **Figure 1**C. After positioning the rectangles on the caudal artery, the MACRO will measure the fluorescence intensity in this region and compare it to the fluorescence intensity of the whole fish (30× magnification images) detected via its transmission signal. The results will be stored in two individual *.txt files (usable by spreadsheet software) for each measurement. The use of these values to determine NP circulation is explained in section "Quantification of the Results Obtained Using the MACRO."

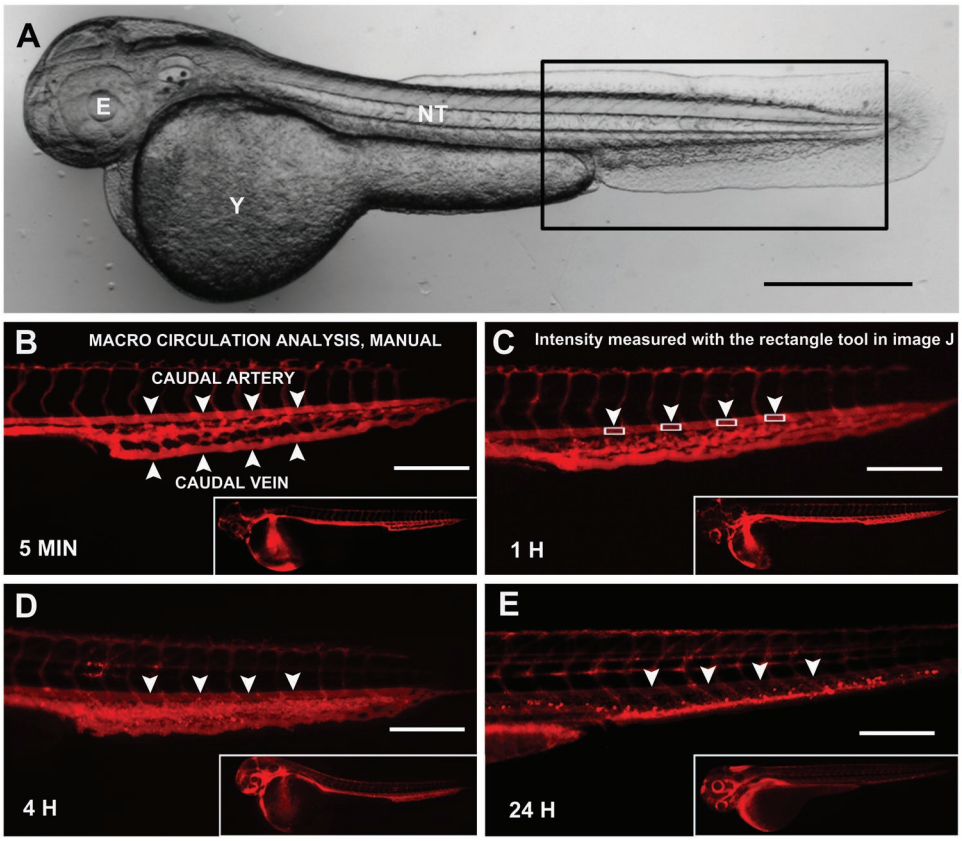

Figure 1. Circulation of NPs in the zebrafish embryo, manual analysis. A) Acquisition of the zebrafish embryo at 48 h post fertilization in the transmission channel; the rectangular inset shows the area where the caudal region images were taken. B–E) Images of the caudal vein of zebrafish injected with fluorescent NPs (here 100 nm liposomes with PEG) imaged at different time points—B) 5 min, C)1 h, D) 4 h, and E) 24 h. B) The main blood components of the caudal region are shown by arrowheads (caudal artery and caudal vein). C) The rectangles used for quantification of fluorescence are shown (arrowheads); these are either manually or automatically placed on the caudal artery and in between intersegmental vessels. D,E) The decrease in fluorescence of the caudal artery (arrowheads) can be seen at 4 and 24 h. B–E, insets) The values for fluorescence in the artery are normalized relative to the overall NP fluorescence in the whole fish. Scale bars: A) 500 nm and B–E) 200 nm.

2.5.2. Circulation Time Analysis: Automatic

In this type of analysis, the MACRO is utilizing the vasculature fluorescence (Tgfli1a:EGFP) signal to automatically detect the caudal vein region(120× magnification images). This detection was based on the muscle segments between the intersegmental vessels (ISVs) branching from the caudal vein and artery relying on an initial automated orientation of the image using the characteristic anatomical features of the zebrafish tail region. The rectangles for the measurement were adjusted to avoid inclusion of branching ISVs or local accumulations using a NP signal threshold and particle analysis. As for the manual analysis, the fluorescence intensity of the whole animal was also analyzed (30× magnification images). The results were stored in two individual *.txt files (usable by spreadsheet software) for each measurement. The use of these values to determine NP circulation is explained in section "Quantification of the Results Obtained Using the MACRO."

2.5.3. Macrophage Uptake Analysis: Automatic

In this analysis, the MACRO will first provide a thresholding of the NP signal (in 120× magnification images) in order to separate free NPs in the blood flow from the ones that have been taken up by cells; the latter, depending on the amount taken up, appear as brighter spots with higher density. Second, the macrophage signal was thresholded and overlapped with the NPs, and only the NPs within macrophages were analyzed for their intensity value. Similar to the NP circulation analysis, the overall NP fluorescence in the zebrafish was measured (30× magnification images) and the results were stored in two individual *.txt files (usable by spreadsheet software).

2.5.4. Endothelial Cells Uptake Analysis: Automatic

Identical to the macrophage uptake analysis, NPs and macrophages were thresholded but in this case, the NPs within macrophages were eliminated before the fluorescence intensity of the thresholded area occupied by the endothelium was measured for the remaining NP signals (120× magnification images). After the analysis of the whole zebrafish fluorescence (30× magnification images) in the NP channel, the results were stored in two individual *.txt files (usable by spreadsheet software) and will contain the estimated uptake of NPs by the endothelium in the caudal area and the overall fluorescence values in the whole zebrafish.

2.6. Further Details About the MACRO

Throughout the MACRO script, several comment lines were used to explain in detail every command.

2.7. Quantification of the Results Obtained Using the MACRO

The output *.txt files obtained from the MACRO contained, for each zebrafish embryo, two values that will be used for the subsequent analyses: the "mean fluorescence value," used for circulation analysis, and the "Raw Integrated Density" (RawIntDen), which is instead used for either macrophage or endothelial uptake and represents the sum of the pixel values in the selected area.

2.7.1. Circulation Analysis: Automatic and Manual

Raw Values: In this analysis for each time point the "mean fluorescence intensity" of the artery (M_{artery}, calculated from a 120× magnification image of the caudal region), and the "mean fluorescence values" of the whole zebrafish (M_{whole}, calculated from a 30× magnification image of the whole animal) were detected. Each point in the graph is represented by the result of the equation: $M_{\text{artery}}/M_{\text{whole}}$.

Percent Conversion: In order to convert results into percentages the value of each NP obtained at 5 min, M_{artery} (5 min)/M_{whole} (5 min) was considered the 100% estimate while the intensity of the background was considered to represent 0%. Thus, the percentage values are obtained as follows

$$\text{Flowing NP, percent} = \frac{\dfrac{M_{\text{artery}}\,(\text{time } x)}{M_{\text{whole}}\,(\text{time } x)} - \text{Background value}}{\dfrac{M_{\text{artery}}\,(5\,\text{min})}{M_{\text{whole}}\,(5\,\text{min})} - \text{Background value}} \times 100 \tag{1}$$

2.7.2. Scoring Macrophage and Endothelial Uptake of Nanoparticles

While for circulation analysis, the mean values of intensity were used, for both macrophage and endothelial analyses RawIntDen was utilized. The RawIntDen of each zebrafish caudal region (120× magnification images) was normalized by the overall fluorescence of the whole fish (also a RawIntDen value, 30× magnification images) and multiplied by 100.

Macrophage Uptake: The fluorescence of the pixels relative to NP fluorescence in the macrophage selection was expressed as the RawIntDen value obtained in the results file for each zebrafish embryo ($\text{RID}_{\text{macrophages}}$). The overall fluorescence intensity of NPs in the whole fish was also calculated as RawIntDen value ($\text{RID}_{\text{whole}}$). In order to obtain the final value, RIDmacrophages was normalized by RIDwhole and multiplied by 100 as shown below

$$\text{Macrophage uptake of NP} = \frac{\text{RID}_{\text{macrophages}}}{\text{RID}_{\text{whole}}} \times 100 \tag{2}$$

Endothelial Uptake: Just as for the macrophage analysis, the fluorescence of the pixels of the NPs which overlap with the endothelium signal was scored as a RawIntDen in the results file for each zebrafish ($\text{RID}_{\text{endothelium}}$). This value was normalized by the overall NP fluorescence ($\text{RID}_{\text{whole}}$) and multiplied by 100 as shown below

$$\text{Endothelial uptake of NP} = \frac{\text{RID}_{\text{endothelium}}}{\text{RID}_{\text{whole}}} \times 100 \tag{3}$$

2.8. Mouse Nanoparticle Circulation Analysis

Prior to the experiment, 6 week old male BALB/cAnNRj mice were divided into groups of six animals per cage according to the type of NPs (100 and 580 nm PEGylated liposomes, 623 nm non-PEGylated liposomes and 47 nm poly(Sar-*b*-pCys(SO_2Et) NP) and time point for blood sampling (5 min, 4 h, 24 h, and 72 h). Next, after 1 week of acclimatization, the mice received a single intravenous injection (200 µL) of NPs or with isotonic PBS solution (control). At the selected time points, the animals were placed under deep anesthesia (Isoflurane 5%) and after the ribcage was exposed, blood extraction was performed by cardiac puncture. This was followed by cervical dislocation to terminate the animals. Heparin-coated syringes and Eppendorf tubes were applied to prevent blood clotting. Samples were put on ice and protected from light by aluminum foil. 5 µL of blood from each animal was inserted into a fluorinated ethylene–propylene (FEP) tube, and an image in the far-red channel was taken with a Leica stereomicroscope DFC365FX. Mice receiving PBS were used as a background control. The NP circulation at each time point was then calculated as

$$\text{Flowing NP, percent} = \frac{\text{Fluorescence}\,(\text{time } x) - \text{Background value}}{\text{Fluorescence}\,(5\,\text{min}) - \text{Background value}} \times 100 \tag{4}$$

Values obtained at 5 min and subtracted of the background were considered the 100% value while the background corresponded to the 0%. Mice experiments were approved by the Norwegian Food Safety Authority, Mattilsynet, FOTS ID: 20607.

2.9. Statistics Used

One-way analysis of variance (ANOVA) was used with Tukey's multicomparison test to compare the different groups for macrophage and endothelial uptake. The test was used to assess if the values come from a Gaussian distribution was the Kolmogorov–Smirnov test with Dallal–Wilkinson–Lille for *P*-value.

3. Results

3.1. Nanoparticle Circulation

The zebrafish embryo can be used to assess the circulation properties of NPs and here we have established two methods,

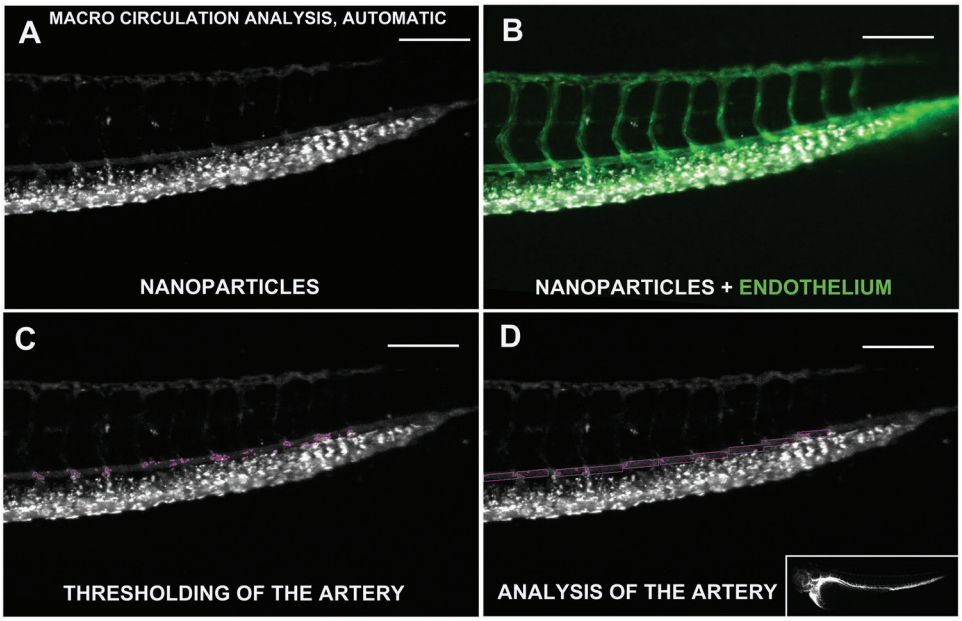

Figure 2. Circulation of NPs in the zebrafish embryo, automatic analysis. This image shows the steps performed by the MACRO for the analysis of the fluorescence in the caudal artery. A) The image processing of zebrafish injected with fluorescent NPs (99 nm PEGylated liposomes with biotin) utilizes B) the fluorescent signal of the vasculature to identify the caudal artery. C) Fluorescence due to NP uptake in the artery is removed, and D) regions in between intersegmental vessels are automatically detected to calculate the relative fluorescence. The results are then normalized relative to the fluorescence of the whole fish (panel (D), lower right image).

one manual and one automatic, to rapidly analyze the images. For this, we focused on the caudal region of the zebrafish which, being relatively thin, allows for better imaging and therefore more precise results compared to other sites in the zebrafish embryo. The main blood components of the caudal region are the caudal vein, the site of NP injection, and the caudal artery, the site of importance for the measurements (Figure 1B, arrowheads). In Figure 1, we show zebrafish embryos that had been injected with 100 nm PEG liposomes with images of the caudal area (Figure 1A) at different time points: 5 min (Figure 1B), 1 h (Figure 1C), 4 h (Figure 1D), and 24 h (Figure 1E). In order to evaluate the circulation time, we measured the average fluorescence of the caudal artery over time, as this relatively big vessel facilitates the analysis due to its size and the absence of NP uptake by macrophages and lower uptake by endothelial cells, which occurs mainly in the caudal vein. As illustrated in Figure 1, the fluorescence signal due to flowing 100 nm PEGylated liposomes in the caudal vein decreases in time. Using the manual option of the MACRO, the user will place rectangles of predefined number and size on the caudal artery, between the intersegmental vessels (as shown in Figure 1B) for the analysis of the fluorescence signal. The MACRO will then automatically measure the fluorescence intensity of the resulting region as well as the whole fish region detected via its transmission signal.

In the automatic circulation analysis (**Figure 2**), it is necessary to use transgenic zebrafish possessing fluorescent vasculature, here we used the Tg(fli1a:EGFP) strain. The information obtained from the blood endothelium is used by the MACRO to detect the regions of the artery contained between two intersegmental vessels (Figure 2B). These regions will be analyzed while areas characterized by high fluorescence, due to endothelial uptake, will be eliminated from the quantification, as shown in Figure 2C. As for the previous analysis, the mean fluorescence intensity in these areas will be measured (Figure 2D) together with the total fluorescence of the whole embryo; the relative values of each zebrafish are provided in two separate *.txt files.

In order to plot the circulation in time (5 min, 1 h, 4 h, 8 h, 24 h, 48 h, and 72 h), the average fluorescence signal in the artery is normalized relative to the overall fluorescence (see "Experimental Section" for details), resulting in the values shown in **Figure 3**. These initially calculated values (Figure 3A) are then converted to percentages (Figure 3B–D). PEGylated liposomes of 100 and 580 nm circulate well, with longer circulation times evident for the smaller 100 nm liposomes which, even after 3 days, had about 5% of the NPs still in circulation. The lack of a PEG layer or the presence of biotin decreases the circulation times of the liposomes, with the former being removed from the blood flow already 8 h after injection while the latter cease to circulate at about 48 h (Figure 3B,C). Further, NPs being expected to be long circulating, possessing a different surface chemistry such as polysarcosine and polyDMA ((poly(Sar-*b*-pCys(SO_2Et)) and poly(DMA-*b*-BzKetAc) NP), show relatively longer circulation times, especially the 41 nm NPs ((poly(Sar-*b*-pCys(SO_2Et)) and 65 nm poly(DMA-*b*-BzKetAc). After 3 days, these embryos still had 15% and 11.5% of the injected NPs still in circulation (3D).

3.2. Nanoparticle Circulation Time in Zebrafish and Mouse

So far, our analysis showed that NPs known from mice experiments to have short circulation times (non-PEGylated

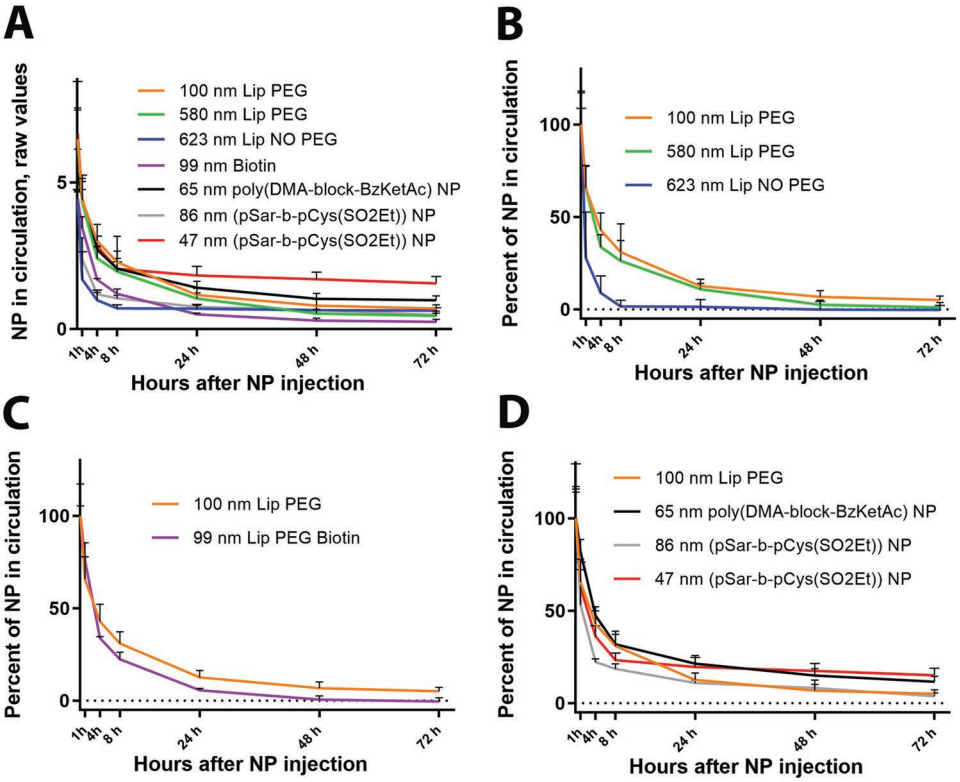

Figure 3. Quantification of the NP circulation times in zebrafish embryos. A) Raw values obtained by dividing the average fluorescence in the caudal artery with the total fluorescence. B–D) Values converted in percentages. B) PEGylated 100 nm liposomes are compared to 580 nm PEGylated liposomes and 623 non-PEGylated ones. C) The presence of biotin in PEGylated liposomes of about 100 nm is evaluated. D) NPs with three different surfaces known to allow long circulation (PEG, polyDMA, and polysarcosine) are compared. Bars indicate standard deviation, $N \geq 3$.

liposomes) or long circulation (PEGylated liposomes, polysarcosine NP, and polyDMA NP) behaved similarly in the zebrafish model. We therefore asked whether the zebrafish embryo could be used to predict NP circulation in mice; for this, we selected four of the analyzed NP mixtures (100 and 580 nm PEGylated liposomes, 623 nm non-PEGylated liposomes, and 47 nm (pSar-*b*-pCys(SO_2Et)) NP) and assessed their circulation in mice by estimating the residual fluorescence at four selected time points, 5 min, 4 h, 24 h, and 72 h. The comparison between these two sets of data is shown in **Figure 4**.

In both animal models, non-PEGylated liposomes of about 623 nm were removed from the circulation in a matter of a few hours. PEGylated liposomes of 100 nm circulated better in both animal models than the 580 nm PEGylated liposomes, although in zebrafish both these liposomes circulated for longer times. The nanoparticles which performed best in both models were the 47 nm (pSar-*b*-pCys(SO_2Et)) NP with comparable circulation at 72 h. In the zebrafish, these NPs, after the first decline, remain stable in circulation, while in the mouse we observed a moderate decline throughout all the time points.

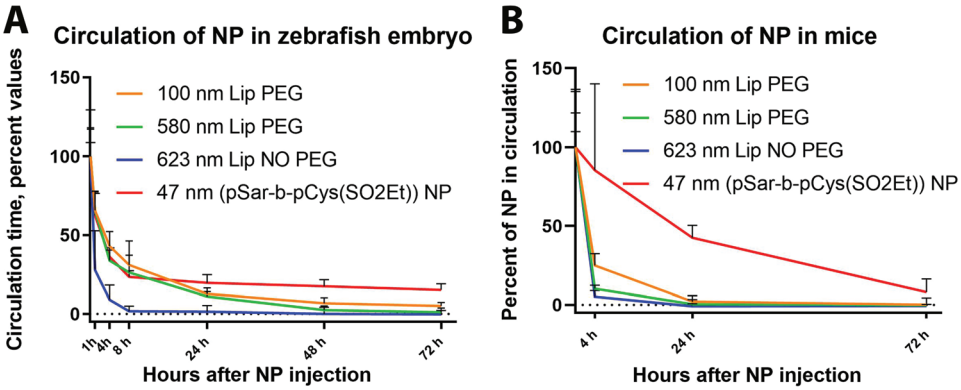

Figure 4. NP circulation in zebrafish embryos and mice. A) The circulation of the four selected NPs in zebrafish embryo: 100 and 580 nm PEGylated liposomes, 623 non-PEGylated liposomes, and 47 nm (pSar-*b*-pCys(SO_2Et)) NP. B) The circulation of the same NPs in the mouse model. $N \geq 4$.

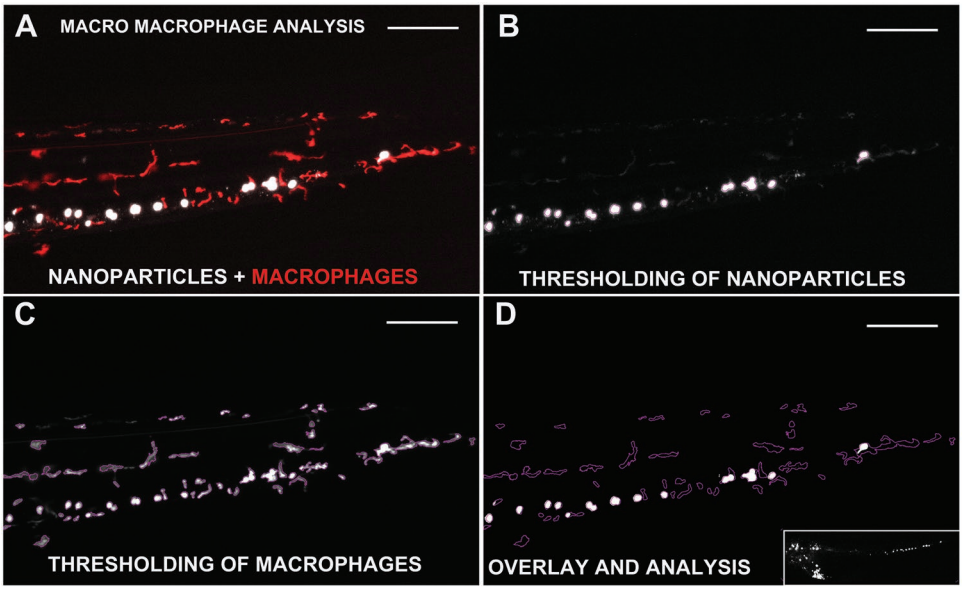

Figure 5. Macrophage uptake of NPs. Illustration of the steps undertaken by the MACRO for macrophage analysis to calculate the uptake of NPs. A) Zebrafish embryos injected with 623 nm liposomes without PEG (white) and fluorescent macrophages (red) are used for the analysis. B,C) NPs and macrophages are first thresholded, and D) their signals subsequently overlapped for analysis. The obtained values are normalized by the fluorescence of the whole zebrafish (panel (D), lower image).

3.3. Macrophage Uptake

The zebrafish embryo is an effective system to evaluate the uptake of NPs by macrophages (Figure 4A) which appear during development already by 24 h post fertilization;[25] for this evaluation it is essential to use a transgenic reporter line with fluorescent macrophages, here Tg(mpeg1:mcherry). The MACRO will first threshold the NP signal (**Figure 5**B), a necessary step in order to eliminate NPs that are still flowing from the evaluation, so that only the brightest NP accumulations are scored. The next step is the thresholding of the macrophages (Figure 5C), so that only the area occupied by these cells will be overlapped with that of the NPs (Figure 5D). Only the NPs found in macrophages are thereby scored for their fluorescence signals. As for all described analyses, this MACRO also evaluates the fluorescence signal of the whole fish and will save the measurements in two *.txt files.

Unlike for the circulation analysis, here the values are calculated as total rather than average fluorescence (RawIntDen rather than mean; see the "Experimental Section" for further details). For this, the macrophage uptake scoring is normalized relative to the overall zebrafish NP fluorescence. PEGylated liposomes of 100 and 580 nm, both poly(DMA-*b*-BzKetAc) NP and poly(Sar-*b*-pCys(SO_2Et)) NP, exhibit a very low uptake by macrophages (all with a score below 10), while non-PEGylated 623 nm liposomes and biotinylated liposomes 99 nm gave high values scoring over 20 and 30, respectively (**Figure 6**).

3.4. Endothelial Uptake of NPs

The use of the zebrafish line Tg(fli1a:EGFP) crossed with Tg(mpeg1:mcherry) allows for estimation of NPs uptake by endothelial cells (**Figure 7**A), a prominent characteristic of several NPs that we have tested in our zebrafish system. As for macrophage uptake, both NPs and macrophages have to be thresholded (Figure 7B,C), but in this case the signal derived from macrophage accumulations is removed (Figure 7D) and the remaining signal overlapped with that of the thresholded

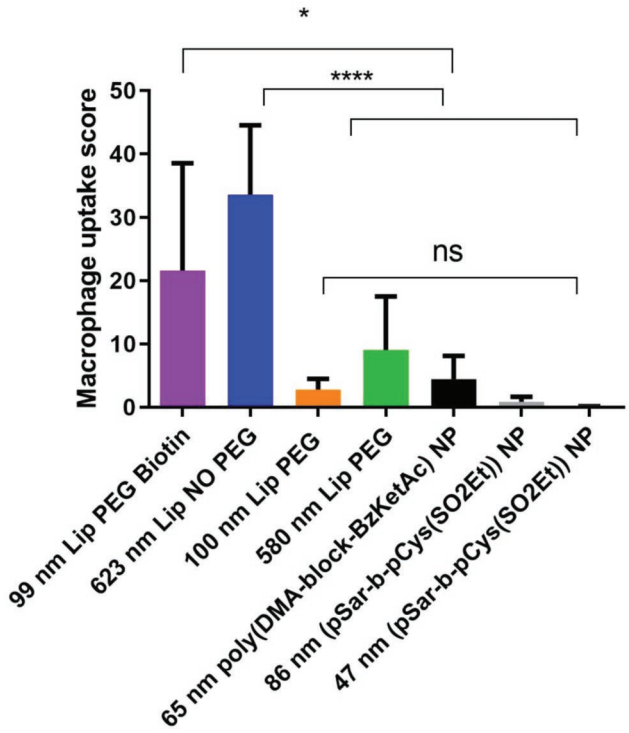

Figure 6. Quantification of NP uptake in the zebrafish by macrophages. The fluorescence scores of each NP are reported in arbitrary units. Statistics: one-way ANOVA with Tukey's multicomparison test: * = $P \leq 0.05$, **** = $P \leq 0.001$. Bars indicate standard deviation, $N \geq 6$.

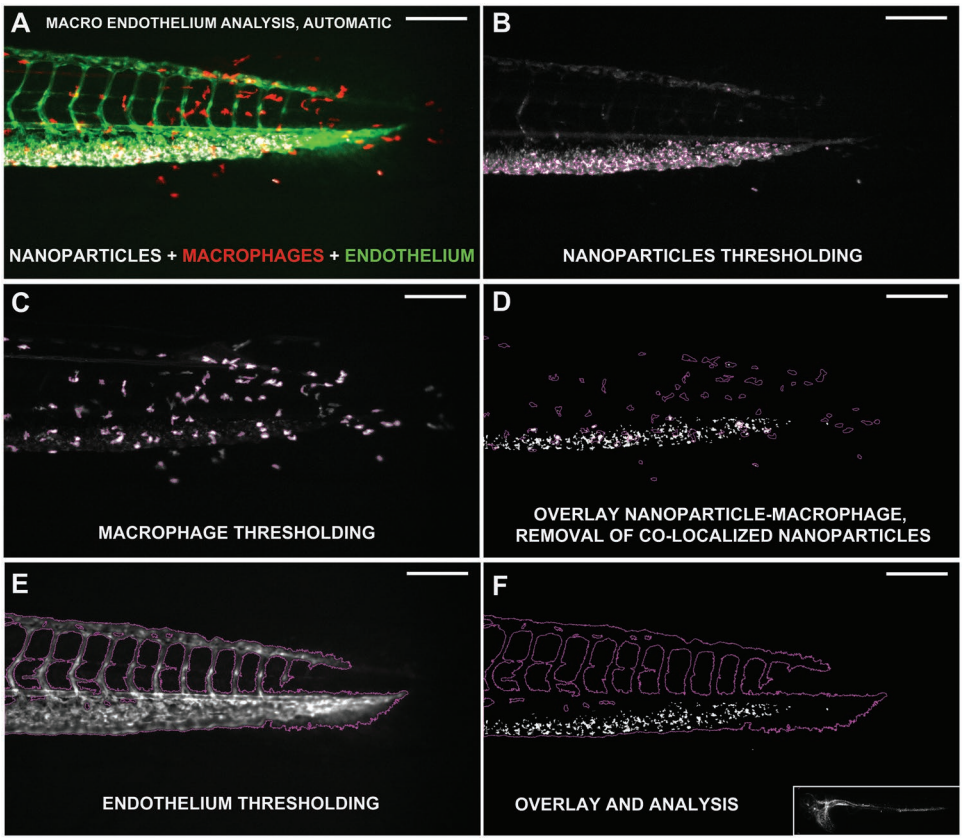

Figure 7. Endothelial uptake of NPs. Illustration of the steps undertaken by the endothelial analysis MACRO. A) Zebrafish embryos injected with 99 nm PEGylated liposomes with biotin (white) and fluorescent macrophages (red) as well as endothelium (green) are used for the analysis. B) NPs and C) macrophages are first thresholded. D) The NP signals in macrophages regions are deleted. Subsequently the signal of the endothelium is E) thresholded and F) overlapped to the residual NP measuring their fluorescence. The obtained values are normalized by the fluorescence of the whole zebrafish (panel (F), lower image).

endothelium in order to provide the final score (Figure 7E,F). As for macrophage uptake, the scored fluorescence intensity in the caudal vein has to be normalized relative to the whole fish total fluorescence signal; both these values are provided, for each zebrafish, in two *.txt files, one containing endothelial uptake score and the other the overall fluorescence signal.

Our results show that long circulating NPs such as PEGylated 100 nm liposomes, poly(DMA-*b*-BzKetAc) NPs, and both poly(Sar-*b*-pCys(SO_2Et)) NPs and for 623 nm non-PEGylated liposomes display a low value for endothelial cell uptake below 2. Biotinylated liposomes 99 and 580 nm liposomes instead exhibit large uptake values by endothelial cells which are significantly higher than the values of all other tested NPs (**Figure 8**) and above the value of 20.

4. Discussion

The vertebrate model zebrafish and the mouse model exhibit high genetic similarity with humans (70% of mouse and 82.2% of the zebrafish genes having a human orthologue)[26] while several important organs are also conserved in the fish, including the heart, brain, liver, kidney, pancreas, and intestine. Although the mouse remains the preclinical model of choice, in the field of nanomedicine, the zebrafish embryo possesses a number of advantages over the mouse model: 1) in the early development stages, the zebrafish is transparent, allowing precise imaging of the whole animal. 2) Several strains of this fish having fluorescent cell types are available so that their interactions with NPs can be easily studied. 3) The zebrafish maintenance costs are much lower than for mice with the estimate, from Boston University, of 1.05 $ for housing a single mouse while 0.25 $ for an entire tank (≈30 adults) of zebrafish.[27] 4) In addition, major differences are evident when it comes to the typical volumes of NPs that one needs to inject for experiments, allowing the researchers to save valuable material. Assuming the average weights of 1 mg for a zebrafish embryo and about 25 g for a mouse, 1 nL NP solution in zebrafish is equivalent to 25 µL in the mouse, a volume 25 000 higher. Despite these advantages, until now the use of the zebrafish has mostly been limited to the analysis of the toxic effects of NPs, especially on development.[28] An important limitation of the vast majority of these studies is that the NPs to be tested are administered only via the water bathing the fish which means the investigator has no control over the dose of NPs that access the vital organs. The only reliable method to overcome this is to microinject the NPs into the embryo, an operation which can be performed in different locations such as the yolk sac, the vasculature, intramuscular,

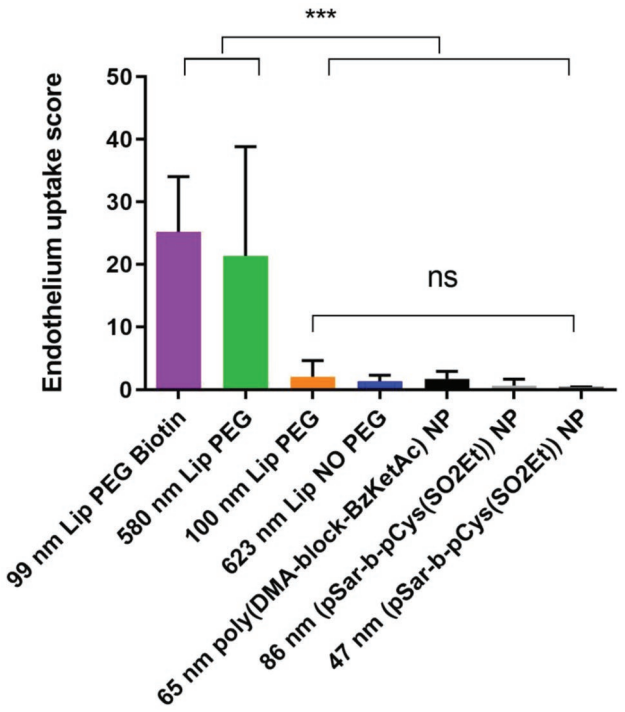

Figure 8. Quantification of NP uptake in the zebrafish by endothelial cells. The fluorescence scores of each NP are reported in arbitrary units. Statistics: one-way ANOVA with Tukey's multicomparison test: *** = $P \leq 0.005$. Bars indicate standard deviation, $N \geq 5$.

or into the hindbrain. In an earlier study, we have used vascular injection to analyze the toxicity of thioridazine, an antipsychotic drug whose promising therapeutic effects against *Mycobacterium tuberculosis* is hindered by its cardiotoxicity. We showed that although the free drug was highly toxic to fish embryos, the same drug concentration, encapsulated in poly(lactic-*co*-glycolic acid) (PLGA) NPs, resulted in no detectable toxicity, using multiple parameters.[29]

Over the past decade we have injected a significant number of different types of fluorescent NPs into zebrafish embryos and realized that for most NP types reproducible patterns of localization could be rapidly detected within a few hours after their injection. After intravenous injection, these patterns, at the extreme were, long or short circulation times and uptake or not by macrophages or vascular endothelial cells. Uptake by endothelial cells would be especially difficult to determine in mice. We were aware that if the zebrafish system is to become a standard model for screening NPs prior to their testing in preclinical mouse models, it would be essential to have available standardized methods for quantification of these different NP patterns. With this goal in mind, we introduce here a robust and simple methodology for reproducible quantification of these patterns for fluorescent NPs relative to their circulation times, and association with macrophages and endothelial cells. These parameters are of paramount importance when designing NPs for the treatment of different diseases. To our knowledge, the only method described in the literature to investigate NP circulation in zebrafish is the semiquantitative analysis proposed by Sieber et al.,[7] evaluating what they referred to as "circulation factor." That parameter is in fact not the actual NP circulation time but rather the ratio, limited to the caudal region, of NPs free flowing in the blood and the caudal vasculature area. In our method, however, we focused on the NP circulation by measuring the decrease of the average fluorescence in the caudal artery, a value which is then divided by the NP fluorescence in the whole zebrafish embryo. This last step of normalization, after transformation into percentages, allows us to obtain direct comparisons between different NPs and even when having different fluorescence intensity. Our method therefore provides an unbiased estimate of the NP circulation time.

With the method we introduced here, we analyzed NPs with a variety of sizes and materials. Our results clearly show that the behavior of NPs possessing a surface coating known to allow for long circulation times (in the range 1–3 days) in mammalian models, such as PEG, polysarcosine, polyDMA,[30–32] show the same behavior in the zebrafish. Importantly, a direct comparison of four selected NP formulations (100 and 580 nm PEGylated liposomes, 623 non-PEGylated liposomes, and 47 nm (pSar-*b*-pCys(SO_2Et)) NP) in the mouse and the zebrafish model revealed that the latter is able to predict with reasonable accuracy the pattern of circulation in mice. We believe that this animal model could be used in the future as an intermediate animal model, prior to the mouse, for testing different NPs having, for example, different surface chemistry. In the fish this could be done at a fraction of the cost in a shorter time.

We also quantified the uptake by macrophages in the zebrafish embryo and observed that NPs lacking surface coats such as PEG or polysarcosine and polyDMA, which are known to be rapidly removed from the circulation by macrophages[33] also exhibit the same behavior in zebrafish embryos; this was evident with our PLGA[4] or non-PEGylated liposomes in this study. Importantly, macrophage uptake, albeit greatly reduced for NPs containing PEG, polysarcosine and polyDMA, could still be observed in all tested NPs. The endothelial analysis also showed the importance of this cell type in determining the circulation of NPs. In particular, the presence of biotin in 100 nm PEGylated liposomes resulted in a high uptake by the endothelium, a behavior also observed in 580 nm PEGylated liposomes, a factor that could explain the reduced circulation times observed for these NPs when compared to plain 100 nm PEGylated liposomes. The mechanism that allows these NPs to be so efficiently taken up by the endothelial cells remains to be identified.

In this study, we did not address the uptake of NPs by neutrophils as; in our experience,[4,18] these cells play only a marginal role in the uptake of the NPs that we have tested after intravenous administration. However, in contrast to macrophages, neutrophils are known to be highly active in the uptake in surface-bound particles, such as bacteria following intramuscular injection of *Escherichia coli*.[34] Our MACRO could be easily customized to study this type of uptake since the zebrafish can be easily injected intramuscularly with NPs.

While our analysis was limited by uptake of NPs in macrophages and endothelial cells, the use of the method and MACRO that we have introduced here is by no mean restricted to these cells and could be easily adapted for analysis of any cell or tissue that can be labeled with a fluorescent protein. Of particular interest in the NP field would be the use of zebrafish

embryos with fluorescent liver,[35] kidney,[36] or heart.[37] Moreover, instead of injecting NPs, it would be possible to inject different types of bacteria and analyze their behavior in a vertebrate host based on quantification of their preferred cell or tissue niche. The generic method that we introduce here strengthens the importance of the zebrafish model as a screening tool for characterizing any type of fluorescent nanoparticles and thereby selecting a restricted number for the more time-consuming and expensive analysis in mammalian preclinical models.

5. Conclusion

The zebrafish embryo is rapidly becoming an important animal model for testing nanosized drug carriers and is capable of greatly reducing the number of formulations to be tested further in rodent animal models. Our study provides a robust instrument for unbiased and automated analysis of essential NP parameters during intravascular flow, thereby extending the advantages of the zebrafish embryo in NP research.

Acknowledgements

N.-J.K.D., A.K., and J.W. contributed equally to this work. The authors acknowledge the generous funding of the Kreftforeningen (Project No. 711091) and Norges Forskningsrådet (Project No. 275873 and Project No. 273319).

Conflict of Interest

The authors declare no conflict of interest.

Keywords

circulation time, macrophages, mice, nanoparticles, zebrafish

Received: December 2, 2019
Published online:

[1] S. Sieber, P. Grossen, J. Bussmann, F. Campbell, A. Kros, D. Witzigmann, J. Huwyler, *Adv. Drug Delivery Rev.* **2019**, *151–152*, 152.
[2] S. Isogai, M. Horiguchi, B. M. Weinstein, *Dev. Biol.* **2001**, *230*, 278.
[3] L. Evensen, P. L. Johansen, G. Koster, K. Zhu, L. Herfindal, M. Speth, F. Fenaroli, J. Hildahl, S. Bagherifam, C. Tulotta, L. Prasmickaite, G. M. Maelandsmo, E. Snaar-Jagalska, G. Griffiths, *Nanoscale* **2016**, *8*, 862.
[4] F. Fenaroli, D. Westmoreland, J. Benjaminsen, T. Kolstad, F. M. Skjeldal, A. H. Meijer, M. van der Vaart, L. Ulanova, N. Roos, B. Nystrom, J. Hildahl, G. Griffiths, *ACS Nano* **2014**, *8*, 7014.
[5] P. L. Johansen, F. Fenaroli, L. Evensen, G. Griffiths, G. Koster, *Nat. Commun.* **2016**, *7*, 10974.
[6] F. Campbell, F. L. Bos, S. Sieber, G. Arias-Alpizar, B. E. Koch, J. Huwyler, A. Kros, J. Bussmann, *ACS Nano* **2018**, *12*, 2138.
[7] S. Sieber, P. Grossen, P. Detampel, S. Siegfried, D. Witzigmann, J. Huwyler, *J. Controlled Release* **2017**, *264*, 180.
[8] E. Blanco, H. Shen, M. Ferrari, *Nat. Biotechnol.* **2015**, *33*, 941.
[9] H. Chang, J. Y. Yhee, G. H. Jang, D. G. You, J. H. Ryu, Y. Choi, J. H. Na, J. H. Park, K. H. Lee, K. Choi, K. Kim, I. C. Kwon, *J. Controlled Release* **2016**, *244*, 205.
[10] F. Fenaroli, U. Repnik, Y. Xu, K. Johann, S. Van Herck, P. Dey, F. M. Skjeldal, D. M. Frei, S. Bagherifam, A. Kocere, R. Haag, B. G. De Geest, M. Barz, D. G. Russell, G. Griffiths, *ACS Nano* **2018**, *12*, 8646.
[11] J. M. Brown, L. Recht, S. Strober, *Clin. Cancer Res.* **2017**, *23*, 3241.
[12] A. R. Poh, M. Ernst, *Front. Oncol.* **2018**, *8*, 49.
[13] L. Pang, J. Qin, L. Han, W. Zhao, J. Liang, Z. Xie, P. Yang, J. Wang, *Oncotarget* **2016**, *7*, 37081.
[14] S. K. Patel, J. M. Janjic, *Theranostics* **2015**, *5*, 150.
[15] P. Zhao, W. Yin, A. Wu, Y. Tang, J. Wang, Z. Pan, T. Lin, M. Zhang, B. Chen, Y. Duan, Y. Huang, *Adv. Funct. Mater.* **2017**, *27*, 1700403.
[16] N. Abed, P. Couvreur, *Int. J. Antimicrob. Agents* **2014**, *43*, 485.
[17] G. Griffiths, B. Nystrom, S. B. Sable, G. K. Khuller, *Nat. Rev. Microbiol.* **2010**, *8*, 827.
[18] L. S. Ulanova, M. Pinheiro, C. Vibe, C. Nunes, D. Misaghian, S. Wilson, K. Zhu, F. Fenaroli, H. C. Winther-Larsen, S. Reis, G. Griffiths, *Dis. Aquat. Org.* **2017**, *125*, 19.
[19] L. Rizzello, J. D. Robertson, P. M. Elks, A. Poma, N. Daneshpour, T. K. Prajsnar, D. Evangelopoulos, J. O. Canseco, S. Yona, H. M. Marriott, D. H. Dockrell, S. J. Foster, B. De Geest, S. De Koker, T. McHugh, S. A. Renshaw, G. Battaglia, *bioRxiv* **2017**, https://doi.org/10.1101/119297.
[20] R. J. Mudakavi, S. Vanamali, D. Chakravortty, A. M. Raichur, *RSC Adv.* **2017**, *7*, 7022.
[21] R. Atanasiu, A. Radu, *Int. J. Pharm.* **1993**, *90*, 119.
[22] Z. Dong, J. Guo, X. Xing, X. Zhang, Y. Du, Q. Lu, *Biomed. Pharmacother.* **2017**, *89*, 297.
[23] J. R. McCarthy, P. Patel, I. Botnaru, P. Haghayeghi, R. Weissleder, F. A. Jaffer, *Bioconjugate Chem.* **2009**, *20*, 1251.
[24] K. Klinker, O. Schäfer, D. Huesmann, T. Bauer, L. Capelôa, L. Braun, N. Stergiou, M. Schinnerer, A. Dirisala, K. Miyata, K. Osada, H. Cabral, K. Kataoka, M. Barz, *Angew. Chem., Int. Ed.* **2017**, *56*, 9608.
[25] P. Herbomel, B. Thisse, C. Thisse, *Development* **1999**, *126*, 3735.
[26] K. Howe, M. D. Clark, C. F. Torroja, J. Torrance, C. Berthelot, M. Muffato, J. E. Collins, S. Humphray, K. McLaren, L. Matthews, S. McLaren, I. Sealy, M. Caccamo, C. Churcher, C. Scott, J. C. Barrett, R. Koch, G. J. Rauch, S. White, W. Chow, B. Kilian, L. T. Quintais, J. A. Guerra-Assuncao, Y. Zhou, Y. Gu, J. Yen, J. H. Vogel, T. Eyre, S. Redmond, R. Banerjee, J. Chi, B. Fu, E. Langley, S. F. Maguire, G. K. Laird, D. Lloyd, E. Kenyon, S. Donaldson, H. Sehra, J. Almeida-King, J. Loveland, S. Trevanion, M. Jones, M. Quail, D. Willey, A. Hunt, J. Burton, S. Sims, K. McLay, B. Plumb, J. Davis, C. Clee, K. Oliver, R. Clark, C. Riddle, D. Elliot, G. Threadgold, G. Harden, D. Ware, S. Begum, B. Mortimore, G. Kerry, P. Heath, B. Phillimore, A. Tracey, N. Corby, M. Dunn, C. Johnson, J. Wood, S. Clark, S. Pelan, G. Griffiths, M. Smith, R. Glithero, P. Howden, N. Barker, C. Lloyd, C. Stevens, J. Harley, K. Holt, G. Panagiotidis, J. Lovell, H. Beasley, C. Henderson, D. Gordon, K. Auger, D. Wright, J. Collins, C. Raisen, L. Dyer, K. Leung, L. Robertson, K. Ambridge, D. Leongamornlert, S. McGuire, R. Gilderthorp, C. Griffiths, D. Manthravadi, S. Nichol, G. Barker, S. Whitehead, M. Kay, J. Brown, C. Murnane, E. Gray, M. Humphries, N. Sycamore, D. Barker, D. Saunders, J. Wallis, A. Babbage, S. Hammond, M. Mashreghi-Mohammadi, L. Barr, S. Martin, P. Wray, A. Ellington, N. Matthews, M. Ellwood, R. Woodmansey, G. Clark, J. Cooper, A. Tromans, D. Grafham, C. Skuce, R. Pandian, R. Andrews, E. Harrison, A. Kimberley, J. Garnett, N. Fosker, R. Hall, P. Garner, D. Kelly, C. Bird, S. Palmer, I. Gehring, A. Berger, C. M. Dooley, Z. Ersan-Urun, C. Eser, H. Geiger, M. Geisler, L. Karotki, A. Kirn, J. Konantz, M. Konantz, M. Oberlander, S. Rudolph-Geiger,

M. Teucke, C. Lanz, G. Raddatz, K. Osoegawa, B. Zhu, A. Rapp, S. Widaa, C. Langford, F. Yang, S. C. Schuster, N. P. Carter, J. Harrow, Z. Ning, J. Herrero, S. M. Searle, A. Enright, R. Geisler, R. H. Plasterk, C. Lee, M. Westerfield, P. J. de Jong, L. I. Zon, J. H. Postlethwait, C. Nusslein-Volhard, T. J. Hubbard, H. Roest Crollius, J. Rogers, D. L. Stemple, *Nature* **2013**, *496*, 498.

[27] A. Weintraub, *Lab. Anim.* **2017**, *46*, 323.

[28] E. Haque, A. C. Ward, *Nanomaterials* **2018**, *8*, 561.

[29] C. B. Vibe, F. Fenaroli, D. Pires, S. R. Wilson, V. Bogoeva, R. Kalluru, M. Speth, E. Anes, G. Griffiths, J. Hildahl, *Nanotoxicology* **2016**, *10*, 680.

[30] V. D. Awasthi, D. Garcia, B. A. Goins, W. T. Phillips, *Int. J. Pharm.* **2003**, *253*, 121.

[31] T. Ishihara, T. Maeda, H. Sakamoto, N. Takasaki, M. Shigyo, T. Ishida, H. Kiwada, Y. Mizushima, T. Mizushima, *Biomacromolecules* **2010**, *11*, 2700.

[32] A. Makino, E. Hara, I. Hara, R. Yamahara, K. Kurihara, E. Ozeki, F. Yamamoto, S. Kimura, *J. Controlled Release* **2012**, *161*, 821.

[33] V. P. Torchilin, V. S. Trubetskoy, K. R. Whiteman, P. Caliceti, P. Ferruti, F. M. Veronese, *J. Pharm. Sci.* **1995**, *84*, 1049.

[34] E. Colucci-Guyon, J. Y. Tinevez, S. A. Renshaw, P. Herbomel, *J. Cell Sci.* **2011**, *124*, 3053.

[35] G. M. Her, Y.-H. Yeh, J.-L. Wu, *Dev. Dyn.* **2003**, *227*, 347.

[36] B. Perner, C. Englert, F. Bollig, *Dev. Biol.* **2007**, *309*, 87.

[37] E. de Pater, L. Clijsters, S. R. Marques, Y. F. Lin, Z. V. Garavito-Aguilar, D. Yelon, J. Bakkers, *Development* **2009**, *136*, 1633.

PAPER II

Journal of Controlled Release 331 (2021) 228–245

Contents lists available at ScienceDirect

Journal of Controlled Release

journal homepage: www.elsevier.com/locate/jconrel

Biodistribution of surfactant-free poly(lactic-acid) nanoparticles and uptake by endothelial cells and phagocytes in zebrafish: Evidence for endothelium to macrophage transfer.

Julien Rességuier [a,b,*], Jean-Pierre Levraud [c,1], Nils K. Dal [b,1], Federico Fenaroli [b], Charlotte Primard [d], Jens Wohlmann [b], Gabrielle Carron [a], Gareth W. Griffiths [b], Dominique Le Guellec [a], Bernard Verrier [a]

[a] CNRS, University Lyon 1, UMR 5305, Laboratory of Tissue Biology and Therapeutic Engineering, IBCP, 7 Passage du Vercors, 69367 Lyon Cedex 07, France
[b] Department of Biosciences, University of Oslo, Blindernveien 31, 0371 Oslo, Norway
[c] Macrophages et Développement de l'Immunité, Institut Pasteur, CNRS UMR3738, 75015 Paris, France
[d] Adjuvatis, 7 Passage du Vercors, 69007 Lyon, France

ARTICLE INFO

Keywords:
Surfactant-free
Biodistribution
Nanoparticles
Zebrafish
Uptake-degradation kinetics
Endothelial cell to macrophage transfer

ABSTRACT

In the development of therapeutic nanoparticles (NP), there is a large gap between *in vitro* testing and *in vivo* experimentation. Despite its prominence as a model, the mouse shows severe limitations for imaging NP and the cells with which they interact. Recently, the transparent zebrafish larva, which is well suited for high-resolution live-imaging, has emerged as a powerful alternative model to investigate the *in vivo* behavior of NP. Poly(D,L lactic acid) (PLA) is widely accepted as a safe polymer to prepare therapeutic NP. However, to prevent aggregation, many NP require surfactants, which may have undesirable biological effects. Here, we evaluate 'safe-by-design', surfactant-free PLA-NP that were injected intravenously into zebrafish larvae. Interaction of fluorescent NPs with different cell types labelled in reporter animals could be followed in real-time at high resolution; furthermore, by encapsulating colloidal gold into the matrix of PLA-NP we could follow their fate in more detail by electron microscopy, from uptake to degradation. The rapid clearance of fluorescent PLA-NP from the circulation coincided with internalization by endothelial cells lining the whole vasculature and macrophages. After 30 min, when no NP remained in circulation, we observed that macrophages continued to internalize significant amounts of NP. More detailed video-imaging revealed a new mechanism of NP transfer where NP are transmitted along with parts of the cytoplasm from endothelial cells to macrophages.

1. Introduction

Since their introduction in the 1960s', a wide variety of nanoparticles (NP) have been developed, although only a few of them have been clinically approved [1]. It can be argued that a major factor contributing to this situation has been the large gap that has formed between *in vitro* testing and *in vivo* experimentation during the development of NP. Accordingly, the common strategy is to test NP at the level of cell culture and to select the most promising formulations for their behavior in an appropriate mouse model, in which the NP can at best be seen only at low resolution, unless one uses invasive methods. This jump from cells to mouse hinders our understanding of the biological interactions of NP, especially at the tissue and cellular level, which would provide helpful hindsight to optimize the design of NP and their use for therapeutic applications.

The success of NP also depends on the choice of scaffold material used to assemble the NP, most commonly polymer-based ones. Widely used polymers are part of the aliphatic family, including Poly Lactic-*co*-Glycolic Acid (PLGA) and Poly Lactic Acid, both materials that are FDA-approved for clinical use. However, in most cases the assembly of non-aggregated NP requires the use of a surfactant, such as Polyvinylpyrrolidone (PVP) or Polyvinyl alcohol (PVA), to reduce the surface tension of the NP and to stabilize them [2]. These surfactants may have undesirable side-effects [3–6] and our group has put significant effort in

* Corresponding author at: CNRS, University of Lyon 1 - UMR5305 / University of Oslo, Department of Biosciences, Norway.
E-mail address: julien.resseguier@ibv.uio.no (J. Rességuier).
[1] Both authors equally contributed to the research article.

https://doi.org/10.1016/j.jconrel.2021.01.006
Received 19 June 2020; Received in revised form 16 November 2020; Accepted 4 January 2021
Available online 11 January 2021

preparing safe-by-design PLA-NP without surfactants and with levels of residual solvent that are in agreement with the European pharmacopeia for human use [7,8]; this idea also fits well with general recommendations to simplify the procedures for making NP [9,10]. Both vaccine [11] and mRNA-vectorization [12] applications have been successfully made and characterized with such PLA-NP. However, like other safe-by-design or surfactant-free NP system, their biological interactions and fate after administration remain poorly understood.

The zebrafish larva is a vertebrate model with the great advantage of being highly transparent, thereby allowing researchers to analyze the biodistribution of NPs at high resolution in real time and in a non-invasive manner [13,14]. Moreover, genetically modified fish are available that selectively express different colored fluorescent proteins in specific cell types. Altogether, the zebrafish model emerges as a reliable intermediary model to bridge *in vitro* experimentation and *in vivo* experimentation in higher vertebrate. In a previous study, we have exploited this powerful system to analyze the uptake of PLA-NP by mucosal surfaces [15]. In this work, we monitored the uptake and fate of safe-by-design, surfactant-free PLA-NPs after intravenous injection. PLA-NPs were cleared from the blood in less than 30 min, and took several days to disassemble. We identify endothelial cells and macrophages as the two cell populations that internalize PLA-NPs, and describe the unexpected transfer of PLA-NPs, along with some cytoplasmic material, from vascular endothelial cells to macrophages.

2. Results

2.1. Characterization of safe-by-design fluorescent PLA-NP

Following a safe-by design strategy to produce nanocarriers as simply as possible, but having high biocompatibility, Poly(D,L lactic acid) particles, were prepared by nanoprecipitation without the addition of surfactant or stabilizer. During this process, the small length of the PLA (<50,000 g/mol) chains enables enough negatively charged carboxyl groups to be exposed at the surface of the PLA-NP, ensuring colloidal stabilization [16]. Importantly, residual solvents (water and acetone) were gently evaporated until their minimal concentration respected the standards established by the European pharmacopeia for human use, as assessed by gas chromatography quantification (data not shown). The visualization of PLA-NP formulations was made possible by the encapsulation of different hydrophobic fluorophores into the polymeric matrix. As measured by dynamic light scattering (DLS), we obtained highly homogeneous (Polydispersity index < 0.05) suspensions of red, green and far-red fluorescent PLA-NP which displayed *Z*-average of 174 nm ± 7 nm (mean(SD)), and strong anionic zeta potentials around −55 mV (Table 1). Throughout our experiments, we injected 3–5 nL of PLA-NP at 5 mg/mL in 3 day post-fertilization (dpf) zebrafish larvae. Since a larva weighs ~ 0.4 mg, this translates to approximatively 50 mg/kg. At this high dose, neither development nor health of injected larvae were visibly impaired by the injection of our fluorescent PLA-NP, reflecting their great biocompatibility.

2.2. Internalization of PLA-NP by endothelial cells from the whole vasculature

Despite their promising potential for nanomedicine, very few studies have been conducted to characterize the fate of surfactant-free NP *in vivo*. Following standard protocols [13,17], fluorescent PLA-NP (5 mg/mL) were intravenously injected into 3 dpf zebrafish, through either the post-cardinal vein or the inferior segment of the caudal vein plexus (Fig. S1). Our initial investigation of the PLA-NP biodistribution was performed by live-imaging, using an epi-fluorescent stereomicroscope, on transgenic fli1a:GFP fish [18], where endothelial cells express a green fluorescent protein in their cytoplasm. Note that in this transgenic line, neural crest cells and some macrophage progenitors can also express GFP.

Two hours following intravenous injection, red fluorescent PLA-NP were observed along the whole vasculature, from the tail region to the heart, brain and ocular vessels (Fig. 1: A). Furthermore, the fluorescence from PLA-NP seemed in close association with the fluorescence of endothelial cells, suggesting possible interactions with these cells (Fig. 1: A'-A"– Yellow arrowheads). To better visualize these potential interactions, we performed high-resolution 3D live-imaging using a high-speed spinning-disk confocal microscope, which minimizes phototoxicity. We observed extensive internalization of PLA-NP by the endothelial cells. Massive clusters of fluorescence from PLA-NP were especially found in those endothelial cells forming the caudal vein plexus (Fig. 1: B-B″). In addition, less striking uptake was seen into the endothelial cells lining the caudal artery and intersegmental vessels (Fig. 1: C).

Analysis of the optical sections revealed that PLA-NP internalized by endothelial cells were contained within large intracellular compartments devoid of GFP and not within the GFP labelled cytosol (Fig. 1: B″ - lower blue panel). In addition, the fluorescence from free-circulating PLA-NP could not be detected within the bloodstream, nor at the plasma membrane surface of endothelial cells. However, large accumulations of PLA-NP were also detected in presumed phagocytes residing in the lumen of blood vessels. Intriguingly, it appeared that some of these phagocytes internalized both PLA-NP and GFP-labelled material (Fig. 1: B″ - upper white panel). A 3D reconstruction of the acquired image is presented in (Video S1).

Experiments in zebrafish embryos have shown essentially exclusive binding and internalization of different anionic NP to scavenger-endothelial cell in restricted venous sites, namely the caudal vein plexus and the dorsal aspect of the post-cardinal vein [19–22]. This uptake process was shown to be dependent on the scavenger receptor Stab2. In contrast, cationic NP were internalized by endothelial cells throughout the vasculature, independently of Stab2. In agreement with the above studies our anionic PLA-NP were massively internalized by endothelial cells that form the caudal vein plexus. Surprisingly however, our NP were also taken up by venous and arterial endothelial cells lining the entire system. Examples of localizations in the dorsal aorta, intersegmental vessels and both dorsal and ventral aspects of the post-cardinal vein are evident in (Fig. 1: C); uptake into the dorsal

Table 1
Fluorescent NP characteristics.

Name	Fluorophore / PHR*	Diameter	PdI	Zeta potential	Fish survival at 24 h post injection
PLA-BODIPY TR	Bodipy TR methyl ester / 0.02 %	182 nm	0.019	-52.8 mV	100 %
PLA-BODIPY FL	Bodipy 500-510 $_{C4,C9}$ / 0.04 %	171 nm	0.024	-57.1 mV	100 %
PLA-DY650	DY650-decylamide / 0.10 %	170 nm	0.018	-56.9 mV	100 %

* parts per hundred of resin

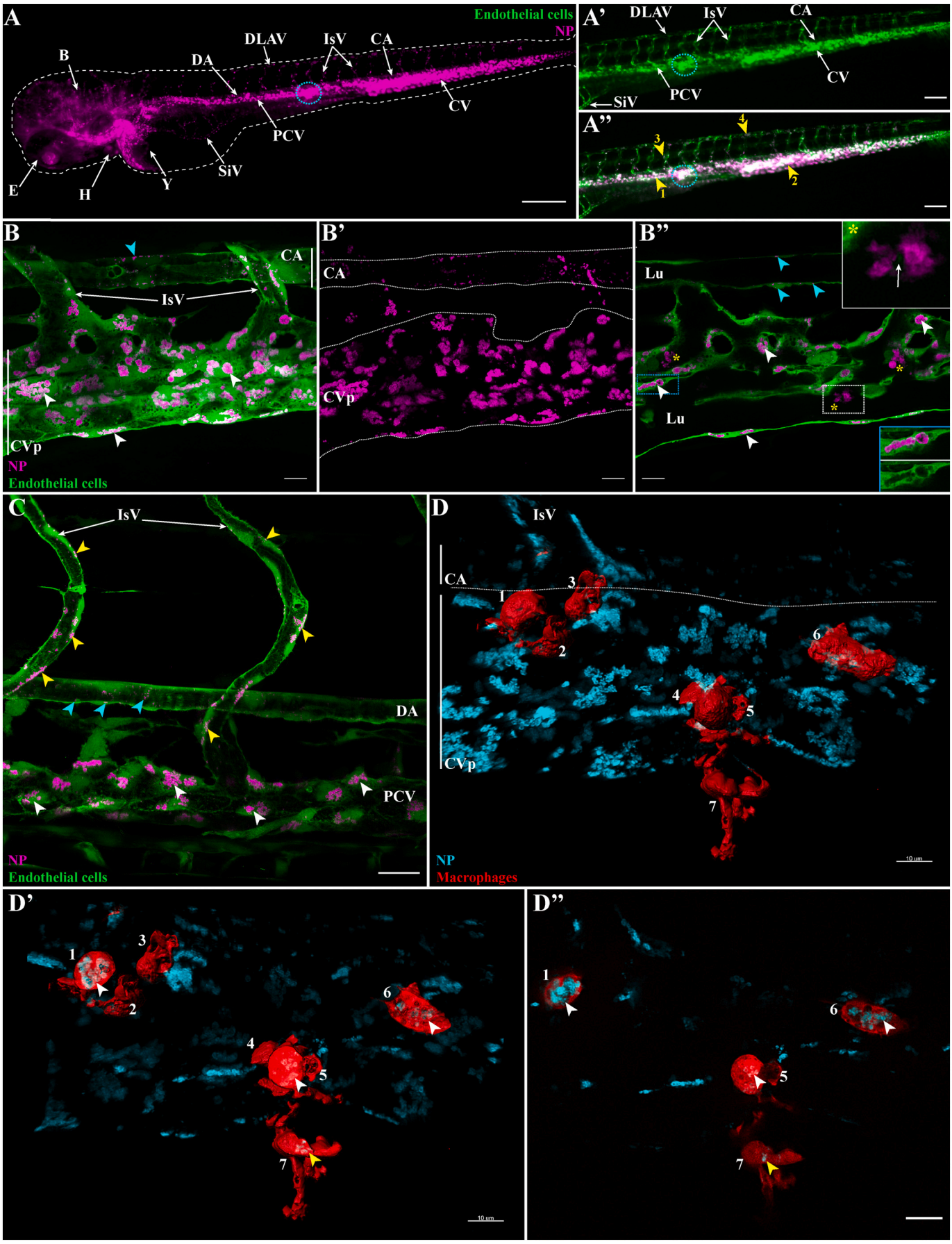

(caption on next page)

Fig. 1. Internalization of PLA-NP by endothelial cells and macrophages. Representative live-acquisitions of 3 dpf zebrafish, 2 h after intravenous administration of PLA-NP, using a stereomicroscope (A-A") or a spinning-disk confocal microscope (B-D"). (A-A") Fluorescent PLA-NP (magenta) appear closely associated (yellow arrows) with the whole vasculature of fli:GFP^{+} fish (green). Injection sites are usually at the post-cardinal veins (blue circle) or within the inferior region of the caudal vein. As illustrated by the maximum intensity projection (MIP), which displays both PLA-NP and endothelial cells (B) and PLA-NP only (B′), strong accumulations of PLA-NP are observed within the endothelial cells of the caudal vein plexus (white arrowheads). PLA-NP are also taken-up by the endothelial cells of the caudal artery (cyan arrowheads). (B″) As revealed by optical sections (B), among both the caudal vein plexus and the caudal artery (white and cyan arrowheads, respectively), PLA-NP within endothelial cells are stored inside GFP negative cellular compartments. This localization is even more striking when the fluorescence signal from PLA-NP is removed (blue panel). Cluster of PLA-NP could be observed among luminal phagocytes (yellow stars). Co-internalization of GFP and PLA-NP within some luminal phagocytes has also been noticed (white arrow within white panel). (C) PLA-NP internalization is not restricted to the caudal vein plexus or the dorsal aspect of the post-cardinal vein. Endothelial cells from the whole post-cardinal vein (white arrowhead), the intersegmental vessels (yellow arrowhead) and the dorsal aorta (cyan arrowhead) are PLA-NP-positive, illustrating the pan-vascular internalization of PLA-NP. (D) From a mpeg1:mCherry zebrafish, MIP illustrating the presence of 7 macrophages (3D surface - red) close to PLA-NP (cyan) within the caudal vein plexus area. Both opening of the stack with a clipping plane (D') and the optic sections (D") reveal internalizations of PLA-NP by macrophage from the lumen (white arrowheads – 1, 5, 6) and outside the lumen (yellow arrowhead - 7). (B-B′) 17 μm MIP (x60 objective) from which (B″) is a 1 μm thick optical section. (C) 50 μm MIP (x60 objective). (D) 13 μm MIP (x60 objective) with a 3D surface reconstruction of the macrophage fluorescence signal. (D') illustrates an opening the MIP with a clipping plane, while (D") is a 1 μm thick optic section from the stack. Annotations: B, brain; CA, caudal artery; CVp, caudal vein plexus; DA, dorsal aorta; DLAV, dorsal longitudinal anastomotic vessel; E, eye; H, heart; IsV, intersegmental vessel; Lu, lumen; PCV, post-cardinal vein; SiV, sub-intestinal veins; Y, yolk. Scale bars: 200 μm (A), 100 μm (A'-A"), 20 μm (C) and 10 μm (B-B″, D-D"). (For interpretation of the references to colour in this figure legend, the reader is referred to the web version of this article.)

longitudinal anastomotic vessels and the sub-intestinal vein are shown in (Fig. S2) and into the cerebral blood vessels and liver sinusoids (Fig. S3). We also localized PLA-NP inside endothelial cells forming the endocardium of the atrium and the ventricle of the heart (not shown).

2.3. Internalization of PLA-NP by professional phagocytes

In order to identify the cells that were accumulating PLA-NP inside the bloodstream at the caudal vein plexus, we focused on the phagocytes already present in the zebrafish embryo at 3 days post-fertilization: macrophages and neutrophils. Therefore, we first injected green fluorescent PLA-NP (5 mg/mL) into mpeg1:mCherry transgenic zebrafish [23], whose macrophages express a red fluorescent cytosolic protein. Two hours later, 3D live-imaging acquisitions at the caudal vein plexus, a region where macrophages are abundant, clearly showed the internalization of PLA-NP by macrophages residing within the lumen (macrophages #1–2–3-5-6) and outside the blood vessel (#7). In addition, macrophages devoid of PLA-NP could also be observed (#4) (Figure: D-D"). A 3D reconstruction of the acquired image is presented in (Video S2). By contrast, neutrophils, labelled in mpx:GFP zebrafish [24], showed no detectable interaction with red fluorescent PLA-NP, even when the particles were injected at higher concentration (10 mg/mL) (Video S3).

2.4. Dynamic of PLA-NP biodistribution from 30 min to 24 h by light microscopy

The biodistribution of NP at a given time is crucial information to understand how the particles interact with the organism and allow one to better design the therapeutic strategy. The above observations showed that PLA-NP could enter endothelial cells and macrophages in significant amounts. We next investigated the kinetics of this uptake process by regular observations (30 min, 4 h and 24 h) following injection of fluorescent PLA-NP in 3 dpf zebrafish (either fli:GFP or mpeg1:mCherry). We then focused on the co-localization of PLA-NP with respect to selectively labelled endothelial cells and macrophages.

Although we monitored live embryos, here we favored the use of cryosections over live-imaging to analyze samples at precise time points and visualize the internal organs in more detail. The cryosections were prepared with a thickness of 30 μm and imaged in the center to avoid the risk of the artefactual displacement of NP, which from our experience is inherent to thinner cryosections (< 20 μm) [15].

The high-resolution imaging of the cryosections confirmed that, once in the circulatory system, fluorescent PLA-NP were promptly taken up by endothelial cells. After 30 min following the administration (Fig. 2: A-A'), while no fluorescence from PLA-NP could be detected inside the bloodstream, strong accumulations of PLA-NP were present inside endothelial cells. These accumulations showed a scattered distribution inside the endothelial cells. At later time-points, 4 h and 24 h post-injection, the association of PLA-NP with endothelial cells was still observed, increasingly, the accumulation of NPs formed massive clusters adjacent to the nucleus (Fig. 2: B-C′), presumably in endocytic organelles [25].

Like the endothelial cells, macrophages were quick to internalize fluorescent PLA-NP, as seen 30 min following the intravenous injections (Fig. 2: D). No striking changes in the localization pattern inside macrophages could be detected at later time-points (Fig. 2: *E*-F). Intriguingly, although based on qualitative observations, we noticed that the fluorescence signal from the PLA-NP seemed more intense in some macrophages at the 24 h time-point. In addition, during our observation on fli:GFP fish, we could observe phagocytes with high concentrations of PLA-NP outside the bloodstream at the 24 h time-point (Fig. 2: C, C′, star).

Finally, by investigating the whole fish, we could evaluate the capacity of PLA-NP to reach certain internal organs: the brain, the kidney and the liver. In the brain, aside from the internalization of PLA-NP by the endothelial cells that form the cerebral blood vessels, no leakage to the parenchyma could be observed at any time-point (Fig. S3: A-C). At this stage, the blood-brain barrier is functional [26]. We could however observe bright accumulations of PLA-NP in a few cells outside the vascular compartment at 24 h post-injection. These cells were later identified as brain macrophages, *e.g.* microglia (Fig. S3: D). The kidney, where glomerular filtration is operational in 3 dpf zebrafish [27], is responsible of the excretion of small material (< 8 nm of hydrodynamic diameter) [28], We could not detect any sign of fluorescence associated to PLA-NP inside the pronephric ducts of the kidney at any time-points. In contrast to mammals, the liver of teleosts plays little role in the reticulo-endothelial system [29]. Still, PLA-NP were internalized by endothelial cells from the sinusoidal vessel, as well as by rare hepatocytes at latest time-point (Fig. S3: *E*-G).

2.5. Dynamic of PLA-NP biodistribution from 10 min to 7 days by electron microscopy

One of the limitations of light microscopy is that its resolution usually does not allow the direct observation of individual NP of 200 nm or below. Therefore, we complemented our observations from light microscopy with the use of transmission electron microscopy to study the biodistribution of PLA-NP at the sub-cellular level. There, we widened the time-span of the experiments (from 10 min to 7 days) to both witness the internalization of PLA-NP and evaluate their integrity over time. Because the poly(lactic-acid) polymer is non-dense to the electrons, in order to facilitate the identification of PLA-NP on electron micrographs, 6–7 nm electron-dense hydrophobic colloidal gold particles were

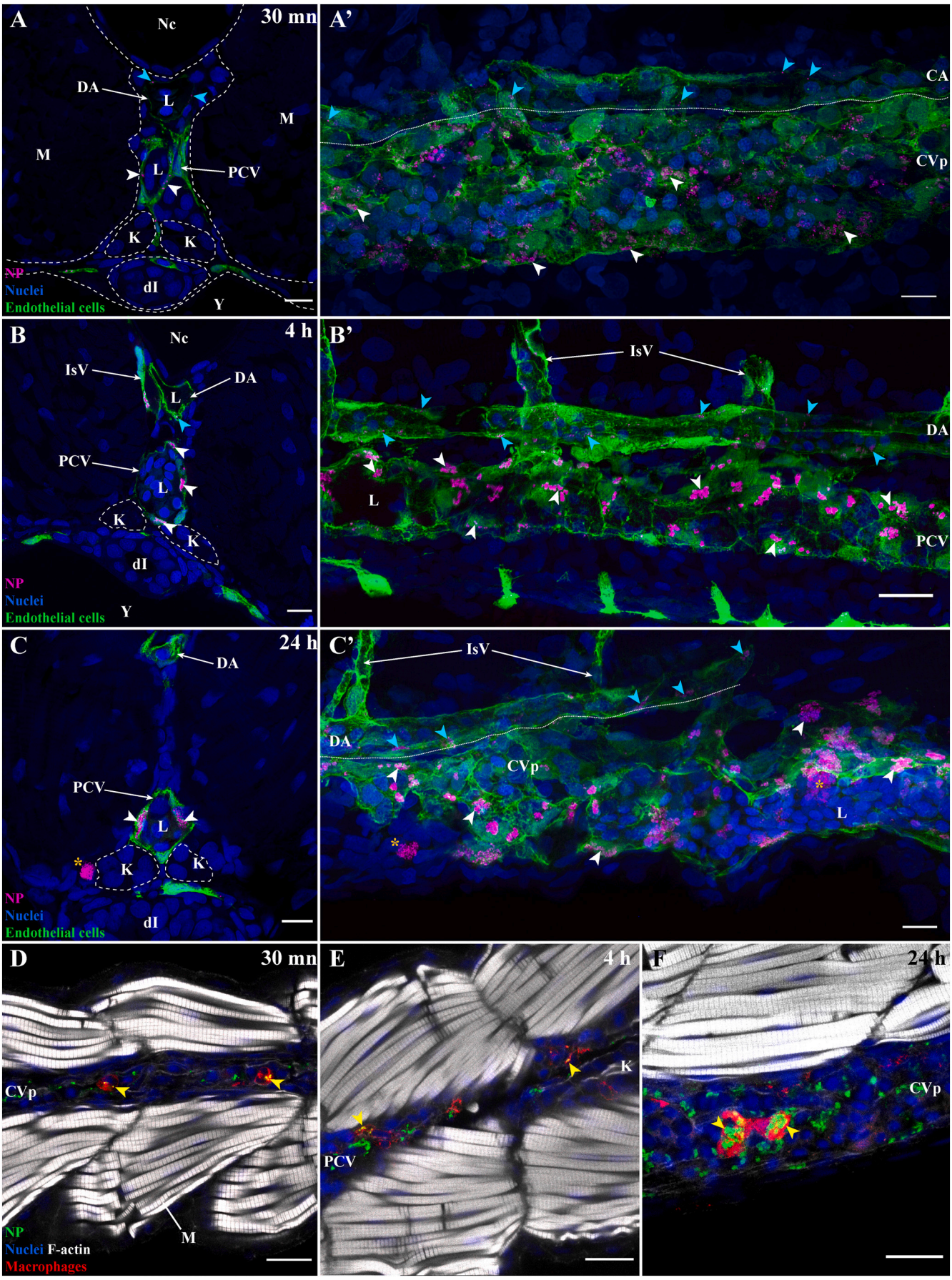

(caption on next page)

Fig. 2. Dynamics of PLA-NP internalization by endothelial cells and macrophages at 30 min, 4 h and 24 h post-injection. Representative images of 3 dpf fli:GFP zebrafish transversally sectioned (A, B, C), para-sagitally sectioned (A',B′,C′) and of 3 dpf mpeg1:mCherry zebrafish para-coronally sectioned (D-F). Images were acquired from 30 μm thick whole-organism cryosections. Images (A-C′) highlight PLA-NP (magenta), endothelial cells (green) and nuclei (blue), while images (D-F) highlight PLA-NP (green), macrophages (red), F-actin (white) and nuclei (blue). (A,A') The internalization of NP by endothelial cells from both veins (white arrowheads) and artery (cyan arrowheads) was already evident 30 min post-administration while no free-circulating PLA-NP could be observed within the blood flow. From this timepoint, no further change in the distribution of PLA-NP among endothelial cells from vein (white arrowheads) and artery (cyan arrowheads) could be detected 4 h (B-B′) and 24 h (C-C′) later, apart from the aggregation of the PLA-NP overtime (A',B′,C′). Note the presence of large aggregates of PLA-NP within phagocytes outside the lumen at the 24 h timepoint (C-C′ – orange stars). Similar observations apply to the internalization of PLA-NP by macrophages with uptake (yellow arrowheads) observed 30 min (D), 4 h (E) and 24 h (F) post-administration. While only qualitative, observations of PLA-NP accumulation among macrophages suggested they were larger at 24 h (F) than at 30 min (D) post-administration. (A,B,C) 1 μm MIP (x60 objective). (A') 20 μm MIP (x60 objective). (B′) 13 μm MIP (x60 objective). (C′) 22 μm MIP (x60 objective). (D,E,F) single optical sections (x60 objectives). Annotations: CA, caudal artery; CVp, caudal vein plexus, DA, dorsal aorta; dI, developing intestines; K, kidney; L, IsV, intersegmental vessel, lumen; M, muscles, Nc, notochord; PCV, post-cardinal vein; Y, yolk. Scale bars: 20 μm (A',B′,*E*-F) and 10 μm (A,B,C-D). (For interpretation of the references to colour in this figure legend, the reader is referred to the web version of this article.)

encapsulated into the PLA-NP. PLA-NP(gold) then appeared as pale spheroids with internal electron dense particles under the electron-beam (Fig. S4).

Within 10 min after the injection, single non-aggregated PLA-NP were still circulating inside the bloodstream while others were already internalized by endothelial cells (Fig. 3: A). We could witness all the steps of PLA-NP internalization from their association to the plasma membrane to their accumulation into the intracellular *endo*-membrane system. While the precise internalization pathways in the cells remain to be characterized, some associations of individual PLA-NP with coated invaginations of the plasma membrane of endothelial cells were highly suggestive of a clathrin-mediated internalization (Fig. 3: B). In addition, figures resembling phagocytosis were also observed (Fig. 3: C). Once internalized, the PLA-NP loaded cellular compartment appeared to fuse into larger cellular structure containing numerous particles (Fig. 3: D). In contrast to the highly dynamic behavior of PLA-NP observed 10 min following the injection, 20 min later PLA-NP were heavily concentrated inside cellular compartments of endothelial cells while none remained inside the blood vessel (Fig. 3: E). The biodistribution of PLA-NP remained largely unchanged at the 4 h and 24 h time-points (Fig. 3: F-G). These results confirm and extend the observations we made from light microscopy, and reveal that the bright fluorescence clusters we observed represent in fact a strong accretion of PLA-NP that occurred after internalization in cells.

Whether internalized by endothelial cells or by phagocytes, the integrity and the colloidal stability of PLA-NP endured the first 24 h post-injection (Fig. 3: F-G). It was only after 3 days following the injection that change in the morphology of PLA-NP could be seen. Among some endothelial cells, gold particles were seen apparently being released from the matrix of PLA-NP; a possible consequence of an early PLA-NP degradation (Fig. 3: H). This change was more pronounced 24 h later (4 days post-injection). While PLA-NP remained intact in some endothelial cells (Fig. 3: I), in others, a shrinkage of PLA-NP was observed, in addition to the release of gold particles (Fig. 3: J). One week after injection, the heterogeneity of PLA-NP disassembly inside endothelial cells was striking. In some endothelial cells, the structure of the PLA-NP was entirely lost, only a paste of amorphous PLA mixed with gold particles remained (Fig. 3: K-L). In other cells, shrunken PLA-NP persisted along with released gold particles (Fig. 3: M). Finally, in some endothelial cells only aggregates of free gold particles remained visible (Fig. 3: N). These results indicate that an augmented release of an encapsulated cargo from surfactant-free PLA-NP could start around one week after intravenous administration.

2.6. Complementary information regarding the internalization of PLA-NP by endothelial cells

To deepen our understanding of the internalization of PLA-NP by endothelial cells, we complemented our investigations with additional live-imaging experiments.

Our previous data indicated that PLA-NP clearance occurs in the first 30 min following the administration. Videos of these first 30 min following the injection revealed that most of the fluorescent PLA-NP had already been taken-up by endothelial cells from both veins and arteries in the few minutes required to prepare the samples before the acquisitions (anesthesia-mounting-setting acquisition parameters) (Fig. S5: A-D'). As illustrated with Video S4, the clearance of PLA-NP from the blood seems to occur in around 20–25 min. Indeed, few PLA-NP could be detected inside the lumen of blood vessels at the beginning of the videos while this amount decreased overtime and past the 20th minute, almost none could be observed in the blood flow (Fig. S5: E-J).

We then investigated if the internalization of our anionic PLA-NP by non-scavenger endothelial cells [19] could be dependent of the amount of administered PLA-NP. In most of our previous experiments, PLA-NP were injected at a concentration of 5 mg/mL. Here we analyzed the biodistribution (30 min) of PLA-NP injected at different concentrations, ranging from 1 mg/mL to 10 mg/mL (Fig. S6-8), For all the different concentrations, the revealed biodistribution was similar to the one we previously described, suggesting that PLA-NP internalization by non-scavenger cells is not dependent on the saturation of the scavenger endothelial cells.

Campbell et al. [19] showed that internalization of numerous anionic NP, which are restricted to the scavenger endothelial cells, is charge-dependent and could be inhibited with a pre-treatment of intravenously injected sulfate dextran (40 KDa) to saturate the scavenger receptor stab2. We then decided to verify if the internalization of our PLA-NP by scavenger and non-scavenger endothelial cells followed similar rules. As dextran sulfate 40 KDa is quite toxic for fish, we applied the refined protocol published by Verweij et al. [30] which instead use a pre-treatment of dextran sulfate (500 KDa) for reduced adverse effects. This pre-treatment, with 3 mg/mL of sulfate-dextran 500 KDa 2 h before the PLA-NP injection, strongly reduced the internalization of PLA-NP by the scavenger endothelial cells while the internalization by non-scavenger endothelial seemed unaffected (Fig. S7: A-B′, D-E). In this configuration, the presence of PLA-NP in the blood flow 30 min following their injection was striking. This experiment suggests that while the internalization of PLA-NP by the scavenger endothelial cells seemed to follow the rules described by Campbell et al. [19], the internalization of PLA-NP by non-scavenger endothelial cells seemed to involve other mechanisms that are independent of the negative-charge of the particles. To evaluate if these other mechanisms could clear the PLA-NP from the blood, we applied a stronger sulfate-dextran pre-treatment (30 mg/mL) and analyzed the biodistribution of PLA-NP 3 h after the injection. We obtained similar results, indicating that the charge-dependent internalization by scavenger endothelial cells appears to be the main driving force behind the clearance of PLA-NP from the blood (Fig. S7: C-C′). Noteworthy is that significant internalization of PLA-NP by phagocytes could still be observed (Fig. S7: F).

2.7. Continuous internalization of PLA-NP by macrophages during the first 24 h

Throughout our investigations, we came across several intriguing peculiarities regarding the internalization of PLA-NP by macrophages.

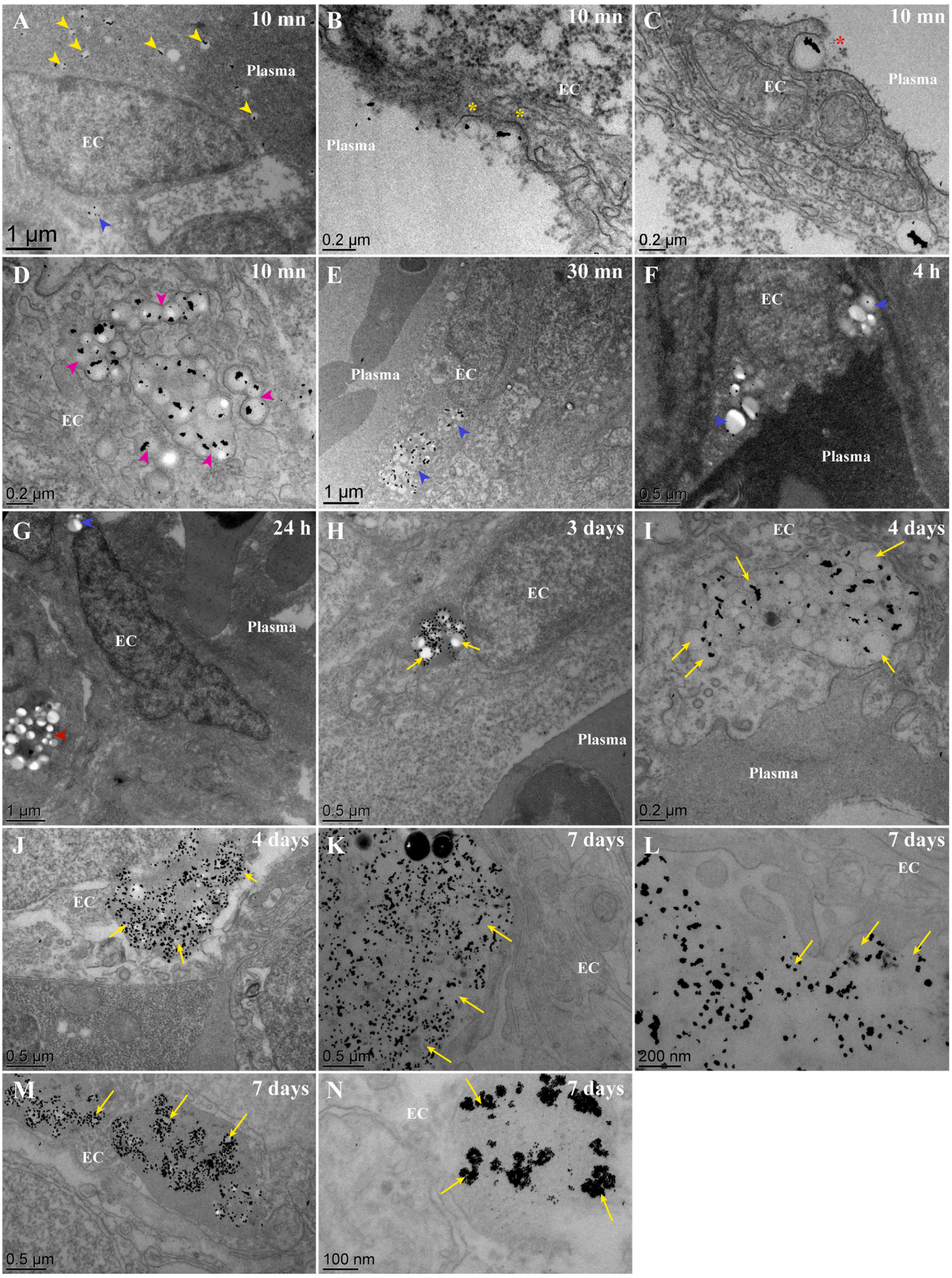

(caption on next page)

Fig. 3. Fate of PLA-NP(Gold) once internalized by endothelial cells, from 10 min to 7 days post-injection, as observed with TEM. Representatives electron micrograph of ultrathin (60 nm) epon sections from zebrafish larvae injected at 3 dpf with PLA-NP encapsulating gold particles (<10 nm), 10 min (A-D), 30 min (E), 4 h (F), 24 h (G), 3 days (H), 4 days (I-J) and 7 days (K-N) post-injection. (A-D) 10 min following intravenous injection, PLA-NP are circulating within the bloodstream (A - yellow arrowhead) and internalized by endothelial cells (A - blue arrowhead). Internalization of PLA-NP by endothelial cells involve an invagination of the plasma membrane, resembling clathrin-mediated internalization (B - yellow stars), as well as figures resembling phagocytosis (C – red stars). Numerous NP were already being condensed within cellular compartment of some endothelial cells (D – magenta arrowheads). 30 min after the injection, no more PLA-NP could be observed within the bloodstream, in contrast to the massive concentration of PLA-NP within endothelial cells (E - blue arrowhead). No sign of degradation could be observed from PLA-NP internalized by endothelial cells (A, *E*-G - blue arrowhead) and underlying phagocytes (G - red arrowhead) during the first 24 h. Starting from 3 days post-injection, change in the colloidal stability of internalized PLA-NP was evident in some cells, encapsulated gold-particles being released from the NP-PLA matrix (H - yellow arrows). PLA-NP degradation was seemingly more pronounced 4 days post-injection, within some endothelial cells PLA-NP could are observed with a shrunken size (I - yellow arrows) while in others there are more gold crystals free rather than inside the PLA matrix (J - yellow arrows). Finally, a week after the injection different shade of PLA-NP degradation could be observed inside endothelial cells, cellular compartment filled with a paste of amorphous PLA containing gold crystals (K-L - yellow arrows), shrunken PLA-NP with released gold crystals (M - yellow arrows) and cellular compartment where only aggregated gold crystals remain (N - yellow arrows). Annotations: EC, endothelial cell. Scale bars: 1 μm (A,E,G), 500 nm (F,H,J-K,M), 200 nm (B-D,I,L) and 100 nm (N). (For interpretation of the references to colour in this figure legend, the reader is referred to the web version of this article.)

For example, it seemed that macrophages could display a more intense PLA-NP fluorescence signal at 24 h than at 30 min post-injection (Fig. 2: *E*-F). In addition, the accumulation of PLA-NP by brain macrophages also raised the question of how could these cells access PLA-NP (Fig. S3: A-D)? Altogether, these elements suggested that the internalization of PLA-NP by macrophages might not be restricted to the first 30 min. We therefore decided to quantify the dynamic of PLA-NP internalization by macrophages in more detail. Because of the minuscule size of the NP, we combined live imaging and flow cytometry to obtain reliable quantification of the PLA-NP uptake by macrophages.

We first performed an automated analysis of the quantity of PLA-NP fluorescence that associate with macrophages using stereomicroscope live-acquisitions and an ImageJ macro previously developed [31]. In agreement with the observations from light microscopy, the automated analysis revealed an increase (plus 56%) in the amount of PLA-NP inside macrophages between 30 min and 24 h (Fig. 4: A). We then performed a flow-cytometry experiment on mpeg1:mCherry zebrafish injected with green fluorescent PLA-NP (2,5 mg/mL) to quantify the fraction of macrophage (mCherry+ cells) involved in the uptake of PLA-NP (Fig. 4: B-B′). Already 10 min after the injection, 8% of the macrophages already contained detectable PLA-NP. The fraction of PLA-NP- containing macrophages then steadily increased until it plateaued around 17% between 4 and 24 h. It is important to note that at this stage, numerous new macrophages are continuously being generated, increasing the pool of PLA-NP negative macrophages over the course of the experiment. Not only could we confirm the continuous uptake of PLA-NP by macrophage, these results also raised an important question: how do macrophages continue to internalize PLA-NP when none remains in the bloodstream, most of them being internalized by endothelial cells?

2.8. Evidence for a transfer of PLA-NP from endothelial cells to macrophages

We thus hypothesized that macrophages might take up PLA-NP from endothelial cells, and focused our efforts on 3D live-imaging after the 30 min timepoint to witness such events. With only a few cells separating it from the exterior environment, the flat endothelial layer surrounding the yolk (Yolk circulation valley) is a favorable region to perform dynamic 3D live-imaging at a high-resolution (Fig. S1). In this region, as illustrated (Fig. S10: A), macrophages are also abundant. During our preliminary image acquisitions, we could assess the internalization of green fluorescent PLA-NP by red fluorescent macrophages, as illustrated (Fig. S10: B-F, Video S5) by a video made 70 min post-injection. At start, this video display a PLA-NP negative macrophage moving to the close proximity of a cell with PLA-NP within cellular compartments, likely an endothelial cell. Following several minutes of apparent contact, the macrophage moved away, then displaying PLA-NP-loaded cellular compartments. This initial investigation suggested the intriguing possibility of a peculiar cell-to-cell transfer of PLA-NP.

We deepened our investigations with the injection of far-red fluorescent PLA-NP in double transgenic zebrafish fli:GFP and mpeg1:mCherry to reveal any potential transfer of material between endothelial cells and macrophages. Both PLA-NP+ endothelial cells and PLA-NP+ macrophages were present in the area, 30 min post-injection (Fig. 5: A). There, we could witness striking transfers of GFP-labelled fragments of endothelial cell cytoplasm, containing far-red fluorescent PLA-NP, from endothelial cells to macrophages. An illustration of the transfer is presented (Fig. 5: B-I, Video S6) with a 3D video acquired 30 min post-injection. In this video, a PLA-NP containing macrophage in the bloodstream can be seen moving very close to PLA-NP-positive endothelial cells. Then, less than 10 min later, internalization of a surprisingly large amount of GFP+ material could be observed inside the macrophage. The optical sections isolated from the video reveal the presence of PLA-NP among the GFP+ internalized material (Fig. 5: J-K). On a 3D image acquisition made after the video, the same macrophage could be seen with a mix of small PLA-NP+ / GFP- cellular compartments, a large PLA-NP+ / GFP+ cellular compartment and a bright GFP+ spot on its plasma membrane (Fig. 5: L-L"). Interestingly, the GFP fluorescence signal seemed more faint (compare Fig. 5: J and Fig. 5: L), possibly because of the acidity of the presumed late endocytic organelle where the NP resided that might be quenching the GFP signal [25].

It is important to note that during the transfer of NP, no GFP fluorescence signal could be observed inside the cytosol of macrophages, likely ruling out the formation of direct openings connecting the cytoplasm of both cells. No cell death could be observed among the donor cells and the neighboring endothelial cells. In addition, using acridine orange to further analyze cell death (Fig. 5: M) [32,33], we found that the intravenous injection of PLA-NP only induced the same level of cell death as the mock-injection after 30 min, likely caused by the mechanical injury. The fish then fully recovered 24 h after the injection, with all cell death level returning the level measure from non-injected fish. Overall, our observations indicate that NP transfer from endothelium to macrophage involve cell-to-cell handover of large cytoplasmic bundles, the precise mechanisms of which remain to be elucidated.

2.9. Evidence of a microvesicle-like transfer from endothelial cells to macrophages

During our investigation, we also encountered the transfer of microvesicle-like structures from endothelial cells to macrophage. This phenomenon is illustrated in (Fig. 6, Video S7). The video first shows the formation of a GFP-labelled microvesicle-like structure budding out of an endothelial cell from the caudal vein plexus (Fig. 6: A-B). After a few minutes, the microvesicle-like structure was then released from the endothelial cell (Fig. 6: C) into the lumen of the blood vessel. The microvesicle-like structure was then quickly internalized by an adjacent macrophage in the bloodstream (Fig. 6: D). Interestingly, the fluorescence signal of the GFP-labelled microvesicle-like structure started to fade after being taken up by the macrophage, until it was no more detectable 13 min later (Fig. 6: *E*-H).

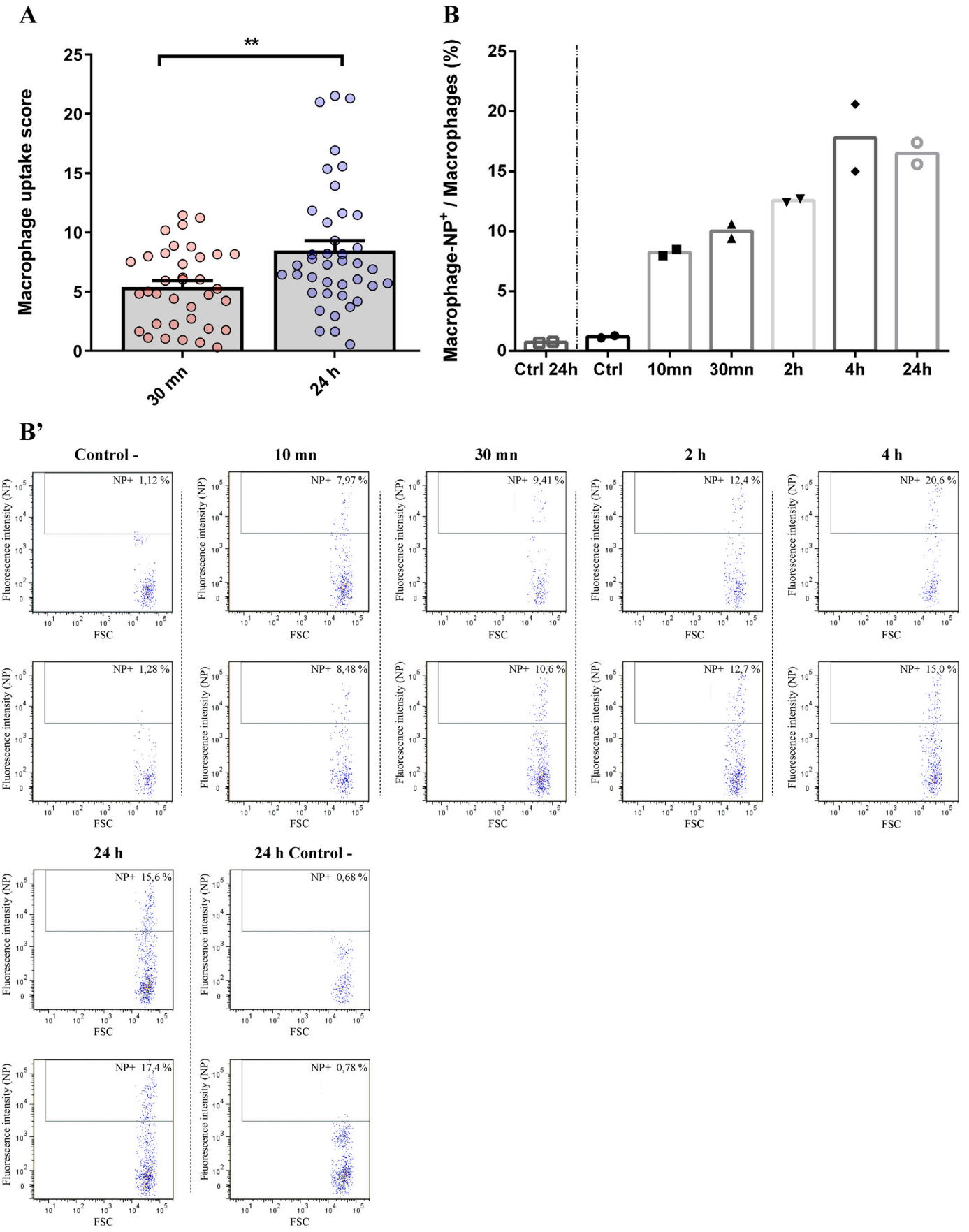

(caption on next page)

Fig. 4. Quantitative analysis of PLA-NP internalization by macrophage from 10 min to 24 h post-injection. (A) Automated analysis of the relative amount of internalized fluorescent PLA-NP by macrophage 10 min and 24 h following intravenous injection of 3 dpf mpeg1:mCherry zebrafish. Stereo-microscope acquisitions of individual zebrafish were put through an ImageJ macro, from which an internalization score was calculated, based on the amount of red PLA-NP fluorescence associating with the green macrophage fluorescence signal, relative to the total amount of red PLA-NP fluorescence detected from the whole fish. Histograms represent the mean internalization score and each dot represents the score of an individual zebrafish. From 30 min to 24 h post-injection, more NP were internalized by macrophages (+56%). (B) Flow cytometry analysis of the fraction of macrophages that had internalized fluorescent PLA-NP relative to the whole population of macrophages, 10 min to 24 h after intravenous injection into 3 dpf zebrafish. Histograms represent the mean percentage of PLA-NP positive macrophages at different time-points following administration, with each dot representing the data acquired from 10 pooled larvae. Almost 8% of macrophages were labelled positive for PLA-NP 10 min after the injection. After this time, the fraction of macrophage internalizing PLA-NP steadily increased over time until it reached a plateau around 17% of PLA-NP-positive macrophages at 4 h and 24 h post-injection. All the flow-cytometry acquisitions are illustrated in (B′), they only display the population of macrophage which was gated based on the mCherry fluorescence intensity. The x axis displays the "size" of the detected events and the y axis the fluorescence intensity corresponding to PLA-NP. Error bars: SEM. Significance level is indicated as: $^{**}p < .01$. Number of fish per condition: (A) 30 min (36) and 24 h (40); (B) 10 larvae per replicate. (For interpretation of the references to colour in this figure legend, the reader is referred to the web version of this article.)

The isolated optical sections from the video highlight the attachment of a GFP-labelled microvesicle-like structure to the macrophage plasma membrane (Fig. 6: I), followed by its internalization inside a mCherry negative cellular compartment (Fig. 6: J). We could not detect any PLA-NP inside the microvesicle-like structures during our observations. However, our data still do not allow us to rule out the possibility of a PLA-NP transfer by such a mechanism. Indeed, as illustrated (Fig. 6: K-L") in a 3D acquisition, we could observe the presence of PLA-NP, inside endothelial cells, that were in very close proximity to budding endothelial microvesicle-like structures. This budding microvesicle-like structures are also embraced by macrophages, that here co-internalized PLA-NP+ and GFP+ labelled materials.

3. Discussion

The objective of the present study was to evaluate the biodistribution of intravenously injected surfactant-free PLA-NP *in vivo* and with a high resolution using the zebrafish model. The goal behind the design of our surfactant-free PLA-NP was to follow the 'safe-by-design' paradigm of developing the most compatible NP for human applications [9,10]. Almost nothing is known about surfactant-free NP *in vivo*, hence our aim was to initiate the analysis of surfactant-free PLA-NP *in vivo* and not to make a direct comparison between PLA-NP with, or devoid of surfactant. Using a combination of live-imaging, cryosections and electron microscopy (EM), our study reveals rapid internalization of NP throughout the vascular endothelium of the zebrafish embryo, as well as into macrophages. We introduce a method allowing colloidal gold particle to be encapsulated in PLA-NP, opening the door for visualizing these NP at the ultrastructural level. Finally, by using automated imaging analysis, flow-cytometry and live-imaging we describe a striking transfer of NP from endothelial cells to macrophages.

In recent years the zebrafish has emerged as a powerful animal model for the study of nanomedicine *in vivo*, especially for live-imaging at a high resolution, as discussed in depth by Sieger et al. [34] It has, for example, recently been used for the live-imaging study of endogenous particles in the nanosized range such as exosomes [35] and tumor extracellular vesicles [36]. In our study, the negatively-charged PLA-NP were quickly internalized by macrophages and by both venous and arterial endothelial cells distributed along the entire vasculature (Fig. 1-2). The internalization of PLA-NP by endothelial cells was stronger in veins than arteries. Once internalized by endothelial cells, PLA-NP did not reach the cytosol and remained in vesicles from the endomembrane system, an aspect of their biodistribution we later confirmed using electron microscopy (Figs. 1–3).

The internalization of our PLA-NP into endothelial cells from all the blood vessels, veins and arteries, was surprising for an anionic NP. Others have described the uptake of different NP by endothelial cells. In a recent study, Campbell *et al* [19] demonstrated that the internalization of a wide range of negatively charged NP (liposomes, polymersomes, polystyrene NP, virus-like particles) was restricted to specific venous regions of zebrafish embryos, namely: the caudal vein plexus, the dorsal aspect of the post-cardinal vein and the primary head sinus. In these blood vessels, the highly endocytic scavenger endothelial cells resemble the mammalian sinusoidal endothelial cells. This pattern of biodistribution, where no NP are internalized by endothelial cells from arteries, has been observed in multiple studies using different families of negatively charged NP [20,21,37]. Even the recent studies on nano-sized endogenous exosomes and tumor extracellular vesicles also described this selective uptake by the scavenger endothelial cells forming the caudal vein plexus [35,36]. Hence, besides showing that our PLA NP can also be internalized by endothelial cells, our study also reveals a pattern of endothelial cell uptakes that was unprecedented for negatively-charged NP. Intriguingly, in the Campbell study [19] it was the positively charged liposomes that displayed a biodistribution similar to our PLA-NP. Our results then further highlight the difficulty of predicting NP biodistribution and raise an important question: why would our anionic PLA-NP behave like cationic NP and not like the other negatively charged NP? Interestingly, our complimentary experiment provided some insight to this question (Fig. S5-S9). The main mechanism responsible of the clearance of PLA-NP is a negative-charge-dependent internalization by the scavenger endothelial cells, in agreement with the model proposed by Campbell et al. [19]. However, they also revealed the involvement of one or several additional mechanism(s) that work in a negative-charge independent manner and that are responsible of the internalization of PLA-NP by the non-scavenger endothelial cells, either venous or arterial. In addition, these unidentified mechanism(s) do not result from a saturation of charge-dependent-mechanism involving the scavenger endothelial cells but occurs at the same time. Still, why only our PLA-NP are internalized this way and not the other described anionic NP remains a mystery.

Using thin cryosections to evaluate the capacity of PLA-NP to escape the vasculature, our results indicate that relatively few PLA-NP accumulate inside internal organs (Brain, Kidney, Liver, *etc.*) (Fig. 2, Fig. S3). This intrinsic targeting of endothelial cells from the whole vasculature by PLA-NP, with minimum accumulation inside internal organs, could be an interesting finding for developing strategies for the treatment of vascular-related diseases.

An important aspect of our study was to evaluate the fate of PLA-NP by both light microscopy and electron microscopy (Figs. 2-3). Although EM can visualize NP in detail it is rarely used to study the fate of nano-sized particles *in vivo* [13,22,35,36]. One of the challenges of using EM to study NP *in vivo* is the preservation and visualization of their structure in order to unequivocally identify them in electron micrographs. A novel approach we developed allowed encapsulation of electron-dense gold particles in the matrix of PLA-NP to guarantee their identification in electron micrographs. This enabled us to observe internalization of our PLA-NP by endothelial cells by clathrin-mediated endocytosis and a process resembling phagocytosis, as soon as 10 min post injection. The high activity of endothelial cells toward PLA-NP is consistent with these cells being highly active in clathrin-mediated endocytosis [38,39] and being able to phagocyte bacteria [40].

Subsequent to their internalization by endothelial cells, PLA-NP were concentrated within vesicles, likely from the endocytic system [25]. Our study reveals that while the distribution of PLA-NP remained almost

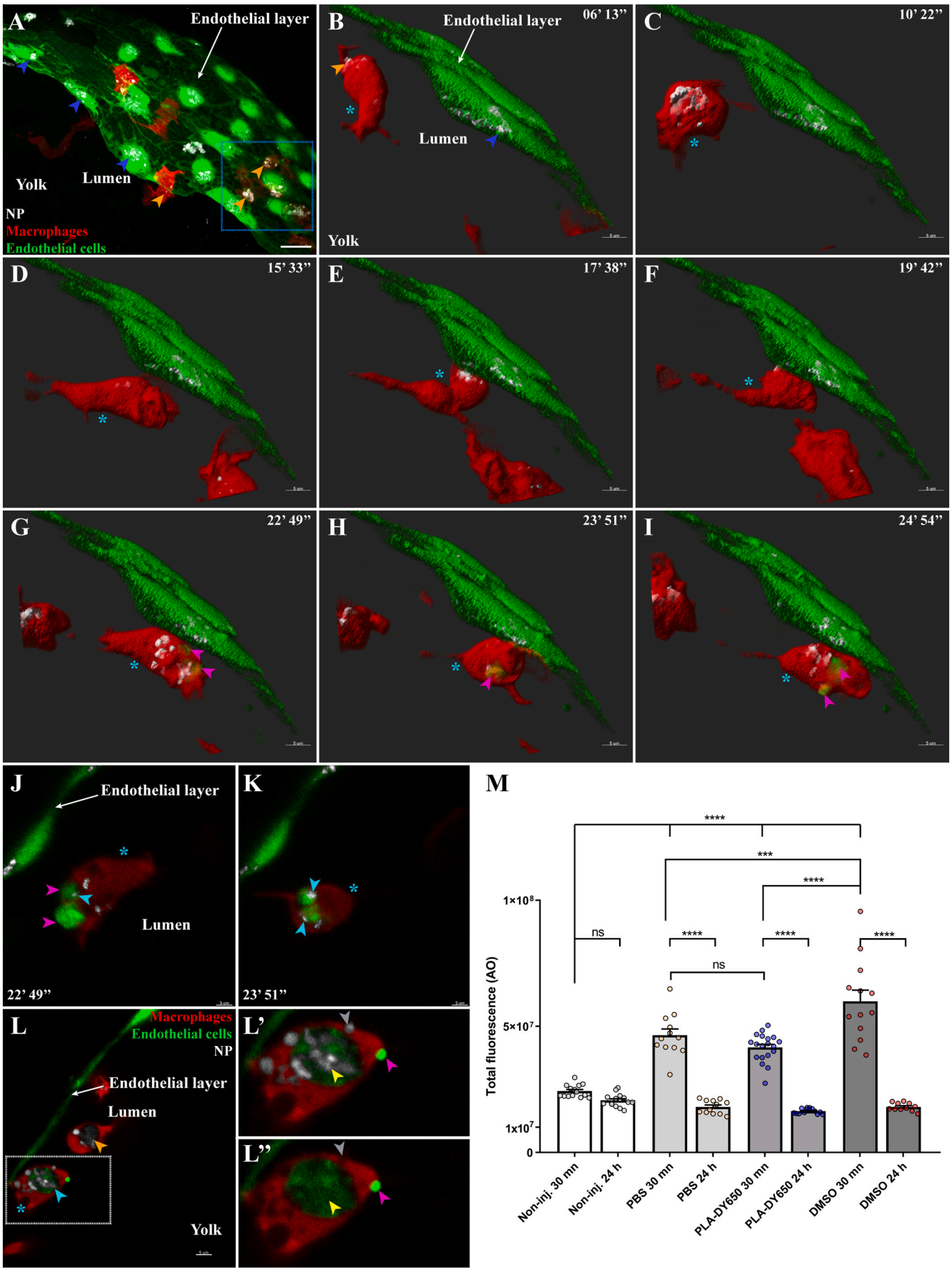

(caption on next page)

Fig. 5. Transfer of PLA-NP from endothelial cells to macrophages. Representative live-acquisitions of 3 dpf mpeg1:mCherry and fli:GFP double transgenic zebrafish, 30 min after the intravenous injection of far-red fluorescent PLA-NP and using a spinning-disk confocal microscope. The acquisitions were made at the yolk circulation valley as illustrated in (A – 53 μm MIP, x63 objective), endothelial cells and macrophages being represented as a 3D surface reconstruction (green and red, respectively) and where PLA-NP (white) internalized by endothelial cells (blue arrowheads) and macrophage (orange arrowheads) can be observed. (B-I) The video (14 μm MIP), made across PLA-NP+ endothelial cells (blue arrowhead) of the endothelial layer covering the yolk, focuses on a macrophage (cyan star) which is already PLA-NP+ (orange arrowheads). At first, the macrophage enters in the proximity of the PLA-NP-positive endothelial cells (B-D). After almost 10 min at this position (*E*-F), GFP-labelled fragments of endothelial cell can be observed within the macrophage (G-I - magenta arrowheads) while the endothelial cells remain alive (J-K). Optical sections (1 μm) from G and H respectively, indicate the presence of PLA-NP (cyan arrowheads) inside the GFP-labelled fragment of endothelial cells (magenta arrowheads) that have been transferred to the macrophage (cyan star). (L) On an acquisition few minutes after the video, PLA-NP can be seen inside a GFP-negative macrophage (orange arrowhead), and within the GFP+ macrophage (cyan star and arrowhead). (L'-L") A close-up of the latter macrophage shows the presence of GFP-/PLA-NP+ cellular compartment (grey arrowhead), along with a massive GFP+/PLA-NP+ one in which both PLA-NP and the GFP+ cytosolic fragments of the endothelial cell co-localize (yellow arrowhead). Note the presence of a bright GFP+ structure at the surface of the macrophage (magenta arrowhead). (M) Analysis of the cell death following PLA-NP injection, assessed by the overall acridine orange fluorescence intensity (y-axis) of the whole zebrafish by stereomicroscopy. Intravenous injection of PLA-NP (DY650) does not induce cell death other than the mechanical injury from the injection, which is healed by 24 h post-injection. Each dot represents one single individual. Error bars: SEM. Significance level is indicated as: $***p < .001$ and $****p < 0{,}0001$. Number of fish per condition (30 min / 24 h): Non-injected (14 / 15), PBS-injected (12 / 12), PLA-DY650-injected (19 / 14), DMSO-injected (13 / 11). Scale bars: 20 μm (A), 5 μm (B-I,L) and 3 μm (J-K). (For interpretation of the references to colour in this figure legend, the reader is referred to the web version of this article.)

unchanged during the first 24 h post-injection, they started to progressively lose their colloidal stability 72 h after being taken up by endothelial cells. The complete disassembly and release of gold particles from within some PLA-NP became evident after 1 week. Very few studies have been able to analyzed the disassembly of NP *in vivo* using imaging techniques [37].

Macrophages and neutrophils are immune cells that are involved in the clearance of foreign materials. Devoid of stealth properties, such as the one conferred by polyethylene (PEG) [41] or polysarcosine [42,43], our PLA-NP remained relatively briefly in the circulation and were rapidly engulfed by macrophages, as we expected. Many NP lacking stealth properties, such as PLGA [14], liposomes [19,44] and polymersomes [45], have been shown to be rapidly taken up by macrophages when intravenously injected into zebrafish larvae, a phenomenon that is also seen in higher vertebrate models [44]. However, in our system there was no detectable uptake of PLA-NP by neutrophils. This was unexpected since neutrophils often internalize circulating NP [46], but it is not unprecedented [22,45]. Neutrophils have been shown to phagocytose bacteria much more efficiently when presented on surfaces (*e.g.* after subcutaneous injection) than in the fluid phase (*e.g.* after intravenous injections) [47]. Yet, we could also not induce neutrophils to ingest PLA-NPs after sub-cutaneous injection (Data not shown).

During our investigation on the interactions of PLA-NP with macrophages, we could assess, using two different techniques (Flow cytometry and quantitative image analysis), a significant increase of PLA-NP internalized by macrophage from 30 min to 24 h following the injection. From this, we realized that macrophages continued to internalize PLA-NP despite the complete absence of detectable NP circulating in the blood flow (Fig. 4). We therefore investigated by live imaging how macrophages could continue to internalize PLA-NP at a time when no obvious pool of free NP was available. This analysis led us to unveil two different types of transfer of cytoplasmic material from endothelial cells to macrophages.

One of these processes involved the production of budding structures by endothelial cells that resemble microvesicles, which are then quickly internalized by adjacent macrophages (Fig. 6). Microvesicles are vesicles of around 100 nm to 1 μm that are generated through the budding outwards of domains from the plasma membrane and are involved in cell-cell communication [48–53]. Although no transfer of PLA-NP could be seen associated with this process, to our knowledge, our study is the first to provide live-observations of the genesis of microvesicles by endothelial cells and their subsequent internalization by adjacent macrophages in the zebrafish.

The second process involved the striking discovery of transfer of large PLA-NP-loaded cellular structures along with GFP-labelled cytoplasmic material from endothelial cells to macrophages (Fig. 5, Fig. S10), a phenomenon not previously described. This kind of transfer showed a consistent pattern with, first, a macrophage engaging contact with an endothelial cell for several minutes, followed by internalization of endothelial GFP-labelled cytoplasmic material containing PLA-NP loaded endocytic organelles. This was followed by the macrophage separating from the endothelial cell, which appeared unharmed. After the internalization, the fluorescence (GFP) from the endothelial material did not co-localize with the fluorescence (mCherry) from the macrophage cytosol, consistent with a phagocytic process internalizing the fragment of the endothelial cell (containing GFP and NP-containing vesicles) into a compartment of the endocytic pathway of the macrophage. This process involving NP transfer from endothelial cells to macrophages appears to be distinct from multiple known mechanisms involved in the transfer of material from one cell to another. As the transfer of NP we report involves the transfer of cytoplasmic fragments, we do not consider transcytosis as a plausible candidate.

Tunneling nanotubes involve the formation of cytoplasmic bridges that connect two cells and can be either long and narrow or short and thick, the latter being able to transfer organelles such as endosomes and mitochondria [54–56]. However, it is unlikely that tunneling nanotubes are related to our observations as they involve a direct connection and mixing of the cytoplasm of two adjacent cells.

We also considered the possibility that the NP transfer we observe might be related to apoptotic events. Apoptosis is a process of programmed cell death by which remnants of the dying cell can be internalized by macrophages through the uptake of apoptotic bodies, or *via* a process called efferocytosis [57,58]. Apoptotic bodies are large extracellular vesicles (1–5 μm) that contain an enclosed fraction of the apoptotic cells they originate from [59,60]. However, no apoptotic endothelial cells were observed in the region from which our videos were acquired and the donor endothelial cells appeared alive after the transfer. This is also consistent with the fact that at the early developmental stages we used, the vascular system of the zebrafish embryo is expanding, not regressing. Furthermore, we showed that the injection of PLA-NP triggers a transient and low induction of cell death that does not surpass the mechanical injury from a mock injection (Fig. 5). Thus, events related to the death of endothelial cell could hardly explain the increase of PLA-NP internalizations by macrophages that we monitored in the 24 h period after PLA-NP left the blood compartment.

We also envisaged the involvement of another described transfer mechanism, which shares similarities with the pattern we observed, especially the prolonged contact between the cells and the storage of the transferred cellular fragments apart from the cytosol. Trogocytosis is an event of partial phagocytosis that has been recently identified. Initially restricted to the nibbling of plasma membrane by T cells [61], since then, the definition of trogocytosis has being widened to include the partial phagocytosis of a donor cell, that remains alive in a healthy condition [62]. It has been reported that macrophages can perform trogocytosis [63], and in contrast to T lymphocytes, trogocytosed cellular fragments by macrophages usually end up being internalized

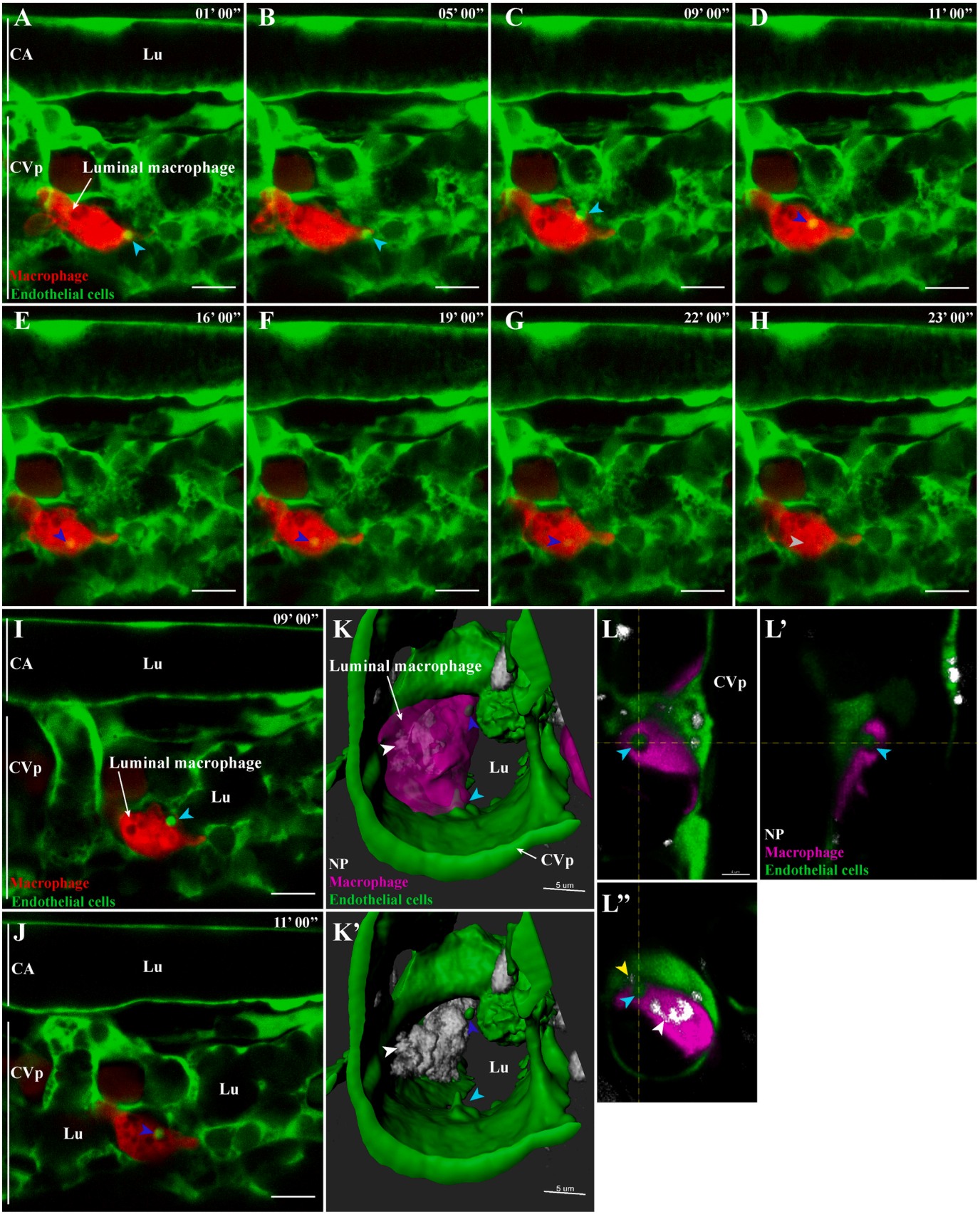

(caption on next page)

Fig. 6. Microvesicle-like transfer from endothelial cells to macrophages. Representative live-acquisitions of 3 dpf mpeg1:mCherry and fli:GFP double transgenic zebrafish, 30 min after the intravenous injection of far-red fluorescent PLA-NP and using a spinning-disk confocal microscope. The acquisitions have been made in the tail region, at the caudal vein plexus. Endothelial cells, macrophages and PLA-NP are highlighted in green, red and white, respectively. (A-B) At the start of the video (9 μm MIP), close to a macrophage residing in the bloodstream, an endothelial cell from the caudal vein plexus is forming a bright GFP+ microvesicle-like structure (cyan arrowhead). (C) Nine minutes later, the microvesicle-like structure is released from the endothelial cell (cyan arrowhead), it is then quickly internalized by the adjacent macrophage (D - blue arrowhead). Once internalized, the fluorescence of the microvesicle-like structure rapidly fades (E-G - blue arrowheads) to finally disappear 13 min after its internalization (H – grey arrowhead). Optical sections (1 μm) from (C) and (D), (I) highlights the contact between the GFP+ microvesicle and the plasma membrane of the macrophage (cyan arrowhead), while (J) emphasize its internalization inside a mCherry negative cellular compartment (blue arrowhead). (K-K′) A luminal macrophage, positive for PLA-NP (white arrowhead) and with a GFP+ cellular compartment (blue arrowhead) is wrapping around a budding microvesicle-like structure of an endothelial cell from the caudal vein plexus (cyan arrowhead). Fluorescence are represented as 3D reconstructions. (L-L") Orthogonal views from (K) reveal the presence of PLA-NP in close proximity to the budding-microvesicle-like structure (yellow arrowhead). Annotations: CA, caudal artery; CVp, caudal vein plexus and Lu, lumen. Scale bars: 10 um (A-J), 5 μm (K-K′) and 4 μm (L). (For interpretation of the references to colour in this figure legend, the reader is referred to the web version of this article.)

[64]. However, the trogocytosis of endothelial cells by macrophage has not been reported yet. The different discussed mechanisms are illustrated in Scheme 1.

The exchange of material from endothelial cell to macrophage we describe raises many questions regarding its biological significance. It is likely that this transfer of PLA-NP hijacks an existing mechanism that developed independently of the presence of foreign polymeric NP arriving *via* the blood stream. A plausible hypothesis could be a mechanism that would be involved in an immune surveillance *via* activation of antigen-presenting cells. Interestingly, a recent study on the internalization of silica nanoparticles (70 nm) by endothelial cells and macrophages did not observe any transfer [22]. Regarding its significance for the field of Nanomedicine, this exchange of NP from endothelial cells to associated macrophages represents a new type of biological interaction to be considered. It is likely to have important implications for the design of future NP treatment for vascular disease as it reveals macrophages as possible off-targets. However, it could also represent an interesting strategy to aim NP toward vascular-associated macrophages or to deliver compound to the microglia in the brain without having to disrupt the blood-brain barrier. This last prospect could also benefit anti-cancer treatment as Sofias et al. [65] showed the involvement of phagocytes in the accumulation of therapeutic nanoparticle from the blood to cancer area through a process called "phagocyte hitchhiking", something we also described in one of our recent study. [66]

4. Conclusion

In this study, we took advantage of the zebrafish model to deepen our understanding of the biological interaction and fate of safe-by-design surfactant-free PLA-NP after intravenous administration. Using live-imaging, flow-cytometry, light-microscopy and electron microscopy, we could follow in detail the interplays between PLA-NP, the endothelium and macrophages at the tissue, cellular and ultrastructural level. Our findings provide new insights into NP interaction with the vascular endothelium. The negatively-charged, surfactant-free PLA-NP were efficiently internalized by endothelial cells and macrophages. In contrast to other studies using anionic NP, our PLA-NP were distributed along the veins and arteries of the whole vasculature. A novelty of our approach was the encapsulation of hydrophobic gold particles into the matrix of PLA-NP to study their fate by electron microscopy, enabling analysis of their internalization by endothelial cells to their ongoing disassembly a week later.

In addition, our study is one of the first to evaluate the biodistribution of a surfactant-free NP system with a high quality of imaging and we believe that it will improve the understanding of how other surfactant-free NP can potentially behave *in vivo*.

Finally, a novel finding of our study is the existence of a new biological mechanism that allow cell-cell transfer of NP, from endothelial cells to macrophages. This could potentially be significant for the development of new NP therapy for vascular related disease and the targeting of macrophages. The precise mechanism and biological significance of this transfer of NP remain to be elucidated.

5. Material and methods

NP Preparation and Characterization.

Poly(lactic acid) nanoparticles were elaborated by nanoprecipitation as previously described [8,67,68] and were provided by Adjuvatis (i-particles®). Fluorophores were encapsulated using different fluorophore:PLA ratio: CellTrace BODIPY TR Methyl Ester ™ (0,02% - Life Technologies), BODIPY 500-510$_{C4,C9}$ ™ (0,04% - Life Technologies) and

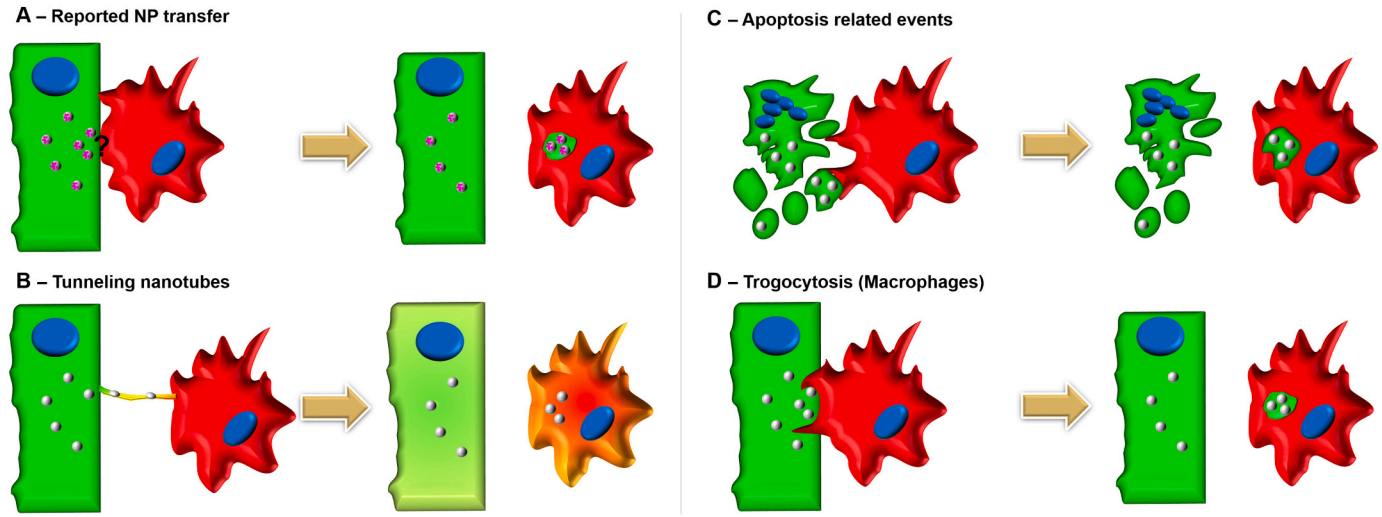

Scheme 1. Illustrations of the reported NP transfer and known Cell-Cell transfer mechanisms.

DY650-decylamide (0,10% - Dyomics GmbH). The characterization, by dynamic light scattering, of the size, as well as the size homogeneity of the different PLA-NP formulations were performed using a Zetasizer nanoS apparatus (Malvern Instrument, UK).

For the electron microscopy analysis, 6–7 nm hydrophobic colloidal gold particles (PlasmaChem) were encapsulated into the PLA-NP. For this, 20 mg of gold particles were dissolved in dichloroethane and poured in an acetone solution containing 90 mg of PLA before initiating the nanoprecipitation process. Solution were then kept for 18 h of storage in static mode to remove the pellet of any aggregated gold particles that had not been encapsulated. After characterization, the obtained PLA-NP(gold) displayed a mean diameter of 211,3 nm, a polydispersity index of 0,199 and an encapsulation yield of gold particles of 90%. As verified with electron microscopy (Fig. S4), essentially no free gold particles remained at the end of this process.

5.1. Animal care and ethic statement

Experiment were performed in accordance with the animal care guidelines, ethical standards and legislation of the European Union, France and Norway. Zebrafish embryos were reared and handled following such guidelines and laws. The experiments were conducted using wild-type AB/Tubingen zebrafish and genetically-modified strains *Tg(mpeg1:mCherry)gl23* [23], *Tg(fli1a:GFP)y1* [18] and *Tg(mpx:GFP)i114* [24].

5.2. Intravenous injection of PLA-NP into zebrafish embryos

Injection needles were produced using borosilicate capillaries (GC100T-10, Harvard Instruments) and a pipet puller (P-97, Sutter Instruments). The needles were loaded with an appropriate sample before being connected to an Eppendorf Femtojet Express pump and mounted onto a Narishige MN-153 micromanipulator that allowed movement in the x, y and z planes. Zebrafish embryos (3 dpf) were anesthetized using a solution of buffered tricaine (120 μg/mL) and 5 nL of PLA-NP (in PBS 1×) were injected into either the caudal vein plexus or the post-cardinal vein using a femtojet (Eppendorf) and a stereomicroscope (Leica DFC365FX). Unless specified, PLA-NP were concentrated at 0,5% (5 mg/mL), such injection represent a quantity of 1.10^6 to 5.10^6 nanoparticles.

To perform the experiment saturating scavenger endothelial cells with an anionic competitor, following the recommendations of Dr. Frederik Verweij [30], fish were administered intravenously 1 nL of dextran sulfate 500 KDa (Sigma), at either 3 mg/mL or 30 mg/mL, 2 h before the administration of PLA-NP. Only fish with regular blood flow were used for live-imaging at high-resolution.

5.3. Live-imaging

Following PLA-NP (0,5%) administration, stereomicroscope (Leica DFC365FX – 1.0× planapo lens) acquisitions were performed on 3 dpf zebrafish larvae that were maintained under anesthesia (buffered tricaine: 120 μg/mL) and placed onto an agarose support.

For the high-resolution live-imaging acquisitions, zebrafish larvae were maintained under anesthesia (buffered tricaine: 120 μg/mL), embedded in 1,5% low-melting agarose onto the coverslip of a round petridish. Images/videos were then acquired at 28 °C using the Zyla camera of a Dragonfly spinning disk confocal microscope (Andor), 40 μm pinholes and a 60×/1.2-water immersion objective. Acquisitions were performed using the Fusion software, while image/video analysis was made using both IMARIS and ImageJ softwares.

5.4. Toxicity and cell death assays

5.4.1. Toxicity

Zebrafish larvae (3 dpf) were injected as described above with 5 nL of either green, red or far-red fluorescent PLA-NP (0,5%), 20 zebrafish larvae were used per fluorescent PLA-NP. Injected fish were then individually placed into the wells of 24 wells-plates with 2 mL of embryo water per fish. Following 24 h at 28 °C, the number of death was counted, taking into account lethal and sub-lethal phenotypes such as no heart-beat, oedema, malformation and weak blood flow.

5.4.2. Cell death assay

Zebrafish larvae (3 dpf) were injected as described above with 5 nL of either green, red or far-red fluorescent PLA-NP (0,5%), PBS 1× or DMSO 80%. At 30 min and 24 h post-injection, fish were incubated in a solution of acridine orange 10 μg/mL (Sigma) for 20 min. After 3 rinses in embryo water, zebrafish larvae were anesthetized with buffered tricaine (120 μg/mL) and placed onto an agarose support to acquire the total fluorescence associated to acridine orange with a stereomicroscope (Leica DFC365FX – 1.0× planapo lens).

5.5. Histology – light microscopy

Zebrafish larvae were injected with fluorescent PLA-NP (0,5%) as previously described and were euthanized with an overdose of buffered tricaine 30 min, 4 h and 24 h later. They were then immediatly fixed with a solution of methanol-free 4% PFA in hepes buffer 60 mM pH 7,4 for 24 h at room temperature, cryoprotected in a solution of sucrose 30% for 24 h, embedded in Tissue-Tek O.C.T. Compound (Sakura Finetek USA), flash frozen in isopentane, and sectioned using a CM1950 cryostat (Leica). The resulting 30-μm cryosections were recovered on superfrost plus slide (Thermofischer). Obtained sections were counterstained with a solution of phalloidin conjugated with either Dylight-633 or Alexa-647 (3 U/mL - Life technologies), and DAPI (5 μg/mL - Sigma). Sections were then mounted with prolong-glass mounting medium (Life technologies) and cured for 24 h to reach a theoretical refractive index of 1,52. Acquisitions were made using the Zyla camera of a Dragonfly spinning disk confocal microscope (Andor), 40 μm pinholes and a 60×/1.4-oil immersion objective. Acquisitions were performed using features from the Fusion software, while image analysis was made using both IMARIS and ImageJ softwares. Some acquisitions were made using a SP5 confocal microscope (Leica).

5.6. Histology – electron microscopy

Zebrafish larvae were injected with PLA-NP(gold) as previously described and euthanized with an overdose of buffered tricaine 10 min, 30 min, 4 h, 24 h, 72 h, 96 h and one week post-injection. They were then immediately fixed in a solution of glutaraldehyde (1,5%) and PFA (1%) buffered with cacodylate 0,1% pH: 7,4 overnight at 4 °C. Following rinses with a solution of cacodylate 0,1 M / sucrose 8%, samples were incubated 1 h with osmium tetraoxyde. Samples were then rinsed with distilled water, progressively dehydrated with ethanol solutions (30–100%) and embedded in Epon at 60C degree for several days. Following complete polymerization, 60 nm ultrathin sections were realized and mounted onto copper grids. Finally, acquisitions without additional contrast were made using an transmission electron microscope MET PHILIPS CM120 with GATAN Orius200 2Kx2K camera with a maximum resolution of 0,34 nm (Centre Technologique des Microstructures, Lyon, France). Image analysis was made using ImageJ softwares.

5.7. Quantification of PLA-NP internalization by macrophages

5.7.1. Flow cytometry

Transgenic mpeg1:mCherry zebrafish (3 dpf) were intravenously injected with less concentrated green fluorescent PLA-NP (0,25%) to reduce the risk of false-positive event detection due to the presence of non-internalized PLA-NP 10 min post-injection. Fish were euthanized by overdose of buffered tricaine at 4 °C 10 min, 30 min, 2 h, 4 h and 24 h post-injection. For each time-point, 10 larvae per replicate were

injected. Samples were chopped in fine pieces using microscissors and incubated in a solution of versene water (Life Technologies) complemented with trypsine (2 g/L), under constant steering. Samples were then placed onto ice, complemented with fetal calf serum (FCS) to inhibite the digestion and processed through 40 μm cell strainers (Thermofisher). Resulting cell suspensions were centrifugated (400 g, 8 min, 4C degree) and resuspended in PBS 1× with 4% FCS. To allow the exclusion of dead cells, samples were complemented with DAPI (2,5 μg/mL) right before the acquisitions by LSRII (Bioscience) flow cytometer. Acquisitions were analyzed using the FlowJo v7.6.5 software.

5.7.2. Automated quantification

The measuring of macrophage uptake has been previously described in a recent publication [31] using a Fiji MACRO which was also used here.

For this experiment, the zebrafish strain *Tg(mpeg1:mCherry)gl23* [23] having red fluorescently labelled macrophages was used. Five nanoliters of green fluorescent PLA NP were injected in the zebrafish posterior cardinal vein and, by using a Leica stereomicroscope DFC365FX (1.0× planapo lens), images of the whole zebrafish (30×) or the caudal region were taken (120×) at 30 min and 24 h after injection. Using the program Fiji, the fluorescence of the pixels (expressed as RawIntDen) relative to PLA NP that were found in Macrophage positive selection was normalized by the overall fluorescence (also expressed as RawIntDen) and multiplied by 100. The formula can be expressed as follows:

$$\text{Macrophage accumulation } (30\ min \text{ or } 24\ \text{h}) = \frac{Raw\ int\ Den\ Macrophages\ (30\ min, 24h)}{Raw\ Int\ Den\ Whole\ zebrafish\ (30\ min, 24\ h)}\ X\ 100$$

5.8. Statistical analysis

Statistical analyses were performed using GraphPad Prism 8.0.1. Normality of samples was tested using Agostino and Pearson omnibus normality test. For the quantification of PLA-NP internalization by macrophages, populations did not display a normal distribution so a non-parametric one-tailed Mann-Whitney test was carried. For the cell death assay, all populations were displaying a normal distribution, thus we carried a one-way ANOVA coupled with Bonferroni's multiple comparisons *post hoc* analysis. Significance level is indicated as $*p < .05$, $**p < .01$, $***p < .001$, $****p < .0001$.

Supplementary data to this article can be found online at https://doi.org/10.1016/j.jconrel.2021.01.006.

Supplementary material

Declaration of Competing Interest

BV and CP declare financial interest in Adjuvatis. The remaining authors declare no competing financial interest.

Acknowledgement

We thank the Norwegian Research Counsil for funding (FRIMEDBIO-No 144642). This work was also supported by the ANR project Fish-RNAVax (ANR-16-CE20-0002-01 and ANR-16-CE20-0002-03) and by Euronanomed III (Flunanoair).

We thank the PRECI fish facility (L.Bernard and R.Renard), the AniRA-Cytométrie platform (T.Andrieu and S.Dussurgey), the PLATIM-Microscopy plateform of SFR Biosciences Gerland-Lyon Sud (UMS3444/US8). We would also like to thank the Primatiss histology plateform (C.Lethias and N. El Kholti) from IBCP, the CTμ (Centre Technologique des Microstructures) electron microscopy plateform from UCBL, the EM-lab from the university of Oslo (N.Roos and head engineers), the fish facility (AC.Tavara and J.Santana) of NCMM, the Oslo NorMIC imaging plateform (O.Bakke, F.Skjeldal and L.Haugen). We address a special thanks to E.Delaune, S.Essayar, D.Ficheux, V. Bjørnestad, F.Verweij, D.Frei and B.Mathiesen for their advices and assistance.

References

[1] K. Park, Facing the truth about nanotechnology in drug delivery, ACS Nano 7 (2013) 7442–7447, https://doi.org/10.1021/nn404501g.
[2] N. Sharma, P. Madan, S. Lin, Effect of process and formulation variables on the preparation of parenteral paclitaxel-loaded biodegradable polymeric nanoparticles: a co-surfactant study, Asian J. Pharm. Sci. 11 (2016) 404–416, https://doi.org/10.1016/j.ajps.2015.09.004.
[3] P.J. Kennedy, I. Perreira, D. Ferreira, M. Nestor, C. Oliveira, P.L. Granja, B. Sarmento, Impact of surfactants on the target recognition of fab-conjugated PLGA nanoparticles, Eur. J. Pharm. Biopharm. 127 (2018) 366–370, https://doi.org/10.1016/J.EJPB.2018.03.005.
[4] L. Araujo, R. Löbenberg, J. Kreuter, Influence of the surfactant concentration on the body distribution of nanoparticles, J. Drug Target. 6 (1999) 373–385, https://doi.org/10.3109/10611869908996844.
[5] S.K. Sahoo, J. Panyam, S. Prabha, V. Labhasetwar, Residual polyvinyl alcohol associated with poly (d,l-lactide-co-glycolide) nanoparticles affects their physical properties and cellular uptake, J. Control. Release 82 (2002) 105–114, https://doi.org/10.1016/S0168-3659(02)00127-X.
[6] N. Grabowski, H. Hillaireau, J. Vergnaud, N. Tsapis, M. Pallardy, S. Kerdine-Römer, E. Fattal, Surface coating mediates the toxicity of polymeric nanoparticles towards human-like macrophages, Int. J. Pharm. 482 (2015) 75–83, https://doi.org/10.1016/j.ijpharm.2014.11.042.
[7] M. Lamrayah, F. Charriaud, S. Hu, S. Megy, R. Terreux, B. Verrier, Molecular modelling of TLR agonist Pam3CSK4 entrapment in PLA nanoparticles as a tool to explain loading efficiency and functionality, Int. J. Pharm. 568 (2019), https://doi.org/10.1016/j.ijpharm.2019.118569.
[8] C. Primard, N. Rochereau, E. Luciani, C. Genin, T. Delair, S. Paul, B. Verrier, Traffic of poly(lactic acid) nanoparticulate vaccine vehicle from intestinal mucus to sub-epithelial immune competent cells, Biomaterials. 31 (2010) 6060–6068, https://doi.org/10.1016/j.biomaterials.2010.04.021.
[9] K. Park, Drug delivery research: the invention cycle, Mol. Pharm. 13 (2016) 2143–2147, https://doi.org/10.1021/acs.molpharmaceut.6b00015.
[10] M. Barz, Complexity and simplification in the development of nanomedicines, Nanomedicine. 10 (2015) 3093–3097, https://doi.org/10.2217/nnm.15.146.
[11] V. Pavot, N. Climent, N. Rochereau, F. Garcia, C. Genin, G. Tiraby, F. Vernejoul, E. Perouzel, T. Lioux, B. Verrier, S. Paul, Directing vaccine immune responses to mucosa by nanosized particulate carriers encapsulating NOD ligands, Biomaterials. 75 (2016) 327–339, https://doi.org/10.1016/j.biomaterials.2015.10.034.
[12] A.-L. Coolen, C. Lacroix, P. Mercier-Gouy, E. Delaune, C. Monge, J.-Y. Exposito, B. Verrier, Poly(lactic acid) nanoparticles and cell-penetrating peptide potentiate mRNA-based vaccine expression in dendritic cells triggering their activation, Biomaterials 195 (2019) 23–37, https://doi.org/10.1016/J.BIOMATERIALS.2018.12.019.
[13] F. Fenaroli, U. Repnik, Y. Xu, K. Johann, S. Van Herck, P. Dey, F.M. Skjeldal, D. M. Frei, S. Bagherifam, A. Kocere, R. Haag, B.G. De Geest, M. Barz, D.G. Russell, G. Griffiths, Enhanced permeability and retention-like extravasation of nanoparticles from the vasculature into tuberculosis granulomas in zebrafish and mouse models, ACS Nano 12 (2018) 8646–8661, https://doi.org/10.1021/acsnano.8b04433.
[14] F. Fenaroli, D. Westmoreland, J. Benjaminsen, T. Kolstad, F.M. Skjeldal, A. H. Meijer, M. van der Vaart, L. Ulanova, N. Roos, B. Nyström, J. Hildahl, G. Griffiths, Nanoparticles as drug delivery system against tuberculosis in zebrafish embryos: direct visualization and treatment, ACS Nano 8 (2014) 7014–7026, https://doi.org/10.1021/nn5019126.
[15] J. Rességuier, E. Delaune, A.-L. Coolen, J.-P. Levraud, P. Boudinot, D. Le Guellec, B. Verrier, Specific and efficient uptake of surfactant-free poly(lactic acid) nanovaccine vehicles by mucosal dendritic cells in adult zebrafish after bath immersion, Front. Immunol. 8 (2017) 190, https://doi.org/10.3389/fimmu.2017.00190.
[16] L. Treuel, K.A. Eslahian, D. Docter, T. Lang, R. Zellner, K. Nienhaus, G.U. Nienhaus, R.H. Stauber, M. Maskos, Physicochemical characterization of nanoparticles and their behavior in the biological environment, Phys, Chem. Chem. Phys. Phys. Chem. Chem. Phys. 16 (2014) 15053–15067, https://doi.org/10.1039/c4cp00058g.
[17] L. Evensen, P.L. Johansen, G. Koster, K. Zhu, L. Herfindal, M. Speth, F. Fenaroli, J. Hildahl, S. Bagherifam, C. Tulotta, L. Prasmickaite, G.M. Mælandsmo, E. Snaar-Jagalska, G. Griffiths, Zebrafish as a model system for characterization of nanoparticles against cancer, Nanoscale. 8 (2016) 862–877, https://doi.org/10.1039/C5NR07289A.
[18] N.D. Lawson, B.M. Weinstein, In Vivo imaging of embryonic vascular development using transgenic zebrafish, Dev. Biol. 248 (2002) 307–318, https://doi.org/10.1006/dbio.2002.0711.
[19] F. Campbell, F.L. Bos, S. Sieber, G. Arias-Alpizar, B.E. Koch, J. Huwyler, A. Kros, J. Bussmann, Directing nanoparticle biodistribution through evasion and exploitation of Stab2-dependent nanoparticle uptake, ACS Nano 12 (2018) 2138–2150, https://doi.org/10.1021/acsnano.7b06995.
[20] X.-Y. Jiang, C.D. Sarsons, M.J. Gomez-Garcia, D.T. Cramb, K.D. Rinker, S.J. Childs, Quantum dot interactions and flow effects in angiogenic zebrafish (Danio rerio) vessels and human endothelial cells, Nanomed. Nanotechnol. Biol. Med. 13 (2017) 999–1010, https://doi.org/10.1016/J.NANO.2016.12.008.

[21] L.Q. Chen, C.Z. Ding, J. Ling, Intensive epidermal adsorption and specific venous deposition of carboxyl quantum dots in zebrafish early-life stages, Chemosphere. 184 (2017) 44–52, https://doi.org/10.1016/J.CHEMOSPHERE.2017.05.173.
[22] Y. Hayashi, M. Takamiya, P.B. Jensen, I. Ojea-Jiménez, H. Claude, C. Antony, K. Kjaer-Sorensen, C. Grabher, T. Boesen, D. Gilliland, C. Oxvig, U. Strähle, C. Weiss, Differential nanoparticle sequestration by macrophages and scavenger endothelial cells visualized in vivo in real-time and at ultrastructural resolution, ACS Nano (2020), https://doi.org/10.1021/acsnano.9b07233.
[23] F. Ellett, L. Pase, J.W. Hayman, A. Andrianopoulos, G.J. Lieschke, mpeg1 promoter transgenes direct macrophage-lineage expression in zebrafish, Blood. 117 (2011) e49–e56, https://doi.org/10.1182/blood-2010-10-314120.
[24] S.A. Renshaw, C.A. Loynes, D.M.I. Trushell, S. Elworthy, P.W. Ingham, M.K. B. Whyte, A transgenic zebrafish model of neutrophilic inflammation, Blood. 108 (2006) 3976–3978, https://doi.org/10.1182/blood-2006-05-024075.
[25] R. Kalluru, F. Fenaroli, D. Westmoreland, L. Ulanova, A. Maleki, N. Roos, M. Paulsen Madsen, G. Koster, W. Egge-Jacobsen, S. Wilson, H. Roberg-Larsen, G. K. Khuller, A. Singh, B. Nyström, G. Griffiths, Poly(lactide-co-glycolide)-rifampicin nanoparticles efficiently clear Mycobacterium bovis BCG infection in macrophages and remain membrane-bound in phago-lysosomes, J. Cell Sci. 126 (2013) 3043–3054, https://doi.org/10.1242/jcs.121814.
[26] J.-Y. Jeong, H.-B. Kwon, J.-C. Ahn, D. Kang, S.-H. Kwon, J.A. Park, K.-W. Kim, Functional and developmental analysis of the blood–brain barrier in zebrafish, Brain Res. Bull. 75 (2008) 619–628, https://doi.org/10.1016/J.BRAINRESBULL.2007.10.043.
[27] A.G. Kramer-Zucker, S. Wiessner, A.M. Jensen, I.A. Drummond, Organization of the pronephric filtration apparatus in zebrafish requires Nephrin, Podocin and the FERM domain protein mosaic eyes, Dev. Biol. 285 (2005) 316–329, https://doi.org/10.1016/J.YDBIO.2005.06.038.
[28] M. Longmire, P.L. Choyke, H. Kobayashi, Clearance properties of nano-sized particles and molecules as imaging agents: considerations and caveats, Nanomedicine (Lond). 3 (2008) 703–717, https://doi.org/10.2217/17435889.3.5.703.
[29] H.W. Ferguson, M.J. Claxton, R.D. Moccia, E.J. Wilkie, The quantitative clearance of bacteria from the bloodstream of rainbow trout (Salmo gairdneri), Vet. Pathol. 19 (1982) 687–699. http://www.ncbi.nlm.nih.gov/pubmed/7147628 (accessed December 8, 2015).
[30] F.J. Verweij, V. Hyenne, G. Van Niel, J.G. Goetz, Extracellular vesicles: catching the light in Zebrafish, Trends Cell Biol. 29 (2019) 770–776, https://doi.org/10.1016/j.tcb.2019.07.007.
[31] N.K. Dal, A. Kocere, J. Wohlmann, S. Van Herck, T.A. Bauer, J. Resseguier, S. Bagherifam, H. Hyldmo, M. Barz, B.G. De Geest, F. Fenaroli, Zebrafish embryos allow prediction of nanoparticle circulation times in mice and facilitate quantification of nanoparticle–cell interactions, Small 16 (2020) 1906719, https://doi.org/10.1002/smll.201906719.
[32] Y.-L. Hu, W. Qi, F. Han, J.-Z. Shao, J.-Q. Gao, Toxicity evaluation of biodegradable chitosan nanoparticles using a zebrafish embryo model, Int. J. Nanomed. 6 (2011) 3351–3359, https://doi.org/10.2147/IJN.S25853.
[33] M. Furutani-Seiki, Y.J. Jiang, M. Brand, C.P. Heisenberg, C. Houart, D. Beuchle, F. J. van Eeden, M. Granato, P. Haffter, M. Hammerschmidt, D.A. Kane, R.N. Kelsh, M.C. Mullins, J. Odenthal, C. Nüsslein-Volhard, Neural degeneration mutants in the zebrafish, *Danio rerio*, Development. 123 (1996) 229–239. http://www.ncbi.nlm.nih.gov/pubmed/9007243 (accessed July 15, 2019).
[34] S. Sieber, P. Grossen, J. Bussmann, F. Campbell, A. Kros, D. Witzigmann, J. Huwyler, Zebrafish as a preclinical in vivo screening model for nanomedicines, Adv. Drug Deliv. Rev. (2019), https://doi.org/10.1016/J.ADDR.2019.01.001.
[35] F.J. Verweij, C. Revenu, G. Arras, F. Dingli, D. Loew, D.M. Pegtel, G. Follain, G. Allio, J.G. Goetz, P. Zimmermann, P. Herbomel, F. Del Bene, G. Raposo, G. van Niel, Live tracking of inter-organ communication by endogenous exosomes in vivo, Dev. Cell. 1 (2019), https://doi.org/10.1016/J.DEVCEL.2019.01.004, 573-589.e4.
[36] V. Hyenne, S. Ghoroghi, M. Collot, J. Bons, G. Follain, S. Harlepp, B. Mary, J. Bauer, L. Mercier, I. Busnelli, O. Lefebvre, N. Fekonja, M.J. Garcia-Leon, P. Machado, F. Delalande, A.A. López, S.G. Silva, F.J. Verweij, G. van Niel, F. Djouad, H. Peinado, C. Carapito, A.S. Klymchenko, J.G. Goetz, Studying the fate of tumor extracellular vesicles at high spatiotemporal resolution using the zebrafish embryo, Dev. Cell 48 (2019), https://doi.org/10.1016/J.DEVCEL.2019.01.014, 554-572.e7.
[37] S.H.C. Askes, N. Bossert, J. Bussmann, V.S. Talens, M.S. Meijer, R.E. Kieltyka, A. Kros, S. Bonnet, D. Heinrich, Dynamics of dual-fluorescent polymersomes with durable integrity in living cancer cells and zebrafish embryos, Biomaterials. 168 (2018) 54–63, https://doi.org/10.1016/J.BIOMATERIALS.2018.03.037.
[38] K.K. Sørensen, P. McCourt, T. Berg, C. Crossley, D. Le Couteur, K. Wake, B. Smedsrød, The scavenger endothelial cell: a new player in homeostasis and immunity, Am. J. Physiol. Regul. Integr. Comp. Physiol. 303 (2012) R1217–R1230, https://doi.org/10.1152/ajpregu.00686.2011.
[39] R. Kjeken, S.A. Mousavi, A. Brech, T. Gjøen, T. Berg, Fluid phase endocytosis of [125 I]iodixanol in rat liver parenchymal, endothelial and Kupffer cells, Cell Tissue Res. 304 (2001) 221–230, https://doi.org/10.1007/s004410100348.
[40] K. Ohtani, Y. Suzuki, S. Eda, T. Kawai, T. Kase, H. Keshi, Y. Sakai, A. Fukuoh, T. Sakamoto, H. Itabe, T. Suzutani, M. Ogasawara, I. Yoshida, N. Wakamiya, The membrane-type collectin CL-P1 is a scavenger receptor on vascular endothelial cells, J. Biol. Chem. 276 (2001) 44222–44228, https://doi.org/10.1074/jbc.M103942200.
[41] J.S. Suk, Q. Xu, N. Kim, J. Hanes, L.M. Ensign, PEGylation as a strategy for improving nanoparticle-based drug and gene delivery, Adv. Drug Deliv. Rev. 99 (2016) 28–51, https://doi.org/10.1016/j.addr.2015.09.012.
[42] H. Tanisaka, S. Kizaka-Kondoh, A. Makino, S. Tanaka, M. Hiraoka, S. Kimura, Near-infrared fluorescent Labeled Peptosome for application to cancer imaging, Bioconjug. Chem. 19 (2008) 109–117, https://doi.org/10.1021/bc7001665.
[43] K. Klinker, M. Barz, Polypept(o)ides: hybrid systems based on polypeptides and polypeptoids, Macromol. Rapid Commun. 36 (2015) 1943–1957, https://doi.org/10.1002/marc.201500403.
[44] S. Sieber, P. Grossen, P. Uhl, P. Detampel, W. Mier, D. Witzigmann, J. Huwyler, Zebrafish as a predictive screening model to assess macrophage clearance of liposomes in vivo, Nanomed. Nanotechnol. Biol. Med. 17 (2019) 82–93, https://doi.org/10.1016/J.NANO.2018.11.017.
[45] L. Rizzello, J.D. Robertson, P.M. Elks, A. Poma, N. Daneshpour, T.K. Prajsnar, D. Evangelopoulos, J.O. Canseco, S. Yona, H.M. Marriott, D.H. Dockrell, S.J. Foster, B. De Geest, S. De Koker, T. Mchugh, S.A. Renshaw, G. Battaglia, Targeting mononuclear phagocytes for eradicating intracellular parasites, 2017, https://doi.org/10.1101/119297.
[46] J.D. Robertson, J.R. Ward, M. Avila-Olias, G. Battaglia, S.A. Renshaw, Targeting neutrophilic inflammation using polymersome-mediated cellular delivery, J. Immunol. 198 (2017) 3596–3604, https://doi.org/10.4049/JIMMUNOL.1601901.
[47] E. Colucci-Guyon, J.Y. Tinevez, S.A. Renshaw, P. Herbomel, Strategies of professional phagocytes in vivo: unlike macrophages, neutrophils engulf only surface-associated microbes, J. Cell Sci. 124 (2011) 3053–3059, https://doi.org/10.1242/jcs.082792.
[48] J. Ratajczak, M. Wysoczynski, F. Hayek, A. Janowska-Wieczorek, M.Z. Ratajczak, Membrane-derived microvesicles: important and underappreciated mediators of cell-to-cell communication, Leukemia. 20 (2006) 1487–1495, https://doi.org/10.1038/sj.leu.2404296.
[49] F. Jansen, Q. Li, A. Pfeifer, N. Werner, Endothelial- and immune cell-derived extracellular vesicles in the regulation of cardiovascular health and disease, JACC. Basic Transl. Sci. 2 (2017) 790–807, https://doi.org/10.1016/j.jacbts.2017.08.004.
[50] M. Colombo, G. Raposo, C. Théry, Biogenesis, Secretion, and Intercellular interactions of exosomes and other extracellular vesicles, Annu. Rev. Cell Dev. Biol. 30 (2014) 255–289. doi:https://doi.org/10.1146/annurev-cellbio-101512-122326.
[51] G. Camussi, M.C. Deregibus, S. Bruno, V. Cantaluppi, L. Biancone, Exosomes/microvesicles as a mechanism of cell-to-cell communication, Kidney Int. 78 (2010) 838–848, https://doi.org/10.1038/KI.2010.278.
[52] C. Hromada, S. Mühleder, J. Grillari, H. Redl, W. Holnthoner, Endothelial extracellular vesicles—promises and challenges, Front. Physiol. 8 (2017) 275, https://doi.org/10.3389/fphys.2017.00275.
[53] A. Słomka, S.K. Urban, V. Lukacs-Kornek, E. Żekanowska, M. Kornek, Large extracellular vesicles: have we found the holy grail of inflammation? Front. Immunol. 9 (2018) 2723, https://doi.org/10.3389/fimmu.2018.02723.
[54] A. Sartori-Rupp, D. Cordero Cervantes, A. Pepe, K. Gousset, E. Delage, S. Corroyer-Dulmont, C. Schmitt, J. Krijnse-Locker, C. Zurzolo, Correlative cryo-electron microscopy reveals the structure of TNTs in neuronal cells, Nat. Commun. 10 (2019) 342, https://doi.org/10.1038/s41467-018-08178-7.
[55] S. Abounit, C. Zurzolo, Wiring through tunneling nanotubes–from electrical signals to organelle transfer, J. Cell Sci. 125 (2012) 1089–1098, https://doi.org/10.1242/jcs.083279.
[56] D.M. Frei, E. Hodneland, I. Rios-Mondragon, A. Burtey, B. Neumann, J. Bulkescher, J. Schölermann, R. Pepperkok, H.-H. Gerdes, T. Kögel, Novel microscopy-based screening method reveals regulators of contact-dependent intercellular transfer, Sci. Rep. 5 (2015) 12879, https://doi.org/10.1038/srep12879.
[57] R.W. Vandivier, P.M. Henson, I.S. Douglas, Burying the dead: the impact of failed apoptotic cell removal (efferocytosis) on chronic inflammatory lung disease, Chest. 129 (2006) 1673–1682, https://doi.org/10.1378/CHEST.129.6.1673.
[58] S.J. Gardai, K.A. McPhillips, S.C. Frasch, W.J. Janssen, A. Starefeldt, J.E. Murphy-Ullrich, D.L. Bratton, P.-A. Oldenborg, M. Michalak, P.M. Henson, Cell-surface Calreticulin initiates clearance of viable or apoptotic cells through trans-activation of LRP on the phagocyte, Cell. 123 (2005) 321–334, https://doi.org/10.1016/J.CELL.2005.08.032.
[59] L. Jiang, S. Paone, S. Caruso, G.K. Atkin-Smith, T.K. Phan, M.D. Hulett, I.K.H. Poon, Determining the contents and cell origins of apoptotic bodies by flow cytometry, Sci. Rep. 7 (2017) 14444, https://doi.org/10.1038/s41598-017-14305-z.
[60] J.C. Akers, D. Gonda, R. Kim, B.S. Carter, C.C. Chen, Biogenesis of extracellular vesicles (EV): exosomes, microvesicles, retrovirus-like vesicles, and apoptotic bodies, J. Neuro-Oncol. 113 (2013) 1–11, https://doi.org/10.1007/s11060-013-1084-8.
[61] E. Joly, D. Hudrisier, What is trogocytosis and what is its purpose? Nat. Immunol. 4 (2003) 815, https://doi.org/10.1038/ni0903-815.
[62] F. Zeng, A.E. Morelli, Extracellular vesicle-mediated MHC cross-dressing in immune homeostasis, transplantation, infectious diseases, and cancer, Semin. Immunopathol. 40 (2018) 477–490, https://doi.org/10.1007/s00281-018-0679-8.
[63] A.K. Sárvári, Q.-M. Doan-Xuan, Z. Bacsó, I. Csomós, Z. Balajthy, L. Fésüs, Interaction of differentiated human adipocytes with macrophages leads to trogocytosis and selective IL-6 secretion, Cell Death Dis. 6 (2015) e1613, https://doi.org/10.1038/cddis.2014.579.
[64] T. Pham, P. Mero, J.W. Booth, Dynamics of macrophage trogocytosis of rituximab-coated B cells, PLoS One 6 (2011) e14498, https://doi.org/10.1371/journal.pone.0014498.
[65] A.M. Sofias, Y.C. Toner, A.E. Meerwaldt, M.M.T. van Leent, G. Soultanidis, M. Elschot, H. Gonai, K. Grendstad, Å. Flobak, U. Neckmann, C. Wolowczyk, E. L. Fisher, T. Reiner, C.L. Davies, G. Bjørkøy, A.J.P. Teunissen, J. Ochando, C. Pérez-Medina, W.J.M. Mulder, S. Hak, Tumor targeting by αvβ3-integrin-specific lipid

nanoparticles occurs via phagocyte hitchhiking, ACS Nano 14 (2020) 7832–7846, https://doi.org/10.1021/acsnano.9b08693.

[66] A. Kocere, J. Resseguier, J. Wohlmann, F.M. Skjeldal, S. Khan, M. Speth, N.J.K. Dal, M.Y.W. Ng, N. Alonso-Rodriguez, E. Scarpa, L. Rizzello, G. Battaglia, G. Griffiths, F. Fenaroli, Real-time imaging of polymersome nanoparticles in zebrafish embryos engrafted with melanoma cancer cells: Localization, toxicity and treatment analysis, EBioMedicine 58 (2020) 102902, https://doi.org/10.1016/j.ebiom.2020.102902.

[67] D. Lamalle-Bernard, S. Munier, C. Compagnon, M.-H. Charles, V.S. Kalyanaraman, T. Delair, B. Verrier, Y. Ataman-Onal, Coadsorption of HIV-1 p24 and gp120 proteins to surfactant-free anionic PLA nanoparticles preserves antigenicity and immunogenicity, J. Control. Release 115 (2006) 57–67, https://doi.org/10.1016/j.jconrel.2006.07.006.

[68] V. Pavot, N. Rochereau, C. Primard, C. Genin, E. Perouzel, T. Lioux, S. Paul, B. Verrier, Encapsulation of Nod1 and Nod2 receptor ligands into poly(lactic acid) nanoparticles potentiates their immune properties, J. Control. Release 167 (2013) 60–67, https://doi.org/10.1016/j.jconrel.2013.01.015.

PAPER IV

© 2022. Published by The Company of Biologists Ltd | Disease Models & Mechanisms (2022) 15, dmm049147. doi:10.1242/dmm.049147

RESEARCH ARTICLE

The zebrafish embryo as an *in vivo* model for screening nanoparticle-formulated lipophilic anti-tuberculosis compounds

Nils-Jørgen Knudsen Dal[1,*], Martin Speth[1,*,‡], Kerstin Johann[2], Matthias Barz[2,3], Claire Beauvineau[4], Jens Wohlmann[1], Federico Fenaroli[1], Brigitte Gicquel[5,6], Gareth Griffiths[1] and Noelia Alonso-Rodriguez[1,‡]

ABSTRACT

With the increasing emergence of drug-resistant *Mycobacterium tuberculosis* strains, new and effective antibiotics against tuberculosis (TB) are urgently needed. However, the high frequency of poorly water-soluble compounds among hits in high-throughput drug screening campaigns is a major obstacle in drug discovery. Moreover, *in vivo* testing using conventional animal TB models, such as mice, is time consuming and costly, and represents a major bottleneck in lead compound discovery and development. Here, we report the use of the zebrafish embryo TB model for evaluating the *in vivo* toxicity and efficacy of five poorly water-soluble nitronaphthofuran derivatives, which were recently identified as possessing anti-TB activity *in vitro*. To aid solubilization, compounds were formulated in biocompatible polymeric micelles (PMs). Three of the five PM-formulated nitronaphthofuran derivatives showed low toxicity *in vivo*, significantly reduced bacterial burden and improved survival in infected zebrafish embryos. We propose the zebrafish embryo TB-model as a quick and sensitive tool for evaluating the *in vivo* toxicity and efficacy of new anti-TB compounds during early stages of drug development. Thus, this model is well suited for pinpointing promising compounds for further development.

KEY WORDS: Zebrafish tuberculosis model, Anti-tuberculosis drugs, Nanoparticles, *In vivo* toxicity, *In vivo* efficacy

INTRODUCTION

Tuberculosis (TB), caused by the bacterium *Mycobacterium tuberculosis* (Mtb), is one of the deadliest infectious diseases worldwide. Annually, ten million people fall ill with TB, of whom ∼1.4 million die (World Health Organization, 2020). Reducing the total burden of TB is difficult due to the extensive reservoir of latently infected individuals who are at risk of developing active disease in their lifetime (Houben and Dodd, 2016). The alarming increase in cases of drug-resistant TB in recent years highlights the urgency for new effective anti TB-drugs or regimens that will shorten the duration of treatment and improve cure rates (Lange et al., 2018; World Health Organization, 2020).

In recent years, the use of phenotypic high throughput screening (HTS) of large-scale compound libraries against whole-cell Mtb or surrogate mycobacteria, such as *Mycobacterium bovis* BCG, has proven to be a powerful strategy in the quest to identify new anti-TB drug candidates. Phenotypic HTS has resulted in the discovery of recently approved anti-TB drugs, such as bedaquiline, pretomanid and delamanid, as well as other anti-TB drug candidates currently in clinical trials (Grzelak et al., 2019). However, the phenotypic HTS approach has been shown to be inherently biased towards identifying lipophilic, and thus less water-soluble, molecules (Goldman, 2013). Indeed, lipophilicity is positively correlated with anti-mycobacterial activity, likely due to the fact that the thick lipid-rich and waxy cell wall structure of Mtb constitutes a close to impenetrable barrier for hydrophilic molecules (Machado et al., 2018). However, high lipophilicity and low water solubility is considered to be a ‘red flag’ in medicinal chemistry due to the potential negative effects on absorption, distribution, metabolism and elimination, which are often associated with toxic properties of candidate compounds (Lipinski, 2000; Tarcsay and Keseru, 2013; Waring, 2010). Such compounds are either rejected from the drug discovery process at early stages or are subjected to chemical modifications, with the aim of reducing their lipophilic nature and increasing their water solubility, thus making them easier to administer and improving their bioavailability (Di et al., 2012). However, alteration of the drug structure presents the risk of reducing the anti-mycobacterial activity (Kondreddi et al., 2013; Manjunatha and Smith, 2015).

In recent years, nanoparticle technology has emerged as a promising alternative approach to improve unfavorable pharmacokinetic characteristics and the low bioavailability of poorly water-soluble compounds (Kirtane et al., 2021). By virtue of their ability to encapsulate drugs in their matrix or core, nanoparticle-based formulations increase the bioavailability of lipophilic drugs and reduce drug-related toxicity (Kirtane et al., 2021; Melariri et al., 2015; Vibe et al., 2016). Importantly, nanoparticles can be designed to release their drug load in a sustained manner, thereby maintaining systemic levels above the minimum effective concentration over prolonged periods and, as a consequence, increasing the efficacy of drugs compared to the application of the free drugs alone (Griffiths et al., 2010; Sharma et al., 2004).

In many cases, overcoming poor solubility is a major challenge when progressing lipophilic drug candidates to the preclinical test stage and, in particular, to efficacy studies in animal models of TB. The *in vivo* efficacy of new anti-TB drug candidates is

[1]Department Biosciences, Faculty of Mathematics and Natural Sciences, University of Oslo, 0371 Oslo, Norway. [2]Department of Chemistry, Johannes Gutenberg University Mainz, 55128 Mainz, Germany. [3]Division of BioTherapeutics, Leiden Academic Center for Drug Research (LACDR), Leiden University, 2333 Leiden, The Netherlands. [4]Chemical Library Institut Curie/CNRS, CNRS UMR9187, INSERM U1196 and CNRS UMR3666, INSERM U1193, Université Paris-Saclay, F-91405 Orsay, France. [5]Unité de Génétique Mycobactérienne, Dep Génomes and Génétique, Institute Pasteur, 75015 Paris, France. [6]Department of Tuberculosis Control and Prevention, Shenzhen Nanshan Center for Chronic Disease Control, 518054 Shenzhen, China.
*These authors contributed equally to this work

‡Authors for correspondence (martin.speth@ibv.uio.no; n.a.rodriguez@ibv.uio.no)

N.D., 0000-0002-4952-4548; M.S., 0000-0002-3338-9820; F.F., 0000-0002-9060-8786; N.A.R., 0000-0001-6816-7892

Handling Editor: David M. Tobin
Received 18 June 2021; Accepted 16 November 2021

Disease Models & Mechanisms (2022) 15, dmm049147. doi:10.1242/dmm.049147

predominately assessed in conventional mouse or guinea pig models of TB. These *in vivo* studies are generally costly, time consuming and require advanced biosafety level-3 research and animal facilities, thereby representing a considerable bottleneck in the drug discovery process (Andreu et al., 2013; Balganesh et al., 2004). In recent years, the zebrafish embryo (*Danio rerio*) has been established as a powerful alternative *in vivo* TB model. Infection of zebrafish embryos with the natural fish pathogen *Mycobacterium marinum* (Mm), a genetically close relative of Mtb, results in disease that recapitulates many key features of the early stages of Mtb infection. Taking advantage of the transparent nature of the zebrafish embryo, major new insights have been achieved into the interaction of mycobacterial pathogens with host cells during early phases of infection (Davis et al., 2002; Johansen et al., 2018; Tobin and Ramakrishnan, 2008; Volkman et al., 2004). Moreover, the zebrafish TB model has been used to evaluate the *in vivo* efficacy of anti-TB drug candidates (Carvalho et al., 2011; Dalton et al., 2017; Makarov et al., 2014; Ordas et al., 2015; Takaki et al., 2012). The zebrafish embryo is also a well-established model organism in toxicology research, and has been widely used to evaluate the *in vivo* toxicity of candidate drugs against a variety of diseases, such as epilepsy, cancer and bacterial infections (Cassar et al., 2020). Embryos can be conveniently kept in multiwell dishes and have been successfully used in numerous high-throughput toxicology screening studies, such as those focusing on cardiotoxicity, hepatotoxicity and adverse behavioral effects (Cornet et al., 2017; Dyballa et al., 2019; Zhang et al., 2017).

In previous work, our group has used the zebrafish embryo model to characterize the toxicity and the efficacy of anti-TB drug-loaded nanoparticles against Mm *in vivo* (Fenaroli et al., 2014; Vibe et al., 2016). This system also allowed us to monitor important parameters of nanoparticles in live animals, such as their persistence and stability in the blood circulation, interaction with host immune cells, biodistribution and dynamics of accumulation at the infection sites, the granulomas. Importantly, a number of key findings from the zebrafish model could be replicated in Mtb-infected mice; in particular, nanoparticles in both model systems exhibited similar accumulation in granulomas and comparable stability in the bloodstream (Dal et al., 2020; Fenaroli et al., 2018).

In this study, we demonstrate the use of the zebrafish embryo to evaluate both *in vivo* toxicity and *in vivo* anti-mycobacterial efficacy of nitronaphthofuran (nNF) compounds that were previously identified to be active against Mtb in a phenotypic HTS at the Institute Pasteur (Paris, France, data not published). The five most promising nNF-derivatives showing potent anti-TB *in vitro* activity (MIC_{90}<8 µg/ml) were selected for this study. As the water solubility of the selected derivatives is low (<12 µg/ml), we opted for formulating the compounds in biocompatible polymeric micelles (PMs), primarily to aid their solubilization and to be able to administer therapeutic doses in the zebrafish embryo model without the use of toxic solvents. Importantly, we delivered the candidate drugs directly into the blood circulation of zebrafish embryos by intravenous injection, thereby circumventing absorption issues associated with delivery by bath immersion, as used in most previously published studies. By using a set of complementary *in vivo* assays we were then able to pinpoint the most promising nNF candidates for further development in the drug discovery process.

RESULTS

In this study we made use of the zebrafish embryo model to evaluate the *in vivo* toxicity and efficacy of new anti-TB compounds, which were initially identified in a previous phenotypic high-throughput screening at the Institute Pasteur (Paris, France). The strategy and methods we used are summarized in Fig. 1 and included *in vitro* cell culture based assays, as well as several complementary assays for *in vivo* toxicity and efficacy in the zebrafish embryo.

In vitro activity of nNF – derivatives against extracellular and intracellular *M. marinum*

As we aimed to evaluate the *in vivo* efficacy of these compounds in the zebrafish TB model using Mm, we first assessed their activity against extracellular Mm in a minimum inhibitory concentration (MIC) assay. We tested five novel nNF derivatives, the molecular structures of which are characterized by a furan ring bearing a nitro group (Fig. 2A). All of them were found to be potent against extracellular Mm, with MIC_{90} values ranging from 0.016 to 0.5 µg/ml (Fig. 2B). To test their activity against intracellular Mm, we treated Mm-infected mouse bone marrow-derived macrophages (BMDMs) with the nNF compounds and the established anti-TB drug rifampicin (RIF), and enumerated intracellular bacteria by counting colony-forming units (CFUs). At the tested concentration range – from 0.125× to 32× the corresponding MIC_{90} – none of the nNF compounds showed cytotoxic effects in BMDM cultures (Fig. S1). With the exception of C20 and RIF, all compounds showed significant efficacy against intracellular Mm with a 2-4 log reduction in bacterial burden at 2× the MIC_{90} (Fig. 2C). Higher concentrations (8× the MIC_{90}) resulted in almost complete eradication of intracellular Mm, with no detectable bacterial colonies in the case of C7 and C12. Compound C20, despite being highly effective against extracellular Mm, showed relatively low efficacy against intracellular Mm within the studied concentration range. In general, compounds C4, C7, C11 and C12 showed comparable activity against intracellular and extracellular Mm, with an IC_{90} (90% inhibitory concentration) against intracellular bacteria lower or equivalent to their respective MIC_{90} (Table S1). In contrast, C20 and RIF showed significantly lower activity against intracellular Mm, with a 26× and 9× higher IC_{90} than their MIC_{90}, respectively.

Formulation of nNF-derivatives and RIF in PMs

The low water solubility of the selected nNF-derivatives (predicted to be between 0.6 and 12 µg/ml) did not allow us to inject therapeutic doses without the use of toxic concentrations of solvents, such as DMSO (data not shown). Therefore, in order to evaluate them in the zebrafish embryo, we opted to encapsulate the nNF-derivatives in biocompatible and biodegradable polypept(o)ide block copolymer [pGlu(OBn)-block-pSar] using dual asymmetric centrifugation. This produced drug-encapsulated PMs with a size (diameter) between 84 and 149 nm, a narrow size distribution (polydispersity index≤0.15) and a slightly negative surface charge ranging from −3.7 mV to −2.5 mV, as measured by zeta-potential (Table S2). By employing this strategy, we were able to significantly increase compound solubility and therefore inject zebrafish embryos with the candidate compounds in a therapeutic dose range, avoiding the use of toxic solvents.

In vivo toxicity of PM-formulated nNF derivatives in the zebrafish embryo

The *in vivo* toxicity of the PM-formulated compounds was tested in zebrafish embryos using a mortality assay after the injection of different doses into the posterior caudal vein (PCV). As expected, PM-C16 was highly toxic and induced significant mortality at the lowest administered dose (5 mg/kg; Fig. 3). Similarly, PM-C20 and PM-C4 showed significant toxicity in zebrafish embryos, causing more than 50% of mortality at concentrations of 10 and 20 mg/kg,

Disease Models & Mechanisms (2022) 15, dmm049147. doi:10.1242/dmm.049147

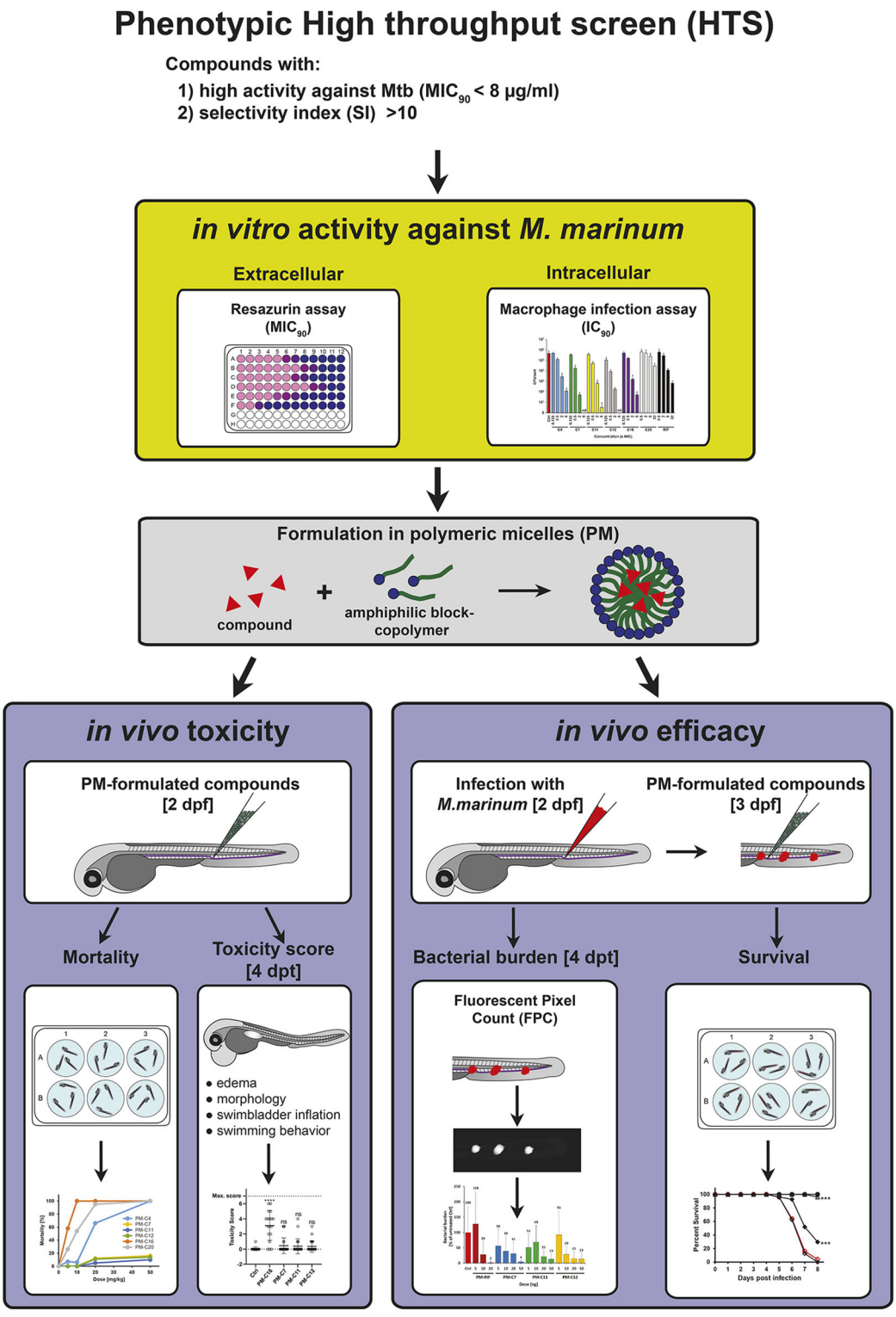

Fig. 1. Schematic summary of the strategy used to evaluate the *in vivo* toxicity and anti-mycobacterial efficacy of HTS-identified lipophilic compounds using the zebrafish embryo model. Candidate compounds with significant anti-mycobacterial activity were identified in a phenotypic HTS campaign using chemical libraries and selected for further evaluation based on their *in vitro* activity against Mtb (MIC_{90}), and their selectivity index (SI). Prior to *in vivo* testing in the zebrafish TB model using the fish pathogen Mm, candidate compounds were tested for their *in vitro* activity against extracellular Mm using a resazurin assay and against intracellular bacteria in mouse macrophages using a CFU assay. Then, candidate compounds were formulated in PMs, primarily to enhance solubility and to enable intravenous injection in the zebrafish embryo. The *in vivo* toxicity of PM-formulated compounds was first evaluated by mortality analysis after a single injection of different doses at 8 days post treatment (dpt), and compounds with significant toxicity were excluded from further analysis. PM-formulated compounds showing low mortality were then characterized in more detail by assigning a toxicity score to individual embryos at 4 dpt based on different morphological and physiological indicators of toxicity, as outlined in Materials and Methods. For the evaluation of *in vivo* efficacy, zebrafish embryos were infected with Mm and treated with different doses of PM-formulated compounds. Therapeutic efficacy was then assessed by bacterial burden (FPC) at 4 dpt and by survival analysis. dpf, days post fertilization.

Disease Models & Mechanisms (2022) 15, dmm049147. doi:10.1242/dmm.049147

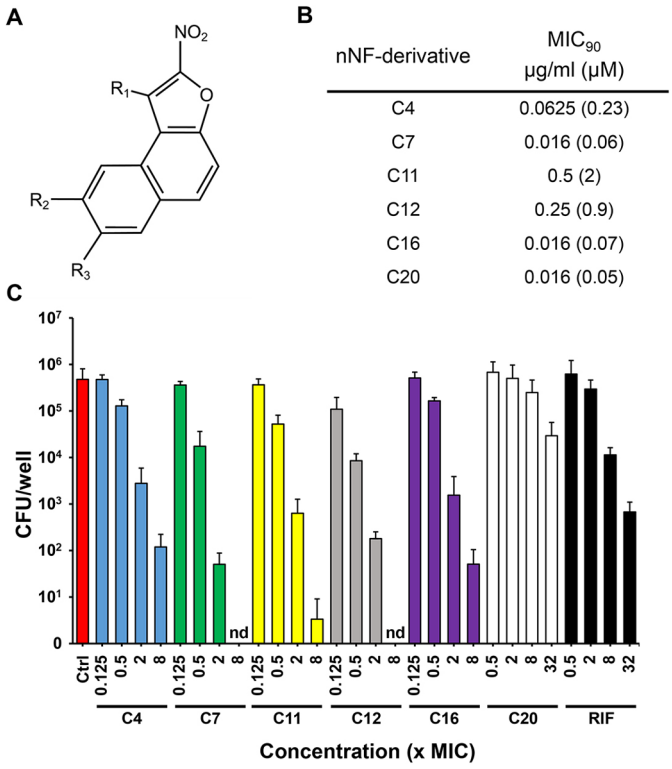

Fig. 2. *In vitro* anti-mycobacterial activity of nNF derivatives against extracellular and intracellular Mm. (A) The nitroaromatic backbone structure of the nNF compounds tested in this study. (B) Activity of nNF derivatives against extracellular Mm determined by MIC_{90}. (C) Anti-mycobacterial activity of nNF derivatives and RIF against intracellular Mm in murine BMDMs. BMDM cultures were infected with Mm at 32.5°C at a MOI of 0.1 and treated with nNF derivatives at different concentrations based on their MIC_{90}. Intracellular mycobacterial burden was determined by CFU plating at 4 days post infection. Data represent the mean±s.d. of three independent experiments. nd, not detected.

respectively, and 100% mortality at 50 mg/kg. Both PM-C4 and PM-C20 were therefore excluded from subsequent analysis. In contrast, PM-C7, PM-C11 and PM-C12 showed low levels of toxicity, with mortality not exceeding 16% at the highest dose tested (50 mg/kg). Unloaded PMs by themselves had no toxic effects and did not induce mortality in injected zebrafish embryos (Fig. S2).

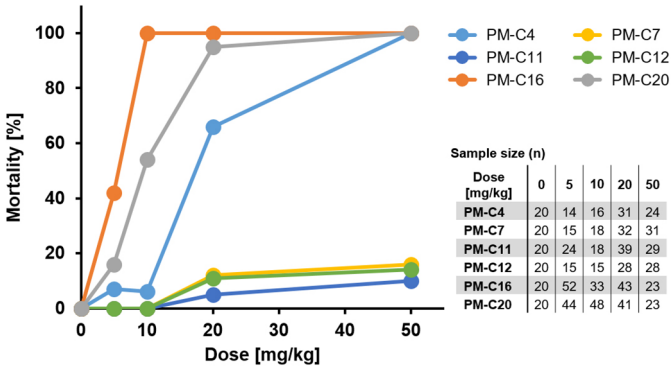

Fig. 3. Evaluation of the *in vivo* toxicity of PM-formulated nNF derivatives in zebrafish embryos by mortality analysis. Zebrafish embryos were treated with different doses of PM-formulated nNF derivatives by intravenous injection, and mortality was recorded at 8 dpt. Results are pooled from at least three independent experiments.

To determine whether the selected compounds PM-C7, PM-C11 and PM-C12 could induce sublethal toxicity in embryos, we set up a sensitive toxicity scoring system based on well-established physiological and behavioral toxicity indicators (Table 1). These features are readily observable in embryos and include malformed or curved body shape, lack of swim bladder inflation, slow or absent blood flow and formation of edemas (Fig. 4A). When tested at their highest dose (50 mg/kg), the three selected compounds did not cause significantly higher sublethal toxic effects compared to the non-injected or PBS-injected control embryos (Fig. 4B). Compound-treated groups displayed a slightly higher mean toxicity score than the mock-injected control, which was due to the higher frequency of embryos with a toxicity score of 1 lacking an inflated swim bladder. A few cases of embryos with a toxicity score of 2 to 4, mainly characterized by a lack of an inflated swim bladder, deficient equilibrium and reduced escape response, were also observed.

In contrast, PM-C16, included as a positive toxicity control, showed a significantly higher toxicity score than the PBS-injected control, at a 10× lower dose (5 mg/kg). In conclusion, PM-C7, PM-C11 and PM-C12 proved to be non-toxic *in vivo*, whereas PM-C4 and PM-C20 were excluded from further analysis due to their significant toxicity.

Evaluation of three experimental methods to determine the bacterial burden in the zebrafish TB model

We initially compared three different methods for evaluating the ability of PM-formulated compounds to reduce the bacterial burden in Mm-infected embryos. Using the three methods in sequence in the same experiment allowed us to directly compare them to each other. First, bacterial burden in individual Mm-dsRed infected embryos was quantified by fluorescence pixel count (FPC) based on the total bacteria-associated fluorescence intensity. Then, embryos within the treatment groups were pooled and homogenized, and the total level of bacterial fluorescence was measured using a plate reader. Finally, the bacterial burden was enumerated by classic CFU plating of the homogenized embryos. Overall, the three methods produced comparable results (Fig. 5A-C), which was reflected in the high degree of correlation observed between them (Fig. 5D-F). Levels of bacterial burden obtained by CFU assay were generally lower than the two other methods, and all three compounds showed a clear dose-dependent efficacy in reducing the number of intracellular bacteria.

In vivo efficacy of PM-formulated nNF derivatives in the zebrafish TB model

Given the excellent concordance between the three methods, we decided to use FPC to evaluate the efficacy of PM-formulated C7, C11, C12 and RIF at a broader range of doses (Fig. 6). All three nNF compounds reduced bacterial burden in infected fish in a dose-dependent manner, consistently showing a significant reduction of bacterial levels at doses of 20 and 50 mg/kg. Compared to treatment with PM-RIF, which was highly effective at a dose of 20 mg/kg, the three tested nNF compounds achieved comparable results at 50 mg/kg, the highest dose tested. Consistent with previous reports by our group (Fenaroli et al., 2014; Trousil et al., 2019), formulation in nanoparticles slightly improved the *in vivo* efficacy of RIF compared to its free form, as measured by bacterial burden in infected zebrafish embryos (data not shown). However, it is unknown whether this is also the case for nNF compounds as it was not possible to test their free form in the zebrafish TB model without the use of high concentrations of toxic solvents.

Disease Models & Mechanisms (2022) 15, dmm049147. doi:10.1242/dmm.049147

Table 1. Toxicity indicators and criteria for scoring

Toxicity indicators	Criteria for scoring drug toxicity	
	0	1
Equilibrium	Upright	Sideways
Escape response to light touch	Quick	Slow or none
Body shape	Normal (straight)	Malformed; curved
Blood flow	Normal	Slow or not in all body parts
Heartbeat	Normal	Irregular; very slow or fast
Edema	Absent	Present
Swim bladder inflation	Normal	Small or absent

In a final step, we analyzed the ability of the PM-formulated compounds to improve survival in Mm-infected embryos. All compounds significantly improved survival (66%-70%) at 8 days post infection at the highest dose (50 mg/kg) (Fig. 7). In contrast, nearly 100% of untreated embryos succumbed to the infection at the endpoint of the survival assay. However, none of the three compounds showed efficacy comparable to PM-formulated RIF, which achieved more than 95% survival at a dose of 20 mg/kg. Unloaded PMs by themselves had no therapeutic effect and did neither reduce bacterial burden nor improve survival in infected embryos (Fig. S3).

In summary, of the initial six selected nNF-derivatives, three compounds (C4, C16 and C20) were excluded from the study due to their toxicity *in vivo*. The remaining three derivatives (C7, C11 and C12) showed minimal *in vivo* toxicity, effectively reduced bacterial burden and improved survival in Mm-infected zebrafish embryos.

DISCUSSION

In the treatment of TB, the need for new antibiotics can only be described as urgent (Bandodkar et al., 2020). Phenotypic HTS of large chemical libraries using Mtb or surrogate mycobacteria provide a powerful approach for the discovery of new compounds with anti-TB activity. Those compounds may target new molecular mechanisms in the pathogen, which is especially important for the development of new drugs for the treatment of drug-resistant TB (Wellington and Hung, 2018). On the downside, this approach tends to be biased towards identifying a high proportion of hydrophobic and less water-soluble compounds, which are often difficult to evaluate in the subsequent drug discovery process (Di et al., 2012; Keseru and Makara, 2009; Lipinski, 2000). Encapsulation of hydrophobic molecules in polymer-based nanoparticles offers a powerful solution that is well suited for solubilizing even highly hydrophobic drugs without the use of potentially toxic excipients. In addition, encapsulation of drugs in nanoparticles has been found to reduce drug-related toxicity and improve pharmacokinetic characteristics and bioavailability (Kirtane et al., 2021; Melariri et al., 2015; Vibe et al., 2016). There exists a plethora of nanoparticles for drug delivery, ranging from inorganic to lipid-based and polymeric nanoparticles, which can display a wide range of characteristics and functionalities (Griffiths et al., 2010; Mitchell et al., 2021). Nanoparticles are increasingly being explored as a substitute for conventional pharmaceutical methods for enhancing drug solubility, such as dry or wet milling, the use of surfactants or solid dispersion preparation. Both lipid-based liposomes and polymer-based nanoparticles, such as solid poly-lactic-co-glycolic acid nanoparticles and PMs, have been found to be suitable for the delivery of anti-TB drugs (Grotz et al., 2018). In this study, we have formulated a set of poorly water-soluble nNF compounds with potent anti-TB activity in PMs in order to enhance their solubility, and evaluated their *in vivo* toxicity and anti-mycobacterial efficacy in the zebrafish embryo model. nNFs are aromatic molecules characterized by a nitro group attached to an aromatic ring, a chemical structure they have in common with clinically approved antibiotics, such as nitrofurans like nifurtimox and the new-generation TB drugs delamanid and pretomanid (Rice et al., 2021). These antibiotics are prodrugs that require bioactivation by specific microbial nitroreductases, leading to the release of the highly reactive radical nitric oxide and subsequent damage of microbial DNA, lipids and proteins (Gurumurthy et al., 2012; Hall et al., 2011; Patterson and Fairlamb, 2019; Singh et al., 2008). Whether the activity of nNF compounds against Mtb is based on a similar mode of action is currently being investigated by our group.

It is increasingly recognized that the zebrafish embryo model is a valuable tool for evaluating both the *in vivo* toxicity and efficacy of new drug candidates, thereby bridging the gap between *in vitro* assays and laborious mammalian *in vivo* studies

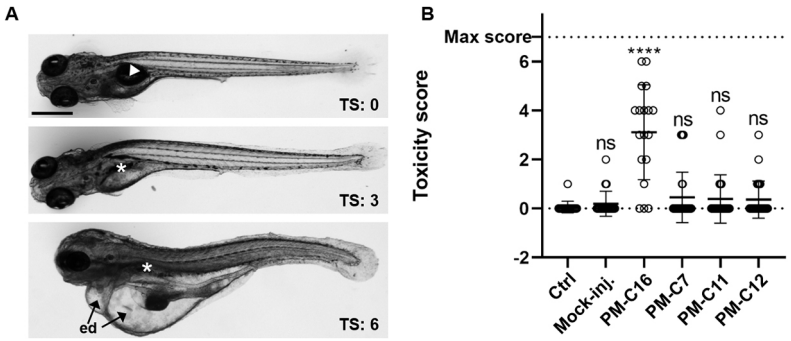

Fig. 4. Evaluation of the *in vivo* toxicity of PM-formulated nNF derivatives in zebrafish embryos by toxicity score. Zebrafish embryos were injected with high doses (50 mg/kg) of PM-formulated C7, C11 and C12, or 5 mg/kg of PM-C16, and the toxicity score (TS) was determined at 4 dpt in individual embryos based on morphological and physiological indicators of toxicity, as specified in Table 1. (A) Representative images of embryos with different toxicity scores displaying normally inflated (arrowhead) or lack of inflated swim bladder (*), severe edemas (ed) and abnormally curved body shape (bottom image). Scale bar: 500 µm. (B) Toxicity scores in embryos injected with PM-formulated compounds. Non-injected (ctrl) and mock (PBS)-injected embryos were used as negative toxicity controls, and embryos injected with PM-C16 as a positive toxicity control. Each symbol represents the toxicity score of an individual larvae and the mean for each group is shown as a horizontal line with error bars denoting the s.d. Ctrl, n=18; Mock-inj., n=21; C16, n=18; C7, n=31; C11, n=26; C12, n=25); ***P<0.001 compared with the non-injected control (ctrl); ns, not significant (non-parametric Kruskal–Wallis H test followed by post-hoc analysis using Dunn's multiple comparisons test).

Disease Models & Mechanisms (2022) 15, dmm049147. doi:10.1242/dmm.049147

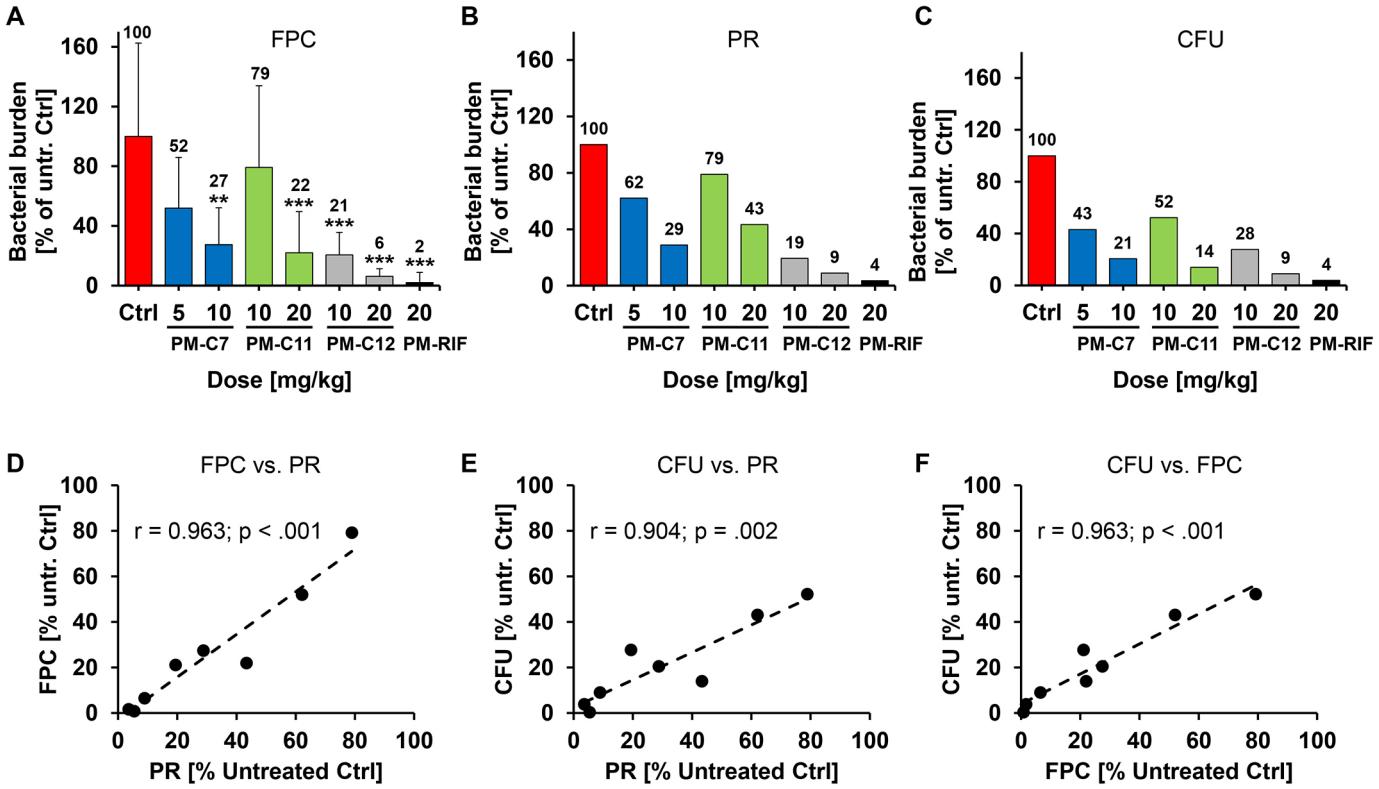

Fig. 5. Quantification of bacterial burden in Mm-infected zebrafish embryos after treatment with PM-formulated nNF derivatives by three different methods. Mm-dsRed-infected zebrafish embryos were treated with the indicated doses of the PM-formulated nNF derivates C7, C11, C12 or PM-formulated RIF by intravenous injection, and bacterial burden was quantified at 4 dpt by three different assays. (A) FPC: untreated or treated embryos were imaged and the total bacterial fluorescence intensity was determined by FPC for individual embryos. Data are mean±s.d. of data normalized to the untreated control (ctrl) pooled from at least three independent experiments (Ctrl, *n*=71; PM-C7 5 mg/kg, *n*=13, and 10 mg/kg, *n*=15; PM-C11 10 mg/kg, *n*=15, and 20 mg/kg, *n*=18; PM-C12 10 mg/kg, *n*=45, and 20 mg/kg, *n*=49; and PM-RIF 20 mg/ml, *n*=51). ***P*<0.01, ****P*<0.001 (non-parametric Kruskal–Wallis H test followed by post-hoc analysis using Dunn's multiple comparisons test). (B) Plate reader (PR) assay: embryos in each treatment group or the untreated control were pooled and homogenized, and fluorescence intensity was measured using a plate reader. (C) CFU count: bacterial burden was enumerated by plating serial dilutions of the pooled homogenate on 7H10 plates. Results in B and C are shown as a percentage relative to the untreated control and represent data from one experiment. The mean values of each group in A-C are displayed above the columns. (D-F) Correlation between the normalized bacterial burden for all four compounds obtained by the three methods. Linear regression plots comparing FPC with the PR assay (D), CFU with the PR assay (E) and CFU with the FPC assay (F). Pearson's coefficient of correlation (r) with *P*-value are denoted in the individual figures.

in the drug discovery process (MacRae and Peterson, 2015). Low space requirements and costs for husbandry, their small size, high fecundity and rapid development makes the zebrafish a very attractive model for large-scale studies on drug effects, i.e. *in vivo* toxicity and activity. In such studies, the drugs to be tested have been almost invariably administered to the embryos in the fish water by bath immersion. Although technically easy and convenient, this way of drug delivery is associated with major limitations, especially when studying poorly water-soluble drugs (Cassar et al., 2020). First, it is not possible to deliver defined doses of drugs to the embryo as the degree and route of drug absorption (e.g. via skin, gills or gastro-intestinal tract) is mostly unknown. Second, compounds with low water solubility may be difficult to test at all, or be tested at concentrations high enough to achieve therapeutic concentrations in the embryo. Ordas et al. (2015) have addressed this problem by quantifying the amount of the adsorbed anti-TB drugs in the yolk of bath immersion-treated embryos by mass spectrometry and indirectly relating that value to the observed therapeutic activity in the zebrafish TB model. They found that the degree of uptake was positively correlated to the lipophilicity of the drugs, which also affected the efficacy of the drugs in the zebrafish embryo TB model.

In contrast, in our study, we directly administered candidate drugs to the zebrafish embryos by intravenous injection after encapsulation in nanoparticles, thereby avoiding the above-mentioned issues associated with administration by bath immersion. This approach enabled us to administer precise and reproducible doses of lipophilic compounds with low water solubility, which otherwise would have been difficult to test in the zebrafish larvae. Although in principle possible, the administration of nanoparticle-formulated drugs by bath immersion would face the same issues, i.e. unclear route and degree of drug uptake in the embryos, thus making such experiments generally difficult to interpret. Additionally, drug administration by intravenous injection requires only minimal amounts of compounds, which is especially advantageous when these are used directly from chemical libraries and are only available in limited amounts. Specifically, only a few milligrams are needed to test compounds in the zebrafish embryo, and the result can facilitate the decision to resynthesize a specific compound in larger amounts for testing in mammalian *in vivo* models.

The zebrafish embryo is one of the most sensitive and rapid monitors of drug toxicity, and is widely used for studying adverse drug effects (Cassar et al., 2020). It provides valuable and rapidly obtainable information about the *in vivo* toxicity of compounds, and

Disease Models & Mechanisms (2022) 15, dmm049147. doi:10.1242/dmm.049147

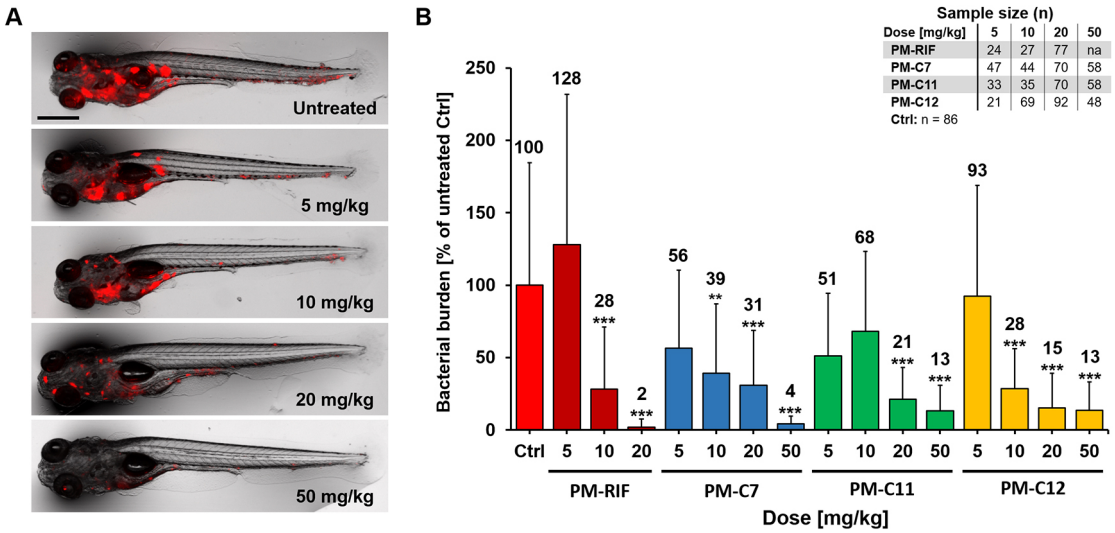

Fig. 6. Evaluation of the *in vivo* efficacy of PM-formulated nNF derivatives in the zebrafish TB model. Zebrafish embryos were infected with Mm-dsRed and treated with different doses of the PM-formulated nNF derivates C7, C11, C12 or PM-formulated RIF by intravenous injection. (A) Representative images of Mm-infected embryos treated with different doses of PM-C7 at 4 dpt. Scale bar: 500 µm. (B) Quantification of bacterial burden by FPC at 4 dpt in embryos treated with the indicated doses of the PM-formulated compounds or RIF. FPC values of individual embryos were normalized to the untreated control (ctrl) group and results are presented as mean±s.d. Results are pooled from at least three independent experiments. The mean values of each group are displayed above the columns. na, not applicable. ***P*<0.01, ****P*<0.001 (non-parametric Kruskal–Wallis H test followed by post-hoc analysis using Dunn's multiple comparisons test).

can be used to screen for, and subsequently discard, toxic compounds early in the drug discovery process. However, in many studies, drug toxicity is still tested exclusively in *in vitro* cell culture systems, which does not allow a reliable extrapolation of drug toxicity to the *in vivo* situation. Our data here provide a clear example of this problem: although the nNF-compound C4 showed minimal toxicity in the cell-based *in vitro* assay, it was highly toxic in the zebrafish embryo, as seen in the mortality assay.

In addition to the mortality assay, which allowed us to identify two of the tested compounds (C4 and C20) as being significantly toxic *in vivo*, we have further defined a simplified toxicity score system in the zebrafish embryo based on previous studies (Palha et al., 2013; Vibe et al., 2016). Using this sensitive toxicity scoring system, we could confirm the low *in vivo* toxicity of the compounds C7, C11 and C12 at the maximum concentration tested (50 mg/kg). Our toxicity score system is uncomplicated and can be further

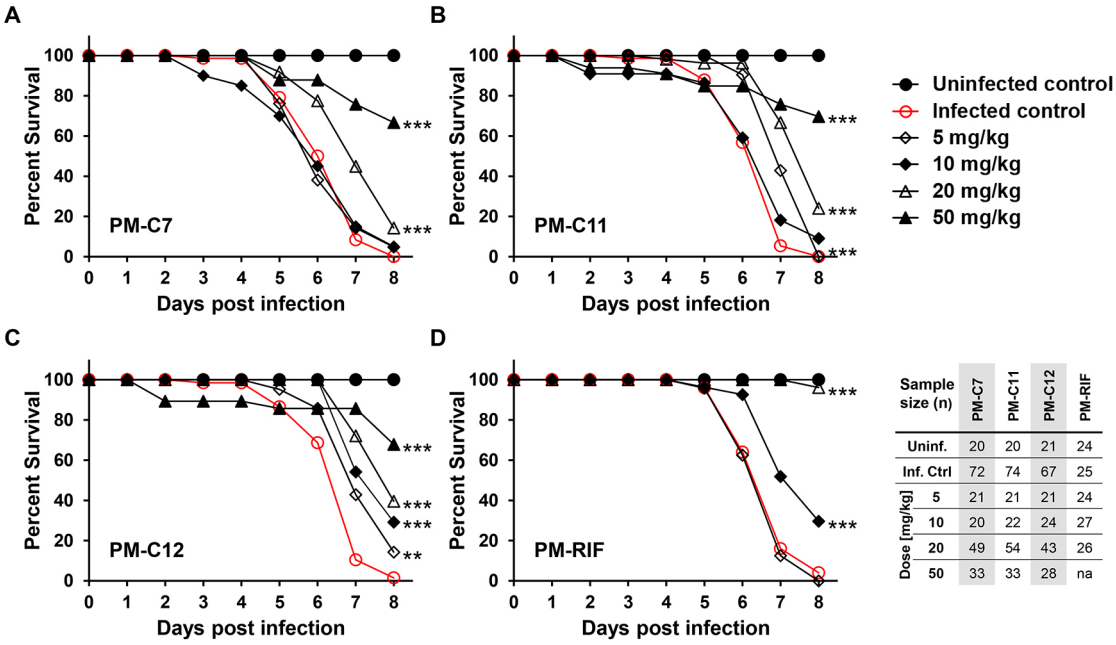

Fig. 7. *In vivo* efficacy of PM-formulated nNF derivatives against Mm infection in zebrafish embryos assessed by survival analysis. Mm-dsRed-infected zebrafish embryos were treated 1 day post infection with the indicated doses of the PM-formulated nNF derivates C7 (A), C11 (B), C12 (C) (5-50 mg/kg) or PM-formulated RIF (D) (5-20 mg/kg) by intravenous injection, and survival was recorded daily. Uninfected untreated embryos were used as a negative control (ctrl) and Mm-infected untreated embryos as an infection control group. Embryos used in this assay are the same as in the FPC assay (Fig. 6). Results are pooled from at least three independent experiments. na, not applicable. ***P*<0.01, ****P*<0.001 (log-rank test of the Kaplan–Meier estimate of survival).

extended and refined, depending on the purposes of the screening, by including additional toxicity indicators. Numerous downstream assays have been developed in the zebrafish embryo for studying tissue-specific toxic effects and mechanisms, including cardiovascular, neuro- and behavioral toxicity and genotoxicity (Cassar et al., 2020; Chakravarthy et al., 2014; Kosmehl et al., 2006). For example, the neurotoxicity of a broad range of drugs has been assessed by studying their effects on the locomotor activity of zebrafish larvae in repeated dark/light cycles (Basnet et al., 2017, 2019). Cardiotoxicity can readily be evaluated as drug-induced bradycardia in the zebrafish embryo was shown to correlate well with QT prolongation in humans (Milan et al., 2003). Importantly, findings from toxicity studies in the zebrafish embryo have been shown to generally correlate well with those obtained in rodent models, such as mice and rats (Ali et al., 2011; Ducharme et al., 2015; Vorhees et al., 2021).

Of relevance here, the zebrafish embryo is an especially well-established model for studying TB (Cronan and Tobin, 2014). Its success has spurred efforts by several research groups to use this model system for the evaluation of the *in vivo* efficacy of new anti-TB drugs. Both clinically approved drugs, such as rifampicin, isoniazid and ethambutol, as well as new drug candidates against TB have been tested in the zebrafish embryo, in part by the use of automated injection and imaging platforms (Dalton et al., 2017; Makarov et al., 2014; Ordas et al., 2015; Takaki et al., 2012). The therapeutic efficacy of anti-TB drugs in the zebrafish TB model is usually scored either by quantifying the survival of Mm-infected embryos or by assessing bacterial burden by the fluorescent pixel count method (FPC), exploiting the transparent nature of the zebrafish in conjunction with fluorescent Mm strains. It is generally accepted that FPC is a good measure of the bacterial burden in Mm-infected zebrafish (Stirling et al., 2020). However, this approach has rarely been directly compared to other methods, in particular CFU enumeration, which is commonly considered to be the gold standard for quantifying bacterial burden in mammalian models of TB (Gumbo et al., 2015).

CFU plating of homogenized whole zebrafish embryos has proven to be quite troublesome because of the high incidence of microbial contamination, most likely due to the presence of commensal bacteria in the gut of the zebrafish larvae and microbial organisms in the surrounding water (Bates et al., 2006; Rawls et al., 2004). Here, we succeeded in establishing a quick and reliable protocol for a quantitative CFU assay in Mm-infected zebrafish embryos that successfully addresses this issue. The most critical steps in our protocol are (1) the incubation of the homogenate with 1% NaOH for 10 min, which effectively eliminates bacterial contamination without affecting Mm viability, (2) the supplementation of the CFU-agar plates with amphotericin B to prevent fungal growth and kanamycin taking advantage of the reporter plasmids carrying a kanamycin resistance cassette as selective antimicrobials, and (3) the dissociation of bacterial aggregates by passaging the homogenate through a 27-gauge needle. When we directly compared the estimation of bacterial burden by CFU plating versus two fluorescence-based methods (FPC and plate reader), we found excellent concordance in the inhibitory activity of the tested drugs between these three methods. In contrast to CFU plating, which detects viable bacteria, fluorescence-based assays may not distinguish between dead and viable bacteria as fluorescent proteins, such as dsRed, can remain stable for several hours in bacteria, even after they are killed (Blokpoel et al., 2003, and our own observation). In contrast, CFU plating might not detect mycobacterial subpopulations, which are viable but grow poorly on solid agar medium (de Knegt et al., 2017; Hu et al., 2015). These two observations may explain the generally higher reduction in bacterial burden seen after drug treatment observed in CFUs compared to FPC or the plate reader assay. Therefore, using both CFU plating and FPC together could represent an ideal experimental combination to improve the accuracy of drug efficacy evaluation in the zebrafish TB embryo model by counterbalancing the drawbacks of the two assays. However, FPC is, in contrast to the classic CFU assay, a non-invasive method that allows one to conduct other assays, such as survival assays in parallel, and therefore often remains the preferred method.

In our study, we have combined several complementary assays in the zebrafish TB model to identify the best compound candidates from a previous drug whole-cell screening in terms of their anti-mycobacterial potency *in vivo*. The nNF compounds C7, C11 and C12 significantly reduced the bacterial burden in infected zebrafish, and improved their survival with minimal toxic effects. These results pinpoint the aforementioned compounds as the most promising candidates for further development and *in vivo* testing in the conventional mouse TB model.

In conclusion, the zebrafish embryo can fill a void in the preclinical evaluation of new TB drug candidates by bridging the gap between *in vitro* studies in bacterial or mammalian cell cultures and time- and cost-intensive *in vivo* studies in mammalian TB models. In a time frame of less than 2 weeks, the zebrafish embryo model can provide valuable information about both the *in vivo* toxicity and efficacy of anti-TB candidate drugs, and thus facilitate the identification of the most promising candidate drugs for further evaluation. The use of nanoparticle technology enables the evaluation of even poorly water-soluble drugs *in vivo*, which otherwise would be difficult to study. Last, but not least, the use of the zebrafish embryo satisfies the desirable principles of reduce, replace and refine (3Rs) for animal studies (NC3Rs, 2021). *In vivo* studies in the zebrafish embryo can efficiently eliminate compounds with significant *in vivo* toxicity and provide important information about the toxic or therapeutic dose range of anti-TB compounds. This, in turn, can contribute to the refinement of experiments in higher vertebrates, such as mice and rats, and reduce the number of animals needed at a later stage in the drug discovery process.

MATERIALS AND METHODS

Anti-TB candidate compounds

nNF derivatives C4, C7, C11, C12, C16 and C20 were selected from a set of 15 nNFs derivatives that were identified as being active against Mtb in a phenotypic HTS campaign at the Institute Pasteur. The selection was made according to their high *in vitro* activity against Mtb (MIC_{90}<8 µg/ml), and their low (C4, C7, C11 and C12; CC_{50}>65 µg/ml) or intermediate (C20; CC_{50}=9 µg/ml) cytotoxicity in VERO cells (data not published). This resulted in a selectivity index (SI), as calculated by the ratio of the CC_{50} to MIC_{90}, of higher than 12.5 for all compounds. The SI measures the window between cytotoxicity and anti-Mtb activity, and is commonly used to evaluate the safety of new compounds for further development after initial screenings (Manjunatha and Smith, 2015; Orme, 2001). The highly cytotoxic compound C16 (CC_{50}=0.3 µg/ml), also known as R7000 (Quillardet et al., 2000), was included in the study and used as a toxicity reference. The water solubility of all the nNF derivatives used in this study was lower than 12 µg/ml.

Preparation of PM drug formulation

Drug-loaded PMs were prepared with the amphiphilic block co-polymer pGlu(OBn)-block-pSar in combination with the appropriate compound by dual asymmetric centrifugation, as described by Fenaroli et al. (2018). Briefly, the amphiphilic block co-polymer was mixed with the different

compounds at a weight ratio specified in Table S2, and centrifugation was performed for 30 min at 3500 rpm with a dual asymmetric centrifuge (SpeedMixer DAC 150.1 CM, Hauschild). The resulting slightly milky solution containing the drug-loaded PM was collected and the size of the PM was measured in 10 mM NaCl by dynamic light scattering, and the surface charge by zeta-potential analysis using a Zetasizer (Malvern Panalytical, UK).

Bacterial cultures

Mm wild-type M strain and M strain expressing dsRed (Mm-dsRed) were obtained from Dr Monica Hagedorn (Bernhard Nocht Institute for Tropical Medicine, Hamburg, Germany). Mm-dsRed expresses the recombinant fluorescent protein dsRed under the control of the MSP12 promoter and carries a kanamycin resistance cassette. Both Mm strains were grown in Middlebrook 7H9 broth (BD Biosciences, Heidelberg, Germany) supplemented with 10% albumin-dextrose-catalase (ADC) and 0.05% tyloxapol (referred to as complete 7H9 medium) at 31.5°C in the dark without agitation. Kanamycin (25 µg/ml, Sigma-Aldrich) was added to the culture medium of Mm-dsRed.

Determination of the MIC_{90} of nNF derivatives in *M. marinum*

The MIC_{90} for nNF derivatives was determined using the resazurin microtiter assay adapted from Franzblau et al. (1998). Briefly, twofold serial dilutions of nNF compounds in a concentration range of 16 µg/ml to 0.008 µg/ml were prepared in sterile 96-well plates using Middlebrook 7H9 broth supplemented with 10% Oleic acid-ADC (OADC). The final concentration of DMSO was kept below 1% in each well. For inoculation, $1\text{-}3\times10^3$ bacteria were added to each well and plates were incubated in sealed plastic bags at 31.5°C for 72 h. Then, resazurin sodium salt (Sigma-Aldrich) was added at a final concentration of 0.003%, and plates were incubated for an additional 48 h. Finally, fluorescence was measured at an excitation wavelength of 535 nm and emission wavelength of 590 nm using a microplate reader (Synergy H1, BioTek). The MIC_{90} was defined as the lowest concentration at which the fluorescence value was equal or lower than 10% of the value for the untreated control.

Isolation of bone marrow-derived macrophages

Wild-type C57BL/6 mice were purchased from Janvier Labs (Le Genest-Saint-Isle, France). BMDMs were prepared as described previously (Speth et al., 2017). Briefly, bone marrow was flushed from the tibias and femurs of 8-12-week-old mice and red blood cells were removed by incubation in RBC lysis buffer (Sigma-Aldrich). Bone marrow cells were then incubated in RPMI medium/10% fetal calf serum (FCS) supplemented with 30% L929 conditioned medium in non-tissue culture-treated dishes at 37°C in a humidified atmosphere containing 5% CO_2 for 7 days, with medium changes after 3 and 6 days. Differentiated BMDMs were harvested, frozen and stored at −80°C until use. Throughout the experiments, BMDMs were maintained in RPMI medium/10% FCS supplemented with 10% L929-conditioned medium (complete BMDM medium).

Anti-mycobacterial efficacy of nNF derivatives in *M. marinum*-infected BMDMs

BMDMs were seeded in 48-well plates at 1.2×10^5 cells per well in complete BMDM medium and incubated overnight at 32.5°C in a humidified atmosphere containing 5% CO_2. Mid-log phase Mm cultures were washed three times with PBS/0.05% tyloxapol, sonicated in a bath sonicator for 10 min and passed ten times through a 27 G needle to disrupt bacterial aggregates and to produce a single cell suspension. The bacterial suspension was then diluted in RPMI/10% FCS and used to infect BMDM cultures at a multiplicity of infection (MOI) of 0.1 for 3 h at 32.5°C, which is within the optimal growth temperature range of Mm and is well tolerated by mouse macrophages (Carlsson et al., 2010; Ramakrishnan and Falkow, 1994; Stamm et al., 2003). BMDM cultures were washed three times with prewarmed PBS and incubated in complete BMDM medium containing 100 µg/ml amikacin for 1 h to kill remaining extracellular bacteria. After one wash with prewarmed PBS, infected BMDMs were incubated in complete BMDM medium for an additional 24 h at 32.5°C. Then, nNF derivatives were added to the infected BMDMs at concentrations in the range of 0.125× to 32× their respective MIC_{90}, and BMDM cultures were incubated for 3 days at 32.5°C. The final concentration of DMSO was kept at 1% for all groups, and BMDMs incubated with 1% DMSO in BMDM medium were used as a negative control. After 72 h of nNF treatment, BMDMs were washed with prewarmed PBS and lysed in 0.005% SDS. Viable intracellular bacteria were quantified by performing serial dilutions of the lysates and plating on Middlebrook 7H10 agar plates supplemented with 10% OADC. Plates were incubated at 31.5°C up to 10 days before CFUs were counted.

Zebrafish embryo husbandry

Wild-type zebrafish embryos were obtained from the zebrafish facility at the Faculty of Medicine, University of Oslo, Norway, and at the Norwegian University of Life Sciences, Oslo, Norway. Zebrafish embryos were kept at 28.5°C in embryo water supplemented with 0.003% phenylthiourea (Sigma-Aldrich) to inhibit melanization, and water was changed daily for the duration of the experiment. Experiments using zebrafish embryos and larvae were conducted in agreement with the provisions enforced by the national animal research authority at the Norwegian Food Safety Authority (Mattilsynet).

Microinjection of the zebrafish embryo in the posterior caudal vein

Microinjections in the PCV of zebrafish embryos were performed as described previously (Fenaroli et al., 2014). Briefly, borosilicate microneedles (GC100T-10, Harvard Instruments) were prepared using a pipet puller (P-97, Sutter Instruments) and backfilled with a solution containing Mm for infection or PM-formulated nNF derivatives for treatment. Zebrafish embryos were sedated by immersion in embryo water supplemented with 0.02% tricaine (Finquel) and placed on a plate containing 2% agarose. Injections were conducted under a stereomicroscope (Leica DFC365FX) using a micromanipulator (Narishige MN-153) and a microinjector pump (Eppendorf Femtojet Express pump). Drug doses (mg/kg) were calculated based on an assumed weight of ∼1 mg for zebrafish embryos at 2-3 days post fertilization (dpf) (Fenaroli et al., 2014; Hu et al., 2000; Vibe et al., 2016).

In vivo toxicity assays in zebrafish larvae

Zebrafish embryos received different doses of PM-formulated nNF derivatives by PCV microinjection at 2 dpf, and mortality was recorded twice a day until 8 days post treatment (dpt). Dead or dying embryos were recorded, removed and euthanized if necessary.

In vivo toxicity of PM-formulated nNF derivatives causing low mortality was evaluated in more detail by establishing a toxicity score in individual larvae based on morphological and physiological indicators of toxicity as described previously (Palha et al., 2013; Vibe et al., 2016). Indicators of toxicity and their criteria for scoring drug toxicity are summarized in Table 1. For this screening, zebrafish embryos were microinjected at 2 dpf with the highest dose (50 mg/kg) of PM-formulated nNF derivatives or PBS as a negative control, and were analyzed at day 4 post treatment. For each indicator, a value of 1 was assigned if signs of toxicity were present, and a value of 0 if absent. The toxicity score for individual larvae was then calculated as the sum of the values assigned to the toxicity indicators with a maximal possible value of 7.

In vivo efficacy assays in zebrafish larvae

Zebrafish embryos at 2 dpf were infected by injecting ∼500 CFU (5 nl of 10^8 CFU/ml) of Mm-dsRed in the PCV. The embryos were allowed to recover for 24 h before receiving different treatment formulations by PCV injection. Different doses were administered by adjusting the injected volume or by different dilutions of the treatment formulation.

Zebrafish survival study

Zebrafish embryos were checked 1 h after the treatment injection, and only alive and healthy fish were included in the experiment. Survival of embryos was recorded daily for all groups at the same time, and dead embryos or embryos at the humane endpoint were removed and euthanized if necessary. The humane endpoint was defined by the presence of one

or more of the following criteria: a heartbeat below 50 beats per minute, the presence of more than one edema and a severely malformed body shape.

Determination of bacterial burden by fluorescent pixel count

Mm-infected zebrafish embryos were imaged at day 4 post treatment using a Leica DFC365FX stereomicroscope, with a 1.0× planapo lens obtaining images of the whole fish (30× magnification). The FPC for each individual embryo was quantified using a customized macro in ImageJ (National Institutes of Health), which is accessible at www.github.com/wohlmann/ZF_FPC. Briefly, background noise and autofluorescence were removed by applying a lower threshold filter, and the total fluorescence of Mm-dsRed in individual embryos was calculated as the sum of pixel fluorescence intensity values.

Determination of bacterial burden by plate reader assay and colony forming unit enumeration

At 4 dpt, zebrafish embryos were euthanized by an overdose with tricaine (3 mg/ml) and carefully rinsed in PBS. Between 10 and 15 larvae in a volume of 500 µl were transferred into a lysing matrix tube containing 1.4 mm ceramic spheres (MP Biomedical). Homogenization was performed using a FastPrep FP120 cell disrupter (Therma; settings: speed=4, time=10 s) and homogenates were placed on ice for 5 min.

For the plate reader assay, 100 µl of the homogenate was transferred to a black 96-well plate and fluorescence was measured at an absorption wavelength of 550 nm and emission wavelength of 583 nm using a microplate reader (Synergy H1, BioTek).

For CFU plating, the homogenate was transferred to a microcentrifugation tube and passed ten times through a 27 G needle to disrupt mycobacterial clumps. Then, NaOH was added to a final concentration of 1% and incubated at room temperature for 10 min before serial dilutions in PBS were plated on 7H10/10% OADC agar plates containing 10 µg/ml amphotericin B and 25 µg/ml kanamycin A. Plates were incubated at 31.5°C for up to 14 days before CFUs were enumerated.

Statistics

All statistical analysis was performed using GraphPad Prism 8 (GraphPad Software, San Diego, CA, USA). The normality of data distribution for control and treatment groups was tested using the D'Agostino–Pearson normality test. In the toxicity score and FPC experiments, treatment groups were compared to the control group using the non-parametric Kruskal–Wallis H test followed by post-hoc analysis using Dunn's multiple comparisons test. The effect of treatment on the survival of Mm-infected zebrafish embryos was analyzed using a log-rank test of the Kaplan–Meier estimate of survival.

Competing interests

The authors declare no competing or financial interests.

Author contributions

Conceptualization: N.K.D., M.S., N.A.-R.; Methodology: N.K.D., M.S., K.J., F.F., N.A.-R.; Software: Validation: N.K.D., M.S., F.F.; Formal analysis: N.K.D., M.S., K.J., N.A.-R.; Investigation: N.K.D., M.S., C.B., N.A.-R.; Resources: N.K.D., M.S., K.J., M.B., C.B., B.G., G.G., N.A.-R.; Data curation: N.K.D., M.S., N.A.-R.; Writing - original draft: M.S.; Writing - review & editing: N.K.D., G.G., N.A.-R.; Visualization: N.K.D., M.S.; Supervision: F.F., G.G., N.A.-R.; Project administration: N.K.D., M.S., G.G., N.A.-R.; Funding acquisition: G.G., N.A.-R.

Funding

This work was supported by the European Seventh Framework Programme Nanotherapeutics against Resistant Emerging Bacterial Pathogens (project 604237); the European Union Horizon 2020 research and innovation program under an H2020 Marie Skłodowska-Curie Actions grant (609020); and Norges Forskningsråd (275873 and 273319).

References

Ali, S., van Mil, H. G. and Richardson, M. K. (2011). Large-scale assessment of the zebrafish embryo as a possible predictive model in toxicity testing. *PLoS ONE* **6**, e21076. doi:10.1371/journal.pone.0021076

Andreu, N., Zelmer, A., Sampson, S. L., Ikeh, M., Bancroft, G. J., Schaible, U. E., Wiles, S. and Robertson, B. D. (2013). Rapid *in vivo* assessment of drug efficacy against *Mycobacterium tuberculosis* using an improved firefly luciferase. *J. Antimicrob. Chemother.* **68**, 2118-2127. doi:10.1093/jac/dkt155

Balganesh, T. S., Balasubramanian, V. and Kumar, S. A. (2004). Drug discovery for tuberculosis: Bottlenecks and path forward. *Curr. Sci.* **86**, 167-176.

Bandodkar, B., Shandil, R. K., Bhat, J. and Balganesh, T. S. (2020). Two decades of TB drug discovery efforts-what have we learned? *Appl. Sci.* **10**, 5704. doi:10.3390/app10165704

Basnet, R. M., Guarienti, M. and Memo, M. (2017). Zebrafish embryo as an in vivo model for behavioral and pharmacological characterization of methylxanthine drugs. *Int. J. Mol. Sci.* **18**, 596. doi:10.3390/ijms18030596

Basnet, R. M., Zizioli, D., Taweedet, S., Finazzi, D. and Memo, M. (2019). Zebrafish larvae as a behavioral model in neuropharmacology. *Biomedicines* **7**, 23. doi:10.3390/biomedicines7010023

Bates, J. M., Mittge, E., Kuhlman, J., Baden, K. N., Cheesman, S. E. and Guillemin, K. (2006). Distinct signals from the microbiota promote different aspects of zebrafish gut differentiation. *Dev. Biol.* **297**, 374-386. doi:10.1016/j.ydbio.2006.05.006

Blokpoel, M. C. J., O'Toole, R., Smeulders, M. J. and Williams, H. D. (2003). Development and application of unstable GFP variants to kinetic studies of mycobacterial gene expression. *J. Microbiol. Methods* **54**, 203-211. doi:10.1016/S0167-7012(03)00044-7

Carlsson, F., Kim, J., Dumitru, C., Barck, K. H., Carano, R. A. D., Sun, M., Diehl, L. and Brown, E. J. (2010). Host-detrimental role of Esx-1-mediated inflammasome activation in mycobacterial infection. *PLoS Pathog.* **6**, e1000895. doi:10.1371/journal.ppat.1000895

Carvalho, R., de Sonneville, J., Stockhammer, O. W., Savage, N. D. L., Veneman, W. J., Ottenhoff, T. H. M., Dirks, R. P., Meijer, A. H. and Spaink, H. P. (2011). A high-throughput screen for tuberculosis progression. *PLoS ONE* **6**, e16779. doi:10.1371/journal.pone.0016779

Cassar, S., Adatto, I., Freeman, J. L., Gamse, J. T., Iturria, I., Lawrence, C., Muriana, A., Peterson, R. T., Van Cruchten, S. and Zon, L. I. (2020). Use of zebrafish in drug discovery toxicology. *Chem. Res. Toxicol.* **33**, 95-118. doi:10.1021/acs.chemrestox.9b00335

Chakravarthy, S., Sadagopan, S., Nair, A. and Sukumaran, S. K. (2014). Zebrafish as an *in vivo* high-throughput model for genotoxicity. *Zebrafish* **11**, 154-166. doi:10.1089/zeb.2013.0924

Cornet, C., Calzolari, S., Miñana-Prieto, R., Dyballa, S., van Doornmalen, E., Rutjes, H., Savy, T., D'Amico, D. and Terriente, J. (2017). ZeGlobalTox: an innovative approach to address organ drug toxicity using zebrafish. *Int. J. Mol. Sci.* **18**, 864. doi:10.3390/ijms18040864

Cronan, M. R. and Tobin, D. M. (2014). Fit for consumption: zebrafish as a model for tuberculosis. *Dis. Model. Mech.* **7**, 777-784. doi:10.1242/dmm.016089

Dal, N. J. K., Kocere, A., Wohlmann, J., Van Herck, S., Bauer, T. A., Resseguier, J., Bagherifam, S., Hyldmo, H., Barz, M., De Geest, B. G. et al. (2020). Zebrafish embryos allow prediction of nanoparticle circulation times in mice and facilitate quantification of nanoparticle-cell interactions. *Small* **16**, e1906719. doi:10.1002/smll.201906719

Dalton, J. P., Uy, B., Okuda, K. S., Hall, C. J., Denny, W. A., Crosier, P. S., Swift, S. and Wiles, S. (2017). Screening of anti-mycobacterial compounds in a naturally infected zebrafish larvae model. *J. Antimicrob. Chemother.* **72**, 421-427. doi:10.1093/jac/dkw421

Davis, J. M., Clay, H., Lewis, J. L., Ghori, N., Herbomel, P. and Ramakrishnan, L. (2002). Real-time visualization of mycobacterium-macrophage interactions leading to initiation of granuloma formation in zebrafish embryos. *Immunity* **17**, 693-702. doi:10.1016/S1074-7613(02)00475-2

de Knegt, G. J., Dickinson, L., Pertinez, H., Evangelopoulos, D., McHugh, T. D., Bakker-Woudenberg, I., Davies, G. R. and de Steenwinkel, J. E. M. (2017). Assessment of treatment response by colony forming units, time to culture positivity and the molecular bacterial load assay compared in a mouse tuberculosis model. *Tuberculosis (Edinb.)* **105**, 113-118. doi:10.1016/j.tube.2017.05.002

Di, L., Fish, P. V. and Mano, T. (2012). Bridging solubility between drug discovery and development. *Drug Discov. Today* **17**, 486-495. doi:10.1016/j.drudis.2011.11.007

Ducharme, N. A., Reif, D. M., Gustafsson, J.-A. and Bondesson, M. (2015). Comparison of toxicity values across zebrafish early life stages and mammalian studies: Implications for chemical testing. *Reprod. Toxicol.* **55**, 3-10. doi:10.1016/j.reprotox.2014.09.005

Dyballa, S., Minana, R., Rubio-Brotons, M., Cornet, C., Pederzani, T., Escaramis, G., Garcia-Serna, R., Mestres, J. and Terriente, J. (2019). Comparison of zebrafish larvae and hiPSC cardiomyocytes for predicting drug induced cardiotoxicity in humans. *Toxicol. Sci.* **171**, 283-295. doi:10.1093/toxsci/kfz165

Fenaroli, F., Westmoreland, D., Benjaminsen, J., Kolstad, T., Skjeldal, F. M., Meijer, A. H., van der Vaart, M., Ulanova, L., Roos, N., Nyström, B. et al. (2014). Nanoparticles as drug delivery system against tuberculosis in zebrafish embryos: direct visualization and treatment. *ACS Nano* **8**, 7014-7026. doi:10.1021/nn5019126

Fenaroli, F., Repnik, U., Xu, Y., Johann, K., Van Herck, S., Dey, P., Skjeldal, F. M., Frei, D. M., Bagherifam, S., Kocere, A. et al. (2018). Enhanced permeability and retention-like extravasation of nanoparticles from the vasculature into tuberculosis granulomas in zebrafish and mouse models. *ACS Nano* **12**, 8646-8661. doi:10.1021/acsnano.8b04433

Franzblau, S. G., Witzig, R. S., McLaughlin, J. C., Torres, P., Madico, G., Hernandez, A., Degnan, M. T., Cook, M. B., Quenzer, V. K., Ferguson, R. M. et al. (1998). Rapid, low-technology MIC determination with clinical Mycobacterium tuberculosis isolates by using the microplate Alamar Blue assay. *J. Clin. Microbiol.* **36**, 362-366. doi:10.1128/JCM.36.2.362-366.1998

Goldman, R. C. (2013). Why are membrane targets discovered by phenotypic screens and genome sequencing in Mycobacterium tuberculosis? *Tuberculosis (Edinb.)* **93**, 569-588. doi:10.1016/j.tube.2013.09.003

Griffiths, G., Nyström, B., Sable, S. B. and Khuller, G. K. (2010). Nanobead-based interventions for the treatment and prevention of tuberculosis. *Nat. Rev. Microbiol.* **8**, 827-834. doi:10.1038/nrmicro2437

Grotz, E., Tateosian, N., Amiano, N., Cagel, M., Bernabeu, E., Chiappetta, D. A. and Moretton, M. A. (2018). Nanotechnology in tuberculosis: state of the art and the challenges ahead. *Pharm. Res.* **35**, 213. doi:10.1007/s11095-018-2497-z

Grzelak, E. M., Choules, M. P., Gao, W., Cai, G., Wan, B., Wang, Y., McAlpine, J. B., Cheng, J., Jin, Y., Lee, H. et al. (2019). Strategies in anti-*Mycobacterium tuberculosis* drug discovery based on phenotypic screening. *J. Antibiot. (Tokyo)* **72**, 719-728. doi:10.1038/s41429-019-0205-9

Gumbo, T., Lenaerts, A. J., Hanna, D., Romero, K. and Nuermberger, E. (2015). Nonclinical models for antituberculosis drug development: a landscape analysis. *J. Infect. Dis.* **211** Suppl. 3, S83-S95. doi:10.1093/infdis/jiv183

Gurumurthy, M., Mukherjee, T., Dowd, C. S., Singh, R., Niyomrattanakit, P., Tay, J. A., Nayyar, A., Lee, Y. S., Cherian, J., Boshoff, H. I. et al. (2012). Substrate specificity of the deazaflavin-dependent nitroreductase from *Mycobacterium tuberculosis* responsible for the bioreductive activation of bicyclic nitroimidazoles. *FEBS J.* **279**, 113-125. doi:10.1111/j.1742-4658.2011.08404.x

Hall, B. S., Bot, C. and Wilkinson, S. R. (2011). Nifurtimox activation by trypanosomal type I nitroreductases generates cytotoxic nitrile metabolites. *J. Biol. Chem.* **286**, 13088-13095. doi:10.1074/jbc.M111.230847

Houben, R. M. G. J. and Dodd, P. J. (2016). The global burden of latent tuberculosis infection: a re-estimation using mathematical modelling. *PLoS Med.* **13**, e1002152. doi:10.1371/journal.pmed.1002152

Hu, N., Sedmera, D., Yost, H. J. and Clark, E. B. (2000). Structure and function of the developing zebrafish heart. *Anat. Rec.* **260**, 148-157. doi:10.1002/1097-0185(20001001)260:2<148::AID-AR50>3.0.CO;2-X

Hu, Y., Liu, A., Ortega-Muro, F., Alameda-Martin, L., Mitchison, D. and Coates, A. (2015). High-dose rifampicin kills persisters, shortens treatment duration, and reduces relapse rate *in vitro* and *in vivo*. *Front. Microbiol.* **6**, 641. doi:10.3389/fmicb.2015.00641

Johansen, M. D., Kasparian, J. A., Hortle, E., Britton, W. J., Purdie, A. C. and Oehlers, S. H. (2018). *Mycobacterium marinum* infection drives foam cell differentiation in zebrafish infection models. *Dev. Comp. Immunol.* **88**, 169-172. doi:10.1016/j.dci.2018.07.022

Keseru, G. M. and Makara, G. M. (2009). The influence of lead discovery strategies on the properties of drug candidates. *Nat. Rev. Drug Discov.* **8**, 203-212. doi:10.1038/nrd2796

Kirtane, A. R., Verma, M., Karandikar, P., Furin, J., Langer, R. and Traverso, G. (2021). Nanotechnology approaches for global infectious diseases. *Nat. Nanotechnol.* **16**, 369-384. doi:10.1038/s41565-021-00866-8

Kondreddi, R. R., Jiricek, J., Rao, S. P. S., Lakshminarayana, S. B., Camacho, L. R., Rao, R., Herve, M., Bifani, P., Ma, N. L., Kuhen, K. et al. (2013). Design, synthesis, and biological evaluation of indole-2-carboxamides: a promising class of antituberculosis agents. *J. Med. Chem.* **56**, 8849-8859. doi:10.1021/jm4012774

Kosmehl, T., Hallare, A. V., Reifferscheid, G., Manz, W., Braunbeck, T. and Hollert, H. (2006). A novel contact assay for testing genotoxicity of chemicals and whole sediments in zebrafish embryos. *Environ. Toxicol. Chem.* **25**, 2097-2106. doi:10.1897/05-460R.1

Lange, C., Chesov, D., Heyckendorf, J., Leung, C. C., Udwadia, Z. and Dheda, K. (2018). Drug-resistant tuberculosis: an update on disease burden, diagnosis and treatment. *Respirology* **23**, 656-673. doi:10.1111/resp.13304

Lipinski, C. A. (2000). Drug-like properties and the causes of poor solubility and poor permeability. *J. Pharmacol. Toxicol. Methods* **44**, 235-249. doi:10.1016/S1056-8719(00)00107-6

Machado, D., Girardini, M., Viveiros, M. and Pieroni, M. (2018). Challenging the drug-likeness dogma for new drug discovery in tuberculosis. *Front. Microbiol.* **9**, 1367. doi:10.3389/fmicb.2018.01367

MacRae, C. A. and Peterson, R. T. (2015). Zebrafish as tools for drug discovery. *Nat. Rev. Drug Discov.* **14**, 721-731. doi:10.1038/nrd4627

Makarov, V., Lechartier, B., Zhang, M., Neres, J., van der Sar, A. M., Raadsen, S. A., Hartkoorn, R. C., Ryabova, O. B., Vocat, A., Decosterd, L. A. et al. (2014). Towards a new combination therapy for tuberculosis with next generation benzothiazinones. *EMBO Mol. Med.* **6**, 372-383. doi:10.1002/emmm.201303575

Manjunatha, U. H. and Smith, P. W. (2015). Perspective: challenges and opportunities in TB drug discovery from phenotypic screening. *Bioorg. Med. Chem.* **23**, 5087-5097. doi:10.1016/j.bmc.2014.12.031

Melariri, P., Kalombo, L., Nkuna, P., Dube, A., Hayeshi, R., Ogutu, B., Gibhard, L., deKock, C., Smith, P., Wiesner, L. et al. (2015). Oral lipid-based nanoformulation of tafenoquine enhanced bioavailability and blood stage antimalarial efficacy and led to a reduction in human red blood cell loss in mice. *Int. J. Nanomedicine* **10**, 1493-1503. doi:10.2147/IJN.S76317

Milan, D. J., Peterson, T. A., Ruskin, J. N., Peterson, R. T. and MacRae, C. A. (2003). Drugs that induce repolarization abnormalities cause bradycardia in zebrafish. *Circulation* **107**, 1355-1358. doi:10.1161/01.CIR.0000061912.88753.87

Mitchell, M. J., Billingsley, M. M., Haley, R. M., Wechsler, M. E., Peppas, N. A. and Langer, R. (2021). Engineering precision nanoparticles for drug delivery. *Nat. Rev. Drug Discov.* **20**, 101-124. doi:10.1038/s41573-020-0090-8

Ordas, A., Raterink, R.-J., Cunningham, F., Jansen, H. J., Wiweger, M. I., Jong-Raadsen, S., Bos, S., Bates, R. H., Barros, D., Meijer, A. H. et al. (2015). Testing tuberculosis drug efficacy in a zebrafish high-throughput translational medicine screen. *Antimicrob. Agents Chemother.* **59**, 753-762. doi:10.1128/AAC.03588-14

Orme, I. (2001). Search for new drugs for treatment of tuberculosis. *Antimicrob. Agents Chemother.* **45**, 1943-1946. doi:10.1128/AAC.45.7.1943-1946.2001

Palha, N., Guivel-Benhassine, F., Briolat, V., Lutfalla, G., Sourisseau, M., Ellett, F., Wang, C.-H., Lieschke, G. J., Herbomel, P., Schwartz, O. et al. (2013). Real-time whole-body visualization of chikungunya virus infection and host interferon response in zebrafish. *PLoS Pathog.* **9**, e1003619. doi:10.1371/journal.ppat.1003619

Patterson, S. and Fairlamb, A. H. (2019). Current and future prospects of nitro-compounds as drugs for trypanosomiasis and leishmaniasis. *Curr. Med. Chem.* **26**, 4454-4475. doi:10.2174/0929867325666180426164352

Quillardet, P., Michel, V., Arrault, X., Hofnung, M. and Touati, E. (2000). Mutagenic properties of a nitrofuran, 7-methoxy-2-nitronaphtho[2, 1-*b*]furan (R7000), in *lacI* transgenic mice. *Mutat. Res.* **470**, 177-188. doi:10.1016/S1383-5718(00)00103-0

Ramakrishnan, L. and Falkow, S. (1994). Mycobacterium marinum persists in cultured mammalian cells in a temperature-restricted fashion. *Infect. Immun.* **62**, 3222-3229. doi:10.1128/iai.62.8.3222-3229.1994

Rawls, J. F., Samuel, B. S. and Gordon, J. I. (2004). Gnotobiotic zebrafish reveal evolutionarily conserved responses to the gut microbiota. *Proc. Natl. Acad. Sci. USA* **101**, 4596-4601. doi:10.1073/pnas.0400706101

Rice, A. M., Long, Y. and King, S. B. (2021). Nitroaromatic antibiotics as nitrogen oxide sources. *Biomolecules* **11**, 267. doi:10.3390/biom11020267

Sharma, A., Sharma, S. and Khuller, G. K. (2004). Lectin-functionalized poly (lactide-co-glycolide) nanoparticles as oral/aerosolized antitubercular drug carriers for treatment of tuberculosis. *J. Antimicrob. Chemother.* **54**, 761-766. doi:10.1093/jac/dkh411

Singh, R., Manjunatha, U., Boshoff, H. I. M., Ha, Y. H., Niyomrattanakit, P., Ledwidge, R., Dowd, C. S., Lee, I. Y., Kim, P., Zhang, L. et al. (2008). PA-824 kills nonreplicating *Mycobacterium tuberculosis* by intracellular NO release. *Science* **322**, 1392-1395. doi:10.1126/science.1164571

Speth, M. T., Repnik, U., Müller, E., Spanier, J., Kalinke, U., Corthay, A. and Griffiths, G. (2017). Poly(I:C)-encapsulating nanoparticles enhance innate immune responses to the tuberculosis vaccine bacille Calmette-Guerin (BCG) via synergistic activation of innate immune receptors. *Mol. Pharm.* **14**, 4098-4112. doi:10.1021/acs.molpharmaceut.7b00795

Stamm, L. M., Morisaki, J. H., Gao, L.-Y., Jeng, R. L., McDonald, K. L., Roth, R., Takeshita, S., Heuser, J., Welch, M. D. and Brown, E. J. (2003). *Mycobacterium marinum* escapes from phagosomes and is propelled by actin-based motility. *J. Exp. Med.* **198**, 1361-1368. doi:10.1084/jem.20031072

Stirling, D. R., Suleyman, O., Gil, E., Elks, P. M., Torraca, V., Noursadeghi, M. and Tomlinson, G. S. (2020). Analysis tools to quantify dissemination of pathology in zebrafish larvae. *Sci. Rep.* **10**, 3149. doi:10.1038/s41598-020-59932-1

Takaki, K., Cosma, C. L., Troll, M. A. and Ramakrishnan, L. (2012). An in vivo platform for rapid high-throughput antitubercular drug discovery. *Cell Rep.* **2**, 175-184. doi:10.1016/j.celrep.2012.06.008

Tarcsay, A. and Keseru, G. M. (2013). Contributions of molecular properties to drug promiscuity. *J. Med. Chem.* **56**, 1789-1795. doi:10.1021/jm301514n

Tobin, D. M. and Ramakrishnan, L. (2008). Comparative pathogenesis of *Mycobacterium marinum* and *Mycobacterium tuberculosis*. *Cell. Microbiol.* **10**, 1027-1039. doi:10.1111/j.1462-5822.2008.01133.x

Trousil, J., Syrová, Z., Dal, N.-J. K., Rak, D., Konefal, R., Pavlova, E., Matějková, J., Cmarko, D., Kubickova, P., Pavlis, O. et al. (2019). Rifampicin nanoformulation enhances treatment of tuberculosis in Zebrafish. *Biomacromolecules* **20**, 1798-1815. doi:10.1021/acs.biomac.9b00214

Vibe, C. B., Fenaroli, F., Pires, D., Wilson, S. R., Bogoeva, V., Kalluru, R., Speth, M., Anes, E., Griffiths, G. and Hildahl, J. (2016). Thioridazine in PLGA

nanoparticles reduces toxicity and improves rifampicin therapy against mycobacterial infection in zebrafish. *Nanotoxicology* **10**, 680-688. doi:10.3109/17435390.2015.1107146

Volkman, H. E., Clay, H., Beery, D., Chang, J. C. W., Sherman, D. R. and Ramakrishnan, L. (2004). Tuberculous granuloma formation is enhanced by a mycobacterium virulence determinant. *PLoS Biol.* **2**, e367. doi:10.1371/journal.pbio.0020367

Vorhees, C. V., Williams, M. T., Hawkey, A. B. and Levin, E. D. (2021). Translating neurobehavioral toxicity across species from zebrafish to rats to humans: implications for risk assessment. *Front. Toxicol.* **3**. doi:10.3389/ftox.2021.629229

Waring, M. J. (2010). Lipophilicity in drug discovery. *Expert Opin. Drug Discov.* **5**, 235-248. doi:10.1517/17460441003605098

Wellington, S. and Hung, D. T. (2018). The expanding diversity of mycobacterium tuberculosis drug targets. *ACS Infect. Dis.* **4**, 696-714. doi:10.1021/acsinfecdis.7b00255

World Health Organization. (2020). Global tuberculosis report 2020. Geneva. https://www.who.int/publications/i/item/9789240013131

Zhang, G., Truong, L., Tanguay, R. L. and Reif, D. M. (2017). A new statistical approach to characterize chemical-elicited behavioral effects in high-throughput studies using zebrafish. *PLoS ONE* **12**, e0169408. doi:10.1371/journal.pone.0169408